1990

Salobo Sequence, Carajas, Brazil: Geology, Geochemistry And Metamorphism

Zara Gerhardt Lindenmayer

SALOBO SEQUENCE, CARAJÁS, BRAZIL: GEOLOGY, GEOCHEMISTRY AND METAMORPHISM

by

Zara Gerhardt Lindenmayer

Department of Geology

Submitted in partial fulfilment
of the requirements for the degree of
Doctor of Philosophy

Faculty of Graduate Studies
The University of Western Ontario
London, Ontario
October, 1990

ISBN 0-315-64264-5

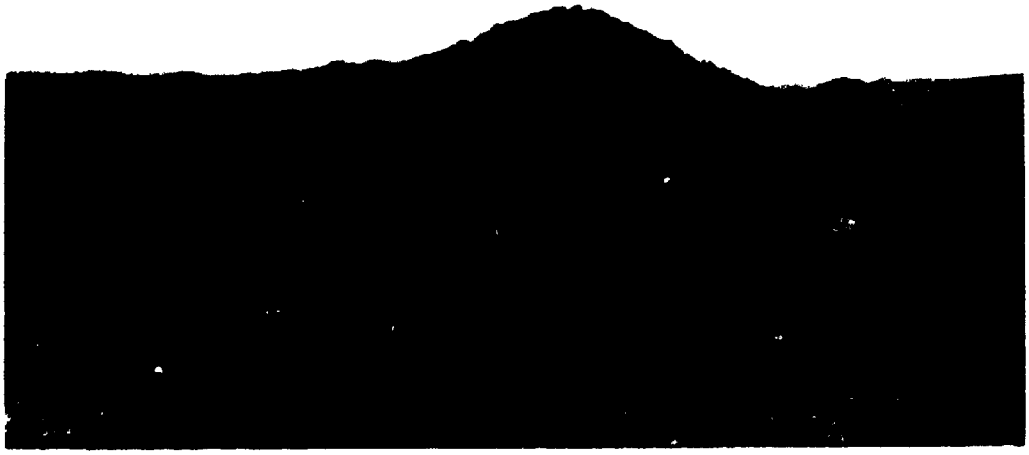

Aerial view of the Salobo copper deposit

ABSTRACT

The Salobo Cu (Au, Ag, Mo) deposit is in the Carajas basin, located in the eastern Amazon craton, southern Para state, Brazil.

The Salobo sequence at the deposit area comprises metamorphosed basaltic rocks, iron formations, graywackes and arkosic arenites deposited at 2758+/-2 Ma on a trondhjemitic basement dated at 2851+/-4 Ma. The amphibolites are continental tholeiitic basalts, indicated by Fe, LIL and LREE enrichment, LREE fractionation and almost flat HREE chondrite-normalized patterns. Silicate-type iron formation grades to an aluminous type and finally to metagraywackes. Geochemical studies show a continuous compositional variation between both iron formation types, with gradual Al, K, Ti and Zr increase and Fe and Si decrease, defining a mixing line between chemical iron formation and volcaniclastic contaminants of the Grao Pará Group.

The highly fractionated REE chondrite-normalized pattern of Type I iron formation (La/Lu_{cn} = 440) and strong positive Eu anomaly (Eu/Eu^{*} = 6.3) indicate a hydrothermal

origin. Hydrothermal provenance for Cu is indicated by a positive correlation between Fe and Cu.

The Salobo sequence underwent progressive metamorphism close to pyroxene hornfels facies, followed by two episodes of hydrothermal alteration, at amphibolite and greenschist facies. The first metamorphic episode took place at low pressure (2-3 kbar) with a temperature of 750°C (garnet-hornblende geothermometer); the associated fluids had $P_{CO_2} > P_{H_2O}$ and log f_{O_2} from -18 to -22. Garnet-biotite and muscovite-biotite geothermometers indicate temperatures of 650 and 550°C for the first hydrothermal alteration episode. The garnet-plagioclase geobarometer shows a pressure of 2.5 kbar for this event, which is also the pressure of the first metamorphism. Mass balance calculations indicate that related fluids were slightly oxidizing, acidic and highly saline promoting hydration accompanied by leaching of Ca and deposition of Si, K, Na and B. The temperature during the second hydrothermal episode was 370°C (garnet-biotite geothermometer). Mass balance calculations show that the associated fluids were acidic, oxidizing, with moderate salinity, depositing Si and leaching Na, K and Mn. The lower temperature (550°C) stage of the first hydrothermal event and the second hydrothermal episode occurred at the time interval of 2581-2551 Ma, which also represents the age of basement ascent.

The Salobo sequence was formed under a high heat flow regime and tectonic instability, with intense volcanism and hydrothermal activity. After deposition, it was rapidly taken to a depth of 8.5 km, with a thermal gradient of 85°C/km, when the first metamorphic episode took place. The cooling was still under a high heat flow regime, which is indicated by hydrothermal activities at 650 and 370°C. Subsequently the area underwent reheating during the emplacement of the post tectonic granitoid intrusion. The entire sequence of events may be explained by a rifting process similar to other Archean Continental basins in the world.

ACKNOWLEDGMENTS

I am thankful to Rio Doce Geologia e Mineracao S/A (Docegeo) for continuing financial support and for granting permission to carry out the research on Salobo copper deposit, allowing collection of samples and use of all the available data during preparation of this thesis.

I thank CNPq - Conselho Nacional de Desenvolvimento Cientifico e Tecnologico - for partial support from 1984 to 1987.

I wish to thank CIDA (Canadian International Development Agency) for providing partial support for whole rock analyses.

I am grateful to Docegeo staff in Belem for the assistance during field work. I am specially indebted to Ricardo Saueressig for being an enormous help during these years, providing additional samples and information, besides stimulating technical discussions. Special mention to Neidemar Farias and Carlos Augusto Medeiros Filho for providing information and organizing field trips.

I wish to thank my advisor, Prof. William S. Fyfe for his encouragement to come to the University of Western Ontario, for his stimulating discussions and enthusiasm. This work benefited much from his suggestions and assistance.

I would like to thank the faculty, staff and students of the Department of Geology for their friendship and support. Thanks to them I had a rewarding experience at the University of Western Ontario.

I am deeply indebted to Carlos Alberto Monte Lopes for his tremendous help and endless patience, writing computer programs and assisting the computer work any time it was necessary.

I am grateful to Mike Powell for helping with the final editing of this thesis.

I am particularly indebted to Prof. Ian McReath for reading and criticizing the first draft. His valuable suggestions were very significant for the final result of this work.

I would like to thank Prof. Nuno Machado for his suggestions and enlightening discussions.

I thank Mauricio Ferreira for making available the necessary material to the final editing of this thesis.

I would like to thank Dr. Augusto Kishida for reviewing and criticizing the first draft, for his continuous encouragement, technical discussions and friendship.

I sincerely thank Dr. Lydia Lobato for reading and criticizing the manuscripts, and for her patience and friendship in correcting any linguistic mistakes.

I wish to express my gratitude to Darci for his inexhaustible patience, encouragement and friendship.

TABLE OF CONTENTS

Page

Page

Page

LIST OF PHOTOGRAPHIC PLATES

LIST OF TABLES

LIST OF FIGURES

CHAPTER 1

INTRODUCTION

The Carajas Range is located in the Amazonian jungle and it is known world-wide for its huge iron deposits. It also hosts important copper, zinc, manganese, nickel, chromium, gold and bauxite deposits.

Geological knowledge of the area is very poor. The first iron ore occurrences were discovered in 1967. In spite of the various efforts to study the geology of this region, little is known about the rock sequences it hosts, their geological environment and the tectonic evolution. Geological investigations are rendered difficult due to inaccessibility coupled with intense forest cover and thick lateritic soil, which can reach a depth of 200 metres at the Carajàsiron ore mine and about 60 metres at Salobo Cu (Au, Ag, Mo) deposit.

The Carajas Range is situated in northern Brazil, in the south of Para State, 550 km SW of Bolem - the State Capital. It comprises a plateau rising about 400 metres above the regional topographic level (low lands), limited at the north by a belt of WNW trending hills.

Archean basement gneisses form the lowlands whereas the plateaus are composed of low grade metamorphosed volcanic flows (mostly basaltic), oxide facies iron formations (iron protore) and clastic sedimentary rocks named the Grao Para Group (Beisiegel et al., 1973; Hirata, 1982) (Figure 2), also of Archean age (Machado et al., 1988). The northern hills comprise high grade metamorphosed silicate iron formation and quartzites which were named the Salobo Group after the copper, gold, silver, molybdenum Salobo deposit it hosts (Farias and Saueressig, 1982; Docegeo, 1988).

The Salobo deposit was discovered by Docegeo (Rio Doce Geologia e MineraçaoS/A) in 1977. This is the largest Brazilian copper deposit, with reserves estimated at 300 million metric tons of ore grading 2.13 % Cu, 0.86 ppm Au, 7.18 ppm Ag, 130 ppm Mo and, 46.95% Fe (Teixeira and Silva, 1987). The copper ore minerals are mostly bornite and chalcocite, with subordinate chalcopyrite in magnetite-rich bands hosted by silicate iron formation (Lindenmayer, 1981; Farias, 1982; Farias and Saueressig, 1982).

This work relied on the study of drill core samples due to the lack of outcrops at the deposit area. It is based on the description of 35 selected drill cores; detailed petrographic description of thin-polished sections from 200 drill core samples; 500 electron microprobe analyses of silicate minerals; 135 whole rock analyses and 12 REE analyses.

The present investigation was carried out at the copper deposit area of the Salobo Group. The objective is to contribute to a better understanding of the Salobo Group stratigraphy, its metamorphic history and geologic evolution. It describes the geology of the study area from mesoscopic to microscopic-scale features, defining the rock types by petrography and lithogeochemistry. It also proposes a stratigraphic and metamorphic history of the Salobo Group, taking into account metamorphic reactions, semi-quantitative estimation of the composition of the fluids involved plus temperatures and pressures of the system as a whole. The data presented in this work, coupled with continued field observations, has led to the reinterpretation of the geology of the Salobo deposit as well as the geology of the Carajas basin.

CHAPTER 2

REGIONAL GEOLOGY

The Carajas region is located in the eastern Amazon Craton (Almeida et al., 1981), south of Para State. It is included in the Carajas Subprovince (Amaral, 1984), a sub division of the Tapajos Province of the Amazon Craton (Almeida et al., 1981) (Figure 2.1).

The Carajas Subprovince, covering an area of 235,000 square kilometers, is limited at the north by the Paleo-Mesozoic sedimentary cover of the Amazon Basin; at the east by the Mid-Upper Proterozoic north trending Tocantins-Araguaia fold belt; at the south by the Quaternary sediments of the Xingu River and at the west by tin-bearing granites, felsic volcanics and associated clastic sediments of the Proterozoic Uatuma Group (Oliveira and Leonardos, 1943).

The Carajas Subprovince is divided into four main units: Xingu Basement Complex (Silva et al., 1974), Andorinhas/Serra do Inaja Supergroup (Docegeo, 1988), Itacaiunas Supergroup (Docegeo, 1988) and Rio Fresco Group (Silva et al., 1974). The southern part of the Subprovince is underlain by greenstone belts of the Andorinhas/Serra do Inaja Supergroup (Ianhez et al., 1980; Docegeo, 1988). The

northern part, where the Carajas Range is situated, contains the remaining three units (Figure 2.2).

The first iron ore occurrences were discovered in 1967. Ever since then, a great effort has been made by a series of investigators attempting to establish the geology of the Carajas Range region. The reader is advised to consult publications by: Beisiegel et al. (1973); Bernardelli and Beisiegel (1978); Cordeiro and Saueressig (1980); Dall'Agnol (1980); Dardenne et al. (1987); Docegeo (1988); Farias and Saueressig (1982); Ferreira Filho (1985); Ferreira Filho and Danni (1985); Figueiras and Villas (1984); Gibbs et al. (1986); Goncalez et al. (1988); Hirata (1982), Hirata et al. (1982); Hirata et al. (1982a); Hutchinson (1979); Machado et al. (1988); Medeiros Filho and Meireles (1986); Medeiros Neto and Villas (1985); Meireles and Teixeira (1982); Olszewski et al. (1989); Peters et al. (1977); Ramos et al. (1984), Silva et al (1974); Suita and Nilson (1988); Silva et al. (1974); Tolbert et al. (1971); Wirth (1986).

The Xingu Basement Complex is composed of tonalitic to granitic banded gneisses, migmatites, trondhjemites and gabbro-norites with subordinate supracrustal rocks in amphibolitic to granulitic metamorphic facies (Tolbert et al., 1971; Silva et al., 1974; Hirata, 1982; Beisiegel et al, 1973). The Xingu Complex underwent migmatization at 2859+/- 2 Ma and retrometamorphism at 2851+/- 4 Ma according to Machado et al.'s (1988) U/Pb geochronological study.

The Itacaiunas Supergroup overlies unconformably or is infolded with the Xingu Complex Basement rocks. It is formed by the Salobo, Pojuca, Grao Para and Rio Fresco Groups (Docegeo, 1988).

The Salobo Group comprises a 150 km long steeply dipping NNW trending belt which parallels the Grao Para Group at the north. It is composed of quartzites, iron formation - hosting Cu (Ag, Au, Mo) mineralization - gneisses and amphibolites (Farias and Saueressig, 1982). According to Machado et al. (1988) the Salobo Group is part of the Xingu Complex due to the presence of zircons dated at 2851 Ma, later metamorphosed at 2761 +/- 3 Ma.

The Pojuca Group forms the north-northwest limit of the Carajas range, at the contact with the Xingu Basement Complex. The Pojuca Group is composed mostly of amphibolites and iron formation hosting Cu-Zn (Au-Ag-Mo) mineralization. Despite of being located in two separate parallel belts, the Pojuca and Salobo Groups have been considered coeval, based mostly on rock types and metamorphic grade (Hirata, 1982; Docegeo, 1988).

The Carajas Range comprises an elongated NNW-ESE trending area of 4,500 square kilometers, located in the central-northern portion of the Carajas Subprovince.It is composed of a thick volcanic and sedimentary sequence of low metamorphic grade designated Grao ParåGroup (Beisiegel et al., 1973). The structure of this Group has the general pattern of a synclinorium, bordered at NW and SW by higher

metamorphic grade rocks of the Pojuca Group. The Grao Parå Group includes three formations, from base to top: Parauapebas Formation, CarajåsFormation and Upper Volcanic Sequence (Beisiegel et al., 1973; Docegeo, 1988).

The Parauapebas Formation is a volcanic unit made up of metamorphosed basalts, basaltic andesites and mafic agglomeratic breccias with subordinate rhyolites (Gibbs et al., 1986; Wirth et al 1986; Olszewski et al., 1989), dated at 2759+/- 2 Ma (Machado et al., 1988). According to Gibbs et al. (1986), the volcanic flows are 4 to 6 kilometers thick. The 200-300 meters thick Carajas Formation overlies this sequence and is composed of finely laminated banded quartz-magnetite-hematite iron formation (Tolbert et al., 1971; Beisiegel et al., 1973), which hosts the largest high-grade iron ore reserves of the planet (1,2 x 10^9 tons of ore grading 66 % Fe). The Upper Volcanic Sequence has an estimated thickness of 1 to 3 kilometers (Olszewski et al., 1989), consisting of locally deformed mafic flows and tuffs, tuffaceous siltstones, phyllites, cherts, graywackes, conglomerates and quartzites (Beisiegel et al., 1973; Gibbs et al., 1986; Olszewski et al., 1989).

Two ore deposits are probably hosted by the Upper Volcanic Sequence: the Azul manganese mine is made up of siltstones, shales, manganiferous beds and fine-grained sandstones (Bernardelli, 1982) and the Bahia Au-Ag(Cu) deposit, associated with mafic to felsic volcanics, with

intercalations of clastic metasedimentary rocks and iron formation (Ferreira Filho, 1985).

Based on the chemical characteristics of the Grao Para volcanics, which are similar to other bimodal continental basalts, Gibbs et al.(1986) and Olszewski et al. (1989) suggested that the Grao Para Group volcanics were deposited on continental crust undergoing extension during Archean time. According to Hutchinson (1979) Salobo, Pojuca and Grao Para rocks could represent lateral facies changes of the same volcano-sedimentary sequence deposited in a rift basin.

The Rio Fresco Group (Docegeo, 1988) comprises coarse clastic sedimentary rocks which occur throughout the Carajas Subprovince, unconformably overlying the Xingu Complex and the Itacaiunas Supergroup. It also occurs at the centre of the Grao Para synclinorium where it is comprised of sandstones, shales, siltstones and conglomerates (Beisiegel et al., 1973; Silva et al., 1974; Bernardelli and Beisiegel, 1978; Meireles and Teixeira, 1982; Ramos et al., 1984; Figueiras and Villas, 1984; Gibbs et al., 1986). The Rio Fresco sedimentary rocks are intruded by the Carajas granite dated at 1880+/- 4 Ma (Machado et al., 1988), which is therefore the minimum age for this Group.

Proterozoic post-tectonic granites, some of them hosting Sn and W deposits, are widespread throughout the Carajas Subprovince. The Carajas, Cigano, Pojuca and, Salobo granites range in age from 1874 to 1883 Ma (Machado et al., 1988).

The geological summary presented above is based solely on previous works. As it will be seen throughout this thesis, new data coupled with further geological field observations has led the author to reinterpretation of the geology, stratigraphy and geotectonics of the Carajàsbasin (see Chapter 7 and 8).

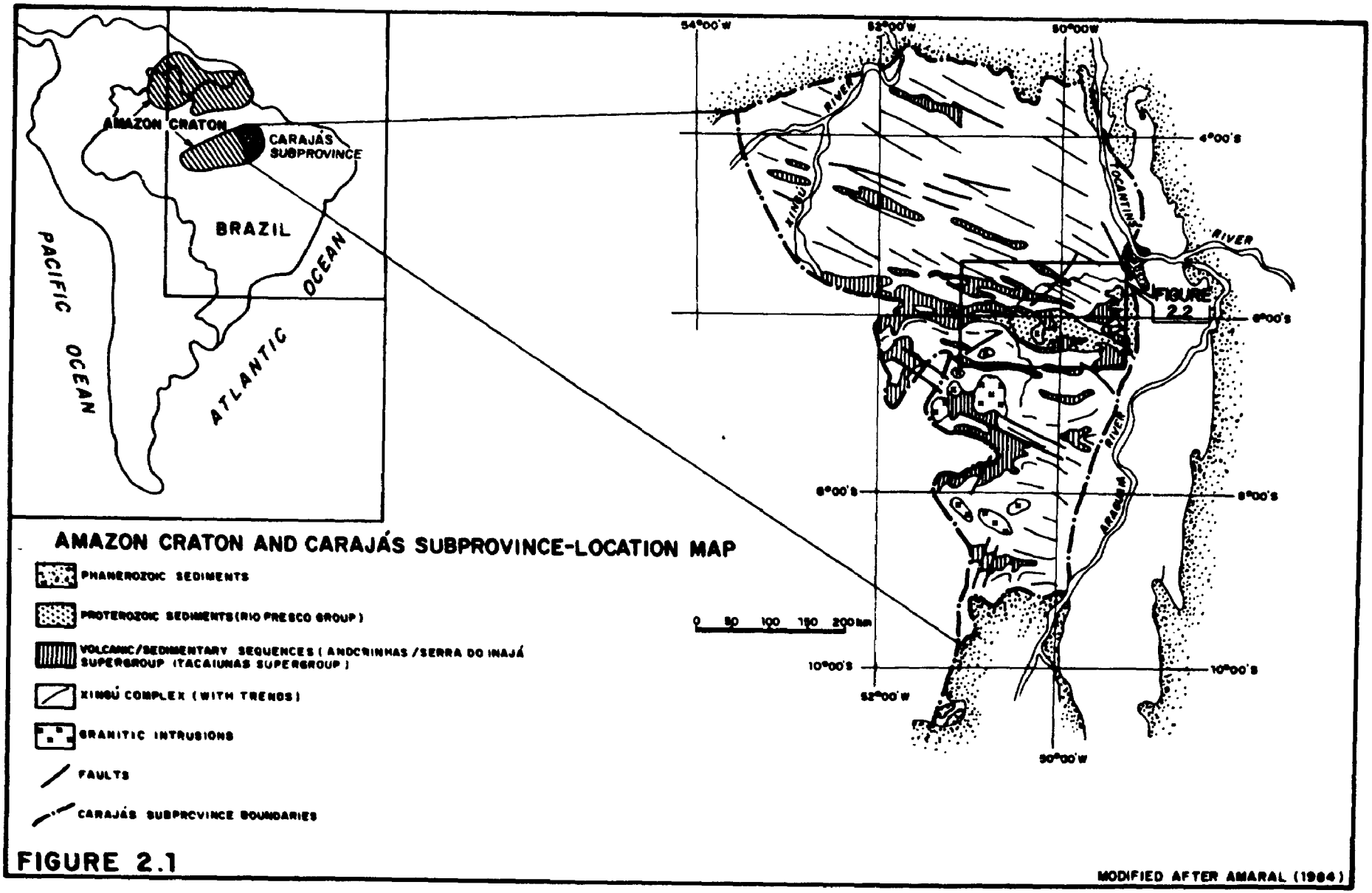

FIGURE 2.1

MODIFIED AFTER AMARAL (1984)

CARAJÁS GEOLOGICAL MAP

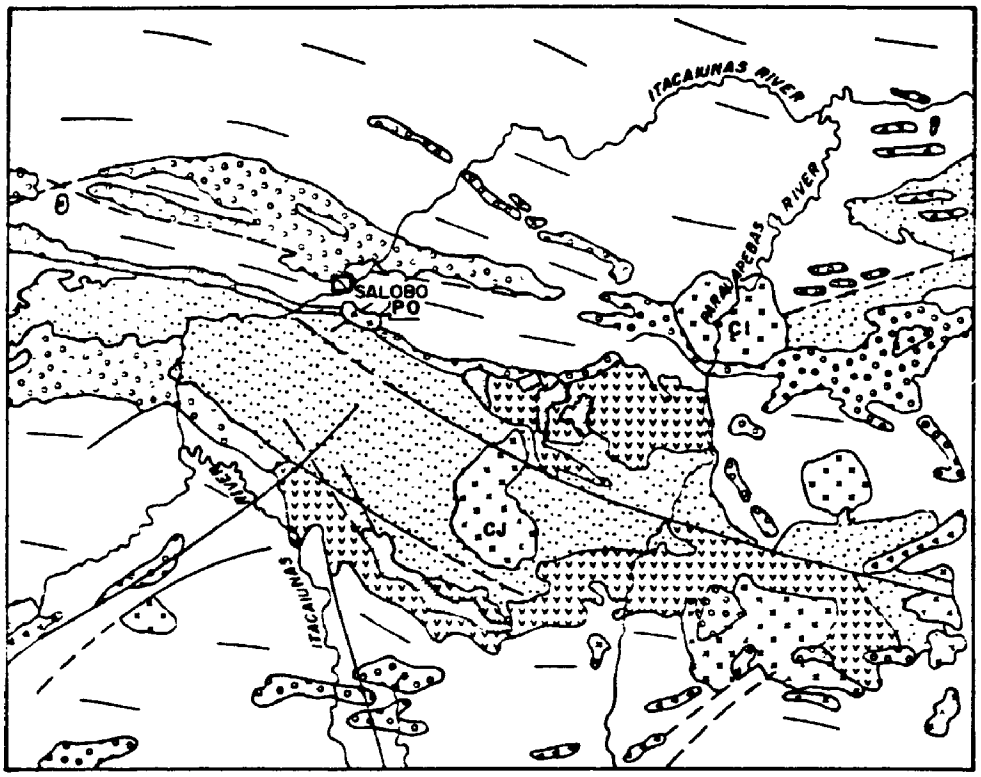

LEGEND

- ANOROGENIC GRANITES (CJ - CARAJÁS / PO - POJUCA / CI - CIGANO
- RIO FRESCO GROUP (SEDIMENTS)
- CARAJÁS FORMATION (BANDED IRON FORMATION) — GRÃO PARÁ GROUP
- PARAUAPEBAS FORMATION (VOLCANIC FLOWS) — GRÃO PARÁ GROUP
- POJUCA / SALOBO GROUPS
- XINGÚ COMPLEX (WITH TRENDS)
- BASIC INTRUSIVES
- GEOLOGICAL BOUNDARY
- STUDY AREA
- FAULT

0 10 20 30Km

FIGURE 2.2

MODIFIED AFTER DOCEGEO (1988)

CHAPTER 3

GEOLOGY OF THE AREA

3.1 Introduction

The Salobo Group underlies a 100 kilometer long range situated 10 km north of Carajas Range. It comprises a N70W striking steeply dipping belt which hosts the Salobo Deposit.

3.2 Previous Works

The Salobo copper deposit was discovered in 1977 and ever since has been the object of study by various workers: Beisiegel and Farias (1978); Cordani (1981); Cordani et al. (1984); Docegeo (1988); Farias (1981); Farias and Saueressig (1982) (1982a) (1982b); Figueiredo (1982); Gaal (1983); Guimaraes (1987); Hasui (1981); Hirata et al. (1982); Lindenmayer (1981); Lindenmayer et al. (1988); Machado et al. (1988); Martins et al. (1982); Meyer and Farias (1980); Tassinari et al. (1982); Teixeira and Silva (1988); Vieira et al. (1984); Vieira et al. (1988); Xavier (1983).

Docegeo (1988) divided the Salobo Group into three formations, from north to south: Cascata Gneisses at the base, Tres Alfa Formation hosting Cu (Au-Ag-Mo) mineralization and Cinzento Formation at the top.

According to these authors, "Cascata Gneisses (former Lower Gneisses of Farias, 1981) consist of fine to medium-grained gray gneisses, with minor amphibolite intercalations, composed of plagioclase, quartz, chlorite and K-feldspar. They are of sedimentary origin having an estimated thickness of several hundred metres",(Docegeo, 1988 page 34).

"The Tres Alfa Formation is a 300 metres thick sequence composed mostly of chemical sediments with subordinate clastic rocks and minor basic to intermediate volcanics. The chemical sediments are oxide-silicate iron formation made up of magnetite, fayalite, almandine, Fe-Mg amphibole, quartz and biotite in varying proportions", (Docegeo, 1988 page 34). Copper sulphides, mainly bornite and chalcocite, are hosted by magnetite-rich layers or lenses in iron formation (Farias and Saueressig, 1982). The authors do not describe the volcanic rocks or the clastic sediments.

"The Cinzento Formation (former Upper Gneisses and Quartzite Units of Farias, 1981) comprises 200 metres thick quartzites with subordinate gneisses and schists, which have gradational contacts with the Tres Alfa Formation. The quartzites are medium-grained gray rocks made up of 90%

quartz, minor sericite and K-feldspar" (Docegeo, 1988 page 34).

Two granitic bodies (Machado et al., 1988) and two diabase dykes (Farias, 1982) intrude the Salobo Group." The rocks of this Group are metamorphosed in amphibolite to greenschist facies" (Docegeo, 1988 page 34). Guimaraes (1986) estimated the highest metamorphic conditions at 650°C and 4.5 kbar.

Based on the geological knowledge at the time, Machado et al. (1988) proposed the following geochrono-logical evolution for the Salobo area:

a. The Salobo Group was considered part of the Xingu Basement Complex due to the presence of zircons dated at 2851 +/-4 Ma, in amphibolites of the Cascata Formation. These gneisses underwent metamorphism at 2761+/- 3 Ma and were intruded by granitic veins at 2758 Ma.

b. A zircon crystallization event at 2732-2742 Ma was interpreted as the main metamorphic episode.

c. An event of titanite growth took place at 2581+/- 5 Ma, interpreted as a later metamorphic episode.

d. Emplacement of the Old Salobo Granite at 2573+/- 2 Ma.

e. Shearing of Salobo Group between 2573 and 2551 Ma.

f. An event of titanite growth at 2497 +/- 5Ma was interpreted as being related to a K-metasomatic episode.

The younger Salobo granite was intruded at 1880+/- 80 Ma (Rb/Sr whole rock conventional age dating, assuming

RI=0.705), and the diabase dykes at 553+/- 32 Ma (K/Ar whole rock analysis) according to Cordani's (1981) study.

3.3 Geology of the area - this work

The geology of the study area presented hereafter is mostly based on the descriptions of drill core samples, as the number of outcrops emerging from the 60 metres thick lateritic soil is very limited (Figure 3.1).

The area comprises a 3.5 km long WNW trending hill, where the Salobo Cu (Au-Ag-Mo) deposit is located.

The rocks at the Salobo hill (except the younger intrusives and veins) show a strong sub-vertical foliation or schistosity which undulates along the strike, forming open folds with vertical axes and sub-vertical NNE axial planes.

From north to south the geology of the area includes the Basement rocks and an overlying metamorphosed Sedimentary Sequence, with interlayered amphibolites (Figure 3.2; see Chapters 5 and 7), named in this work Salobo Sequence.

Two granitoid intrusions, two diabase dykes, and post-tectonic veins cut the Salobo Group rocks at the Deposit area.

Two shear zones transect the area, at the northern contact between Basement rocks and the Sedimentary Sequence and at the south, cutting through the sedimentary rocks.

3.2.1. Basement Rocks

The basement rocks in the north of the study area consist of banded gneisses. There are intercalations of amphibolites and metasedimentary rocks ranging from a few centimeters to 5-10 metres in thickness, at the sheared contact between basement and sedimentary rocks.

The basement gneisses are composed of two main rock types: the first type is trondhjemitic in composition, and represent 95% of the gneisses studied, with oligoclase-albite as the only feldspar. The second type, constituting the remaining 5% is a two feldspar-bearing gneiss of granitic to quartz-monzonitic composition. The contacts between different gneisses are always gradational.

Trondhjemitic gneisses are medium to fine-grained, light gray banded rocks, frequently exhibiting mylonitic bands. They are chiefly composed of plagioclase (oligoclase-albite) and quartz with minor amphiboles, biotite, chlorite and accessory tourmaline, magnetite, ilmenite, allanite and titanite. They host lenses or layers of granitic and amphibolitic composition; along the contacts between the latter and the gneisses, the mafic bands in the gneisses increase in frequency and thickness and usually display diffuse contacts.

The granitic to quartz-monzonitic gneisses are medium-grained, light pinkish, strongly foliated rocks, with K-

feldspar, plagioclase (oligoclase-albite) and quartz, and subordinate biotite and chlorite.

3.3.2. Amphibolites

The amphibolites occur as 2 to 5 m thick layers intercalated at the contact between the basement gneisses and the iron formation, and as layers or lenses included in the gneisses and in iron formation.

Amphibolite intercalations in iron formation are a few centimeters thick (Photograph 1). The lenses in gneisses range from a few centimeters to less than 2 m in thickness. At the contact between amphibolite lenses and host gneisses there is a mixed banded zone composed of both rock types. They are medium to fine-grained dark green rocks composed of hastingsite and plagioclase (andesine to albite), with subordinate biotite, cummingtonite and chlorite, minor tourmaline and accessory ilmenite, magnetite, zircon and titanite. Thicker amphibolite lenses show granoblastic texture at the centre grading to foliated and mylonitic textures towards the margin, while thin amphibolite lenses usually display an exclusively foliated texture.

3.3.3. Metasedimentary Sequence

The Salobo metasedimentary sequence of iron formation, metagraywackes (see chapter 5) and quartzites can be traced

along strike for about 10 kilometers. In the deposit area, these metasedimentary rocks range in thickness from at least 300 to more than about 600 metres.

The metasedimentary sequence is mostly chemical in nature at the base, where the iron formation dominates, becoming increasingly clastic towards the top where quartzites constitute the only lithology. The intermediate zone between iron formation and quartzites is mainly composed of metagraywackes (Figure 3.3).

a) Iron Formation

The iron formation constitutes the lowermost 200 metres of the sedimentary sequence. It has a sheared contact with the basement at the north and a gradational contact with the metagraywackes at the south.

In this work the unit here referred to as iron formation is composed of interlayered iron formation and minor metagraywackes.

On the basis of mineral assemblage and rock composition two types of iron formations were recognized:
Type I iron formation consisting of black to dark green massive or foliated rocks, with fayalite *q* grunerite, magnetite and minor hastingsite, biotite and almandine garnet, and Type II iron formation composed of pink spotted greenish gray to dark green foliated or schistose rocks, displaying magnetite, almandine garnet, grunerite *q* fayalite, biotite and minor hastingsite, quartz and

tourmaline (Photographs 2 tp 6). Type I is Fe-Si-rich, corresponding to silicate iron formation, while Type II is variably Al-rich indicating a detrital contribution.

Type I iron formation grades to Type II, and the latter to metagraywackes through gradual increase in the amount of Al-bearing minerals, indicating periodic detrital contribution to the chemical sediments (Photograph 7).

Both iron formation types comprise sedimentary cycles characterized by a magnetite-rich layer at the base, along a sharp contact; the amount of Al and K-rich minerals increase towards the top of each cycle. Each complete sedimentary cycle, composed of Type I + Type II iron formation *a* metagraywackes, ranges in thickness from a few centimeters to 5 metres. The individual magnetite-rich layers are usually a few centimeters thick (Photographs 8 to 11).

Banded iron formations as defined in the literature (Trendall, 1965; Gole and Klein, 1981; Klein, 1983; Dymek and Klein, 1988) are seldom encountered. There are only two known occurrences (drill holes 50 and 56), where 10 to 50 centimeters thick banded iron formations were observed. They consist of 1 to 2 mm thick bands of alternating quartz and fayalite (grunerite)-magnetite-hastingsite levels (Photograph 12). As described above, these banded rocks also grade to aluminous Type II iron formation. These scarce examples of banded iron formations are probably representative of strictly chemical-dominated time intervals in the sedimentation basin.

b) Metagraywackes

The metagraywackes dominate the intermediate 50 to 200 metres of the metasedimentary sequence. Their northern contact with the iron formation is gradational, while the southern contact with quartzites is along a 50 metres wide shear zone.

The metagraywackes form individual layers 10 to 30 metres thick, interlayered with iron formation. They are strongly schistose or foliated, spotted white or pink, greenish-brown to brownish-gray in color, with biotite, almandine garnet and quartz, subordinate muscovite, tourmaline and plagioclase, minor sillimanite, cummingtonite and chlorite and accessory magnetite, allanite and zircon.

They are medium-grained rocks with mylonitic bands a few millimeters thick (Photographs 13 and 14).

c) Quartzites

Quartzites form a layer about 200 metres thick. The northern contact with metagraywackes is sheared, but the southern contact with Xingú Complex does not outcrop.

The quartzites are grayish-white, medium to fine-grained massive to foliated rocks composed of quartz (average 75%), subordinate muscovite and minor chlorite, sillimanite, biotite, feldspar, magnetite and garnet with

accessory tourmaline, zircon and allanite (Photograph 15). They form a very sheared and massive layer with varying amounts of minor constituents. Scattered quartz druses with crystals up to 10 or 15 cm long occur within the quartzites.

3.3.4. Intrusive Rocks

There are two types of intrusive rocks at the Salobo Deposit area: granitoid rocks and diabase.

a) Granitoid rocks

Two granitoid intrusions cut the Salobo area, dated at 2573 +/- 2 Ma (Machado et al., 1988) and 1880 +/- 80 Ma (Cordani et al., 1981), here referred as Old Salobo Granite (OSG) and Young Salobo Granite (YSG), respectively.

a.1) Old Salobo Granite

The OSG crops out at the Salobo camp clearing. Its shape and size is unknown, but it must have an extension of at least 3 km, as indicated by a drill hole at the Mirim area, located 3 km north of Salobo.

The OSG is a foliated pinkish-gray medium to coarse-grained granite made up of K-feldspar (orthoclase-microcline), oligoclase, quartz, augite, hornblende, chlorite and magnetite, and is often mylonitic (Photograph 16). No major contact metamorphic effects are observed in

the host rocks. Only thin deformed pegmatite veins are observed at the contact zones.

Mylonitic textures in the OSG, as well as in the host rocks indicate a pre-syn shearing emplacement. The lack of contact metamorphic effects together with the thin pegmatitic veins at the contact zone, indicate that OSG was probably emplaced under mesozonal conditions, according to Buddington's (1959) concepts (in: Hughes, 1982).

a.2). Young Salobo Granite

The Young Salobo Granite (YSG) consists of a NNW trending sill, 1,300 metres long and 50 metres thick hosted by basement gneisses.

The rock here named YSG is in fact a pink massive porphyritic quartz-syenitic rock composed of albite phenocrysts in a groundmass of albite, orthoclase and quartz, with minor chlorite and accessory fluorite and magnetite. YSG is an undeformed intrusive rock with isotropic structure (Photograph 17). The rocks surrounding YSG and composed of quartz, almandine garnet, cordierite, anthophyllite, plagioclase and biotite, described by Guimaraes (1987) correspond to its contact-metamorphic aureole.

The isotropic structure indicates that the YSG was post tectonic. The porphyritic texture, together with the contact metamorphic aureole indicate that this intrusion was probably emplaced under epizonal conditions, according to Buddington's (1959) concepts (in: Hughes, 1982).

b) Diabase Dykes

Two undeformed diabase dykes cut the area. The first occurs in the central part, mainly hosted by iron formation, whereas the second occurs near the western end of the deposit, mainly crosscutting quartzites. Both are about 500 m long and 15 to 50 m thick, striking N70W and N20W, respectively.

Both diabase dykes show chilled vitreous margins grading towards the centre into porphyritic and sub-ophitic granular rocks. The vitreous margins often exhibit amygdules.

They are dark grayish-green rocks composed of plagioclase, augite, magnetite, ilmenite and quartz with chlorite filling the amygdules.

There are two age determinations by K/Ar whole rock analyses in these dykes (Cordani, 1981). One fine textured sample from a dyke margin yielded 553+/- 32 Ma, whereas a medium-grained sample from a dyke centre yielded 561+/- 16 Ma. Both ages represent the last recorded magmatic event in the area.

c) Veins

There are deformed and undeformed veins in the Salobo area, the former being less frequent. Together they represent less than 1% of all rocks present. Both vein types have thicknesses ranging from 1 millimeter to 1 metre. They are more common in the basement rocks and in shear zones, seldom cutting the iron formation.

Deformed veins contain quartz or tourmaline-quartz.

Undeformed veins show a large variation in mineral content, depending on the host rock composition. Quartzite hosted veins display quartz and minor calcite-fluorite; veins in metagraywacke are made of quartz, calcite, fluorite, quartz and chlorite; veins in iron formation have greenalite-uraninite, greenalite-fluorite, stilpnomelane, chlorite-gold and molybdenite; veins in basement rocks are composed of quartz (Photograph 18), calcite-fluorite, calcite-quartz-fluorite, calcite-epidote, chalcopyrite-epidote-calcite-stilpnomelane and chalcopyrite-quartz-epidote.

Undeformed veins in shear zones present albite druses filled with quartz and surrounded by muscovite.

Undeformed molybdenite-bearing pegmatitic veins, up to 30 centimeters thick are also observed, mainly in the basement gneisses.

The mineralogy together with the undeformed nature of these veins strongly suggest that they are related to the Young Salobo Granite.

3.3.5 Shear Zones

There are two main shear zones in the study area. One is at the contact between the iron formation and the basement rocks at the north, and the other is situated between metagraywackes and quartzites at the south, hereafter referred to as the northern and southern shear zones, respectively.

The northern shear zone (NSZ), 20 to 30 metres thick, is mostly composed of mylonitized basement gneisses and amphibolites with minor metasedimentary rocks. The mylonitic gneisses and amphibolites are made up of hastingsite, albite and subordinate grunerite and quartz.

The southern, 50 metres thick, shear zone (SSZ) is composed of chloritized and mylonitized gneisses, amphibolites, iron formation, metagraywackes and quartzites showing brecciated structures.

3.3.6 Ore

The copper ore consists of magnetite-rich layers or lenses in Type I iron formation. This iron formation comprises medium to fine-grained granoblastic to foliated rocks, consisting mostly of magnetite with minor almandine garnet, grunerite *q* fayalite, biotite and sulphides.

The sulphides are predominantly disseminated, although some massive lenses, less than 1 metre thick have been observed. The ore deposit may be classified as strata-bound disseminated according to Wolf's (1976) concepts.

The copper ore minerals are mostly bornite-chalcocite and minor chalcopyrite. In addition to these, molybdenite with minor gold, safflorite [$(Co,Fe)As_2$] and cobaltite [(Co,Fe)AsS] are also present.

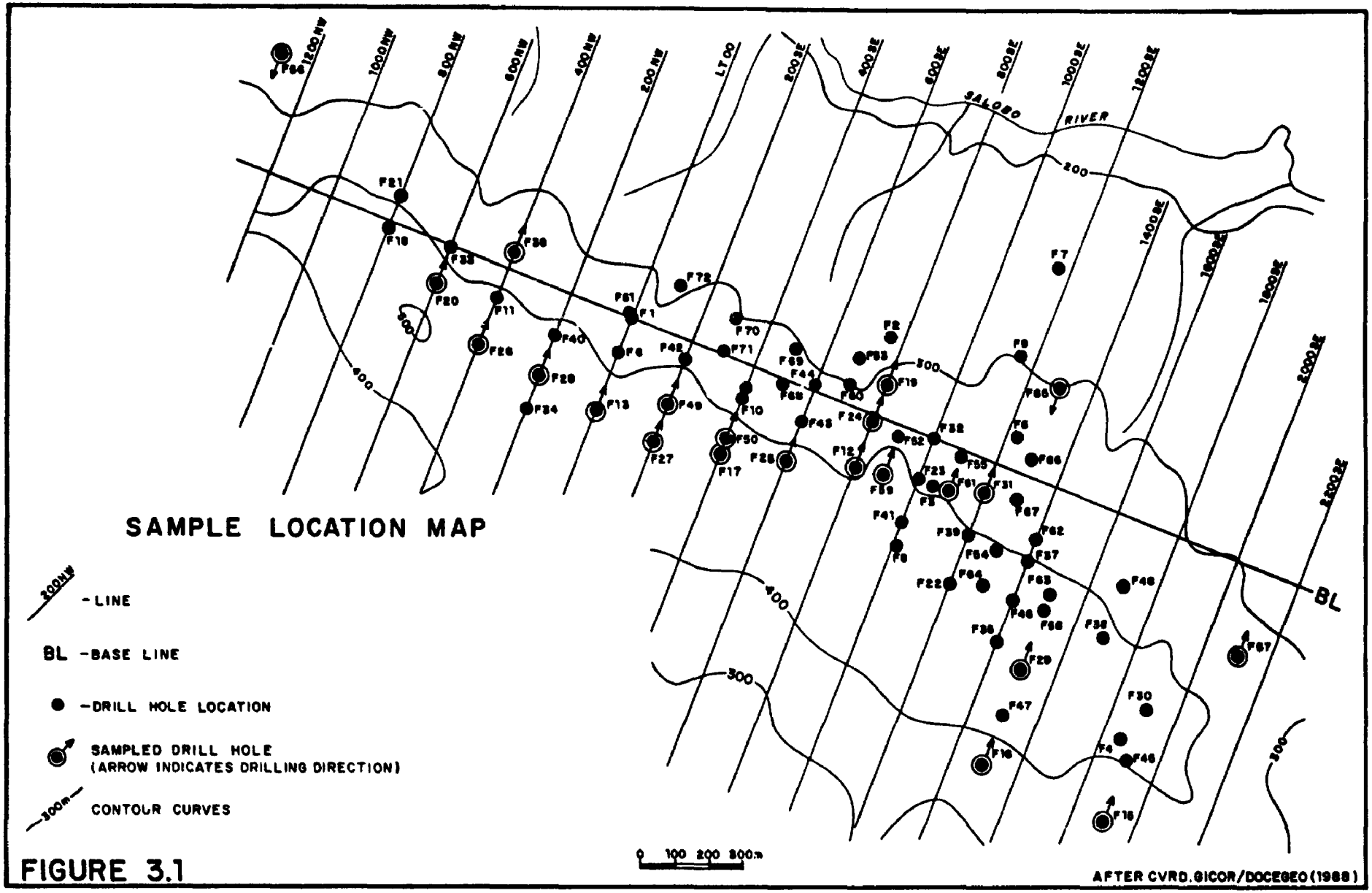
SAMPLE LOCATION MAP
1200NW
1000NW
800NW
600NW
400NW
200NW
LT 00
200SE
400SE
600SE
800SE
1000SE
1200SE
1400SE
1600SE
1800SE
2000SE
2200SE
SALOBO RIVER
BL
200
300
400
500
-LINE
BL -BASE LINE
-DRILL HOLE LOCATION
SAMPLED DRILL HOLE
(ARROW INDICATES DRILLING DIRECTION)
CONTOUR CURVES
0 100 200 800m
AFTER CVRD, GICOR/DOCEGEO (1988)

FIGURE 3.1

SALOBO DEPOSIT GEOLOGICAL SKETCH MAP

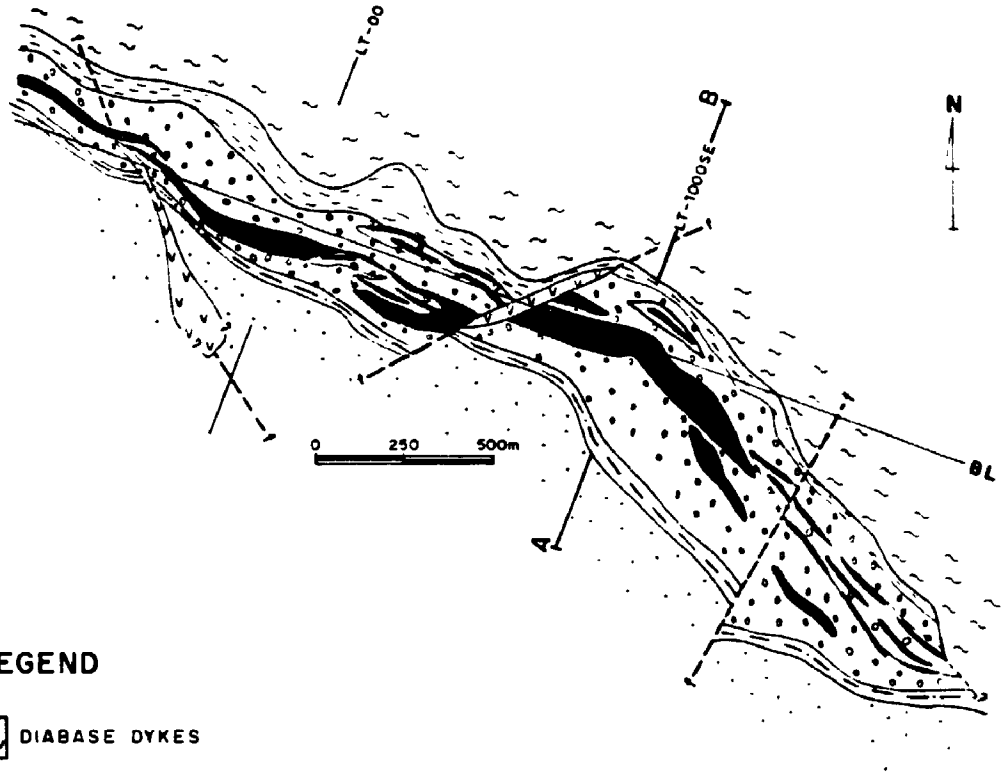

LEGEND

- DIABASE DYKES
- SOUTHERN SHEAR ZONE
- NORTHERN SHEAR ZONE
- QUARTZITES
- METAGRAYWACKES
- TYPE II IRON FORMATION (ALUMINOUS)
- TYPE I IRON FORMATION (SILICATE) HOSTING COPPER ORE

} SEDIMENTARY SEQUENCE

- BASEMENT GNEISSES
- GEOLOGIC BOUNDARIES
- FAULTS
- SECTION (FIGURE 3.3)

LT - LINES

BL - BASE LINE

FIGURE 3.2

MODIFIED AFTER DOCEGEO (1988)

SALOBO DEPOSIT A-B SCHEMATIC SECTION

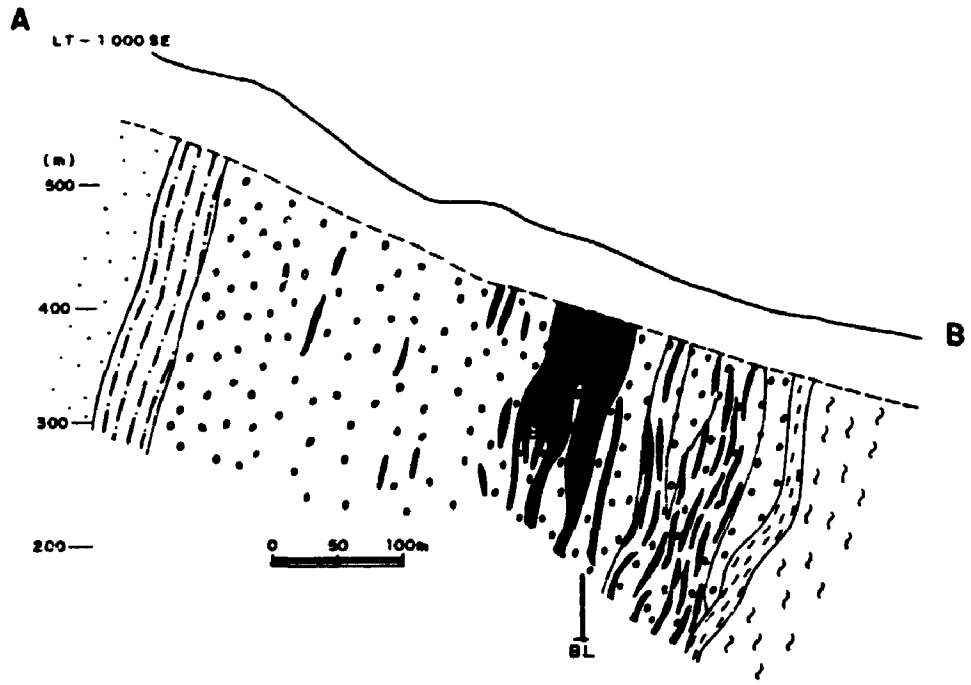

LEGEND

- LATERITIC SOIL
- SOUTHERN SHEAR ZONE
- NORTHERN SHEAR ZONE
- QUARTZITES
- METAGRAYWACKES
- TYPE II IRON FORMATION (ALUMINOUS)
- TYPE I IRON FORMATION (SILICATE) HOSTING COPPER ORE

} SEDIMENTARY SEQUENCE

- BASEMENT GNEISSES

LT - 1000 SE - TRANSVERSAL LINE

BL - BASE LINE

FIGURE 3.3

MODIFIED AFTER DOCEGEO (1988)

Plate 1 - Photographs of iron formations.

1. Intercalations of amphibolite (a) in iron formation (if) composed of magnetite and grunerite. Arrows point to the contacts. Bar is 2 cm long.
2. Coarse-grained sample of Type I iron formation. Fayalite (f), (large crystal outlined) is surrounded by biotite and grunerite. Garnet is also observed in the sample.
3. Garnet I (gn) in Type II iron formation. Coarse-grained garnet I is in a matrix of biotite, grunerite and quartz. Bar is 2 cm long.
4. Type II iron formation composed of garnet, biotite and magnetite. Dark magnetite layers surround garnet.
5. Type II iron formation made up of biotite, garnet and quartz. Arrows point to quartz lenses. Bar is 2 cm long.
6. Type II iron formation. The sample shows three layers with different compositions: a) magnetite-biotite-garnet±grunerite, b) grunerite-garnet-biotite, and c) garnet-grunerite-magnetite. Arrow points to the sheared contact between (b) and (c). Bar is 2 cm long.

PLATE 1

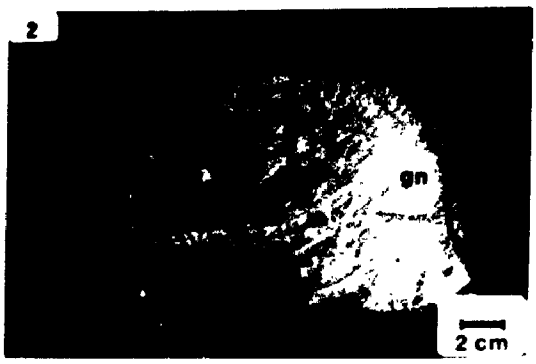

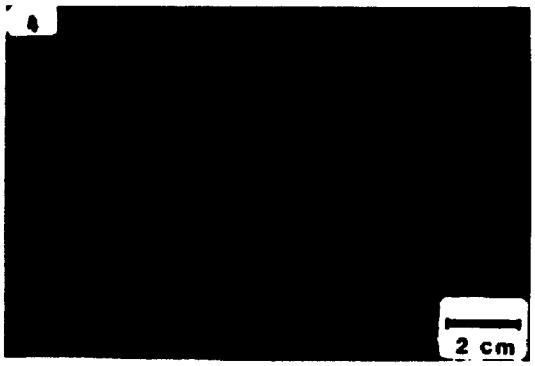

Plate 2 - Photographs of iron formations.

7. The sample shows gradation between Type I (a) and Type II (b) iron formations (arrow points to the contact). Layer (a) is composed of magnetite and garnet. The latter increases towards layer (b). Layer b is composed of grunerite, quartz and biotite. Bar is 2 cm long.
8. Type I iron formation, made up of fayalite (f) and magnetite, grades to Type II iron formation formed of grunerite, biotite, garnet (rounded), magnetite and fayalite (f).
9. Iron formation showing four different rock types (the arrows point to the contacts). From left to right: banded biotite(bt)-quartz(qz)-magnetite(mag)-rock, grunerite(g)-biotite(bt)-rock, garnet(gn)-grunerite(g)- biotite(bt)-rock, and garnet(gn)-biotite(bt)-magnetite (mag)-rock.
10. Grunerite-garnet-biotite-rock (Type II iron formation) showing lenses enriched in biotite. Arrow points to one of these lenses. Bar is 2 cm long.
11. Grunerite-garnet-biotite-rock (a) grades to quartz-garnet-biotite-rock (b). Both rock types correspond to Type II iron formation. Arrow points to the approximate contact between (a) and (b). Bar is 2 cm long.
12. Banded iron formation (Type I) showing a) quartz-magnetite and b) quartz-grunerite-magnetite. Arrow points to the sharp contact between (a) and (b). Bar is 2 cm long.

PLATE 2

Plate 3 - Photographs of metagraywackes, quartzite, granitoid rocks and undeformed vein.

13. Metagraywacke showing fine-grained bands composed of quartz, plagioclase, cummingtonite and biotite, alternating with medium-grained bands, formed of biotite, plagioclase and cummingtonite. Arrows point to tourmaline. Bar is 2 cm long.
14. Metagraywacke displaying quartz-plagioclase lenses (white) in a mylonitic matrix composed of biotite, muscovite and cummingtonite.
15. Quartzite. Arrows point to garnet replaced by chlorite.
16. Old Salobo Granite (OSG) exhibiting intensive fracturing, mylonitization and chloritization.
17. Alkali-feldspar quartz syenite (YSG) showing isotropic texture.
18. Undeformed quartz-hematite vein in chloritized gneiss.

PLATE 3

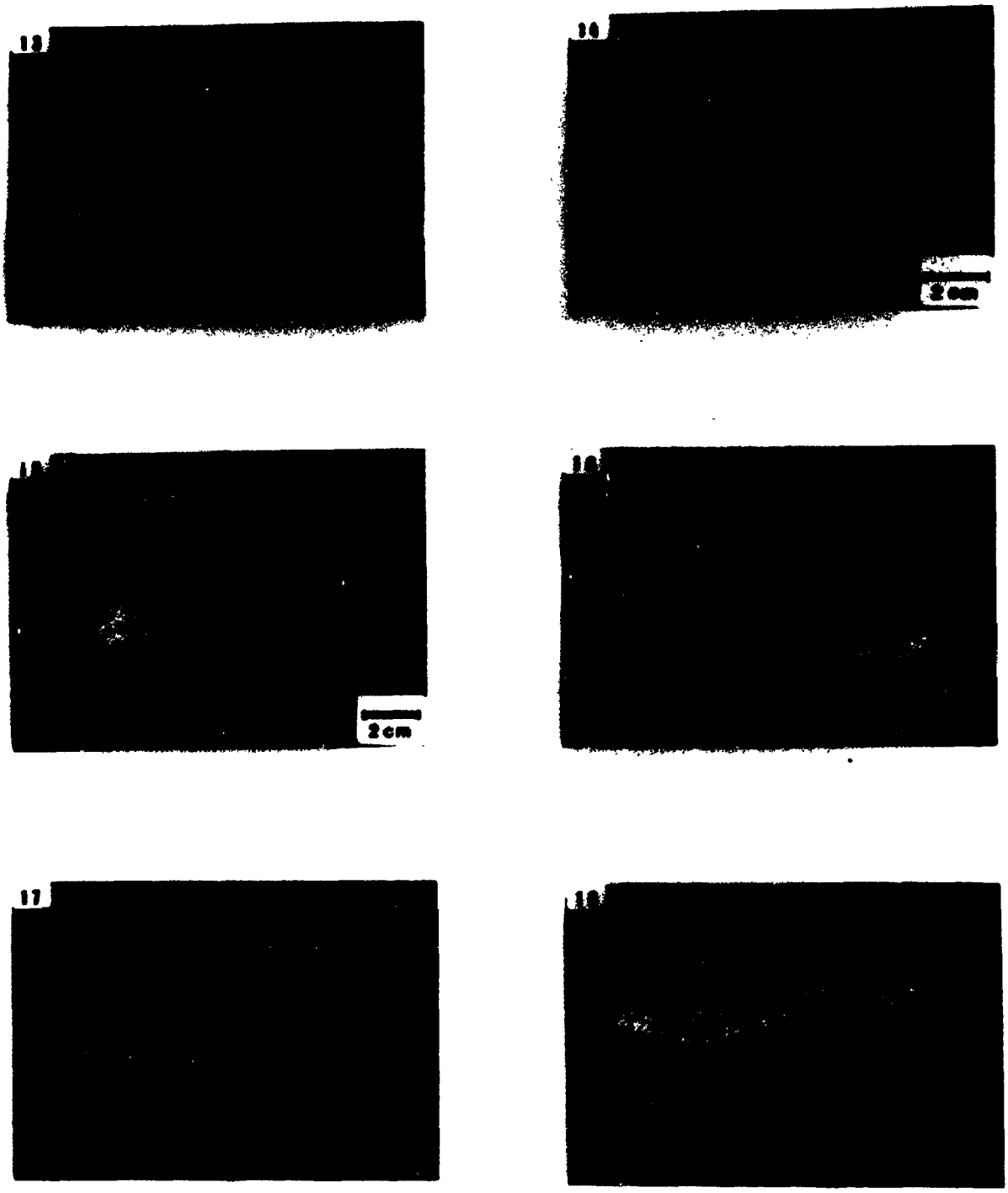

CHAPTER 4

PETROGRAPHY

4.1. Introduction

This chapter presents a summary of the description of 93 thin sections and 109 thin-polished sections. They include 49 samples of gneisses, 11 of amphibolites, 90 of iron formations, 18 of metagraywackes, 19 of quartzites, 5 of veins and 10 of granitoid rocks.

4.2. Gneisses and amphibolites

Gneisses and amphibolites show very similar mineralogy and textures, for that reason their petrography will be described together.

Trondhjemitic gneisses and amphibolites are composed, in different proportions, of plagioclase feldspar (andesine to albite), quartz, hastingsite, biotite, cummingtonite and chlorite with minor tourmaline and accessory magnetite, allanite, titanite and zircon. Granitic to quartz monzonitic gneisses are composed of microcline feldspar, plagioclase (oligoclase to albite), quartz and biotite with accessory allanite, titanite, zircon and apatite.

4.2.1 Gneisses

Gneisses are banded foliated rocks, frequently displaying protomylonitic to mylonitic textures, with hastingsite, biotite and elongated quartz lenses showing preferred orientation. Relicts of less deformed gneisses exhibit granoblastic polygonal textures and are observed in felsic bands (Photomicrograph 19).

Protomylonitic to mylonitic rocks are made up of a very fine-grained matrix, composed mainly of quartz and angular to rounded porphyroclasts of plagioclase felsdpar or less commonly, hastingsite or tourmaline (Photomicrographs 20, 21 and 22).

Foliated or mylonitic gneisses may have intense pervasive fracture zones cutting the rocks. The individual fractures are a few millimetres apart, and are filled with chlorite.

4.2.2. Amphibolites

Amphibolites are usually medium to fine-grained rocks with strong foliation and/or schistosity, but granoblastic polygonal (Photomicrograph 23) or mylonitized (Photomicrograph 24) amphibolites are also observed. The foliation is defined by the preferred orientation of amphibole prisms or plagioclase lenses and the schistosity is marked by oriented biotite. Granoblastic amphibolites may

be solely composed of hastingsite or hastingsite plus plagioclase, with straight boundaries and triple points. Some amphibolites show mixed granoblastic-schistose structure, where the preferred orientation of biotite laths defines the schistosity in a granoblastic matrix (Photomicrograph 25). Protomylonitic to mylonitic amphibolites display angular and irregular mineral grains.

a) Mineral Descriptions of gneisses and amphibolites

Plagioclase feldspar forms irregular to rounded, frequently clouded porphyroclasts, with sutured or embayed boundaries. Grain size ranges from 0.1 to 0.5 millimetres. They are rarely twinned, with twin planes bent or fractured. In less deformed varieties, characterized by granoblastic textures, plagioclase is andesine to oligoclase, showing straight boundaries and triple point junctions. With increasing mylonitization, the porphyroclasts become smaller, rounder and acquire a more albitic composition.

In amphibolites, plagioclase also varies from sodic andesine to albite (An_{31} to An_{4}), forming granular to lenticular crystals 0.5 to 1.5 mm long, untwinned, displaying straight, embayed or lobate boundaries. It is of interest to note that only in mylonitic rocks plagioclase is albite. In addition, plagioclase in these rocks has angular shapes, undulose extinction and cloudy cores.

In granitic to quartz monzonitic gneisses, potassic felsdpar is microcline occurring mainly as irregular to lenticular cloudy porphyroclasts, ranging in size from 0.5 to 0.7 millimetres, showing sutured grain boundaries and ribbon perthites and fine-grained inclusions of magnetite and sericite. Ghosts of Carlsbad plane twinning may be observed in albite-pericline twinned crystals.

In gneisses, quartz (0.25 to 2 mm in size) is lenticular with undulose extinction and sutured boundaries, or comprises fine grained (0.08 mm) recrystallized aggregates in the mylonitic matrix. The amount of quartz in the gneisses increases with the Ab content of plagioclase.

In amphibolites quartz is a minor mineral, forming lenticular aggregates interstitial to amphibole and plagioclase. Individual crystals have undulose extinction, sutured borders and subgrain boundaries. This mineral occurs mostly in protomylonitic albite-bearing amphibolites.

Preferentially oriented biotite (0.08 to 1.2 mm in size) occurs as strongly pleochroic laths in the gneisses (Z= dark green, brownish green or brown; Y= green or yellowish brown and X= light yellow to colorless) and contains magnetite arranged in thin films along cleavage planes or in rims of small grains.

Biotite in amphibolites forms oriented laths, 1.0 to 1.5 mm long and the pleochroism displays Z= reddish brown, Y= brown and X= yellowish brown.

Biotite sometimes surrounds cummingtonite in albite-rich mylonitic gneisses and amphibolites.

Amphiboles observed in gneisses and amphibolites, display the same colors, pleochroic schemes and intergrowth relationships. They are hastingsite and cummingtonite. The former is strongly pleochroic with Z= dark bluish green, Y= green or yellowish green and X= light green and the latter is greenish to colorless. Both amphibole types show irregular or lenticular shapes with straight, curved or serrated boundaries, with dimensions ranging from 0.5 to 2 mm for the porphyroclasts or 0.04 to 0.08 mm in the matrix . The two amphiboles usually display intergrowth textures with optical continuity. Cummingtonite forms narrow rims around hastingsite, or penetrates the latter along fracture and cleavage planes, suggesting substitution of Ca-amphibole by Fe-Mg amphibole. Such features are mainly observed in albite-rich mylonitic rocks.

Amphiboles in amphibolites grade from 0.1 to 2 mm. They are prismatic or lenticular with straight, embayed or lobate boundaries in foliated amphibolites and granoblastic with straight boundaries and triple points, in granoblastic polygonal-textured amphibolites.

Tourmaline in gneisses forms sub-idioblastic porphyroclasts, about 0.3 mm long, strongly pleochroic, from blue or bluish green to brownish or light blue, and dravitic in composition.

Tourmaline in amphibolites occurs as idioblastic prisms up to 2.5 mm long. It is schorlitic to dravitic in composition and pleochroic from yellowish brown to dark brown.

In both rock types tourmaline is surrounded by chlorite which also penetrates along its fractures.

Chlorite, in gneisses and in amphibolites, is an alteration product of most mafic minerals, surrounding or pseudomorphically replacing biotite and hastingsite. It is also found interstitial to quartz in the mylonitic matrix.

The accessory minerals in basement rocks are: magnetite, ilmenite, zoned zircon, apatite, allanite and titanite.

Allanite is strongly pleochroic from dark brown to brownish green forming monomineralic micro lenses, mainly in gneisses.

Titanite consists of very small idioblastic crystals, always occurring together with chlorite, in microfractures or arranged like pearl necklaces, around partially or completely chloritized hastingsite or biotite (Photomicrographs 25 and 27).

4.3 Metasedimentary Rocks

The Metasedimentary Sequence consists of iron formation, metagraywackes and quartzites.

4.3.1 Iron Formation

Based mostly on mineral assemblage, the Salobo iron formation was divided into two types:

Type I, with fayalite-magnetite or grunerite-magnetite, minor hastingsite, biotite, garnet almandine, greenalite and fluorite, and accessory graphite, ilmenite, allanite, apatite, copper sulphides, uraninite and molybdenite, and

Type II, formed of magnetite-almandine garnet-grunerite-(fayalite)-biotite, with subordinate to minor hastingsite, tourmaline, chlorite, fluorite, greenalite, and quartz and accessory apatite, allanite, zircon, graphite, copper sulphides, molybdenite and uraninite.

Type I and Type II iron formations are fine to very coarse-grained (hornfelsic) rocks, massive to strongly foliated or schistose. Massive rocks are composed of granular minerals such as fayalite and almandine garnet, the foliated iron formation of grunerite or oriented quartz lenses, and the schistose varieties of oriented biotite. Magnetite is observed in all types of iron formations. Millimetric to sub-millimetric mylonitic bands are common in all iron formations.

a) Mineral Descriptions of Iron Formation

Fayalite exhibits irregular crystals, rounded to elongated, grading from 1 millimetre to 10 centimetres. They are greenish, with embayed, cuspate or lobate boundaries showing fractures filled with magnetite.

Garnet shows two different types of textures, here denominated garnet I and garnet II.

Garnet I forms large and irregular grains, 1 to 10 centimetres in size, and comprises about 70% of all the garnets observed in iron formation. It is is dark pink and strongly zoned, from a very dark pink (or burgundy) core to a pink rim. The cores often show sieve texture, with inclusions of magnetite, ilmenite, graphite, fayalite, hastingsite and rarely biotite. The garnets have fractures filled with green biotite or chlorite along with magnetite, bornite and chalcocite (Photomicrograph 28).

Garnet II consists of light pink, idioblastic to sub-idioblastic grains, varying from 0.1 to 0.5 millimetres in diameter. It is unzoned, displaying straight, curved or embayed boundaries. Garnet II may also occur as skeletal crystals, surrounding quartz in a fish-net texture. Inclusions are mostly quartz and additionally grunerite, biotite and tourmaline (Photomicrographs 28, 29 and 30).

Chlorite may pseudomorphically replace both types of garnet.

The amphiboles are Ca amphiboles (hastingsite /Fe-pargasite) and Fe-Mg amphiboles (grunerite-gedrite) hereafter referred as hastingsite and grunerite.

Hastingsite is more frequently observed in Type I iron formation. It forms irregular and lenticular grains, 0.15 to 1.2 mm long, mostly associated with fayalite, with straight or lobate boundaries. Pleochroism is strong from Z= deep bluish green; Y= green to brownish green and X= greenish yellow. In mylonitic iron formation it may form porphyroclasts with subgrain boundaries made up of grunerite. Hastingsite and grunerite present intergrowth with optical continuity, similarly to the hastingsite-cummingtonite intergrowth described in the gneisses, where thin grunerite prisms penetrate hastingsite along borders, cleavage or fracture planes, leading to a complete pseudomorphic substitution.

Grunerite occurs as rims around fayalite with small acicular prisms penetrating fayalite borders, and as rounded to lenticular aggregates including magnetite, as product of pseudomorphic substitution of fayalite (Photomicrographs 31 to 36).

Grunerite also exhibits acicular prisms (0.015 to 10 millimetres) with strong preferred orientation, straight to serrated boundaries and polysynthetic twinning, in strongly foliated rocks. It is colorless to slightly pleochroic, with: Z= greenish to greenish gray; Y= yellowish to yellowish gray and X= greenish, yellowish or colorless.

Grunerite and gedrite also occur as fibrous reaction rims surrounding fayalite, magnetite and hastingsite in quartz bearing rocks (Photomicrographs 37, 38 and 39).
In protomylonitic to mylonitic rocks grunerite is observed as porphyroclasts and matrix (Photomicrograph 41 and 42), and as subgrain boundaries around hastingsite porphyroclasts (Photomicrograph 43).

Biotite displays irregular laths interstitial to granoblastic minerals, in Type I iron formation, or preferred oriented laths in Type II iron formation (where it is a major mineral) (Photomicrograph 44). It is 0.05 to 5 millimetres long in both types of iron formation, often forming rims around grunerite. In mylonitic rocks it may occur as porphyroclasts or in the matrix. Biotite porphyroclasts are frequently observed bent or with kinked cleavage planes, they may also show sub grain boundaries made up of biotite and magnetite or chlorite, magnetite and ilmenite, the second association indicating alteration. Biotite displays different colors and pleochroic formulae depending on host rock composition and Fe/Mg ratios, as will be seen in Chapter 5. In Type I iron formation, biotites are red, showing Z= dark brownish red; Y= reddish brown and X= yellow, whereas in Type II iron formation, biotites are brown, displaying Z= dark brown: Y= greenish and X= light yellow.

Quartz occurs almost exclusively in Type II iron formation and it is never in contact with fayalite.

It comprises two textural types:

The first is made up of irregular, elongated to lenticular aggregates, with undulose extinction and 0.5 to 2 millimetres in dimensions, showing sutured borders and/or subgrain boundaries, seldom occurring as granoblastic grains.

The second type consists of fine grained and recrystal'ized quartz in mylonite matrix, or quartz ribbons.

Tourmaline consists of idioblastic prisms, 0.02 to 3 millimetres long, defining a lineation in the schistosity plane. It is schorlite in composition, showing pleochroism from dark bluish green to pink. It occurs mostly associated with biotite.

Chlorite consists of three textural types: the first was already described and comprehends chlorite replacing garnet, hastingsite and biotite (Photomicrograph 45). The second occurs in shear planes or in mylonitic matrices and the third fills undeformed fractures.

Fluorite occurs mostly interstitial to fayalite in Type I iron formation (Photomicrograph 46) or penetrati ıg garnet I along fractures. The association fluorite-hastingsitc is not observed.

Greenalite occurs in three different ways: in thin films (reaction rims) around fayalite (Photomicrograph 47), in fluorite-fayalite iron formation, preventing direct contact between fayalite and fluorite; surrounding and replacing pseudomorphically fayalite (Photomicrograph 48) or

in rims around grunerite, often associated with uraninite (Photomicrograph 49).

The accessory minerals are apatite, allanite, zircon and graphite. Allanite is concentrated in microlayers, in rounded to elongated grains, showing intense fracturing and pleochroism from dark brown to deep green.

Zircon consists of very fine grained crystals often associated with quartz lenses.

Graphite shows rosettes included in garnet I, (Photomicrograph 50) or is interstitial to grunerite prisms. It also occurs along sheared microfractures.

4.3.2 Metagraywackes

The metagraywackes are medium grained rocks, displaying strong schistosity or foliation (Photomicrograph 51), with mylonitic bands, made up of biotite, almandine garnet and quartz, subordinate muscovite, tourmaline, and plagioclase, minor sillimanite, grunerite and chlorite and accessory magnetite, allanite and zircon. These rocks show relicts of granoblastic texture in plagioclase-rich bands, where straight boundaries and triple points are still observed.

a) Mineral Descriptions of Metagraywackes

Biotite forms oriented laths, 0.02 to 0.5 millimetres long, which show lobate boundaries, surrounded by very fine-grained muscovite and magnetite (Photomicrograph 52). It is strongly pleochroic with Z= reddish brown; Y= orange-yellow to greenish gray and X= light yellow to light green. Biotite also shows muscovite intergrowth, with optical continuity.

Almandine garnet occurs in two different forms. The first is light pink idioblastic with straight boundaries and inclusions of quartz and tourmaline (0.1 to 0.4 mm) and the second consists of large (1 to 2 mm), dark pink, xenoblastic grains including quartz in a fish net texture (Photomicrograph 53).

Quartz displays elongated, lenticular aggregates with strong preferred orientation and 0.15 to 2.00 millimetres in dimensions, showing an augen-like texture. Individual quartz crystals also exhibit sutured borders and undulose extinction.

Muscovite consists of laths 0.01 to 5 millimetres long with straight or lobate boundaries. It occurs in small randomly-oriented laths penetrating biotite boundaries, or in intergrowth with optical continuity with biotite (Photomicrographs 52 and 54).

Tourmaline is very small and idioblastic (0.1 to 0.5mm). It is zoned, with blue core and greenish rim, dravitic to schorlitic in composition and pleochroic from blue to bluish green. Tourmaline occurs in aggregates

associated with biotite, often at biotite boundaries (Photomicrographs 52 and 54).

Plagioclase is observed forming lenticular aggregates of twinned grains, arranged in microlayers. It has highly variable composition ranging from An_{20} to An_{70}.

Sillimanite is fibrous or idioblastic and prismatic. Both crystal shapes may form lenticular aggregates associated with biotite, muscovite and tourmaline. Fibrous and curved sillimanite is often included in muscovite (Photomicrographs 52 and 55).

Grunerite shows preferred oriented colorless prisms, with serrated boundaries at basal sections, surrounded by biotite.

Chlorite displays rims composed of small laths, surrounding biotite and garnet, partially replacing these minerals. It also occurs as randomly oriented laths included in biotite and muscovite.

Accessory minerals are minute crystals of apatite, zircon and allanite. Allanite is frequently included in biotite pseudomorphically replaced by chlorite.

4.3.3 Quartzites

Quartzites are medium to fine grained rocks, mostly foliated (Photomicrograph 56), showing mylonitic bands. They are made up of quartz (48 - 94%), muscovite (6 - 44%), chlorite (0 - 15%), biotite (0 - 10%), sillimanite (0 -7%),

feldspar (0 - 3%), almandine garnet (0 - 1%) and magnetite (0 - 3%) (Table 4.4).

Assuming that muscovite, sillimanite and feldspars are derived from clastic feldspars, and also assuming that biotite, chlorite, almandine garnet and magnetite are derived from rock fragments, the results of modal analyses were plotted in Figure 4.1. It can be seen that, all but one sample plot in the fields of subarkose and arkosic arenite of Pettijohn's (1975) sandstone classification diagram (Figure 4.1).

a) Mineral Descriptions of Quartzites

Quartz displays lenticular aggregates 2 to 7 mm long , showing undulose extinction, sutured borders and subgrain boundaries, with strongly preferred orientation,.

Muscovite is seen as large, lens-shaped crystals, minute laths and intergrown with chlorite or sillimanite. Large (0.5 to 3 mm) lens-shaped muscovite has lobate boundaries. Very small laths, with strongly preferred orientation, are interstitial to quartz and may also form inclusions in that mineral. Muscovite is intergrown with chlorite (Photomicrograph 57) along cleavage planes or with sillimanite along crystal boundaries (Photomicrograph 58).

Sillimanite is included in quartz, forming very small oriented-prisms or occurs as lenses of fibrous aggregates interstitial to quartz.

Biotite shows small oriented-laths, 0.5 to 1 mm long, with serrated boundaries and with magnetite films included along cleavage planes. It is pleochroic from Z= green or greenish brown; Y= greenish brown to yellowish green and X= light yellow to brownish yellow.

The feldspars in the quartzites are K-feldspar and plagioclase. The K-feldspar is microcline, which is very altered, cloudy and partially replaced by muscovite and chlorite with ghosts of albite pericline twinning planes. Albite ($An_{1.5}$) is clear, rounded to irregular shaped, interstitial to quartz and seldom twinned.

Chlorite pseudomorphically replaces biotite and garnet (Photomicrograph 59). Chlorite pseudomorphs after biotite contain rutile needles and are surrounded by very fine-grained magnetite.

Almandine garnet is idioblastic (0.1 to 2.5 mm) pink and with green biotite along fractures.

The accessory minerals are zoned and rounded zircon and allanite.

4.4 Intrusive Rocks

There are two types of intrusive rocks in the study area: granitoid rocks and diabase dykes.

4.4.1 Granitoid Rocks

The modal compositions of the Old Salobo Granite (OSG) and of the Young Salobo Granite (YSG) plot in the fields of granite and alkali-feldspar quartz syenite, respectively, in Streckeisen's (1976) classification of plutonic rocks (Figure 4.2).

a) Old Salobo Granite

The OSG is a medium grained, granular hypidiomorphic rock, with protomylonitic to mylonitic bands, composed of orthoclase and microcline (27-32%), oligoclase (30-37%), quartz (23-29%), augite (0-6%), hornblende (2-6%), chlorite (0-2%) and magnetite (0-1%) (Table 4.5).

a.1) Mineral Descriptions of OSG

Perthitic orthoclase includes patches of microcline. Alkali feldspars are irregular to lenticular shaped, displaying undulose extinction and sutured boundaries. They are 2 to 4 mm long and often surrounded by a very thin and clean rim of albite.

Oligoclase (An_{14}) is subidiomorphic, in 1 to 2 mm long crystals, and with subgrain boundaries. It shows kinked or bent twinning planes.

Quartz constitutes a fine-grained matrix composed of unstrained-mosaic grains (0.05 to 0.08 mm), or occurs as

larger crystals (1.5 mm), interstitial to feldspars, with undulose extinction and serrated boundaries.

Augite is observed in large irregular grains, with embayed boundaries. It is interstitial to feldspars and has many inclusions of rounded quartz and magnetite, it also shows two rims: the inner one made up of deep green hornblende and the outer one formed of chlorite.

Zoned zircon, allanite and magnetite are accessory minerals.

b) Young Salobo Granite

The rock referred to here as YSG is in fact an alkali-feldspar quartz syenite sill-like body (Figure 4.2) composed of orthoclase (43-47%), albite (25-30%), quartz (5-15%), chlorite (8-12%) and magnetite (4-10%), with minor fluorite, allanite, zircon, calcite, epidote, sericite and chalcopyrite (Table 4.5).

The YSG has porphyritic seriate or glomeroporphyritic texture (Photomicrograph 60) with an aphanitic groundmass at the contact with the host rock which grades to a phaneritic groundmass towards the centre. In the central part of the sill a granular hypidiomorphic texture predominates.

b.1) Mineral descriptions of YSG

Albite occurs as phenocrysts in porphyritic rocks or equant grains in hypidiomorphic ones. Albite porphyries are idiomorphic with dimensions ranging from 0.25 to 1 mm. They are always twinned, with composition ranging from $An_{1.5}$ to $An_{8.0}$. Sericite, calcite and epidote incipiently replace albite, indicating slight alteration. Rims of orthoclase are also observed, indicating rapakivi texture.

Orthoclase constitutes the aphanitic groundmass in porphyritic varieties or occurs as 0.5 to 1.0 mm long crystals in granular rocks. It is subidiomorphic, untwinned and surrounded by myrmekitic rims (Photomicrograph 60). Sericite, calcite and epidote are observed in orthoclase grains, along fractures or cleavage planes, suggesting alteration.

Quartz is always in the groundmass, interstitial to feldspars. It shows unstrained extinction and is 0.05 to 0.2 mm long.

Chlorite is anhedral, forming biotite pseudomorphs, with inclusions of magnetite films along cleavage planes. Chlorite often shows rosettes, 0.1 to 0.5 mm in diameter, interstitial to feldspars and quartz.

Magnetite is in the groundmass, showing idiomorphic cubic shapes.

Lilac-colored fluorite, chalcopyrite, zircon and allanite are accessory minerals.

4.4.2. Diabase Dykes

Diabase dykes show chilled vitreous margins with amygdules and hyalocrystalline texture, grading towards the centre to fine to medium grained, porphyritic and sub-ophitic rocks (Photomicrograph 61). Myrmekitic textures, in fine sub-ophitic rocks are also observed in the centre of the dykes.

Diabase dykes are made up of plagioclase (An_{42} to An_{54}) and Ti-augite, with minor hornblende and chlorite and accessory ilmenite, quartz and apatite.

a). Mineral descriptions of diabase

Plagioclase forms zoned, idiomorphic laths surrounded by myrmekites and showing chlorite along cleavage planes. The albite content of plagioclase increases from An_{42} near the borders, to An_{54} in the centre of dyke.

Ti-augite is interstitial to plagioclase, forming agglomerates of unequant grains often surrounded by a rim of brown hornblende, chlorite and magnetite. These rims are more frequent in the centre of the dyke.

Quartz is interstitial, forming irregular grains whose amount increases towards the centre of dyke.

Acicular apatite, magnetite and ilmenite are accessory minerals.

4.4.3 Veins

Two types of veins are observed in the Salobo area: deformed and undeformed.

Deformed veins are composed of quartz and tourmaline. Quartz is strained, with undulose extinction and sutured boundaries. Tourmaline is equant to unequant, very fractured, often showing lobate boundaries.

Undeformed veins are mostly zoned and show a large variation in mineral content, depending on host rock composition.

Veins in metagraywacke have the walls incrusted with quartz and/or chlorite flakes and calcite occupying the centre. Fluorite may form lenses included in calcite.

Veins in iron formation are formed of: greenalite and uraninite, with green greenalite forming veinlets with minute uraninite grains included in grunerite at the vein margins; greenalite and fluorite, with greenalite and minute magnetite lining the vein walls and fluorite in the centre; stilpnomelane showing thin bands, parallel to the vein margins, grading from green at margins to brownish green towards the centre (Photomicrograph 62); chlorite lining the margins with minor quartz in the centre. A gold flake was observed in one chlorite vein.

Veins in basement rocks are composed of: quartz, calcite and fluorite. Small projecting quartz crystals line the vein walls while calcite and fluorite occur in the centre of the veins. Epidote and calcite veins display walls

incrusted of zoned, brown to greenish, idiomorphic epidote and calcite occupying the centre (Photomicrograph 63). Chalcopyrite, quartz, epidote and cobaltite veins, with projecting idiomorphic epidote lining the walls and chalcopyrite with quartz and cobaltite in the centre (Photomicrographs 64 and 65) and chalcopyrite, epidote, calcite and stilpnomelane veins where the walls are incrusted with idiomorphic epidote, which is rimmed, towards the centre of the vein, by brownish green stilpnomelane showing crustiform texture. The centre of the vein is formed by chalcopyrite, with inclusions of calcite patches.

Veins in Southern Shear Zone comprise mostly albite and quartz. Quartz may occur in open or closed fractures, forming idiomorphic prisms, perpendicular to the vein walls. Albite occurs in rounded to lenticular druses, forming small projecting idiomorphic crystals lining the interior surface of the druse (Photomicrograph 66). The centre of the druse is occupied by quartz and the walls are externally surrounded by muscovite.

4.5. Shear zones

There are two main shear zones in the study area: the Northern Shear Zone (NSZ) and the Southern Shear Zone (SSZ).

The NSZ comprises mylonitized basement rocks and iron formations. In the iron formation, the mylonitized rocks are formed of hastingsite, grunerite, quartz and magnetite.

Hastingsite shows augen-like shapes with subgrain boundaries made up of grunerite. In basement rocks, the NSZ is represented by mylonitic gneisses and amphibolites formed of hastingsite or cummingtonite porphyroclasts, in a matrix of albite and quartz.

The SSZ comprises mostly mylonitized metagraywackes and quartzites. The most important features of this zone, besides the intense fracturing, is the widespread chloritization of Ca-amphiboles, biotite and garnet, along with plagioclase albitization.

4.6. Ore

Salobo ore is Type I iron formation containing copper sulphides. There is a sympathetic relationship, in the ore, between the amount of magnetite and copper sulphides. Type I iron formation consists mostly of magnetite with minor garnet almandine, grunerite *q* fayalite, biotite and sulphides.

The copper sulphides are mostly bornite and chalcocite, with subordinate chalcopyrite and covellite. The ore minerals consist also of molybdenite, graphite, ilmenite, safflorite and cobaltite.

The sulphides are mostly interstitial to magnetite and less commonly to silicate minerals (Photomicrograph 67). The crystal shape of copper sulphides as well as their mineralogy are strongly dependent on host rock composition.

Granular ore is more frequent in granoblastic fayalite-garnet host rocks, and is lenticular in foliated grunerite-biotite host rocks (Photomicrograph 68).

The copper sulphide mineralogy is also closely related to the host-rock silicate mineral assemblages. Chalcopyrite occurs in magnetite-fayalite bearing rocks (Photomicrograph 67); bornite dominates in magnetite-grunerite rocks (Photomicrograph 68) and bornite-chalcocite are predominant in magnetite-grunerite-biotite-chlorite iron formation (Photomicrograph 69).

4.6.1 Ore Mineral Description

The petrography of transparent minerals of Type-I iron formation has been already described in item 4.2.1. Only the oxide-sulphide minerals will be described here

Magnetite constitutes about 85% of the oxide-sulphide assemblage. It occurs in thin discontinuous bands or irregular lenses (Photomicrograph 70), gently folded and interlayered with quartz or in granular mosaic-like aggregates with straight boundaries and triple points. These granular aggregates are the silicates and sulphides matrix in fayalite-garnet I bearing iron formation.

Chalcopyrite consists of xenoblastic aggregates (0.1 - 7 mm), interstitial to fayalite or to fayalite pseudomorphically replaced by grunerite (Photomicrograph

67). It occurs also as thin films around garnet I, fayalite or hastingsite; as inclusions in magnetite or rimmed by minute-idioblastic magnetite (Photomicrograph 71).

Bornite occurrence can be divided into three types: a) interstitial to magnetite, in magnetite rich layers, showing myrmekitic intergrowth with chalcopyrite or chalcocite; b) interstitial to and associated with silicates (Photomicrographs 68 and 69), in elongated shapes or dust-like forms, surrounding grunerite and in garnet I fractures with green biotite and chlorite; c) in chlorite-rich rocks, showing two concentrical rims, the inner one consisting of chalcocite and the outer one of covellite.

Chalcocite occurs mainly in intergrowth with bornite in biotite-bearing rocks (Photomicrograph 69). It is observed in garnet I fractures together with bornite and in thin films along biotite cleavage planes.

Graphite shows rosettes 0.5 to 1.0 millimetre in diameter. It is also observed as inclusions in garnet I (Photomicrograph 50) and grunerite; at garnet borders; interstitial to quartz and in fractures, associated to chlorite and magnetite.

Ilmenite is commonly observed as inclusions in garnet I or magnetite.

Safflorite and cobaltite, occur in undeformed veins along with magnetite, chalcopyrite and epidote (Photomicrographs 64 and 65). Gold bearing safflorite and cobaltite were also described by Figueiredo (1982).

Molybdenite occurs principally associated with micro shear planes, undeformed quartz veins and minor pegmatitic veins.

Gold flakes were observed in undeformed chlorite (Photomicrograph 72) and stilpnomelane veins, cutting iron formation. They also occur associated with As-rich minerals.

Table 4.1 MINERALOGICAL COMPOSITION OF TYPE I IRON FORMATION

Sample no.	1 50-92	2 50-135 /1	3 50-135 /3	4 56-217 /1	5 56-217 /2	6 56-217 /4	7 56-217 /5	8 61-230 /4	9 49-351 /4
MAGNETITE	■	■	⊥	■	■	■	■	■	■
FAYALITE			P					■	■
GRUNERITE	⊥	■	■	⊥	■	■	■	⊥	■
QUARTZ	■	■	⊥	■	■	■	■		
HASTINGSITE					⊥	⊥		-	
GARNET		-	⊥						
BIOTITE	⊥	-	⊥					-	
ALLANITE					⊥	⊥			
GRAPHITE									-
APATITE								-	⊥
TOURMALINE					-				
CHLORITE			⊥	-			-		
GREENALITE	⊥	⊥						⊥	⊥
FLUORITE								⊥	
CHALCOPYRITE				-					-
BORNITE	-		-	-	-	-	-	-	
CHALCOCITE			-		-			-	
URANINITE									-

■ MAJOR ⊥ MINOR - TRACES P PSEUDOMORPHS (GRUNERITE)

Table 4.1. MINERALOGICAL COMPOSITION OF TYPE I IRON FORMATION (continued)

Sample no.	1 17-312 /2	2 49-337 /1	3 50-86	4 56-217 /3	5 56-280 /3	6 61-120 /1	7 61-120 /2	8 61-230 /3
MAGNETITE		■	■	■	■	■	■	■
FAYALITE						P		■
GRUNERITE		■	⊥	■	■	■	■	⊥
QUARTZ	■	■	■	■	-	-	■	
HASTINGSITE				-				-
GARNET	■	⊥			-	■	⊥	⊥
BIOTITE	■		⊥		⊥			
CHLORITE	-	-	-		-	⊥		
GREENALITE						⊥	-	-
FLUORITE								⊥
ALLANITE	-						⊥	
APATITE							-	
GRAPHITE						-	-	-
URANINITE		-						
BORNITE	-	-	-	-	-	-	-	-
CHALCOCITE	-	-		-	-	-	-	-

■ MAJOR ⊥ MINOR - TRACES P PSEUDOMORPHS (GRUNERITE)

Table 4.2. MINERALOGICAL COMPOSITION OF TYPE II IRON FORMATION

Sample no.	1 17-312 /3	2 49-243 /3	3 49-299	4 49-337 /3	5 49-337 /2	6 49-351 /3	7 49-351 /5	8 50-135 /2	9 50-470 /1
MAGNETITE	■	■	■	■	■	■	⊥	⊥	■
FAYALITE				P			P	P	P
GRUNERITE			■	■	■	■	■	⊥	■
QUARTZ	■	■	⊥	⊥	⊥			■	
GARNET		■	■		■	■	⊥	■	⊥
BIOTITE	■	–		■	■	⊥	■	■	■
TOURMALINE			⊥				⊥		⊥
CHLORITE		–			⊥	⊥	⊥		
GREENALITE								⊥	
ALLANITE	–			–	–	–			
ZIRCON	–		–						–
GRAPHITE		–				–	–		
BORNITE	–				–	–		–	–
CHALCOCITE	–				–				–

■ MAJOR ⊥ MINOR – TRACES P PSEUDOMORPHS (GRUNERITE)

Table 4.2. MINERALOGICAL COMPOSITION OF TYPE II IRON FORMATION (continued)

Sample no.	1 50-582 /3	2 50-682 /1	3 50-682 /3	4 56-280 /1	5 61-109 /2	6 61-124 /1	7 61-124 /3	8 61-230 /1	9 49-230 /5
MAGNETITE	⊥	–	⊥	⊥	–	⊥	⊥	⊥	⊥
FAYALITE	P					P	P	■	
GRUNERITE		■	■	⊥		■	■		
QUARTZ	–	■	■	■	–	⊥	■		⊥
HASTINGSITE								⊥	■
GARNET	■	■	■	■		■	■	■	⊥
BIOTITE	■	■	■	■	■	■		■	■
TOURMALINE		⊥			■				
CHLORITE	⊥		–	–		–	–		⊥
GREENALITE								–	
ALLANITE	–	–				–	–	–	
APATITE	–	–						–	–
GRAPHITE						–	–		
FLUORITE								–	–
URANINITE	–	–	–						
ILMENITE				–		–			
BORNITE	–			–		–	–	–	
CHALCOCITE	–			–		–	–	–	
GOLD							–		

■ MAJOR ⊥ MINOR – TRACES P PSEUDOMORPHS (GRUNERITE)

Table 4.2. MINERALOGICAL COMPOSITION OF TYPE II IRON FORMATION (continued)

Sample no.	1 50-470 /2	2 50-470 /3	3 50-470 /4	4 50-470 /5	5 50-569 /1	6 50-569 /2	7 50-582 /1	8 50-582 /2
MAGNETITE	⊥	■	⊥	–	⊥	⊥	■	⊥
FAYALITE						P	P	P
GRUNERITE	■	■	■	■	■	■		■
QUARTZ		⊥		–	–	–		■
GARNET					■	■	■	■
BIOTITE	■	■	■	–		■	–	⊥
TOURMALINE	–	–	–			–		
CHLORITE		⊥		–	–	–		–
GREENALITE					–			
ALLANITE							–	
GRAPHITE					–			
BORNITE					–		–	
CHALCOCITE							–	

■ MAJOR ⊥ MINOR – TRACES P PSEUDOMORPHS (GRUNERITE)

Table 4.2. MINERALOGICAL COMPOSITION OF TYPE II IRON FORMATION (continued)

Sample no.	1 17-312 /b	2 17-312 /4	3 36-277 /1	4 36-277 /2	5 36-277 /3	6 36-277 /4	7 36-277 /5	8 49-243 /1	9 49-366 /1
MAGNETITE	-	-	⊥	⊥	⊥	-	⊥	⊥	-
GRUNERITE				■	■		■		
QUARTZ	■	■	■	⊥	■	■	⊥	■	■
GARNET	⊥	⊥	■	■	■	■	■	■	■
BIOTITE	■	■	■	■	■	■	■	■	■
TOURMALINE									-
CHLORITE		-	-	-	-	-	-		
ALLANITE	-					-		-	-
APATITE						-		-	
ZIRCON	-								

■ MAJOR ⊥ MINOR - TRACES

Table 4.3. MINERALOGICAL COMPOSITION OF METAGRAYWACKES

Sample no.	1 12-214	2 17-350 /1	3 17-350 /4	4 17-350 /6	5 17-350 /7	6 17-350 /8	7 20-520	8 31-283	9 31-298
QUARTZ	■	■	■	■	■	■	■	■	■
BIOTITE	■	■	■	■	■	⊥	■	■	■
GARNET	■	■	⊥			⊥			
MUSCOVITE			■	■	■		■		
TOURMALINE	■		⊥	■	⊥		–	–	⊥
PLAGIOCLASE			⊥	⊥	⊥		⊥	■	–
GRUNERITE							⊥	■	
MAGNETITE	–	–	–	–	–	–	–	–	–
ALLANITE	–		–		–	–	–	–	–
ZIRCON		–	–	–		–	–		–
CHLORITE	–	⊥	–	–	–		–	–	⊥
SILLIMANITE			–	–	⊥				

■ MAJOR ⊥ MINOR – TRACE

Table 4.4. MODAL COMPOSITION OF QUARTZITES

Sample no.	1 20-162	2 20-184	3 20-190	4 28-202	5 28-214	6 28-400	7 28-417	8 28-449
Quartz	84.00	78.00	85.00	55.00	47.00	67.00	76.00	94.00
Muscovite	15.00	12.00	8.00	30.00	44.00	13.00	20.00	6.00
Chlorite	1.00	5.00	4.00			15.00		
Biotite			1.00	10.00				
Feldspar		3.00	1.00		1.00	1.00		
Garnet			1.00					
Sillimanite		1.00		4.00	7.00	1.00	2.00	
Magnetite			0.50			3.00	2.00	

Table 4.5. MODAL COMPOSITION OF GRANITOID ROCKS

Sample no.	1 19-199	2 19-206	3 12-477	4 6-88	5 6-88A	6 6-88B
K-feldspar	43.00	47.00	43.00	27.00	32.00	29.00
Albite	26.00	31.00	28.00			
Oligoclase				37.00	37.00	31.00
Quartz	9.00	5.00	15.00	23.00	24.00	30.00
Augite				6.00		5.00
Hornblende				2.00	6.00	3.00
Chlorite	12.00	8.00	9.00	3.00		
Magnetite	10.00	8.00	4.00	1.00		1.00

1 - 2 - 3 - YSG (Young Salobo Granite=alkali-feldspar quartz syenite)
4 - 5 - 6 - OSG (Old Salobo Granite)

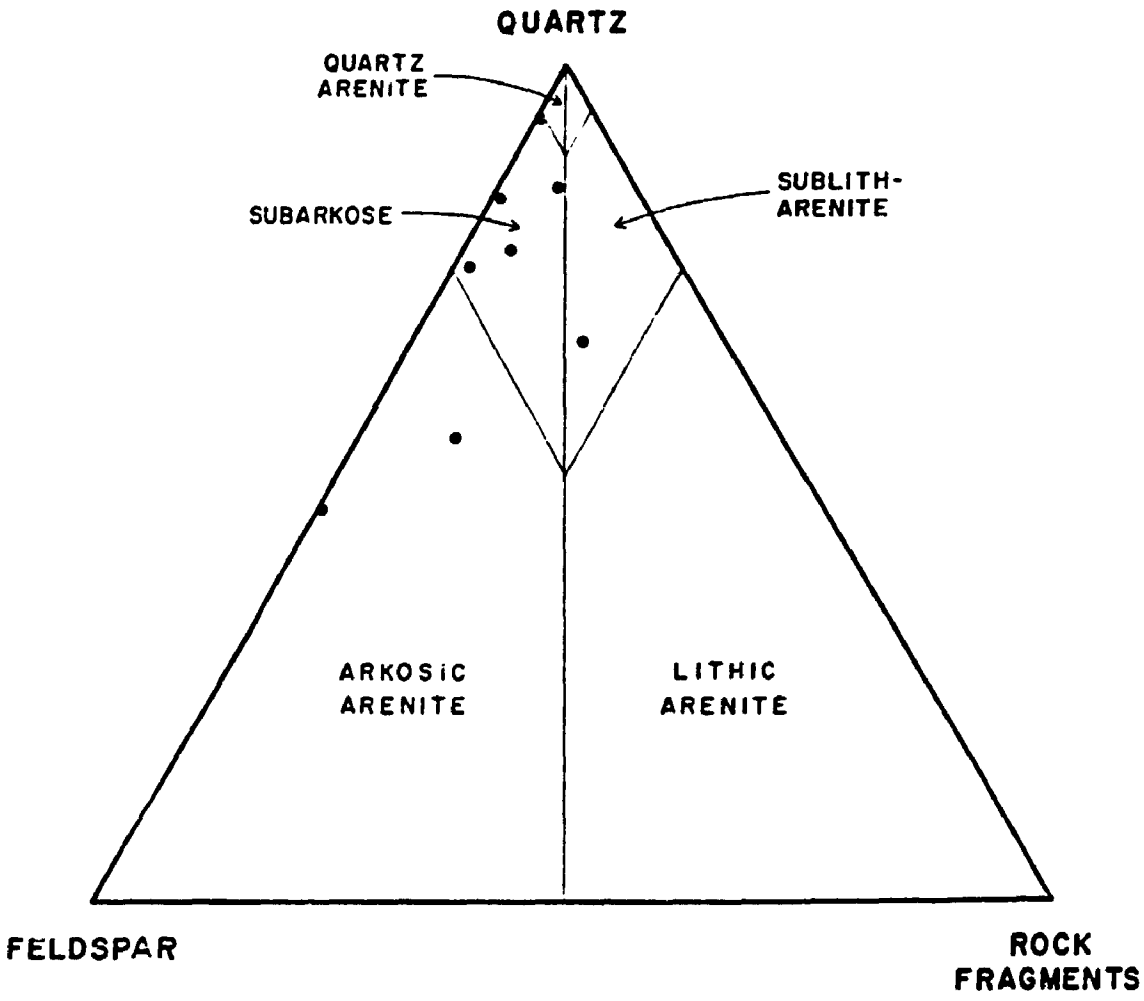

FIGURE 4.1. Classification of Salobo Quartzites
Assuming:
Feldspar = muscovite + sillimanite+ feldspar
Rock fragments = biotite + chlorite+ garnet + magnetite
Quartz = quartz

According to Pettijohn's (1975) classification of terrigenous sandstones.

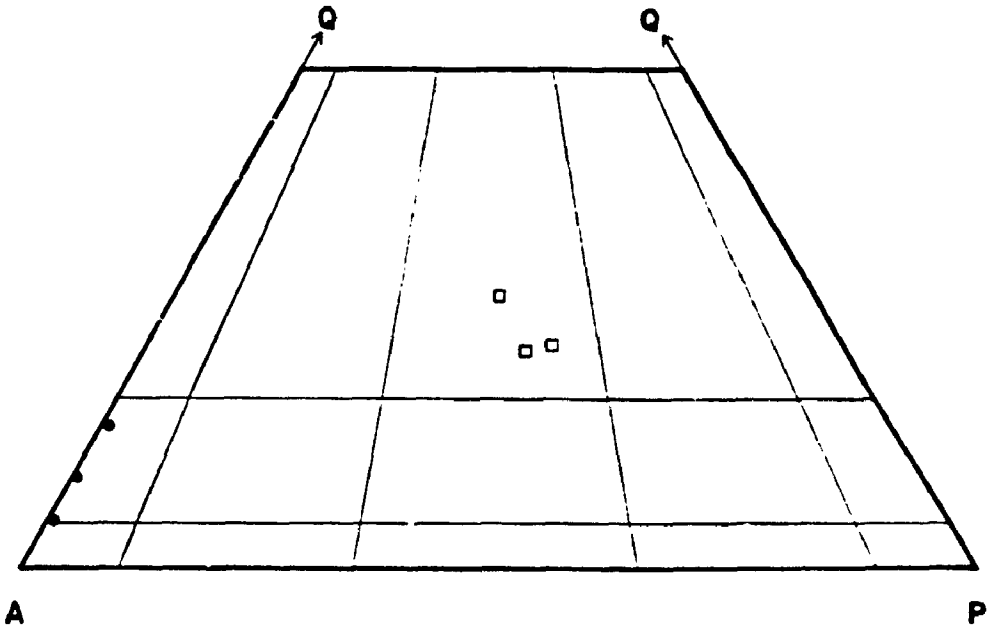

FIGURE 4.2. Classification of plutonic rocks:
Alkali-feldspar quartz syenite (YSG)
(solid circles)
Granite (OSG) (squares)

Fields according to Streckeisen (1976).

Plate 4 - Photomicrographs of gneisses and amphibolites.

19. Trondhjemitic gneiss showing equant to lenticular plagioclase (An_{10}), with subgrain boundaries made up of quartz and hastingsite. This sample represents the less deformed gneiss.

20. Trondhjemitic gneiss displaying protomylonitic texture, with irregular to lenticular-shaped albite (An_{5}) porphyroclasts in a matrix of quartz and albite.

21. Protomylonitic trondhjemitic-gneiss. Hastingsite and albite (An_{3}) occur as porphyroclasts and in the matrix. Arrow points to a partial rim of cummingtonite around hastingsite.

22. Foliated trondhjemitic gneiss exhibiting lens-shaped oligoclase (An_{14}). This mineral also has a cloudy aspect and is untwinned. Quartz is irregular-shaped, and with undulose extinction occurring in annealed aggregates. Cummingtonite is in oriented laths.

23. Granoblastic amphibolite with hastingsite showing triple points. Quartz (qz) and plagioclase (pl) are interstitial to hastingsite. Chlorite is in two shear planes, seen at the top and bottom of the photomicrograph.

24. Mylonitic amphibolite composed of hastingsite, albite (An_{7}) and quartz, with minor biotite and cummingtonite. This sample was dated by Machado et al., (1988), yielding a zircon U/Pb age of 2555+4/-3Ma.

PLATE 4

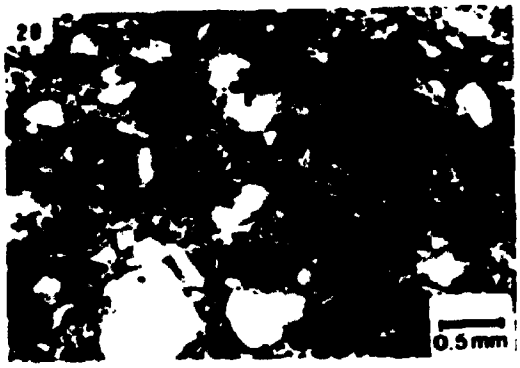

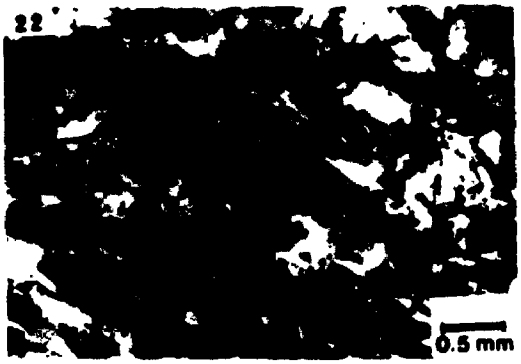

Plate 5 - Photomicrographs of amphibolites and iron formations.

25. Oriented biotite, defining the schistosity in a granoblastic-textured amphibolite.
26. Chlorite and titanite vein cutting amphibolite. At the vein contact, dark green hastingsite is altered to cummingtonite, and plagioclase to epidote and sericite. The opaque is magnetite. Arrows point to titanite.
27. Detail of pervasive chloritization in amphibolite. The lenticular relict of hastingsite is surrounded (partially replaced) by chlorite with inclusions of titanite. Cloudy plagioclase is altered to sericite, epidote and calcite. Arrows point to titanite.
28. Garnet I and garnet II side by side. Zoned garnet I at left is pinkish showing inclusions of magnetite, whereas garnet II at right is unzoned and devoid of inclusions.
29. Deformed garnet II in Type II iron formation displaying inclusions of quartz and biotite. The matrix is protomylonitic and composed of quartz, biotite and magnetite.
30. Idioblastic garnet II with inclusions of quartz, biotite and grunerite in the core, and tourmaline in the rim. This feature indicates that tourmaline formed later than biotite and grunerite. Arrows point to tourmalines.

PLATE 5

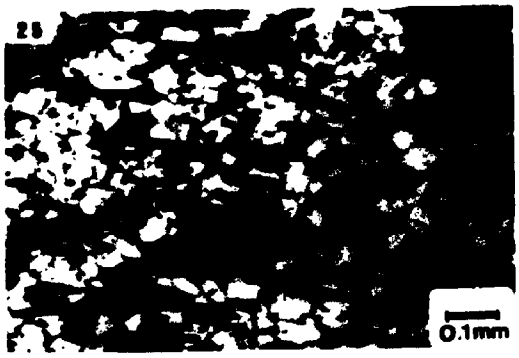

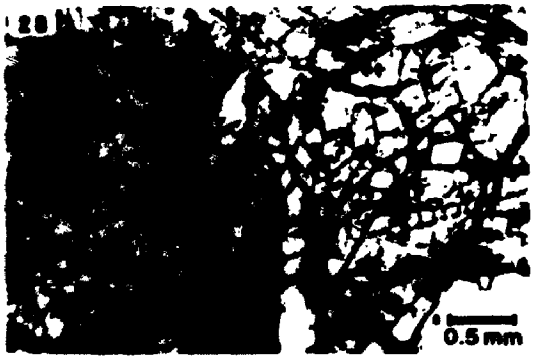

Plate 6 - Photomicrographs showing the progressive alteration of fayalite-magnetite to grunerite-magnetite iron formation.

31. Unaltered granoblastic fayalite displaying triple-point contacts.
32. Incipient stage of alteration. Fayalite subgrain-boundaries are composed of grunerite.
33. This photomicrograph shows a more advanced stage of alteration than the previous one (32). Grunerite prisms penetrate fayalite from borders and fractures. Arrows indicate grunerite prisms.
34. Lenticular fayalite exhibiting partial substitution by grunerite and magnetite. Arrows point to grunerite.
35. Complete substitution of fayalite by grunerite is shown by the lenticular aggregate of grunerite, pseudomorphic of fayalite.
36. Foliated grunerite-magnetite without vestiges of the previous fayalite-magnetite iron formation.

PLATE 6

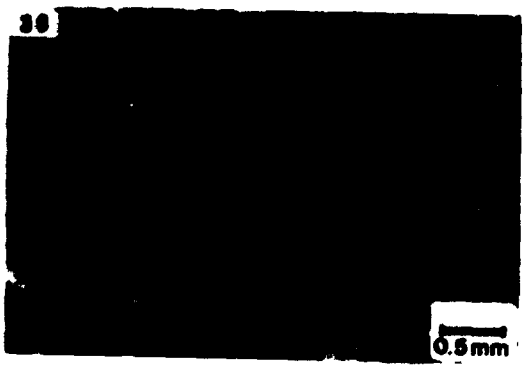

Plate 7 - Photomicrographs of iron formations.

37. Fayalite enveloped by fibrous gedrite with inclusions of magnetite in a quartz matrix. This feature is representative of the reaction of fayalite (fay) plus quartz (qz), producing gedrite (g) and magnetite. Note the absence of direct contacts between quartz and fayalite.

38. Magnetite surrounded by fibrous gedrite (g) in quartz (qz) matrix. These relationships correspond to the completion of the reaction shown in previous photomicrograph (37).

39. Grunerite rimming hastingsite (h) and penetrating fayalite (fay). This is a feature which indicates simultaneous alteration of both, hastingsite and fayalite. Arrow points to grunerite prism in fayalite.

40. Hastingsite surrounded by fibrous grunerite, which shows inclusions of biotite and magnetite in quartz matrix. This feature indicates reaction of hastingsite plus quartz producing grunerite, biotite and magnetite. Arrows indicate biotite.

41. Mylonitic iron formation displaying grunerite porphyroclasts in a matrix of quartz, grunerite and magnetite.

42. Protomylonitic iron-formation with grunerite forming the matrix and porphyroclasts.

PLATE 7

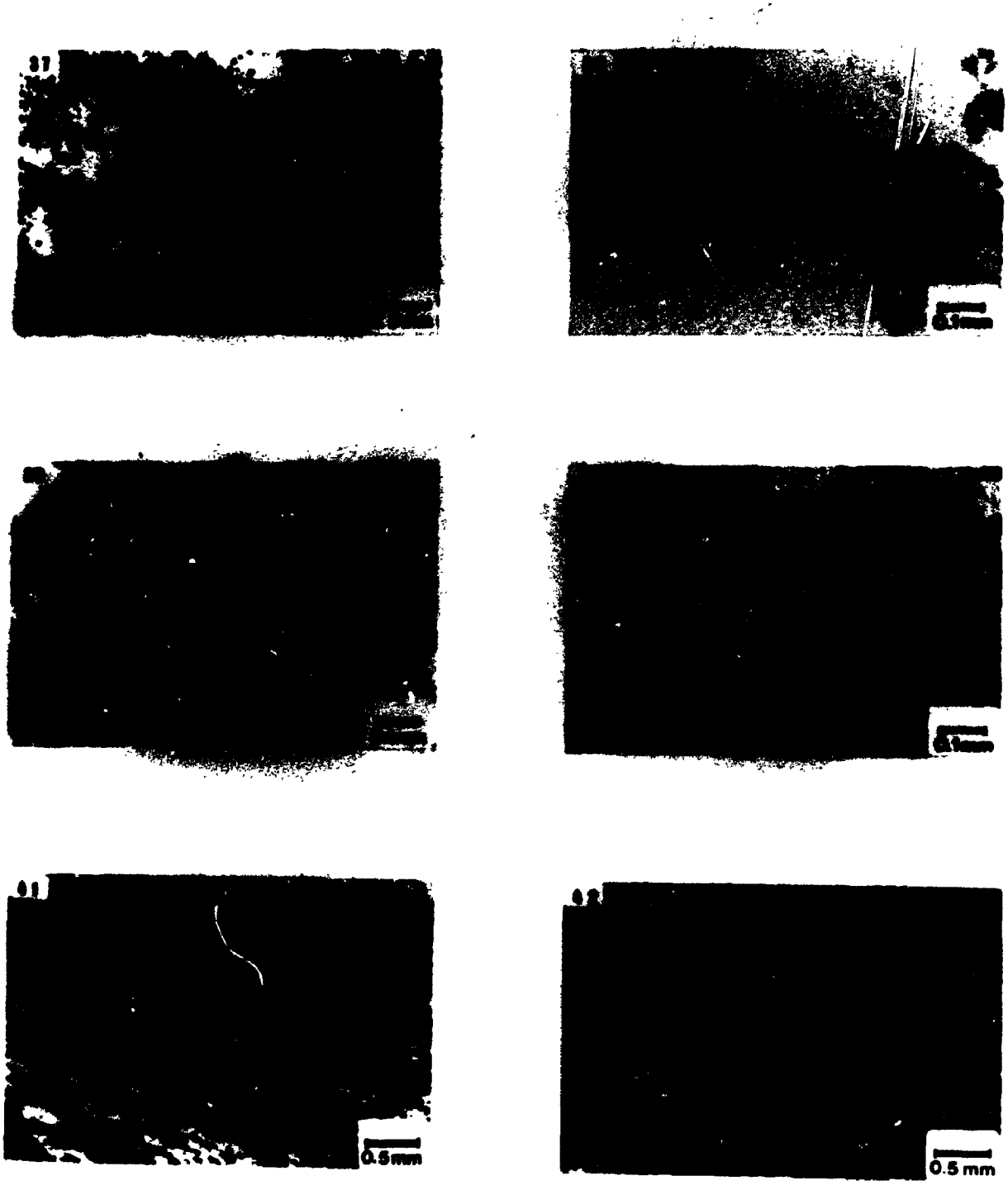

Plate 8 - Photomicrographs of iron formation.

43. Hastingsite phenoclast with grunerite subgrain boundaries, occurring in mylonitic iron formation. The matrix consists of quartz and magnetite.
44. Detail of garnet I rim with inclusion of biotite. Note the contact between the garnet core, with magnetite, ilmenite and graphite inclusions and rim, devoid of opaque inclusions. Note also the sharp contact between garnet and biotite.
45. Pervasive chloritization in Type II iron formation. Lens-shaped relicts of biotite are surrounded by chlorite, magnetite and titanite. Quartz, sericite and epidote are interstitial to chlorite.
46. Granoblastic and fractured fayalite and magnetite in a fluorite matrix.
47. Detail of the previous photomicrograph (46) showing fayalite rimmed by greenalite in the fluorite matrix. This feature indicates that greenalite is a reaction product of fluorite and fayalite. Opaque is magnetite.
48. Substitution of fayalite by greenalite and magnetite. Fayalite in contact with fluorite on the right, displays an inner rim of greenalite and an outer one of magnetite.

PLATE 8

Plate 9 - Photomicrographs of iron formations and metagraywackes.

49. Grunerite enveloped by a deep green film of greenalite. Uraninite is responsible for the dark brown pleochroic haloes observed in grunerite. Note that uraninite is in grunerite fractures, near the contact with greenalite. (fay)-fayalite, (qz)-quartz.

50. Graphite and magnetite (mt) as inclusions in garnet I (gn). Arrows point to graphite.

51. Compositional variation in metagraywacke. The microlayers are formed of: a) cummingtonite ± biotite ±tourmaline, b) biotite ±tourmaline ±quartz ±magnetite, and c) biotite, quartz and cummingtonite.

52. Biotite encircled by thin films of muscovite and magnetite, associated to tourmaline and to lenticular aggregate of fibrous sillimanite. These relationships indicate reaction of sillimanite (s) and biotite (bt), producing muscovite (mu), tourmaline (t) and magnetite.

53. Metagraywacke composed of quartz, garnet, biotite and minor tourmaline. Garnet surrounds quartz in a fish-net texture.

54. Biotite (bt) enveloped by thin films of muscovite (mu) plus magnetite, associated with tourmaline (t) and quartz. Well developed muscovite is seen upper left. The absence of sillimanite along with the well developed muscovite and tourmaline indicate completion of the reaction shown in photomicrograph 52, above.

PLATE 9

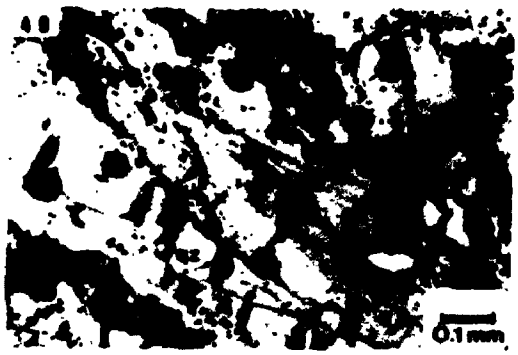

Plate 10 - Photomicrographs of metagraywacke, quartzites and alkali feldspar quartz-syenite.

55. Detail of a lenticular aggregate of sillimanite in metagraywacke. Basal sections are surrounded by prismatic to fibrous sillimanite. Compare this unaltered aggregate with the partially altered one shown in photomicrograph 52, plate 9.

56. Foliated to schistose quartzite. Quartz with undulose extinction exhibits sutured borders and thin subgrain boundaries. There are also flakes of biotite (bt) and muscovite (mu).

57. Detail of chlorite-muscovite (mu) intergrowth in quartzite. Magnetite aggregates are at chlorite core and rim. Arrow indicates rutile needles along cleavage planes of chlorite.

58. Muscovite-sillimanite intergrowth in quartzite indicating replacement of sillimanite (s) by muscovite (mu).

59. Garnet pseudomorph composed of chlorite and quartz (qz) in quartzite. Some garnet (gn) relicts still persist. Muscovite (mu) is observed at bottom left.

60. Alkali feldspar quartz-syenite (YSG) displaying porphyritic seriated-texture. Albite phenocrysts are surrounded by orthoclase. Myrmekites may also be observed in the matrix.

PLATE 10

Plate 11 - Photomicrographs of diabase and undeformed veins.

61. Medium-grained diabase showing subophitic texture. Sample collected at the centre of the dyke.

62. Stilpnomelane vein in iron formation displaying crustiform texture. The color variation from green (ferro-stilpnomelane) to yellowish green (ferri-stilpnomelane) is indicative of Fe oxidation state.

63. Epidote (ep) and calcite (c) vein in gneiss.

64. Epidote with chalcopyrite (cpy) and cobaltite (cb) in undeformed vein, cutting trondhjemitic gneiss

65. Detail in reflected light of the same vein shown in photomicrograph 64, exhibiting chalcopyrite (cpy) and cobaltite (cb). The black portion is an aggregate of epidote.

66. Albite druse with quartz in the centre. Muscovite is in the sheared microplane seen at bottom left, as well as interstitial to albite at top left of the photomicrograph.

PLATE 11

Plate 12 - Photomicrographs of ore minerals.

67. Magnetite-chalcopyrite intergrowth is interstitial to fayalite in Type I iron formation. Dark needles seen in fayalite are composed of grunerite.

68. Bornite-chalcopyrite intergrowth in iron formation. The host rock is formed of grunerite (g), quartz and minor biotite (bt). The straight boundaries and lenticular forms of the copper sulphides are mostly controlled by amphibole and biotite shapes. Bornite (bn), chalcopyrite (cpy).

69. Intergrowth of chalcocite (cs) and bornite (bn) in iron formation. The host rock is formed of magnetite-grunerite (g) - biotite (bt) ± chlorite. Arrow points to graphic intergrowth chalcocite-bornite.

70. Magnetite in Type I iron formation. The rock is composed of grunerite, hastingsite and quartz. Arrows indicate minute inclusions of chalcopyrite and bornite.

71. Magnetite-chalcopyrite intergrowth in veinlets, cutting grunerite-biotite-garnet iron formation.

72. Gold flakes in undeformed chlorite-vein cutting garnet (gn). Inclusions of magnetite (mt) are also observed in the garnet.

PLATE 12

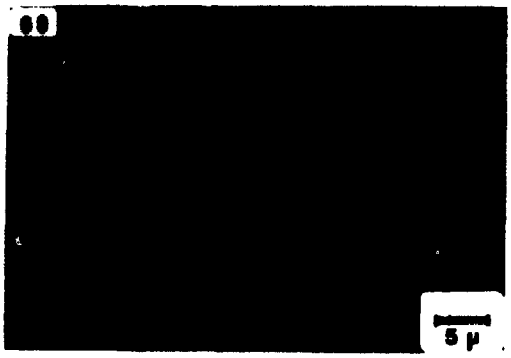

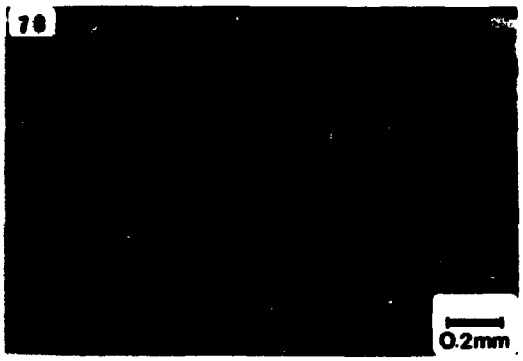

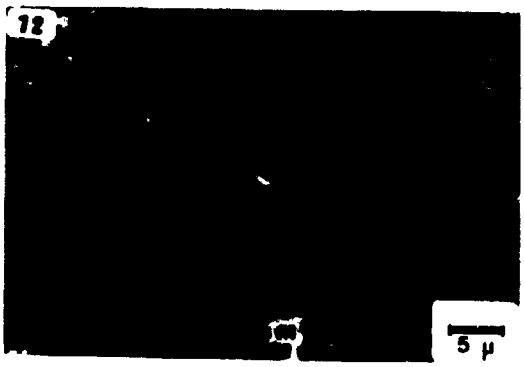

CHAPTER 5

LITHOGEOCHEMISTRY

5.1. Introduction

This chapter is the summary of the lithogeochemical data of the study area, obtained by the interpretation of major, minor, trace and rare earth element analyses.

A total of 98 samples were analyzed, including 13 samples of gneisses, 7 of amphibolites, 55 of iron formation, 6 of metagraywackes, 8 of quartzites, 3 of diabase and 6 of granitoid rocks.

Analytical techniques, and tables of rock analyses are presented in Appendices B and A, respectively.

5.2. Basement Rocks

5.2.1. Gneisses

The basement gneisses show normative compositions of trondhjemites, granites, granodiorites and quartz-monzonites, according to O'Connor's (1965) classification (Tables 5.1, 5.2; Figure 5.1).

Trondhjemitic gneisses are sodic rocks presenting K/Na ratios varying from 0.04 to 0.44. They also have high SiO_2/Al_2O_3 ratios, ranging from 5 to 7, very low Ca/Al (0.07) and Ca/Na (0.192) ratios and slightly high Na/Al (0.350) ratio.

They are low Al_2O_3 trondhjemitic gneisses, according to Barker's (1979) classification of trondhjemites.
The compositional deviation of the Salobo trondhjemitic gneisses from "normal" trondhjemite composition may be visualized in figure 5.2. The average of the major oxides for the studied trondhjemites was plotted, normalized by the average composition of Archean trondhjemites from Scotland (Rollinson and Windley, 1980), Antarctic (Sheraton and Black, 1983; Sheraton et al., 1985) and Wyoming (Barker et al., 1979) and Phanerozoic trondhjemites from French Central Massif (Nicollet et al., 1979) and Norway (Barker and Millard Jr., 1979) (Table 6.3). It may be observed in the diagram that the studied rocks have very low CaO, lower TiO_2, P_2O_5 and Al_2O_3, and higher FeO* and MgO than the average trondhjemites.

Trondhjemitic gneisses show low Zr and very low Sr and Ba and extremely high La, Ce, Th and U (Figure 5.3). Their K/Rb (221), Ba/Sr (3.69) and Rb/Sr (1.098) ratios are ten times higher than the average values of trondhjemites around the world (table 5.3).

The trondhjemitic gneiss analyzed exhibits REE enrichment (σREE 571.98 ppm) and a slight negative Eu

anomaly ($Eu/Eu^* = 0.77$). It also shows a strongly fractionated pattern ($Ce/Yb_{cn} = 47.41$), LREE enrichment (250 x chondrite) and HREE depletion (10 x chondrite), see table 5.4 and figure 5.4.

Granitic and quartz-monzonitic gneisses are potassic rocks with K/Na ratios ranging from 1.2 to 1.4. They present low TiO_2, CaO, Al_2O_3 and P_2O_5, and high MgO and MnO in comparison to the average of rocks of the same composition from Manitoba (Ermanovics et al., 1979), Australia, Greenland (Kolbe and Taylor, 1966, in: Collerson and Bridgwater, 1979), Antarctic (Sheraton and Black, 1983) and Scotland (Rollinson and Windley, 1980), listed in table 5.3.

In granitic gneisses only Y, Ga, and Pb are similar to average values of granitic-gneisses as displayed in table 5.3. They also present high Rb/Sr and K/Ba ratios.

Discussion

Trondhjemitic gneisses are albitized rocks (chapter 4). Their low Ca/Na and Ca/Al ratios, slightly high Na/Al ratio, along with the low calcium content seen in figure 5.2, indicate that the albitization took place rather by calcium leaching than by Na intake. The low Sr and Ba contents of these rocks are in accordance with the above conclusion. Sr and Ba tend to act like calcium rather than sodium in the plagioclase structure (Drake and Weill, 1975), following calcium in the leaching process. Therefore, the low Ca, Sr

and Ba contents may be attributed to a leaching process resulting in a pervasive albitization of these rocks.

The low absolute Al_2O_3 value, which led to the classification of low Al_2O_3 trondhjemite (according to Barker's 1979 classification) should not be taken into account, because these rocks were submitted to metasomatic processes.

Granitic gneisses are also albitized rocks. Similarly to trondhjemitic gneisses, they show low Ca, Ba and Sr contents indicating that they were submitted to the same albitization process (granitic and trondhjemitic gneisses are intercalated), where Sr and Ba might follow Ca during the leaching process. Their high Rb/Sr and K/Ba ratios are due to low Sr and Ba contents, but their Rb content is only slightly low.

Speculations about the origin

Archean granitic gneisses have been considered as the result of the partial melt of continental rocks, mainly metagraywackes, or of a mixture of sedimentary and igneous rocks, followed by fractional crystallization (Condie and Hunter, 1976; Condie, 1978; Hanson, 1978; Sheraton et al., 1985).

Trondhjemites and tonalites have been considered as resulting from the: progressive partial melting of a tholeiitic, amphibolitic, and eclogitic source; melting of

enriched mantle and its fractional crystallization (Anderson et all., 1986).

The low Al_2O_3 and Sr values of trondhjemitic gneisses of the study area are similar to those of oceanic trondhjemites defined by Arth (1979). The REE pattern of Salobo trondhjemitic gneisses is analogous to the patterns observed for continental trondhjemites (Arth, 1979): highly fractionated and absence of significative Eu anomaly (or with a slight negative anomaly). According to what was discussed above, the absolute values of Al_2O_3 and Sr cannot be used for geological environment considerations. The other hypothesis of a continental trondhjemite-related origin is favored, considering that the REE were not later mobilized.

The negative Eu anomaly might indicate that plagioclase was the residual phase, if the partial melting or fractional crystallization model is considered (Barker et al., 1979). In addition to that, the HREE depletion might be due to the presence of residual hornblende and garnet; besides, the low TiO_2 would require an Fe and Ti oxide residual phase.

5.3. Amphibolites

The amphibolites plot in the field of subalkaline basalts on the discrimination diagram of magma types (Winchester and Floyd, 1976) of figure 5.5. They have normative compositions corresponding to olivine tholeiites, except for one sample which shows a small quantity of normative nepheline (Tables 5.5 and 5.6).

The amphibolites are Fe enriched, with FeO^* varying from 15.12 to 17.66%, corresponding to ferro-tholeiites according to Jensen's (1976) classification. They are enriched in incompatible elements, such as K_2O, Rb, Ba and LREE and depleted in Sr, Zn, Ni and Cr. They also have low CaO and MgO and slightly high Na_2O.

They present average ratios of the less mobile elements, i.e. Ti, Al, Zr, Y, Nb (Al_2O_3/TiO_2 = 7.01; Ti/Zr = 71.6; Ti/Y = 264; Zr/Y = 3.69; Zr/Nb = 17.22; Ti/V = 38) within the range of tholeiitic rocks (Winchester and Floyd, 1977; Pearce and Cann, 1973; Pearce, 1975; Floyd and Winchester, 1978) or of Archean tholeiitic basalts (Condie, 1984; 1989).

The amphibolites are metamorphosed continental tholeiites as may be observed in figure 5.6, where the average of hygromagmatophile element abundances (trace elements with bulk distribution coefficients (D) less than one, Wood et al., (1979)), normalized to primordial mantle composition, plots within the field of tholeiitic basalts from continental environment, presented by Holm (1985).

The amphibolites are chemically similar to the volcanic rocks of Grao ParàGroup. Although, they are FeO^*, TiO_2 and REE enriched and Cr depleted, presenting K_2O and Ba contents analogous to the intermediate unit of the Parauapebas volcanic rocks.

In the diagram TiO_2-FeO^* of figure 5.7 Salobo amphibolites are the most differentiated rocks, plotting in

The amphibolites show REE chondrite-normalized patterns analogous to the Phanerozoic continental basalts (Cullers and Graf, 1984) and to the Archean Grao Para Group basalts (Gibbs et al., 1986). Although, Salobo amphibolites are more REE enriched and less fractionated than Grao Parà basaltic rocks.

The continental setting of Salobo amphibolites, along with its position in the same differentiation trend as are the volcanic rocks of Grao ParàGroup (Figure 5.7), strongly suggest that both rocks are related to the same magmatic event.

Amphibolites are partially albitized rocks. Their low Ca and Sr values indicate that they were subjected to the same Ca leaching process, experienced by the gneisses and which gave origin to albitization of plagioclase. The slightly high Na_2O and high K_2O values may also indicate Na and K introduction during the metasomatic alteration.

The high K content, as well as the enrichment of other incompatible elements, such as Rb, Ba, Zr and LREE may be original, because this is a chemical characteristic of continental basaltic-rocks.

One can also speculate that Na, Ca, K and Si had already been mobilized during a possible spilitization process, if the amphibolites were originally volcanic rocks. In this case they should have had Na, K, Si and Rb increasing and and Ca decreasing content, with the

the same trend as do the volcanic rocks of the Grao Parà Group (Gibbs et al., 1986; Ferreira Filho and Danni, 1985), and between the intermediate and the top basaltic unit in the diagram K_2O - Fe/Mg of figure 5.8.

The amphibolites are REE-enriched, with $\sum$REE varying from 98.32 to 154.17 ppm (Table 5.7). They also show $(La/Lu)_{cn}$ from 0.63 to 1.35 and Eu/Sm from 0.24 to 0.44, presenting an approximately flat normalized pattern, slight LREE fractioning and Eu anomaly varying from slightly positive ($Eu/Eu^* = 1.21$), to moderately negative ($Eu/Eu^* = 0.56$) (Figure 5.9).

The amphibolites have a very homogeneous chemical composition. They do not present by themselves a differentiation trend as it would be expected from basaltic flows. This fact may be due to sampling, because the samples were collected in the centres of less altered amphibolite lenses, or these rocks may represent undifferentiated flows, dykes or sills. The limited number of analyzed samples (7) does not permit drawing conclusions about the primary origin of amphibolites: intrusive or extrusive.

Discussion

The amphibolites show REE chondrite-normalized patterns analogous to the Phanerozoic continental basalts (Cullers and Graf, 1984) and to the Archean Grao Para Group basalts (Gibbs et al., 1986). Although, Salobo amphibolites are more REE enriched and less fractionated than Grao Parå basaltic rocks.

The continental setting of Salobo amphibolites, along with its position in the same differentiation trend as are the volcanic rocks of Grao ParåGroup (Figure 5.7), strongly suggest that both rocks are related to the same magmatic event.

Amphibolites are partially albitized rocks. Their low Ca and Sr values indicate that they were subjected to the same Ca leaching process, experienced by the gneisses and which gave origin to albitization of plagioclase. The slightly high Na_2O and high K_2O values may also indicate Na and K introduction during the metasomatic alteration.

The high K content, as well as the enrichment of other incompatible elements, such as Rb, Ba, Zr and LREE may be original, because this is a chemical characteristic of continental basaltic-rocks.

One can also speculate that Na, Ca, K and Si had already been mobilized during a possible spilitization process, if the amphibolites were originally volcanic rocks. In this case they should have had Na, K, Si and Rb

increasing and and Ca decreasing content, with the spilitization (Fyfe and Lonsdale, 1981; Fyfe, 1983; Fyfe, 1987).

The data discussed above indicate that Salobo amphibolites are metamorphosed tholeiitic basaltic-rocks emplaced in continental environment. The data also suggest that these rocks are coeval to the basaltic rocks of Grao ParáGroup. Nevertheless, their present chemical composition still reflects the metasomatic alteration process: Ca and Sr leaching, slight Na enrichment and possible K mobilization, with the consequent albitization of plagioclase.

5.4. Metasedimentary Sequence

5.4.1. Iron Formation

The iron formation of the study area was divided into two types: Type I (Fe-Si) and Type II (aluminous), as described in chapters 3 and 4.

Type I iron formation is in the field of iron formations defined by James (1966) (Figure 5.10), whereas, Type II iron formation exhibits an Al_2O_3 and SiO_2 enrichment progressing towards the point representing the average composition of basaltic rocks. This indicates that the aluminous contamination of Type II iron formation is probably due to volcaniclastic rocks of basaltic composition.

The Al_2O_3-FeO^*-(K_2O x 5) diagram of figure 5.11 indicates that the volcanic rocks of the Grao Para Group could be the volcaniclastic contaminants in Salobo Type II iron formation.

In the diagram of figure 5.12, Type I iron formation shows all but one major oxide (MgO) contained in the compositional field of world iron formations (Gole and Klein, 1981), whereas Type II iron formation shows higher Al_2O_3, TiO_2 and K_2O and lower SiO_2 and MgO than the world average iron formations.

The positive correlation shown by TiO_2-K_2O, TiO_2-Al_2O_3 and TiO_2-Zr in Type II iron formation indicates that Ti, Al, K and Zr are probably related to the same homogeneous source (Figures 5.13, 5.14 and 5.15).

MgO in Type II iron formation does not present sympathetic relationship with any other element. In Type I MgO has a negative correlation with FeO^* (Figure 5.16).

Type II iron formation also displays negative correlation between TiO_2-FeO^* and Al_2O_3-FeO^* indicating an antipathetic relationship between Fe and Ti-Al (Figures 5.17 and 5.18).

The trace elements in Type I and Type II iron formations are in the range presented by Dymek and Klein, (1988), Gross and McLeod, (1980), Gole, (1981), and Davy, (1983), except for higher contents of Cu, Ag, Au and REE. From Type I to Type II iron formation there is an increase in Zr, Y, Zn, Co and V and a decrease in Cu, Ni and Cr

contents. Positive correlations between Cu-FeO*, Cu-La and Cu-$\sum$REE are also observed, indicating a common homogeneous source for these elements (Figures 5.19, 5.20 and 5.21). Au and Ag show positive correlation solely between themselves (Figure 5.22).

Both iron formations are strongly REE-enriched, with total REE varying from 230 to 2,200 ppm, which represents 60 to 300 times the chondrite value.

The REE chondrite-normalized pattern of Type I iron formation (figure 5.23) is LREE enriched and highly fractionated, with $(La/Lu)_{cn}$ = 441.8, $(La/Sm)_{cn}$ = 19 and $(Gd/Lu)_{cn}$ = 18.09, showing strong positive Eu anomaly (Eu/Eu^* = 6.34). Type II iron formation exhibits REE chondrite-normalized patterns with more moderate slopes than Type I. They are also LREE-enriched, with $(La/Lu)_{cn}$ = 22 to 53, $(La/Sm)_{cn}$ = 8 to 13 and $(Gd/Lu)_{cn}$ = 1.3 to 5.7, showing positive or negative Eu anomaly (Eu/Eu^* = 2.13, 1.17 and 0.52) (Figure 5.24).

Discussion

Type I iron formation

Recent chemical sediments depositing from ocean waters such as Fe-Mn deposits, close to the Mid Oceanic Ridges, accurately reflect the depletions of Ce and Eu in ocean waters (Piper and Graef, 1974; Piper, 1974; Fleet, 1984). This fact led Fryer (1977) to suggest that the iron

formations would be the best rocks to register the secular variations of REE behavior in ocean waters. He proposed that the Eu behavior in iron formations was time-dependent, and that Archean iron formations should be enriched in Eu, consequently showing positive Eu anomalies, whereas Proterozoic chemical sediments would only show slightly positive or slightly negative Eu anomalies.

However, Graf (1978) showed that Paleozoic volcanic-related iron formations also presented strong positive Eu anomalies, resulting from the influence of hydrothermal solutions and not from secular variations of REE behavior in ocean waters. He also suggested that the hydrothermal solutions were Eu-enriched due to preferential alteration of feldspar.

REE chondrite-normalized pattern of Type I iron formation (REE-enriched, highly fractionated and showing a strong Eu positive anomaly) is analogous to patterns of recent hydrothermal solutions, principally to those collected in the East Pacific Rise (EPR) by Michard et al., (1983). Although Type I iron formation is more REE enriched than EPR.

Therefore, based on REE data of Type I iron formation and the discussion above, it is possible to conclude that the chemical sediments of the study area were strongly influenced by hydrothermal solutions.

Type II iron formation

High Al_2O_3 contents in chemical sediments, as observed in Type II iron formation, have been attributed to contamination from a clastic detrital or volcaniclastic source (Gole, 1981).

Similar compositional gradations were found by Gole (1981) among iron formations, Fe-shales and associated basalts from Yilgarn Block and Hamersley Basin (Australia) and by Breitkopf (1988), between aluminous iron formations and associated amphibolites from Damara (SW Africa). Volcaniclastic layers were also recently described in the Gunflint and Sokoman iron formations in Canada, by Hassler and Simonson (1989). Therefore, iron formations with a volcaniclastic contribution, as Type II Salobo iron formation, are relatively frequent.

The igneous origin of the non-chemical components of Type II iron formation is enhanced by the positive correlation presented by K_2O-TiO_2, TiO_2-Al_2O_3 and TiO_2-Zr (Figures 5.13, 5.14 and 5.15), all of them probably derived from the same igneous homogeneous source. In opposition, the negative correlation between TiO_2-FeO^* and Al_2O_3-FeO^* (Figures 5.17 and 5.18) can be attributed to different rock sources, since Fe is hydrothermally derived.

Thus, the observed gradation between Type I and Type II iron formations described in chapter 3 reflects increasing

volcaniclastic contribution to the hydrothermal chemical sediments of Type I iron formation.

The low MgO content of Type II iron formation (figure 5.12) may either be an inheritance from the original precursor or reflect the metamorphic/metasomatic mobilization. The lack of MgO correlation with any other oxide or trace element (except for a slight negative correlation with FeO^*, in Type I iron formation whose samples are less affected by metasomatic processes) seems to suggest that the MgO behavior is chiefly due to metasomatic mobilization.

The REE pattern of Type II iron formation is approximately compatible with that of Archean sha . (Jenner et al., 1981; Taylor et al., 1986). The dip slope shown by the curves reflecting LREE enrichment, may be attributed to the influence of the hydrothermal source, whereas the HREE attenuation of the curves may be due to the volcaniclastic components. The positive Eu anomaly was probably originated by the hydrothermal solutions, although its relation to plagioclase accumulation may not be discarded. The HREE convexity shown by the samples 50-682-1 and 49-351-5 may be credited to the presence of garnet in these rocks. The negative Eu anomaly in sample 49-351-5 is not easily explained; this is the only sample showing chloritization, suggesting that the Eu anomaly could be related to the metamorphic/metasomatic process.

Implications for Carajas stratigraphy

There is no doubt that the data and discussion presented above indicate that Type II iron formation has a volcaniclastic contribution of composition compatible with that of basaltic rocks.

The known basaltic rocks in the Carajas region include volcanic rocks of the Parauapebas Formation (Docegeo, 1988) at the base of the Carajas iron formation (iron ore). Volcanic rocks are also encountered at the top of the Carajas iron-formation described at the Bahia (Au-Ag-Cu) deposit (Ferreira Filho, 1985) and they are included in the "Upper Volcanic Sequence" (Docegeo, 1988) (chapter 3). These two volcanic sequences are therefore the best candidates for the volcaniclastic source of Type II iron formation.

The good positive correlation between K_2O-TiO_2, TiO_2-Al_2O_3 and TiO_2-Zr (Figures 5.13; 5.14 and 5.15) suggests that these elements were derived from the same igneous source. However, K_2O could be derived either from K_2O-rich continental volcanics or from a later process of water-rock interaction.

The volcanic rocks of Parauapebas Formation, (Gibbs et al., 1986) (Table 5.11), show K enrichment towards the top of the volcanic pile; the Upper Volcanic Sequence (Bahia deposit) is also K-enriched (Ferreira Filho, 1985) (Table 5.11), as well as Salobo amphibolites. The Al_2O_3-FeO^*-

(K_2Ox5) diagram (figure 5.11) indicates that either Parauapebas Formation or Upper Volcanic Sequence rocks could be the source of the volcaniclastic contaminants in Salobo Type II iron formation. This strongly suggests that Type II iron formation and the Salobo Sequence are coeval to Grao Para Group.

More studies on Carajas stratigraphy are necessary to establish if the Salobo sequence was deposited at Parauapebas or at Upper Volcanic Sequence time. By any means, taking into account the present knowledge on the area, the best correlation of Salobo is with the Upper Volcanic Sequence, the only known unit where clastic sediments predominate.

5.4.2. Metagraywackes

The rocks classified as metagraywackes in chapters 3 and 4 show chemical composition analogous to the Archean metagraywackes presented by Taylor et al., (1986), Jenner et al., (1981) and Nance and Taylor, (1977) (Table 5.12). In general however, they exhibit higher TiO_2 and Fe_2O_3 and lower MgO and CaO than the Archean metagraywackes referred to in the literature.

The existing gradation between Type II iron formation and metagraywackes, described in chapter 3 is chemically represented by an increase in SiO_2, TiO_2, Al_2O_3, Na_2O and K_2O and a decrease in Fe_2O_3, MnO, MgO and CaO contents.

The metagraywackes display a positive correlation between Al_2O_3-TiO_2 and K_2O-TiO_2, suggesting a common homogeneous source for these elements (Figures 5.25, 5.26).

The Al_2O_3-FeO^*-(Al_2O_3 x 3) diagram of figure 5.27 is a plot of the average of Archean basalts (Condie, 1981; 1984; 1989) metagraywackes, iron formations and Salobo quartzites. From this diagram, it is concluded that the Salobo metagraywackes are on a mixing line between quartzites and basalts.

The Salobo metagraywackes exhibit higher Zr, Nb and Cu and lower Sr, Cr, Ni, Zn and Pb contents than Archean greenstone belt metagraywackes from Kambalda, Yellowknife and Kalgoorlie (Nance and Taylor (1977); Bavington and Taylor (1980) and Jenner et al., (1981)). They also show higher Zr, Nb, Cu and Co and lower Cr and Ni contents than the shelf sediments of the Limpopo Province (Southern Africa) and Western Gneiss Terrain (Australia) (Taylor et al., 1986).

They display relatively uniform REE patterns, analogous to Archean sedimentary rocks (Taylor et al., 1986; Bavington and Taylor, 1980; Nance and Taylor, 1977 and Jenner et al., 1981) (Table 5.13).

The metagraywackes are LREE-enriched ($\sum$LREE 438-724 ppm; $\sum$HREE 23-28 ppm), showing a well fractionated pattern (La/Lu_{cn} 21.74-63.19) with positive Eu anomaly (Eu/Eu^* 1.73-1.86) (Figure 5.28). However, the total REE content is

higher than Archean sedimentary rocks ($\sum$REE 472.8-953.58 ppm).

Discussion

The positive correlation between Al_2O_3-TiO_2 and K_2O-TiO_2 suggests that Al, Ti and possibly K have the same provenience from an homogeneous source area. This source may be inferred as being volcaniclastic in origin, if the position occupied by the metagraywackes on the mixing line between basaltic rocks and quartzites in the SiO_2-FeO^*-(Al_2O_3 x 3) diagram of figure 5.27 is taken into account. In addition to this, Type II iron formation, which is interlayered or grades to metagraywackes, presents volcaniclastic contribution, according to the conclusions pointed out in item 5.4.1.

On the other hand, the high Fe_2O_3 content of the studied metagraywackes may reflect either volcaniclastic or a chemical contribution.

The low MgO and CaO contents may be original or attributed to a later alteration process. Low MgO is also a characteristic of the amphibolites and iron formation, and low CaO was observed in trondhjemitic gneisses and amphibolites. There are not enough data on metagraywackes to draw a conclusion about the origin of low Mg and Ca in these rocks. However, by analogy to the rock types already discussed in the study area, it is possible that these

elements were mobilized in the metagraywackes by later processes.

The higher Zr and Nb content in metagraywackes seems to be closely related to the composition of the volcaniclastic source. The Parauapebas volcanics, probable volcaniclastic source of these rocks (and Type II iron formation), are described by Gibbs et al., (1986) as within plate continental volcanics, and rocks occurring in this geological setting are normally Zr and Nb enriched (Pearce and Cann, 1973; Winchester and Floyd, 1976).

Besides, the low Cr, Ni, Zn and Pb in the metagraywackes also seem to reflect the source composition, either volcaniclastic or hydrothermal, in parallel to what was observed in the iron formation. On the other hand, the low Sr may be possibly assigned to later mobilization processes as described in trondhjemitic gneisses.

The presence of positive Eu anomalies, as occur in Salobo metagraywackes, are common features in Archean sedimentary rocks. They are also described in Kalgoorlie and Kambalda (Australia), Fig Tree and Moodies (Southern Africa) and Yellowknife (Canada) (Jenner et al., 1981; Wildeman and Condie, 1973; Bavington and Taylor, 1980; Nance and Taylor, 1977; McLennan and Taylor, 1984; Taylor and McLennan, 1985). There are many hypothesis attempting to explain the origin of the absence of Eu negative anomalies, or even positive Eu anomalies, in Archean sedimentary rocks and the nature of the source rock, which originated these Eu anomalies. The Eu

enrichment has been attributed to the effect of detrital feldspar accumulation during the sedimentary processes (Nance and Taylor, 1977), or Eu addition by metasomatic solutions, or chemical interaction between rocks and ocean waters (Bavington and Taylor, 1980). In addition to that, the chondrite-normalized pattern has been assigned to: rocks derived from mixtures of mafic volcanics, tonalites, trondhjemites and dacites or rocks derived from calc-alkaline andesites, which present chondrite-normalized REE patterns very similar to Archean sediments (although these rocks are not commonly found in the Archean: McLennan and Taylor, 1984), or still derived from Na-granites (Nance and Taylor, 1977).

It seems that the best fit hypothesis for the Eu positive anomaly of the studied metagraywackes is the plagioclase accumulation from volcaniclastic sources. The LREE enrichment could be attributed either to a felsic detrital source or to the influence of hydrothermal solutions. In addition to that, the flatter REE pattern presented by sample 12-214 might be related to an increased volcaniclastic contribution of basaltic composition.

Therefore, the major and trace element data, as well as REE in metagraywackes suggest that these rocks were derived from a mixed detrital-volcaniclastic source with a possible chemical (hydrothermal) contribution.

5.4.3. Quartzites

Salobo quartzites are probably metamorphosed subarkoses and arkosic arenites (chapter 4). They are highly siliceous (SiO_2 75.1-96.30%) and mature sediments presenting Al_2O_3/TiO_2 ratios ranging from 22 to 52 (Table 5.14).

The quartzites show a well defined negative correlation between SiO_2 and TiO_2, Al_2O_3, Fe_2O_3, MnO, MgO, CaO, K_2O, Zr, Nb, Rb, Ba, Cr and REE, suggesting that these elements were diluted by SiO_2.

It is also observed in these rocks a good positive correlation between TiO_2-Zr and Al_2O_3-K_2O suggesting, for each element pair, a common homogeneous source (Figures 5.29, 5.30).

Total REE contents in quartzites are very low ($\sum$REE 19.52 to 41.43 ppm). They show LREE-enriched (La/Sm_{cn} = 5.49 to 9.54) fractionated pattern, strongly HREE depleted (2 out of 3 analyzed samples present HREE below the detection limits), with moderate Eu positive anomaly (Eu/Eu^* = 1.5-2.01) (Table 5.15, figure 5.31).

Discussion

In an attempt to determine the source rocks of the quartzites, the percentage of modal quartz (SiO_2%) of each quartzite sample was subtracted from the respective SiO_2 value from the whole-rock analyses. "Quartz-free" bulk rock

compositions were then obtained by recalculating the major oxides to 100%. The normative composition of these "quartz-free" quartzite was calculated and plotted on O'Connor's (1965) normative classification diagram, based on feldspar ratio (Table 5.16, Figure 5.32) where most samples are in the field of granitic rocks. Therefore, granitic rocks might have been the principal source rocks of Salobo quartzites, if the above assumptions are correct, if there were not significant chemical changes during source rock weathering, transport, sedimentation and diagenesis, and if the quartzites were not submitted to major metasomatic alteration.

The quartzites also plot around the reference line ratios for granite and tonalitic-trondhjemitic gneisses (Laskowski and Kroner, 1985) in the diagram TiO_2-Cr of figure 5.33, what is also in accordance to the "granitic" source rock previously suggested.

If the above reasoning is correct, the common homogeneous source for K, Al, Ti and Zr, seen in figures 5.29 and 5.30, may be the basement rocks.

The low REE content and the absence of Eu negative anomalies, presented by the quartzites, are characteristic patterns from Archean sedimentary rocks as discussed in item 5.4.2. Although the REE content of Salobo quartzites are much lower than Archean shales cited in the literature (Jenner et al., 1981; Wildeman and Condie, 1973; McLennan and Taylor, 1984; Taylor and McLennan, 1985), this could

reflect the large REE dilution by SiO_2, normal in quartzites.

Taken into account the major oxides along with the trace elements and REE it is possible to suggest that the Eu positive anomalies may be assigned to accumulation of detrital feldspars from a granitic to trondhjemitic source area.

In summary, the data and discussion above suggest that Salobo quartzites are metamorphosed mature clastic-sedimentary rocks, arkoses to arkosic arenites in composition, whose source area was possibly granitic to trondhjemitic.

5.5. Intrusive rocks

5.5.1. Granitoid rocks

There are two granitoid intrusions in the study area, the older is granitic in composition (OSG) and the younger is an alkali-feldspar quartz syenite (YSG) (chapters 3 and 4).

Both intrusions show homogeneous mineralogical and chemical compositions (Table 5.17). They are alkalic, either according to Vogt's (1932) alkalinity index or Wright's (1969) classification (Table 5.18, Figure 5.34), and metaluminous, with Al_2O_3 /(Na_2O+K_2O+CaO) 0.84 (OSG) and 0.86

(YSG) and $Al_2O_3/(Na_2O+K_2O)$ 1.32 (OSG) and 1.37 (YSG). They also display K+Na/Al>1.

OSG shows K/Na ratios of 0.88, whereas YSG presents K/Na equals to 1.49, indicating a sodic nature for OSG and a potassic one for YSG.

The granitoid intrusions show high $Fe^{3+}/(Fe^{3+}+Fe^{2+})$ (0.45 OSG and 0.49 YSG), which indicates high oxygen fugacity.

YSG is more enriched than OSG in Na_2O+K_2O, Ga, Zr, Nb, Ce, F and REE. It also shows average Ga/Al ratio of 3.27, whereas OSG presents Ga/Al equals to 2.63 (Figures 5.35 to 5.37).

Both granitoids show a fractionated chondrite-normalized REE pattern, with moderate negative Eu anomalies (Figures 5.38 and 5.39). YSG shows a more fractionated pattern than OSG, either referring to total REE, or HREE and LREE. YSG displays La/Yb = 80.27; $(Ce/Sm)_{cn}$ = 3.62 and $(Tb/Yb)_{cn}$ = 3.62, whereas OSG presents La/Yb = 14.84; $(Ce/Sm)_{cn}$ = 1.97 and $(Tb/Yb)_{cn}$ = 1.28. OSG shows La 460 and Lu 25 times the chondrite, whereas YSG displays La 400 and Lu 4 times the chondrite.

OSG shows a more pronounced Eu negative anomaly than YSG, with Eu^*/Eu = 0.48 and 0.74, respectively. It may indicate that OSG would required a source with abundant plagioclase, to produce the negative Eu anomaly in the melt, whereas YSG would be produced from a less plagioclase-rich provenance (Cullers and Graf, 1984).

Discussion

Ishihara (1981) defined two types of granitoids named the ilmenite series (I) and the magnetite series (M). These two series evolved under different oxygen fugacity conditions. The first is more reduced, ilmenite-bearing, and presents low Fe_2O_3 /FeO ratio, whereas the second shows high Fe_2O_3 /FeO ratio in addition to modal magnetite >2%. I-type granitoids are considered to have originated from a mixture of felsic and mafic magmas or from a melt of igneous and sedimentary rocks in the lower crust, while M-type is considered as formed in deep levels of the upper mantle, where the water would be trapped at early stages of magma evolution (Ishihara, 1981).

Chappell and White (1974, 1982) defined two granitoid rock suites in Phanerozoic granites from Australia denominated I-type (igneous or infracrustal), formed from melts derived from igneous source rocks, and S-type (sedimentary or supracrustal), formed from melts of sedimentary rocks. These two types show different chemical and mineralogical characteristics reflecting their source rocks. Thus, S-type presents lower Fe^{3+}/Fe^{2+} than I-type, which is attributed to the presence of graphite in the sedimentary source (Flood and Shaw, 1975).

Loiselle and Wones (1979) and Collins et al.,(1982), based on a suite of Phanerozoic granitoids from Australia,

defined A-type granites as alkalic, anorogenic and anhydrous intrusions, with high SiO_2, Na_2O+K_2O, Fe/Mg, Ga/Al, Zr, Nb, Ga, Y and Ce and low CaO and Sr. According to Whalen et al., (1987) A-type granitoids are also metaluminous rocks, whose distinction from Chappell and White's (1982) I-type granitoids is the enrichment in highly charged cations such as Nb, Ga, Zr, Y and REE, and the depletion in Al, Mg and Ca. They are also more enriched in Na_2O+K_2O and F than there are I-type granitoids.

Both Salobo intrusions are analogous to Ishihara's (1981) M-type Phanerozoic granitoids.

The $Fe^{3+}/(Fe^{3+}+Fe^{2+})$ ratios of OSG (0.45) and YSG (0.49) approximate more Chappell and White's (1982) I-type (0.315) than S-type (0.173), granitoids. They are also metaluminous, presenting $Al_2O_3/(Na_2O+K_2O+CaO) < 1$ and $Al_2O_3/(Na_2O+K_2O) > 1$. These geochemical characteristics are similar to that of I-type granitoids defined by Chappell and White (1982).

YSG is enriched in Na_2O+K_2O (10.13%), Ga (24 ppm), Zr (506 ppm), Ce (230 ppm), F (2066 ppm), Nb (43 ppm) and REE (466.2 ppm), showing high Ga/Al and Fe/Mg ratios. It is also alkalic, anorogenic and almost anhydrous indicating that this alkali-feldspar quartz syenite is analogous to the Australian Phanerozoic A-type granitoids.

Tectonic Setting

It may be observed in figure 5.40 diagram (Pearce et al,.(1984) that, both granitoids present Ocean Ridge-normalized patterns analogous to Phanerozoic within plate granites, like Rb and Th enrichment compared to Nb, in addition to Ce and Sm enrichment compared to the neighbor elements. They also show high K, Rb and Th; Hf and Yb near the normalization values; a strong negative Ba anomaly and a general increase in the normalized values from Yb to Rb.

OSG also shows Nb depletion, which according to Pearce et al., (1984) is characteristic of granites emplaced in attenuated continental crust.

Both intrusions plot in the field of within plate granites on Pearce et al.,(1984) Rb-(Y+Nb) diagram of tectonic setting discrimination (Figure 5.41), indicating that, as well as concerning to the above elements the intrusions are analogous to the Phanerozoic within-plate granites.

In summary, OSG is an alkalic, sodic and metaluminous granite, presenting chemical characteristics similar to I-type granite. The data also suggest that OSG is analogous to Phanerozoic within-plate granites, emplaced in attenuated continental crust. YSG is an alkalic, metaluminous and potassic, alkali-feldspar quartz syenite sill, with

chemical, mineralogical and textural features analogous to A-type Phanerozoic granitoids, within-plate emplaced.

5.5.2. Diabase Dykes

There are two Cambrian undeformed diabase dykes cutting the study area (Chapters 3 and 4).

These diabases are tholeiitic rocks, with quartz-tholeiitic normative composition in the margin and in the centre of the dyke (Table 5.20 and 5.21). They plot in the field of sub-alkaline or tholeiitic basalts in Winchester and Floyd's (1976) (Nb/Y)-SiO_2 diagram (Figure 5.42).

These rocks present a decrease of Fe_2O_3, MnO, CaO, Cu and S and an increase of Na_2O, K_2O, Ba and La contents from margin to centre of the dyke. The sample collected midway between margin and centre (24-190) is enriched in CaO, Na_2O and K_2O referring to the neighbor samples, which may indicate hydrothermal alteration.

This diabase is enriched in Fe, Ti and K, plotting in the field of within-plate basalts, of Pearce and Cann's (1973) diagram of tectonic-setting discrimination (Figure 5.43). Its high K/Rb ratio (average 329) is analogous to that of continental basalts (Heier and Billings, 1972).

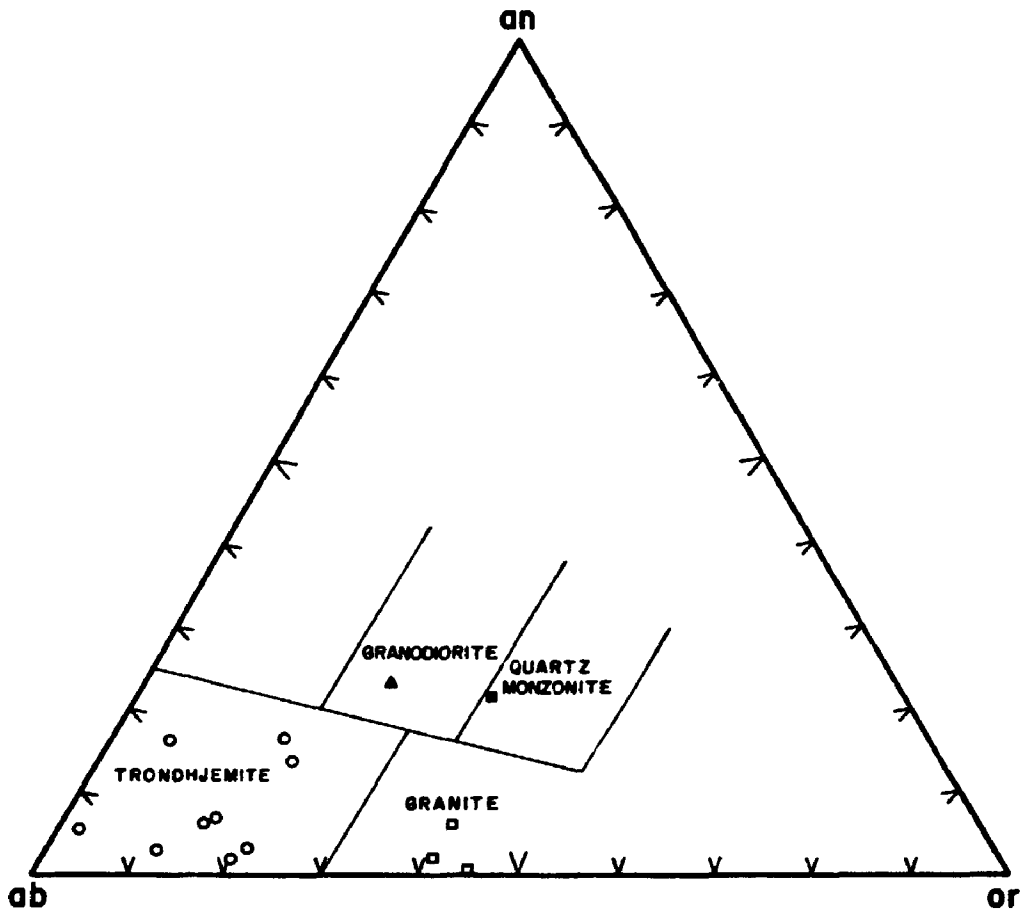

FIGURE 5.1. Normative classification of gneissic rocks based on feldspar ratio. Fields according to O'Connor (1965).

FIGURE 5.2. Composition of Salobo trondhjemitic-gneisses, normalized by the world average of trondhjemitic rocks (major elements). See Table 5.3 for references. Note the very low CaO value.

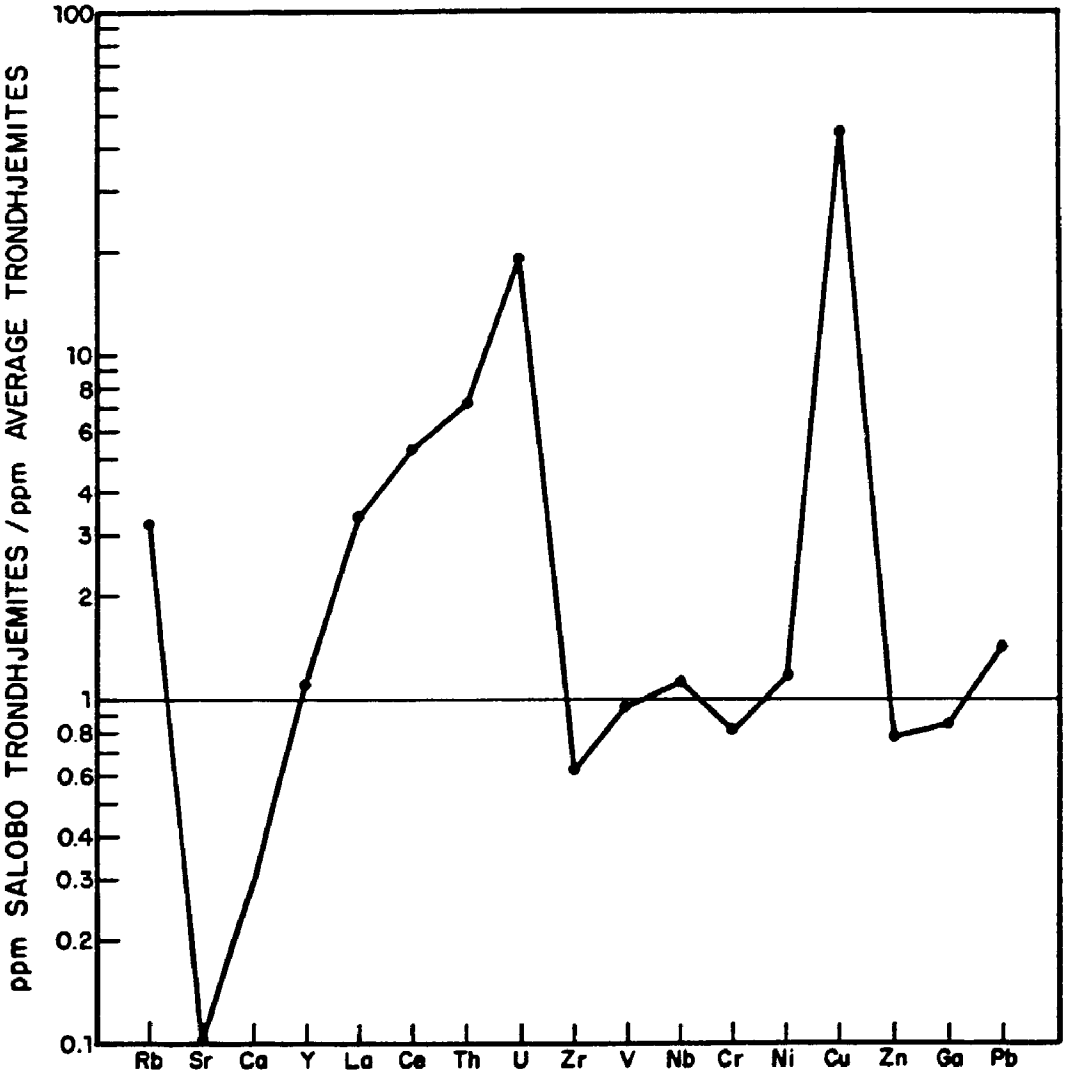

FIGURE 5.3. Composition of Salobo trondhjemitic-gneisses, normalized by the world average of trondhjemitic rocks (trace elements).
See Table 5.3 for references.

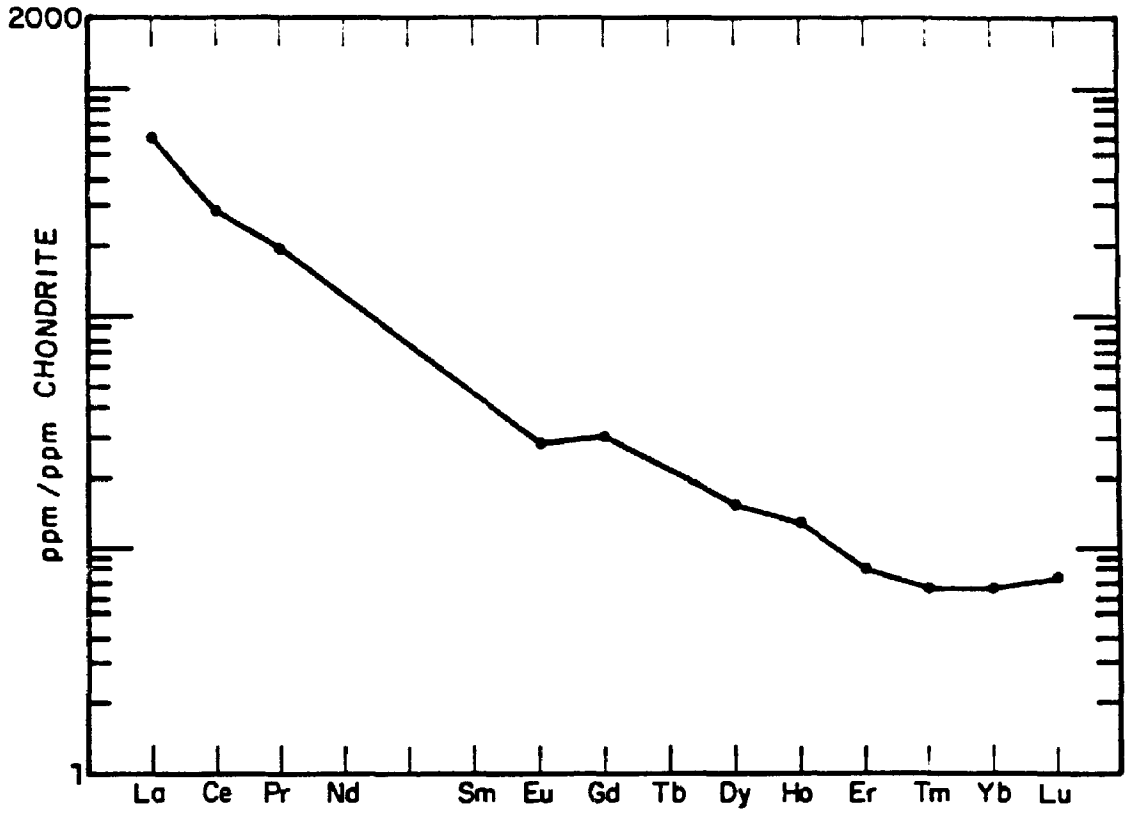

FIGURE 5.4. Chondrite-normalized REE pattern of trondhjemitic gneiss.

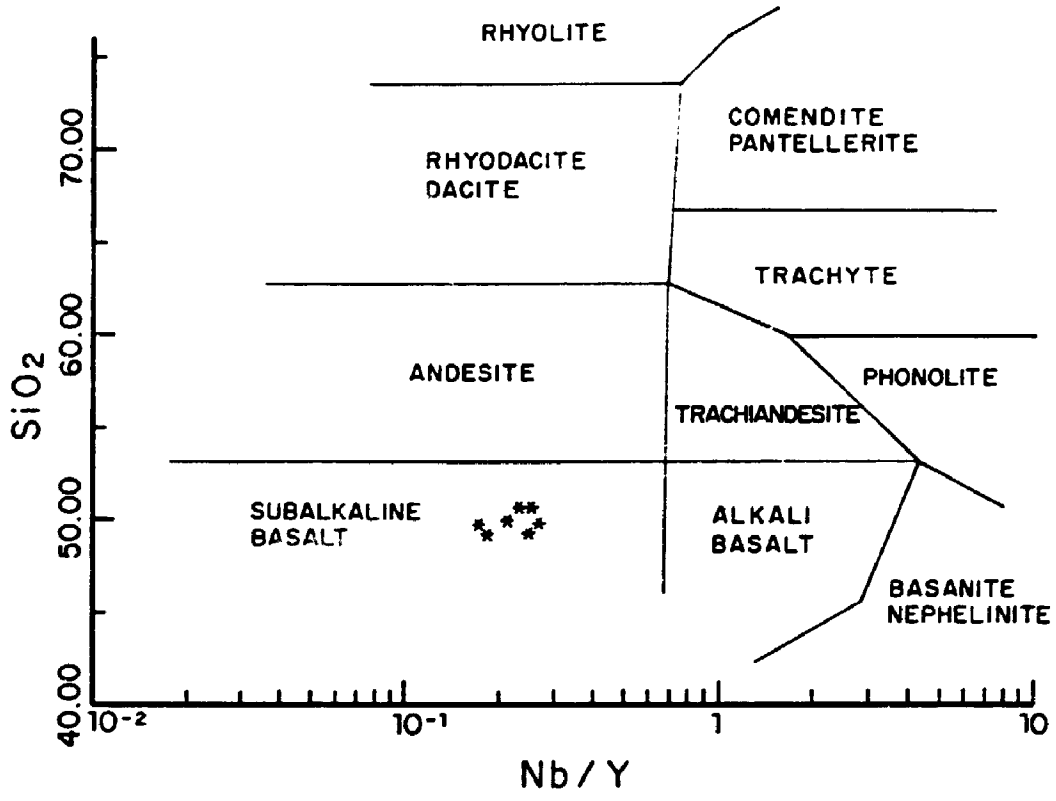

FIGURE 5.5. Amphibolite composition plotted on Winchester and Floyd's (1976) diagram of discrimination of magma types.

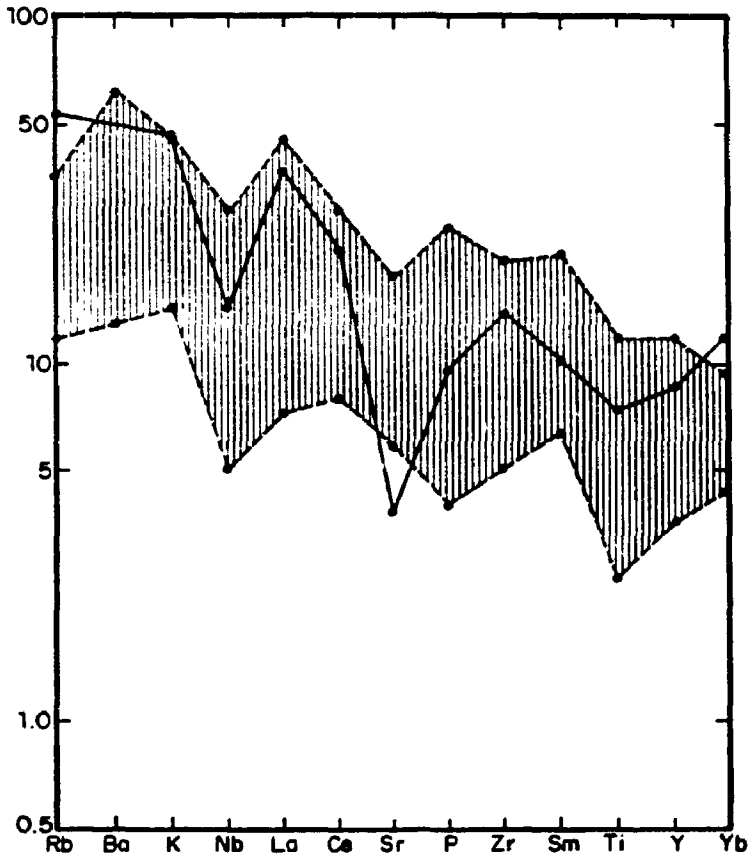

FIGURE 5.6. Average of hygromagmatophile* element abundances in Salobo amphibolites (normalized to primordial mantle composition of Wood et al., 1979), compared to the field of tholeiitic basalts and basaltic andesites from the continental environment, presented by Holm (1985).
* Trace elements with bulk distribution coefficients (D) less than one, also LIL or incompatible elements (Wood et al., 1979).

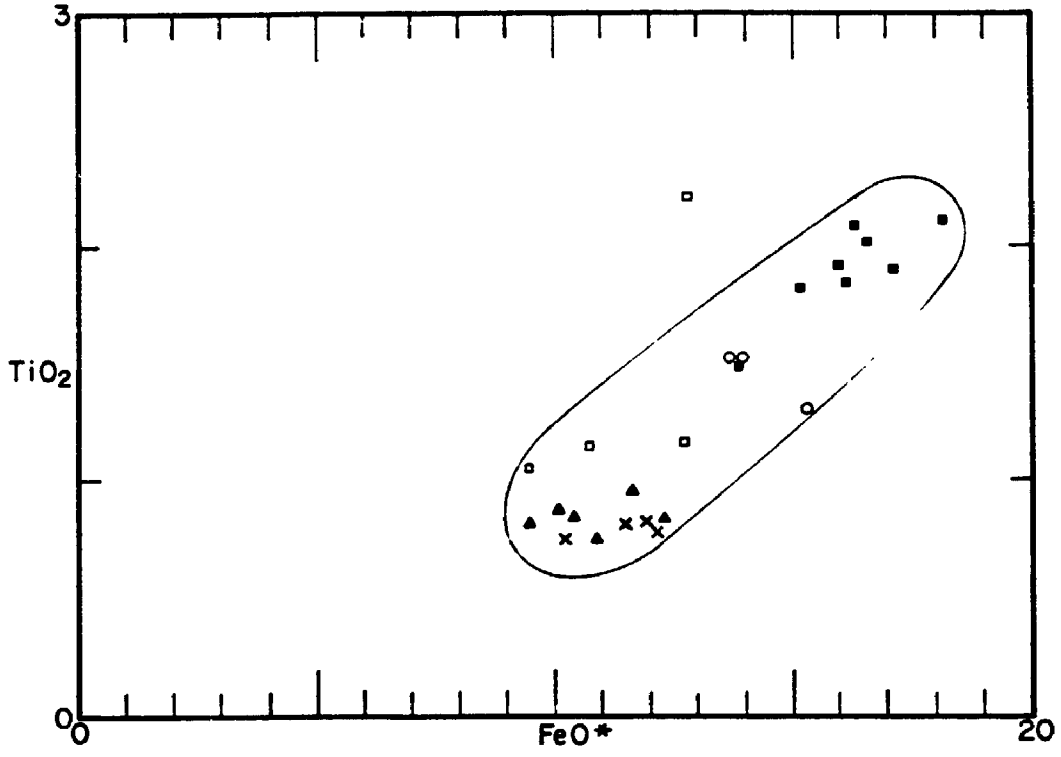

FIGURE 5.7. FeO* versus TiO_2 for volcanic rocks of Grao Para Group and Salobo amphibolites. Parauapebas Formation: (o) lower unit, (x) intermediate unit, (triangles) upper unit. (open squares) "Upper Volcanic Sequence", (full squares) Salobo amphibolites.

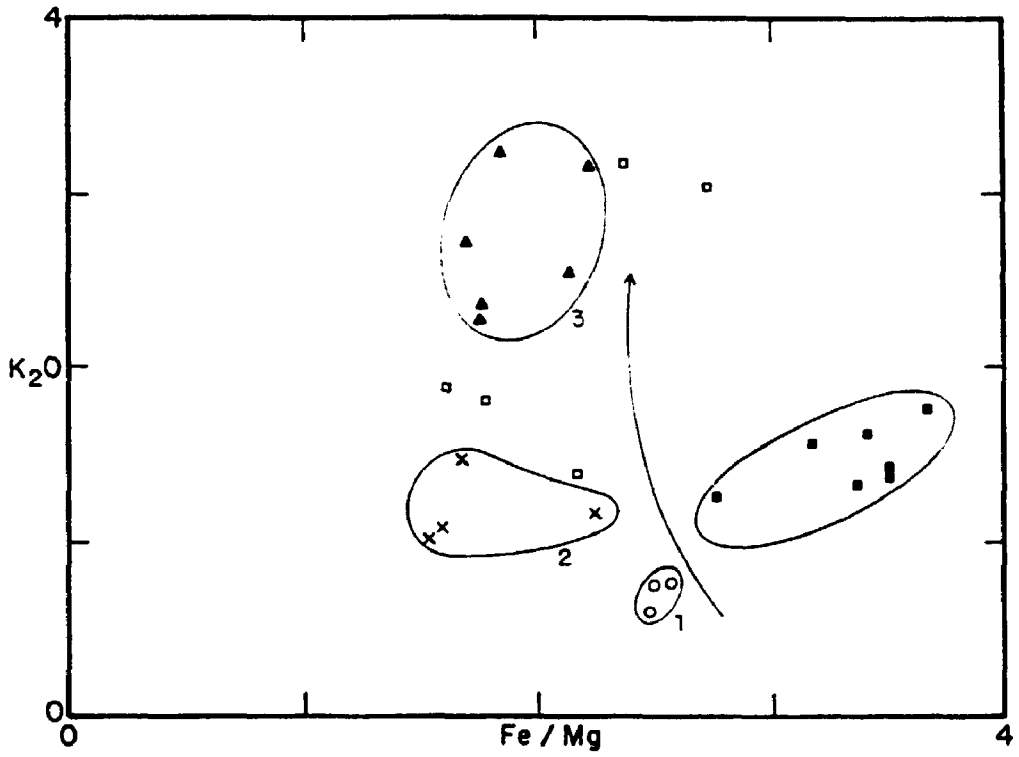

FIGURE 5.8. Fe/Mg ratio versus K_2O for volcanic rocks of Grao Para Group and Salobo amphibolites. Parauapebas Formation: (o) lower unit, (x) intermediate unit, (triangles) upper unit. (open squares) "Upper Volcanic Sequence", (full squares) Salobo amphibolites.

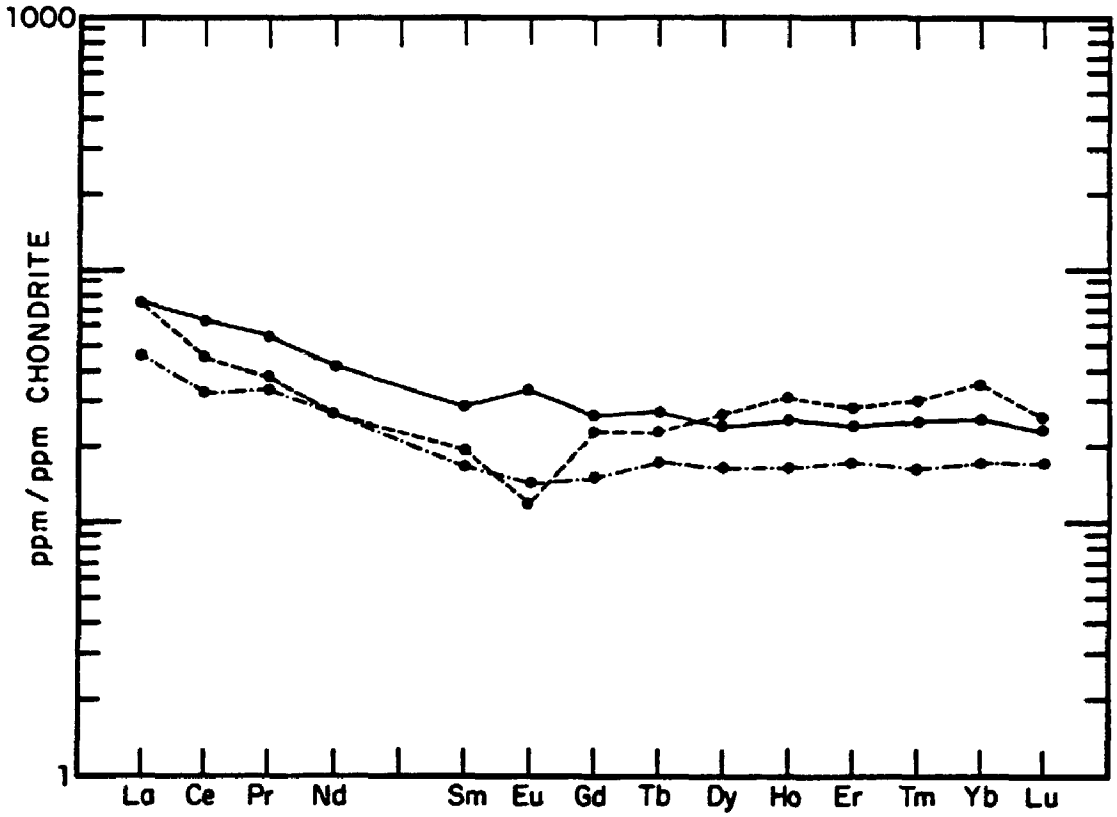

FIGURE 5.9. Chondrite-normalized REE patterns of Salobo amphibolites.

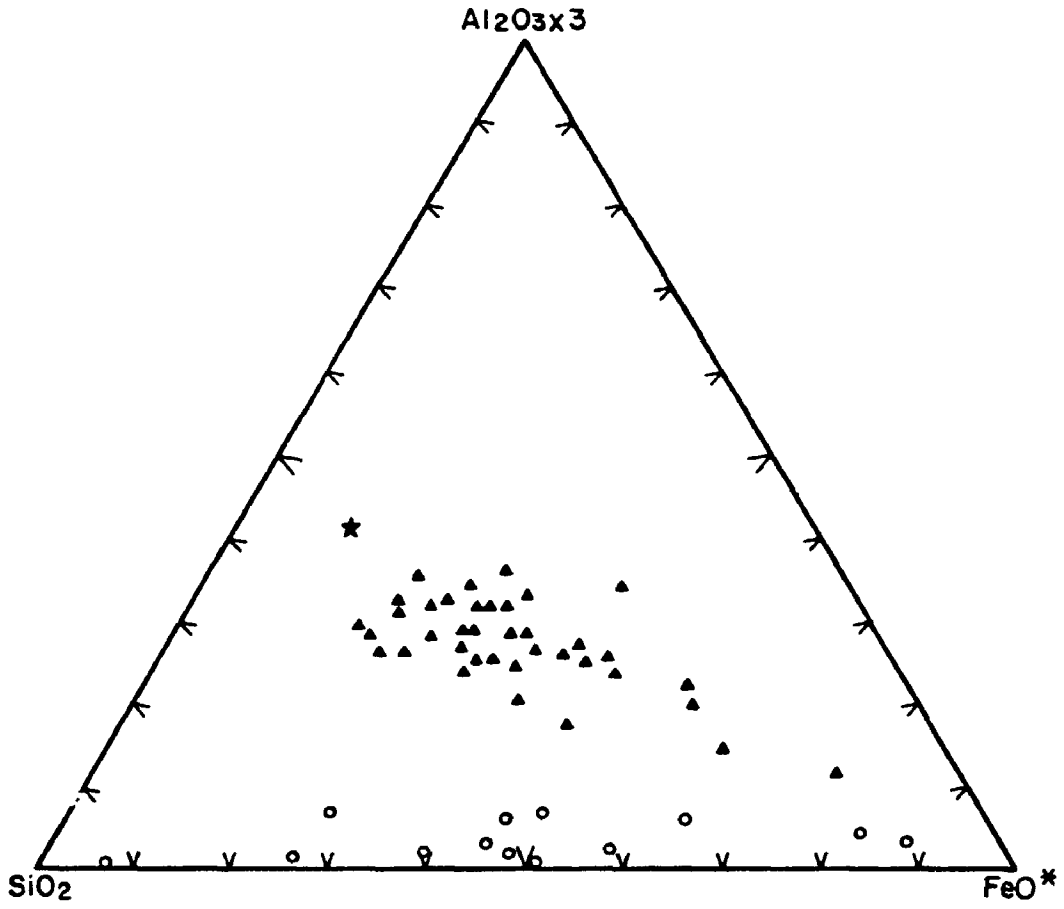

FIGURE 5.10. Graphical representation of Salobo Type I (circles) and Type II (triangles) iron formations plotted on the SiO_2-FeO*-(Al_2O_3 x 3) diagram, along with the average composition of basalts (star).

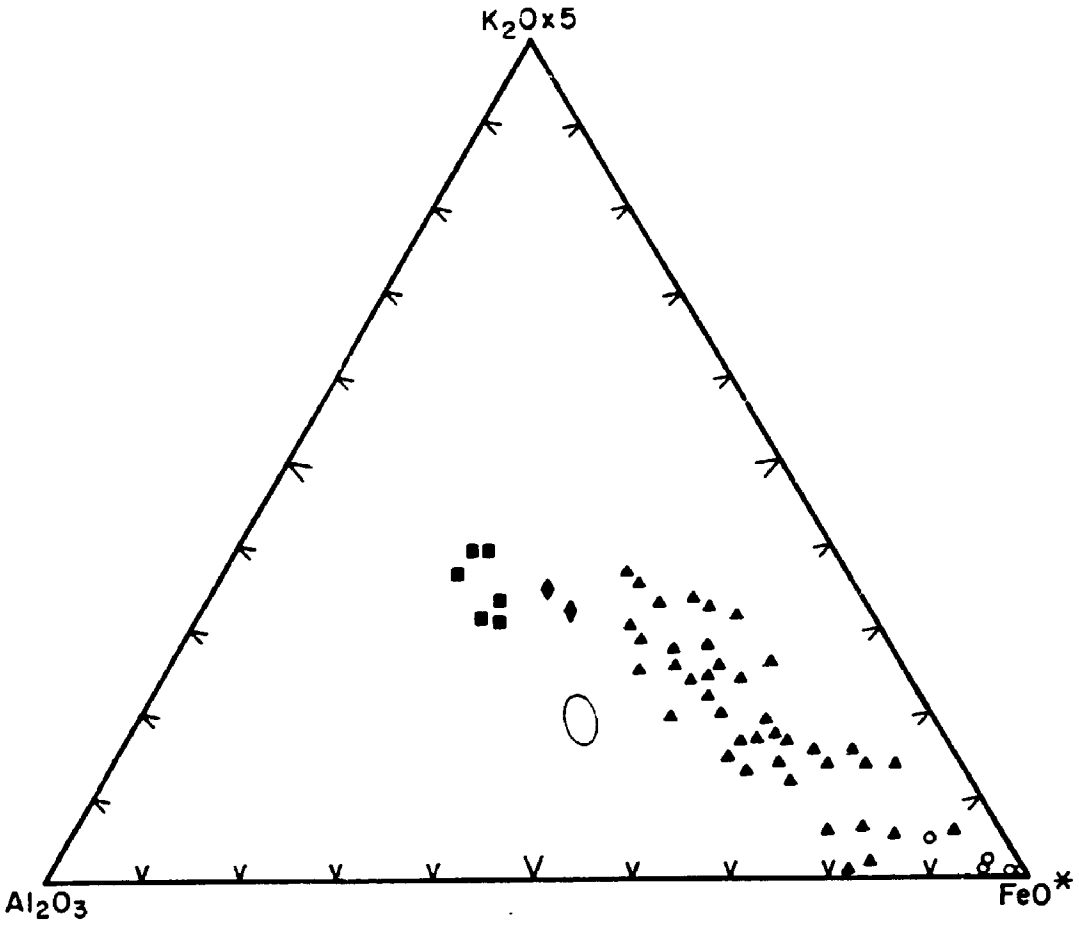

FIGURE 5.11. Graphical representation of Salobo Type I (circles) and Type II (triangles) iron formations, Bahia (diamonds) and Parauapebas volcanic rocks (squares) plotted on the Al_2O_3-FeO*-(K_2O x 5) diagram, along with the field of Salobo amphibolites. Note that the samples of Type II iron formation are along a mixing line between the chemical iron formation and the volcanic rocks.

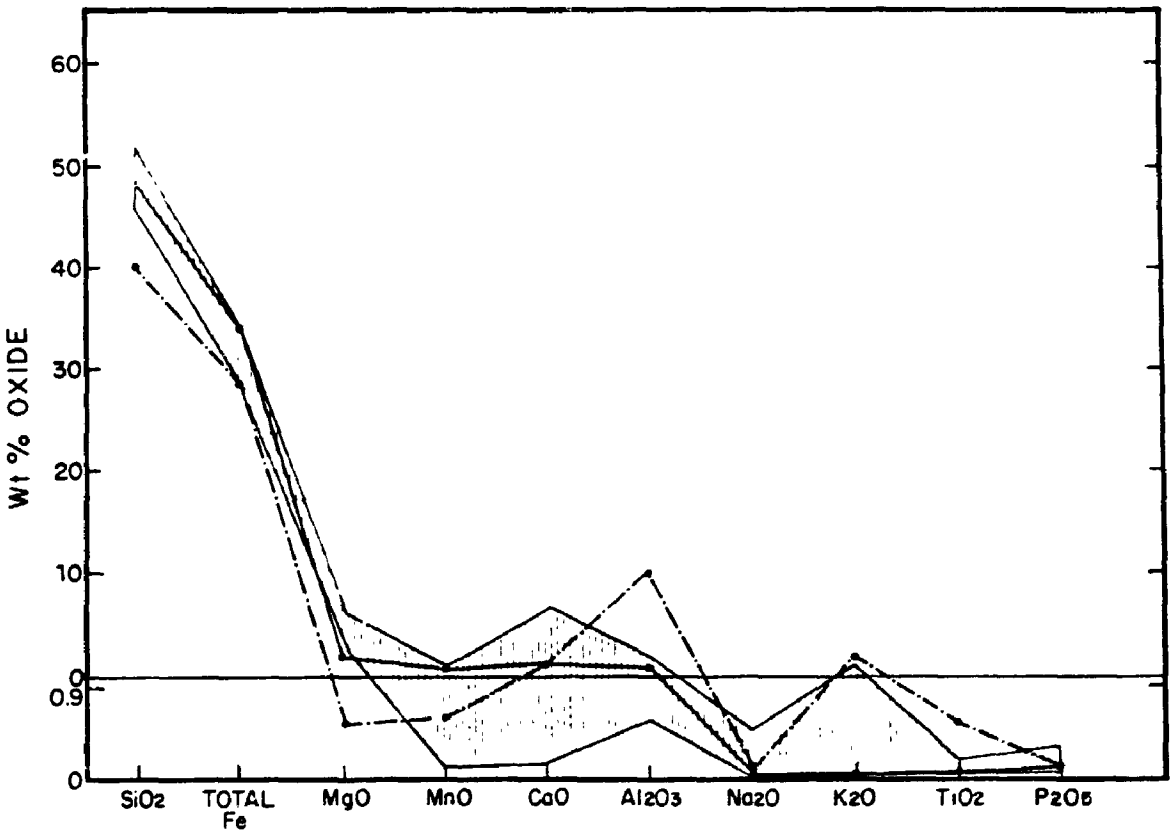

FIGURE 5.12. Average major-element compositions of Salobo Type I (full line) and Type II (dash-dot line) iron formations, compared to the range of average BIF compositions, presented by Gole and Klein (1981).

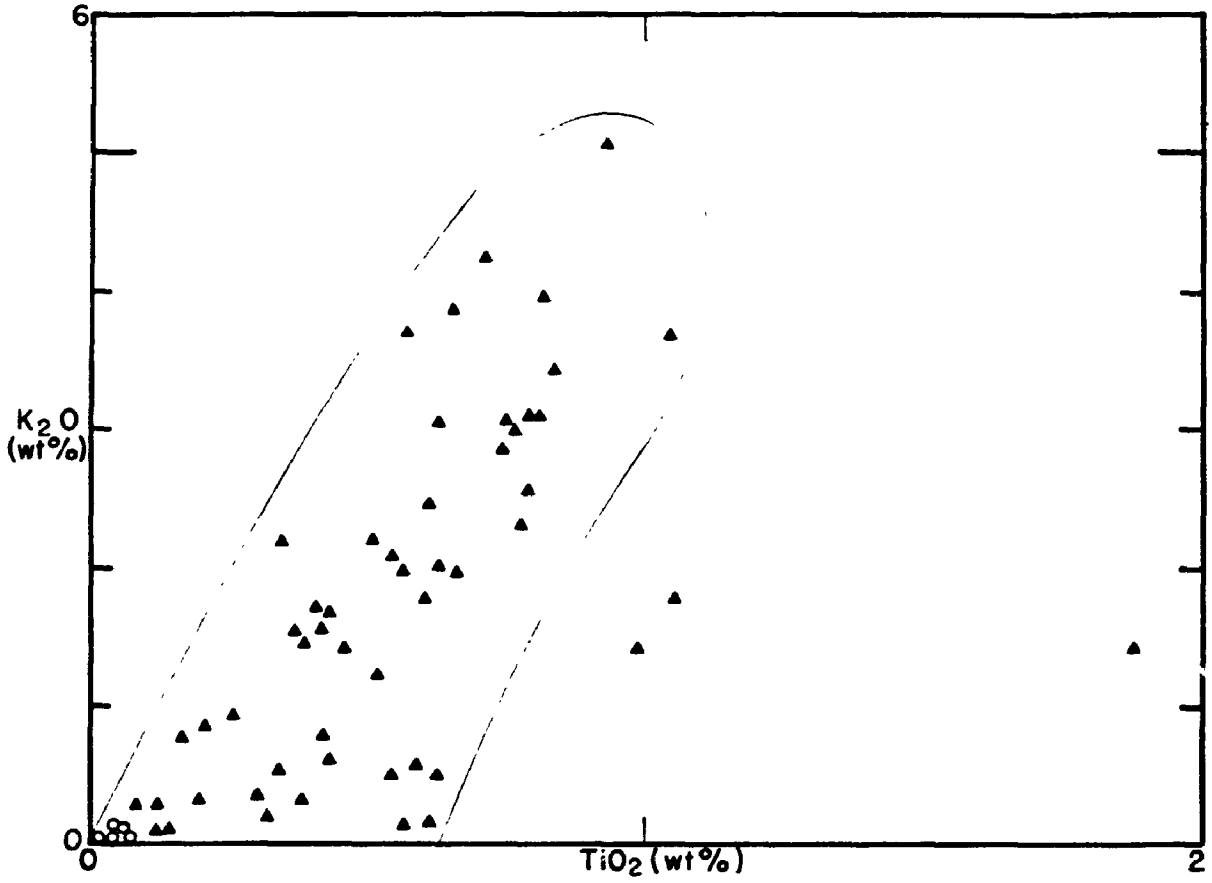

FIGURE 5.13. K_2O versus TiO_2 for Type I (circles) and Type II (triangles) iron formations. Note the fairly good correlation.

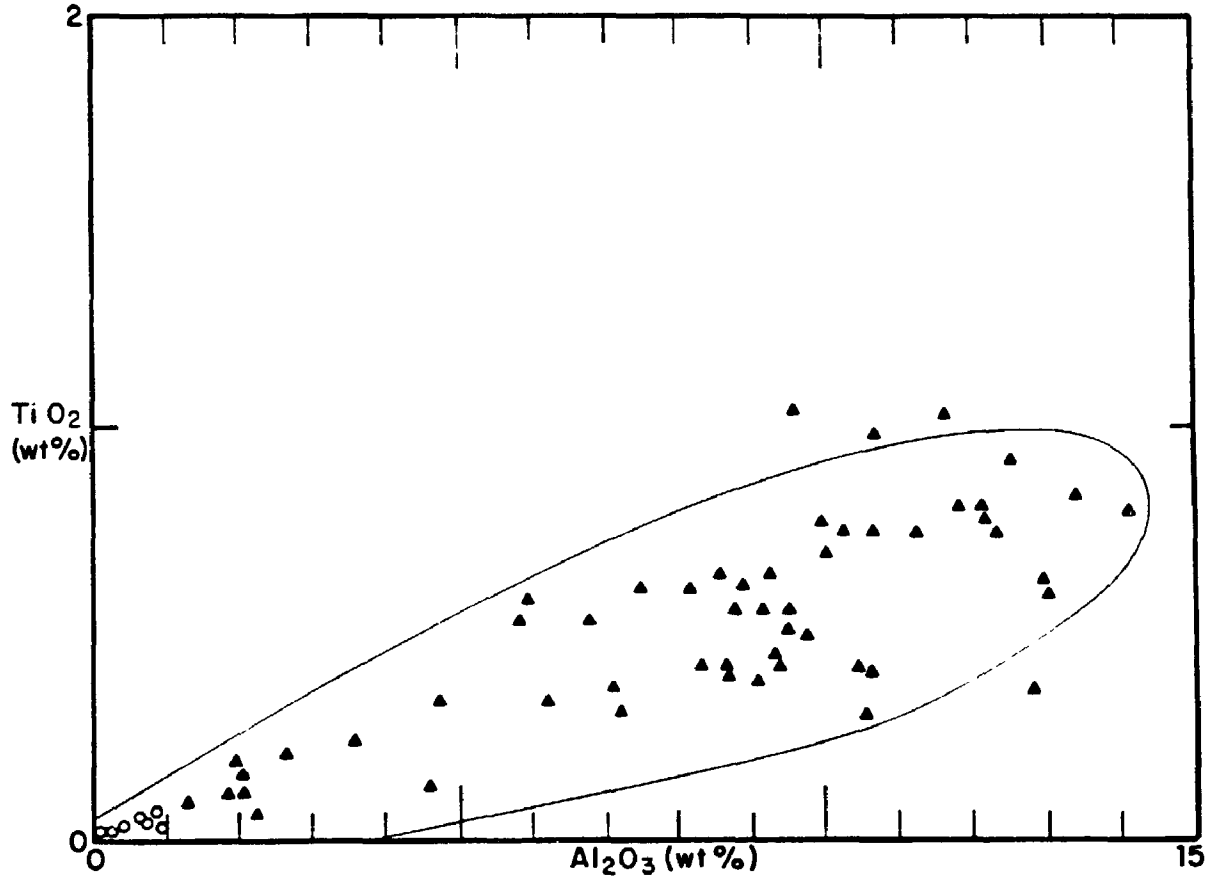

FIGURE 5.14. TiO_2 versus Al_2O_3 for Type I (circles) and Type II (triangles) iron formation.

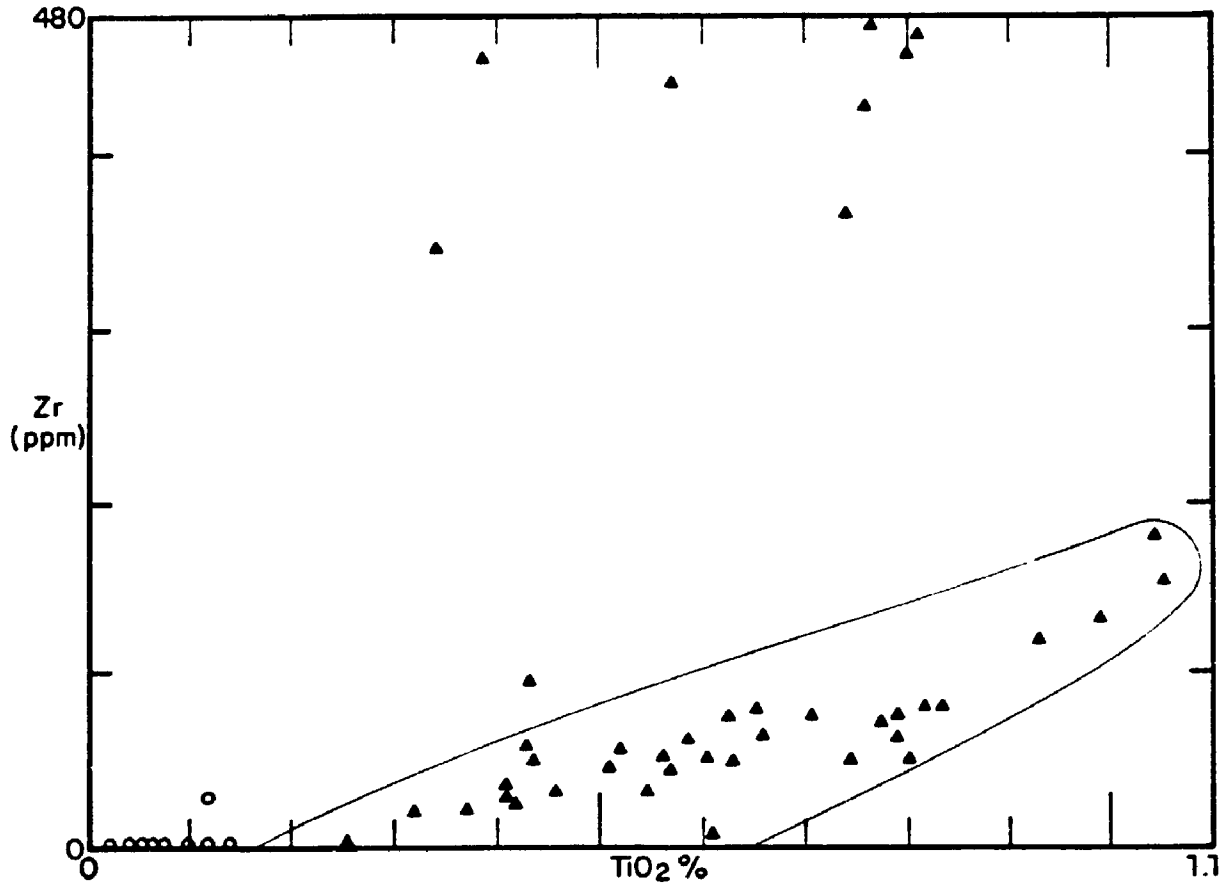

FIGURE 5.15. TiO_2 versus Zr for Type I (circles) and Type II (triangles) iron formation.

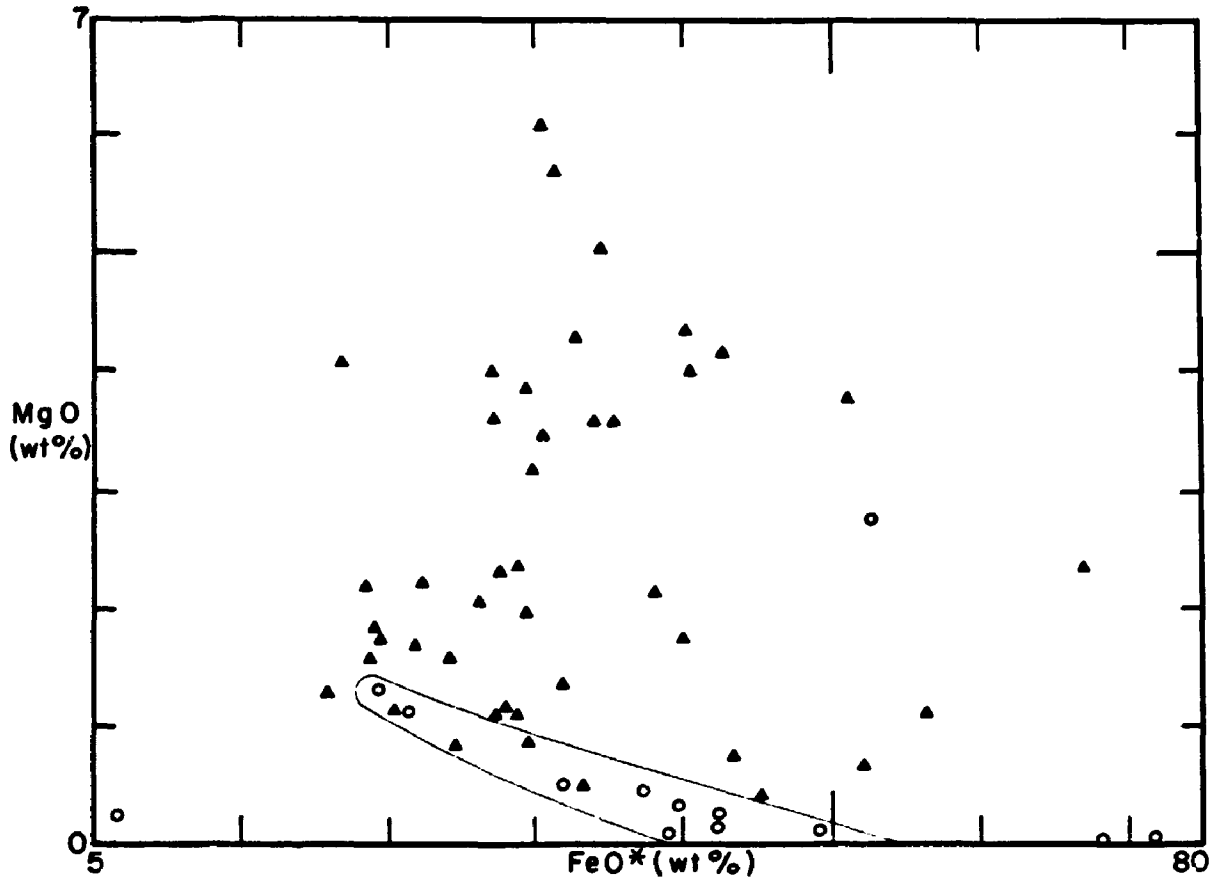

FIGURE 5.16. FeO* versus MgO for Type I (circles) and Type II (triangles) iron formation.

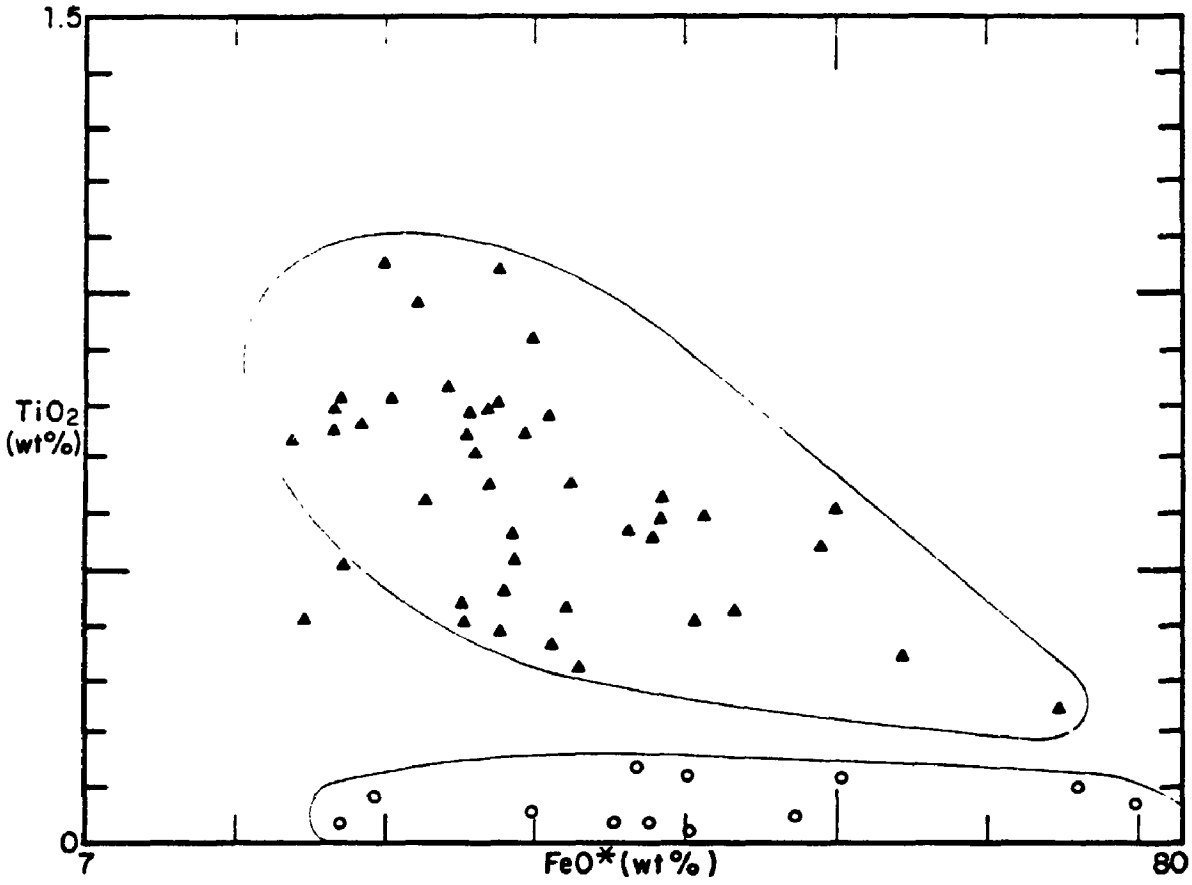

FIGURE 5.17. TiO_2 versus FeO* for Type I (circles) and Type II (triangles) iron formation.

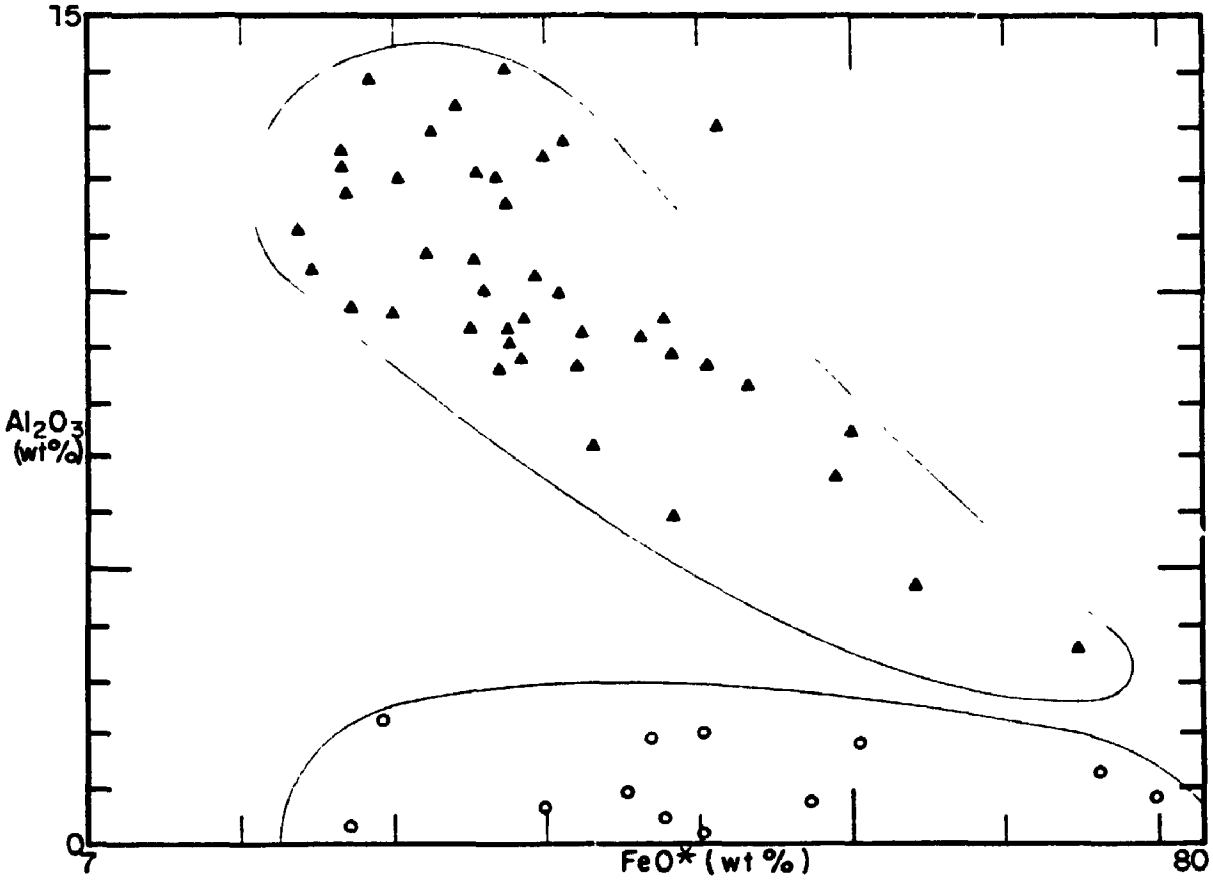

FIGURE 5.18. Al_2O_3 versus FeO* for Type I (circles) and Type II (triangles) iron formation.

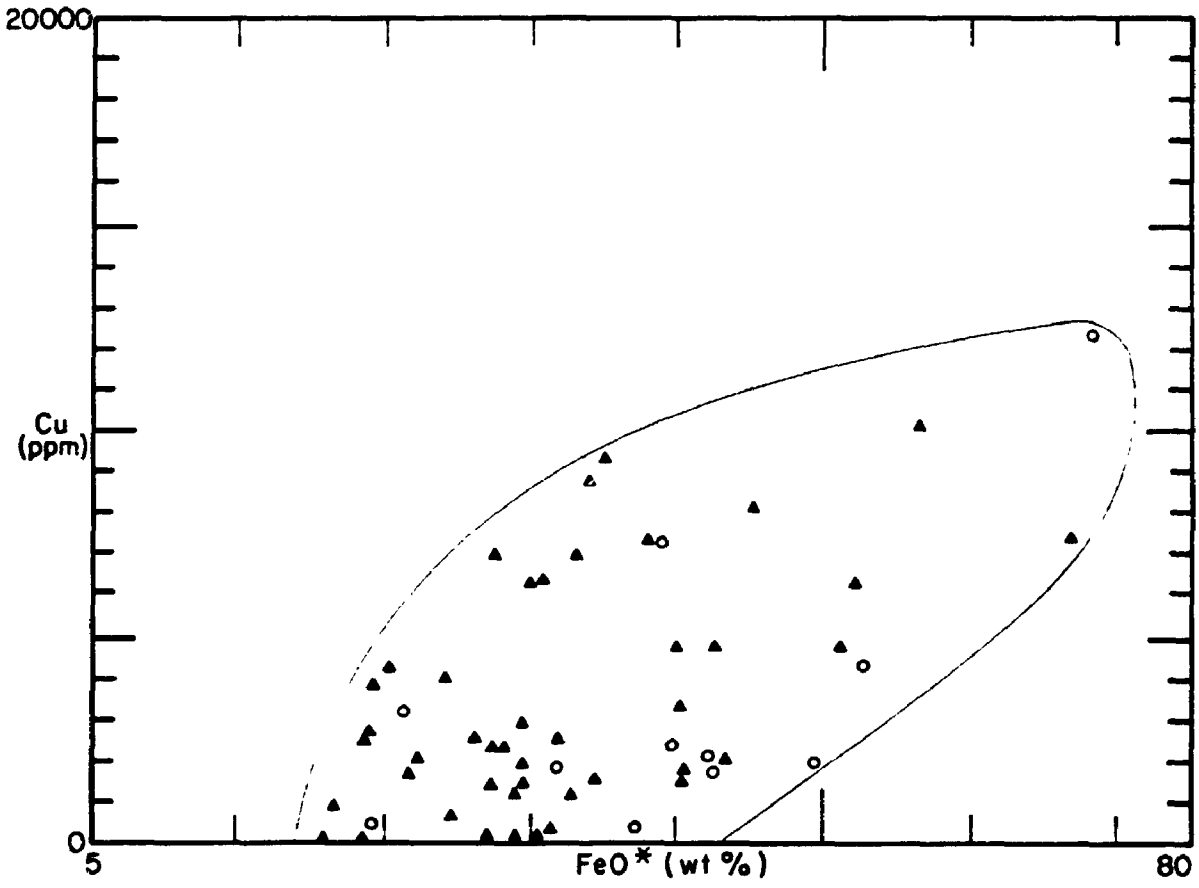

FIGURE 5.19. FeO* versus Cu for Type I (circles) and Type II (triangles) iron formation.

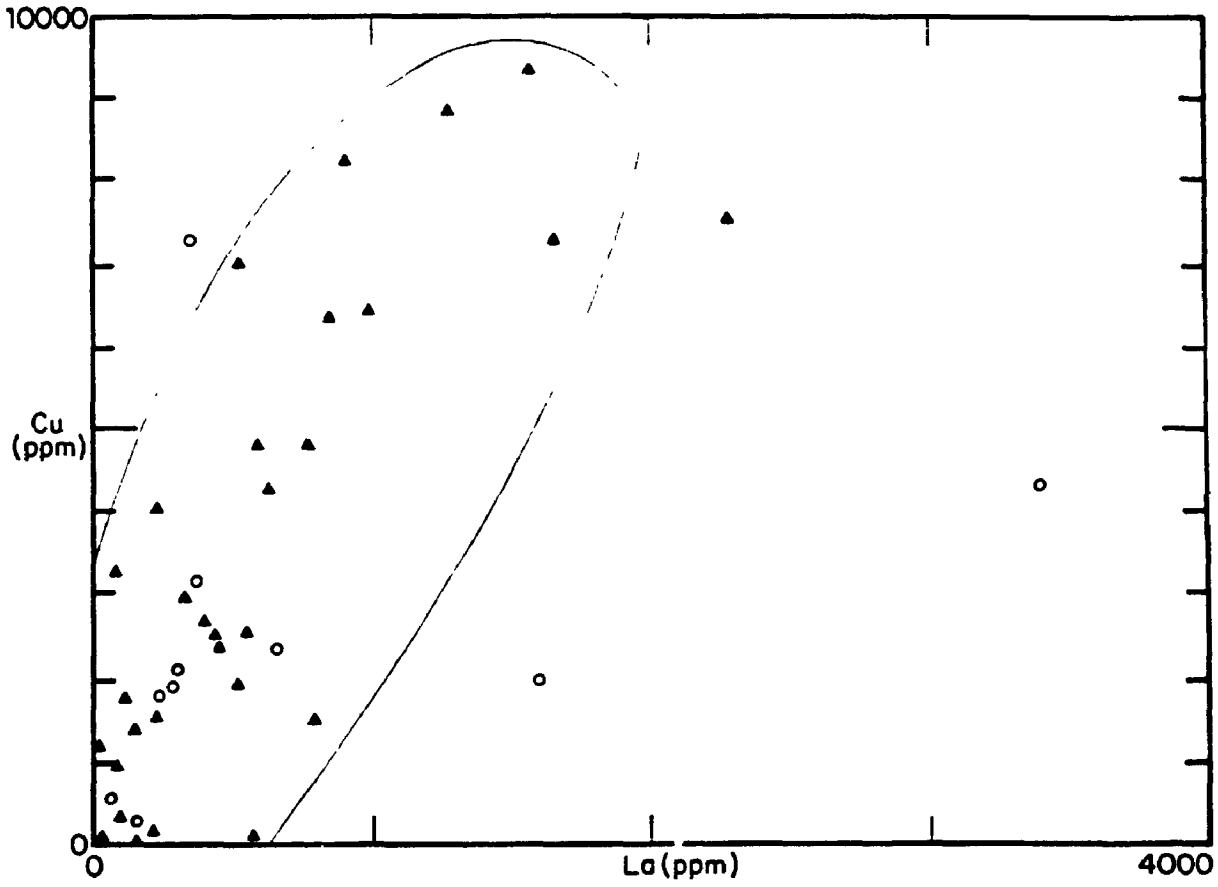

FIGURE 5.20. Cu versus La for Type I (circles) and Type II (triangles) iron formation.

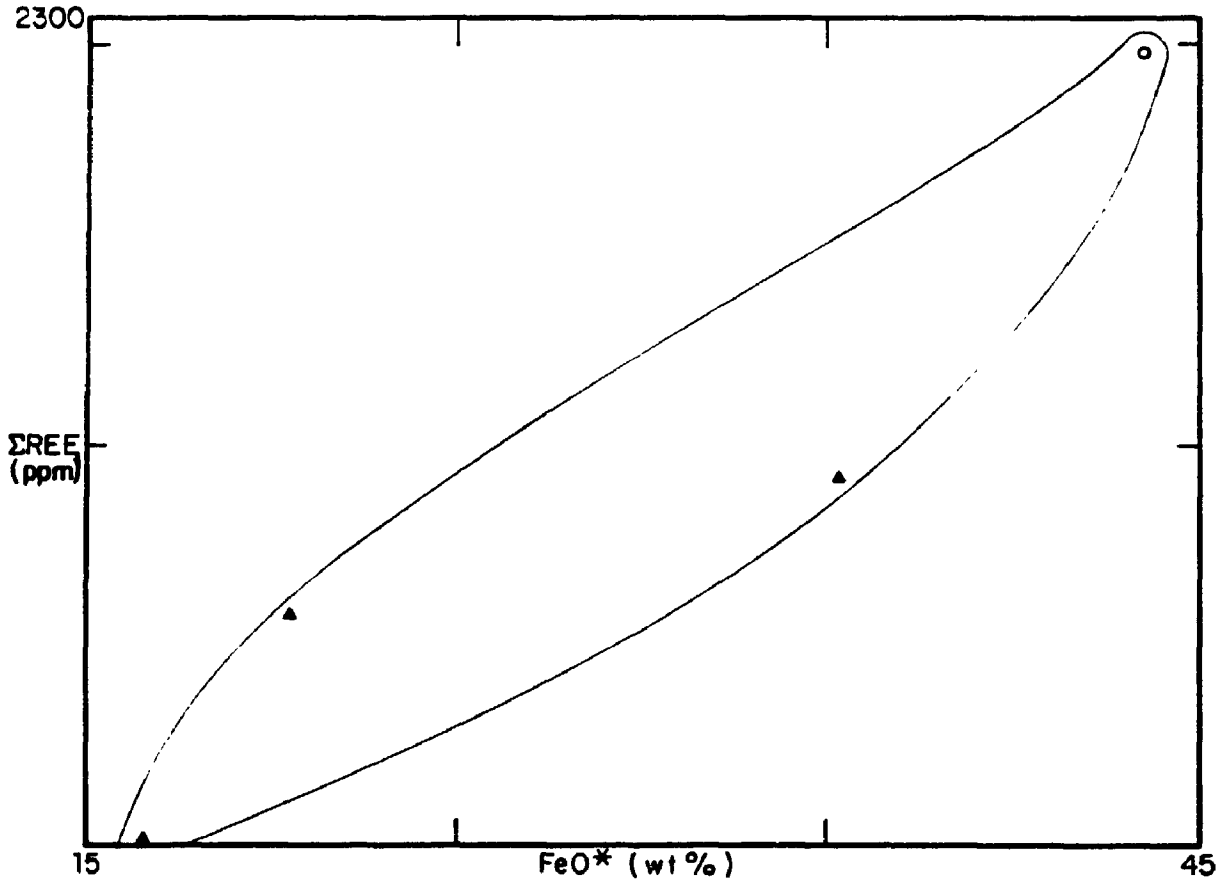

FIGURE 5.21. FeO* versus ΣREE for Type I (circles) and Type II (triangles) iron formation.

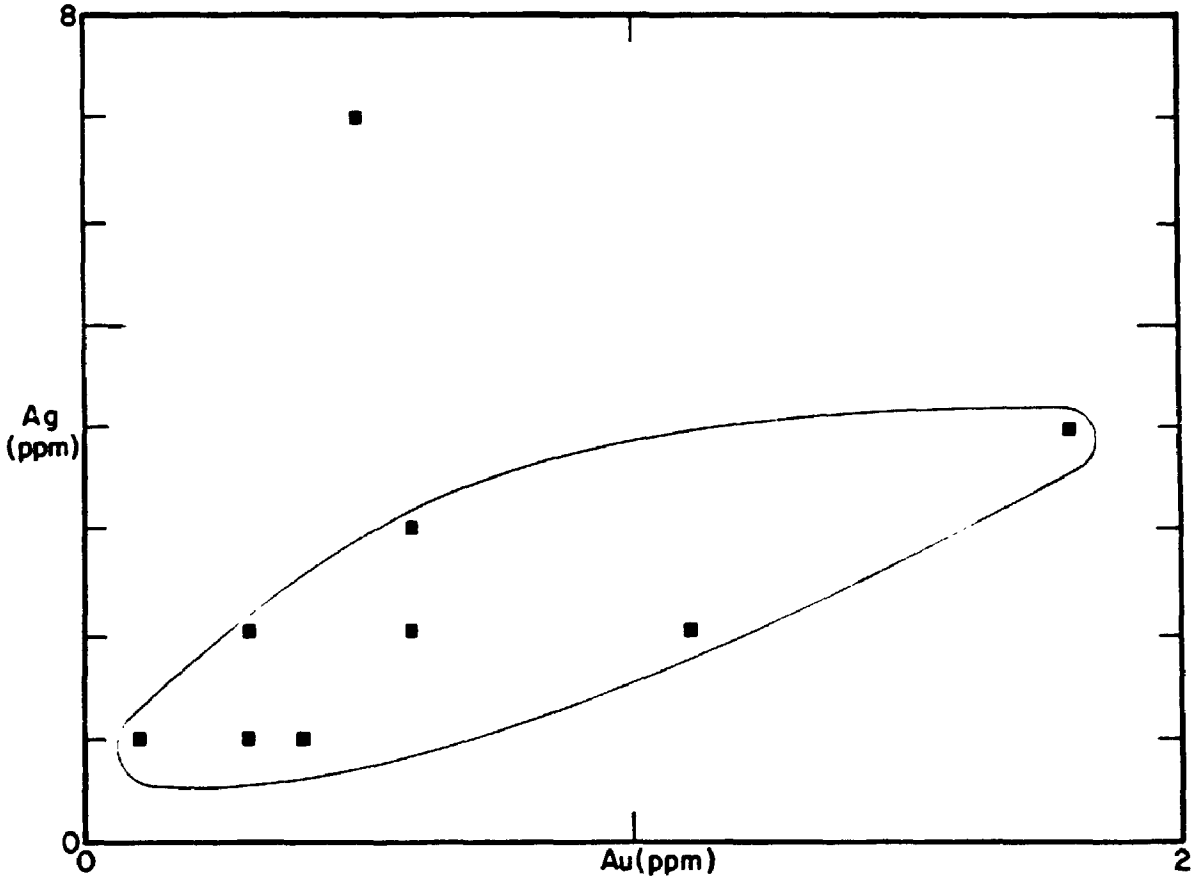

FIGURE 5.22. Au versus Ag for iron formations.

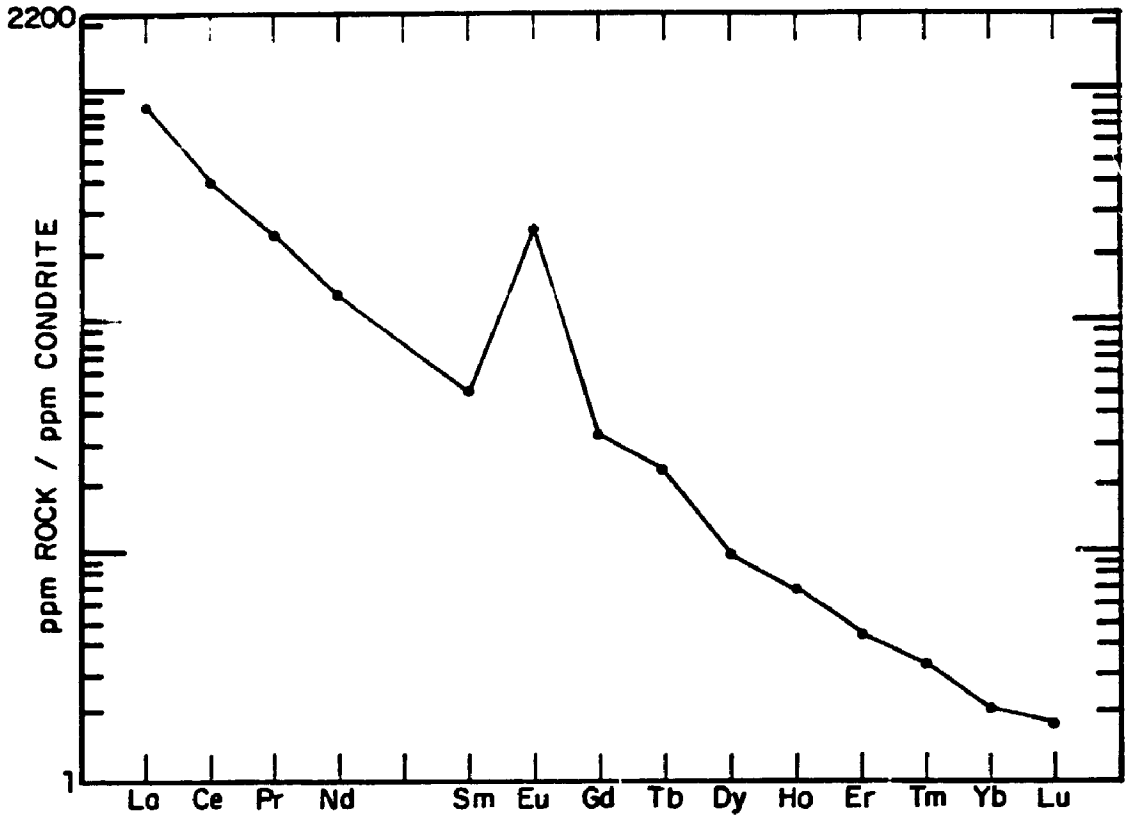

FIGURE 5.23. Chondrite-normalized REE pattern for Type I iron formation.

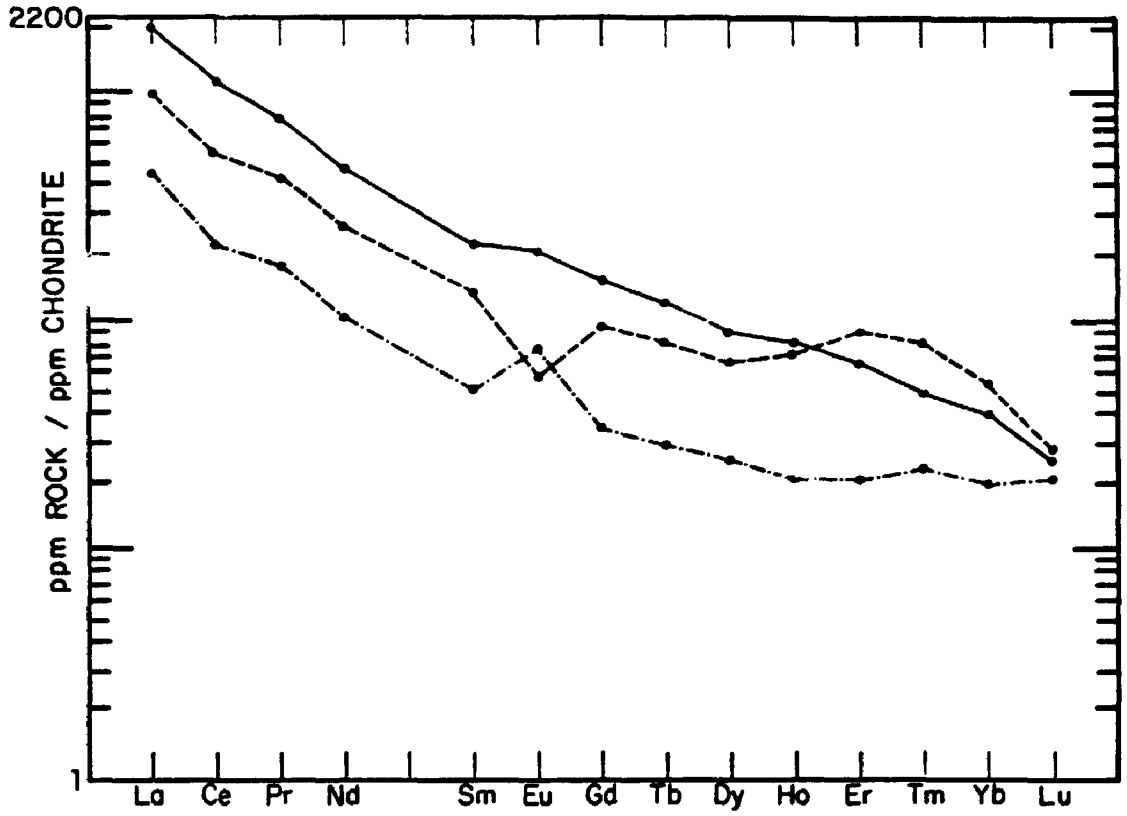

FIGURE 5.24. Chondrite-normalized REE pattern for Type II iron formation.

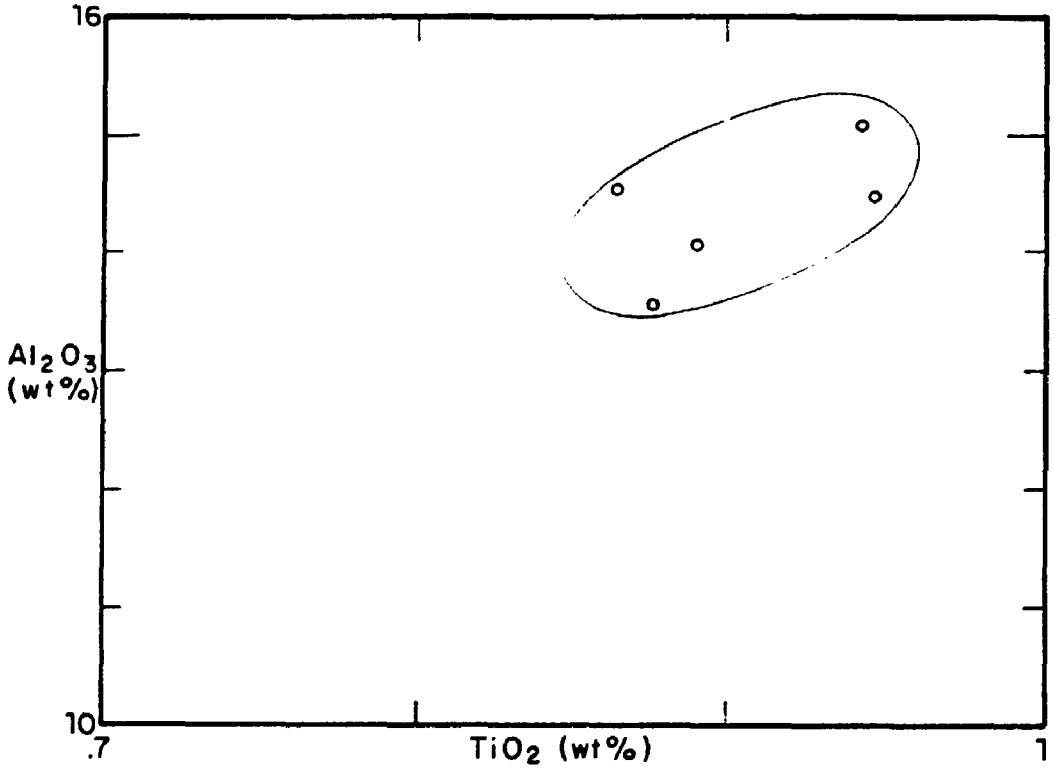

FIGURE 5.25. Al_2O_3 versus TiO_2 for metagraywackes.

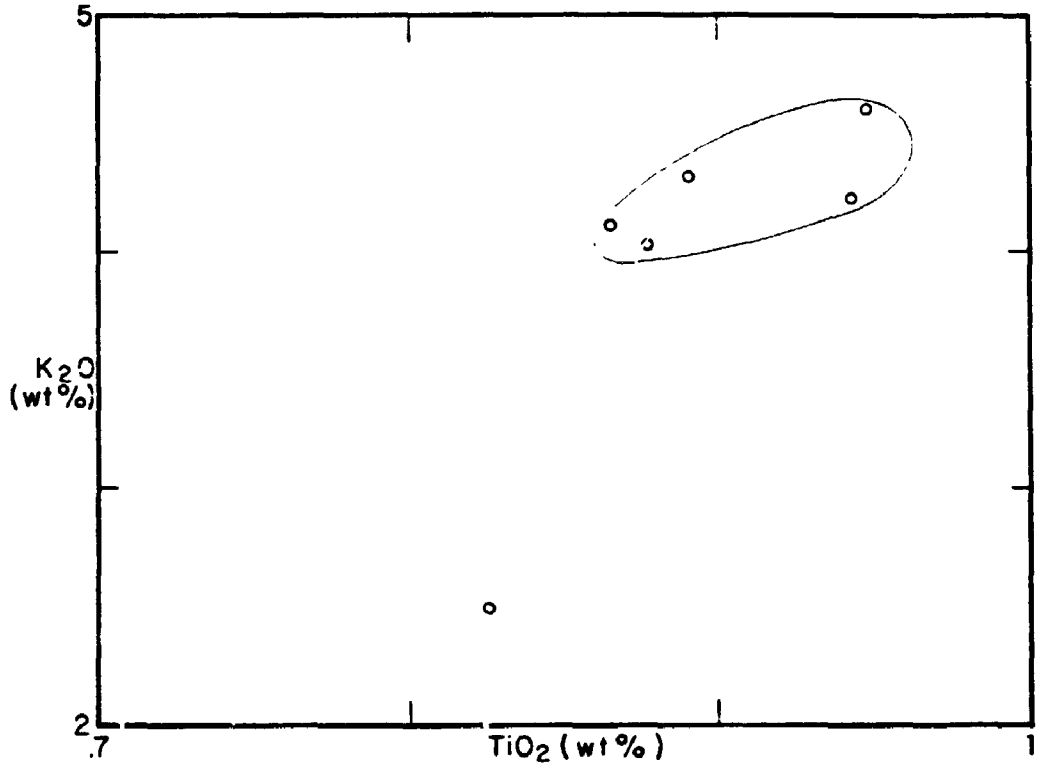

FIGURE 5.26. K_2O versus TiO_2 for metagraywackes.

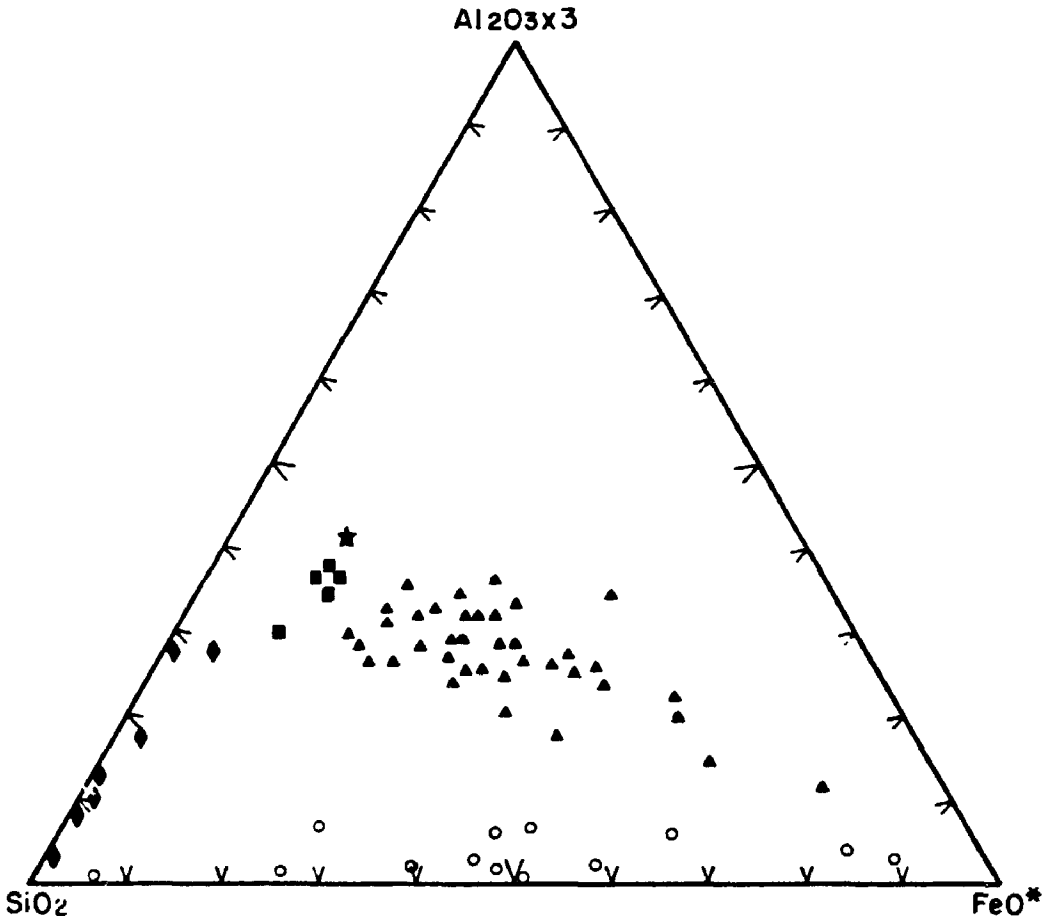

FIGURE 5.27. Graphical representation of Salobo metagraywackes (squares) and quartzites (diamonds) plotted on the SiO_2–FeO*–(Al_2O_3 x 3) diagram, along with the average composition of basalts (star), Type I (circles) and Type II (triangles) iron formation.

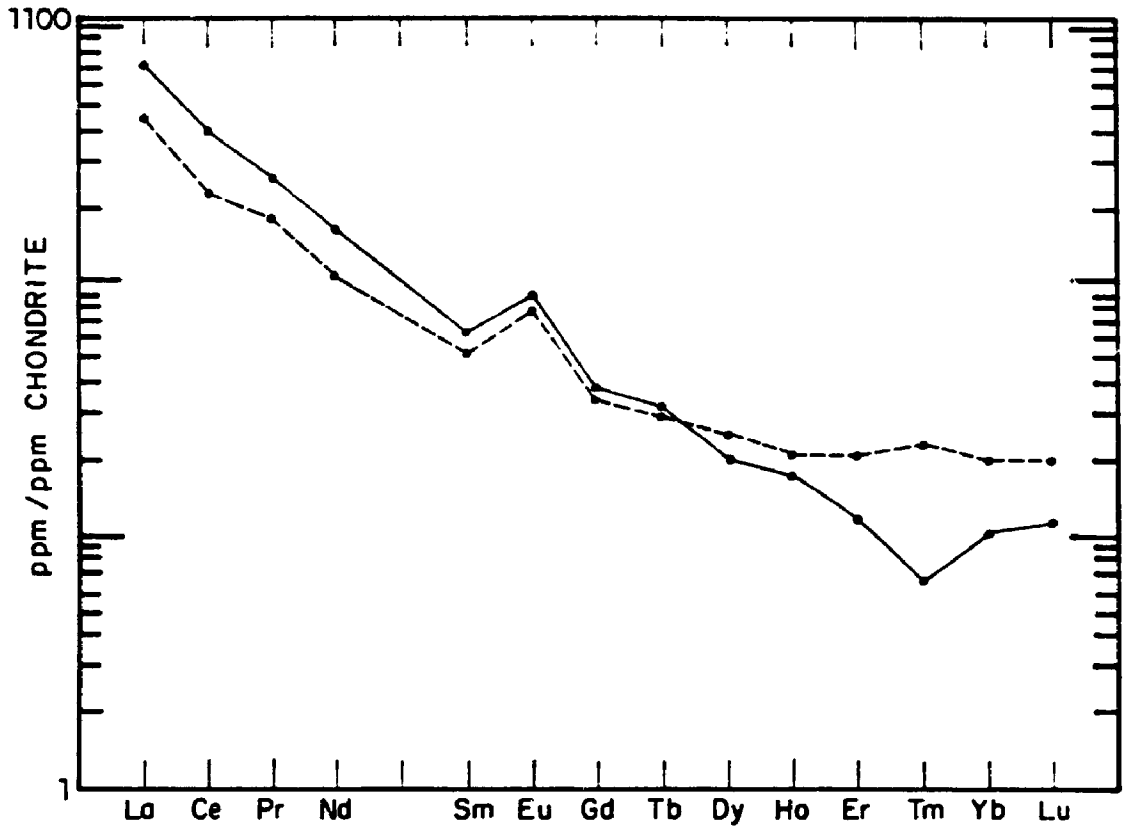

FIGURE 5.28. Chondrite-normalized REE pattern for metagraywackes.

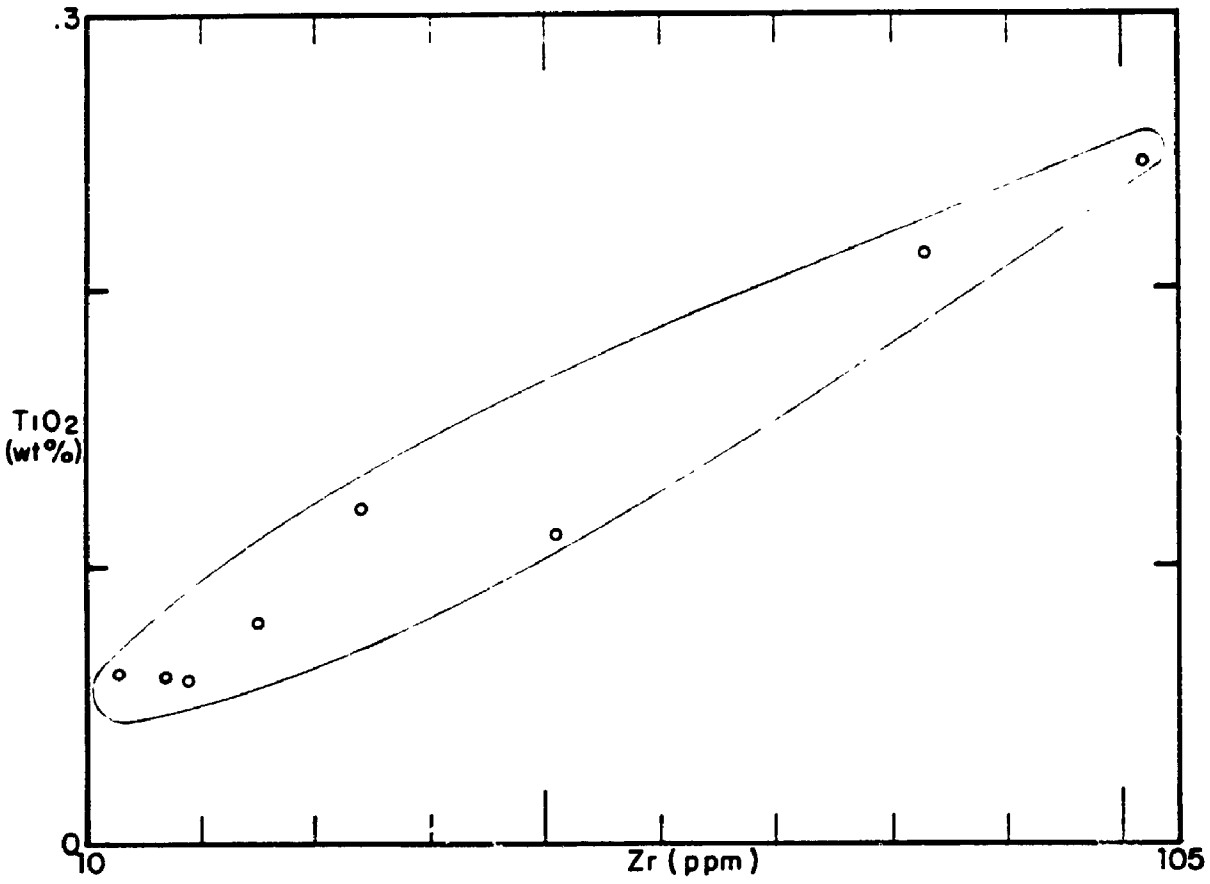

FIGURE 5.29. TiO_2 versus Zr for quartzites

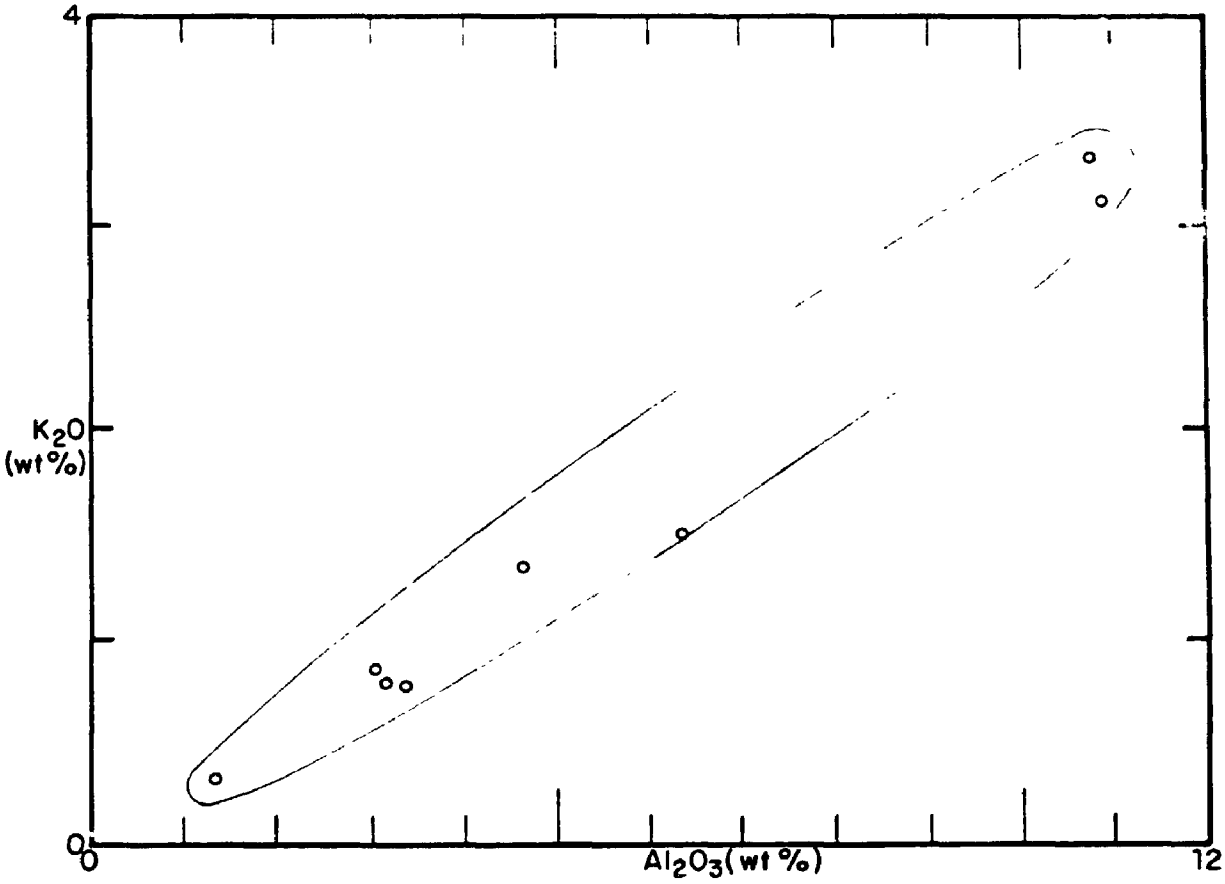

FIGURE 5.30. K_2O versus Al_2O_3 for quartzites

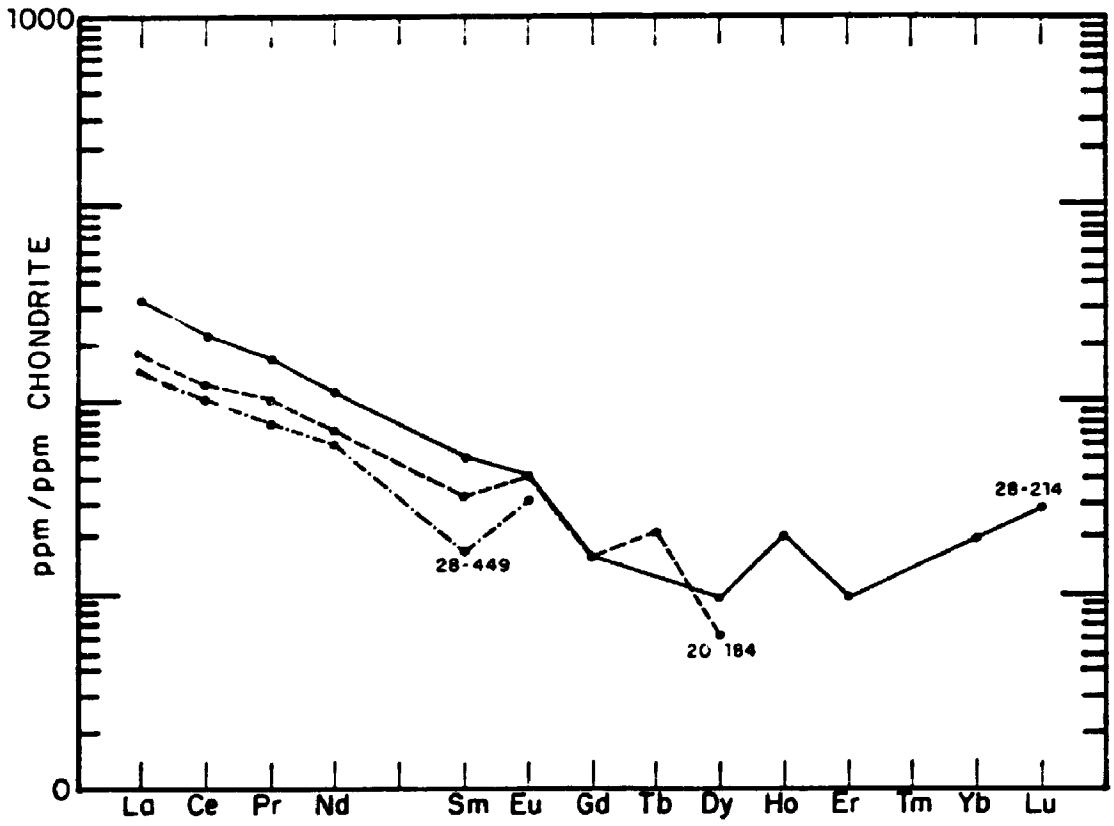

FIGURE 5.31. Chondrite-normalized REE pattern for quartzites.

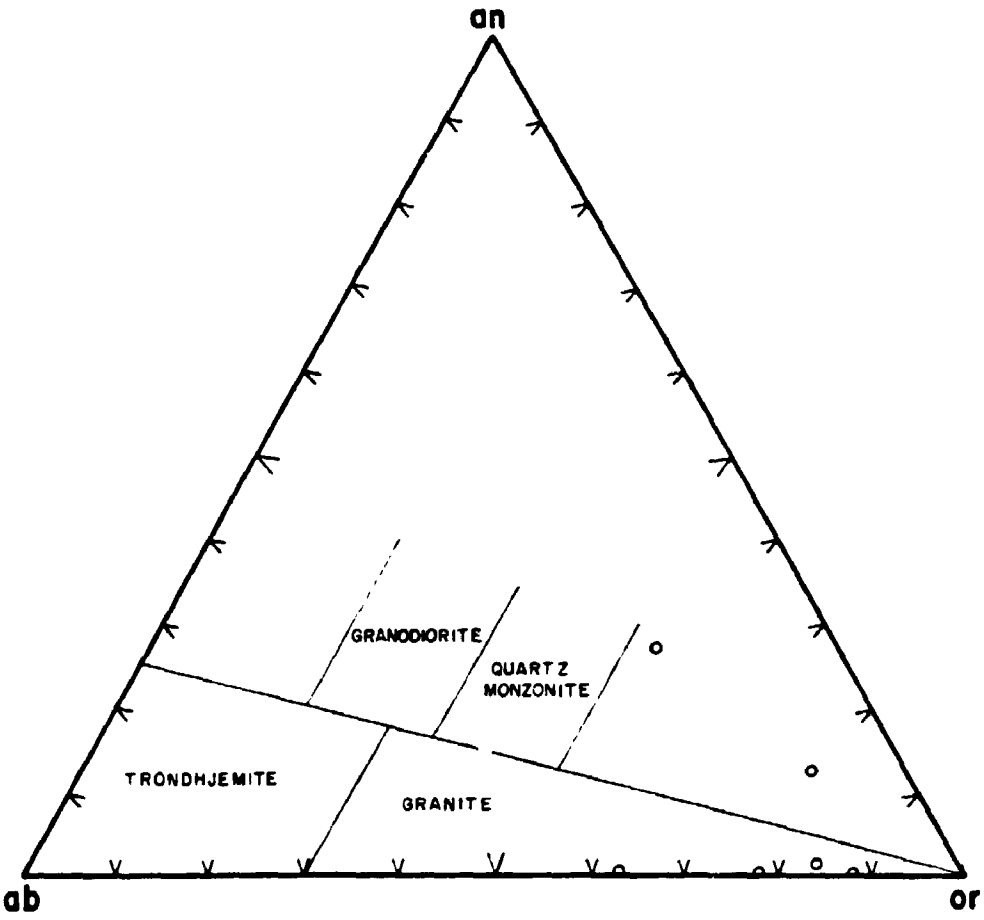

FIGURE 5.32. Normative classification of "quartz-free fraction" of quartzites, based or feldspar ratio.
Fields according to O'Connor (1965).

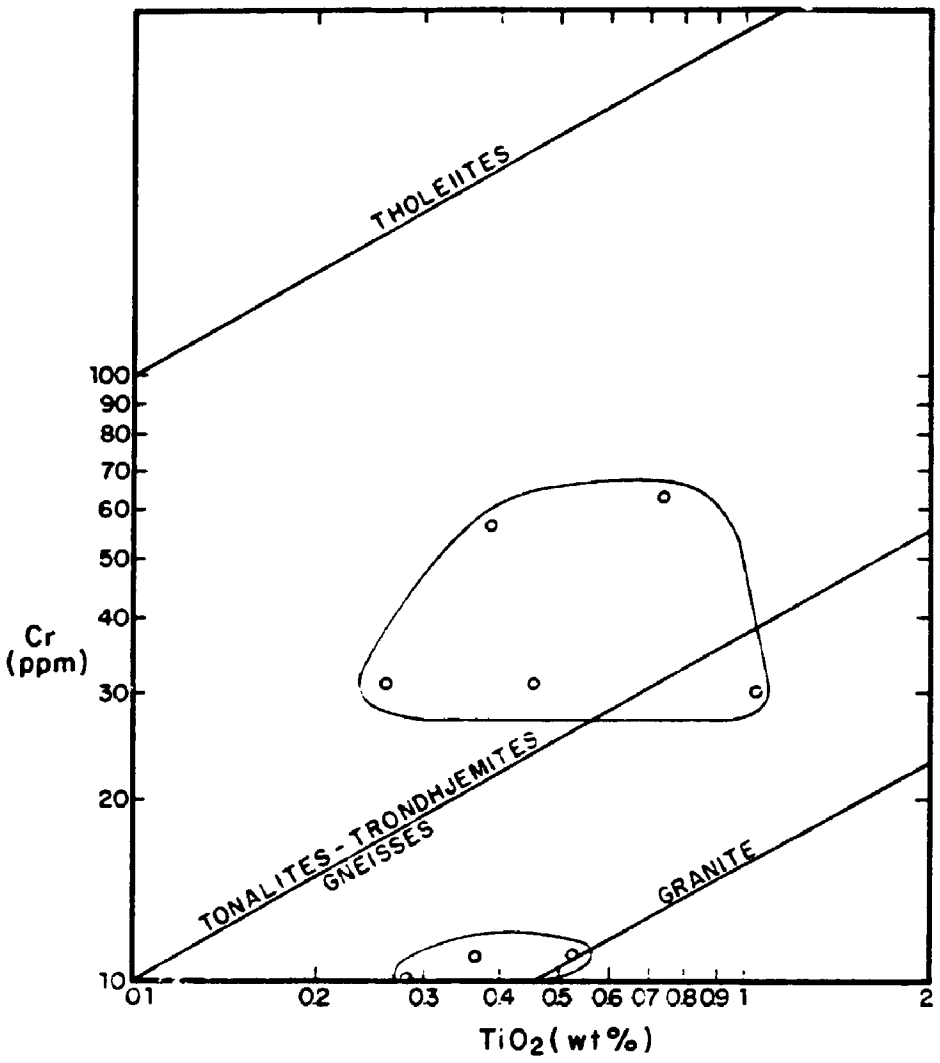

FIGURE 5.33. Discrimination of the source area for Salobo quartzites, based on Cr/TiO_2 ratios. Reference line-ratios for tholeiites, tonalite-trondhjemites and granites from Laskowski and Kroner (1985).

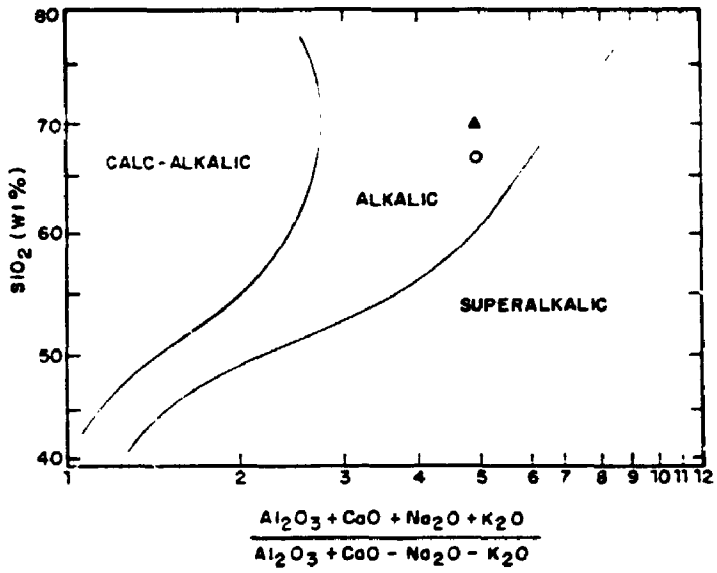

FIGURE 5.34. Average-composition of Salobo granitoids plotted on Wright's (1969) diagram of alkalinity variation . Note that both intrusions, OGS (triangle) and YSG (circle), plot in the alkalic field.

FIGURE 5.35. SiO_2 versus Zr for OSG (triangle) and YSG (circle).

FIGURE 5.36. SiO_2 versus Y for OSG (triangle) and YSG (circle).

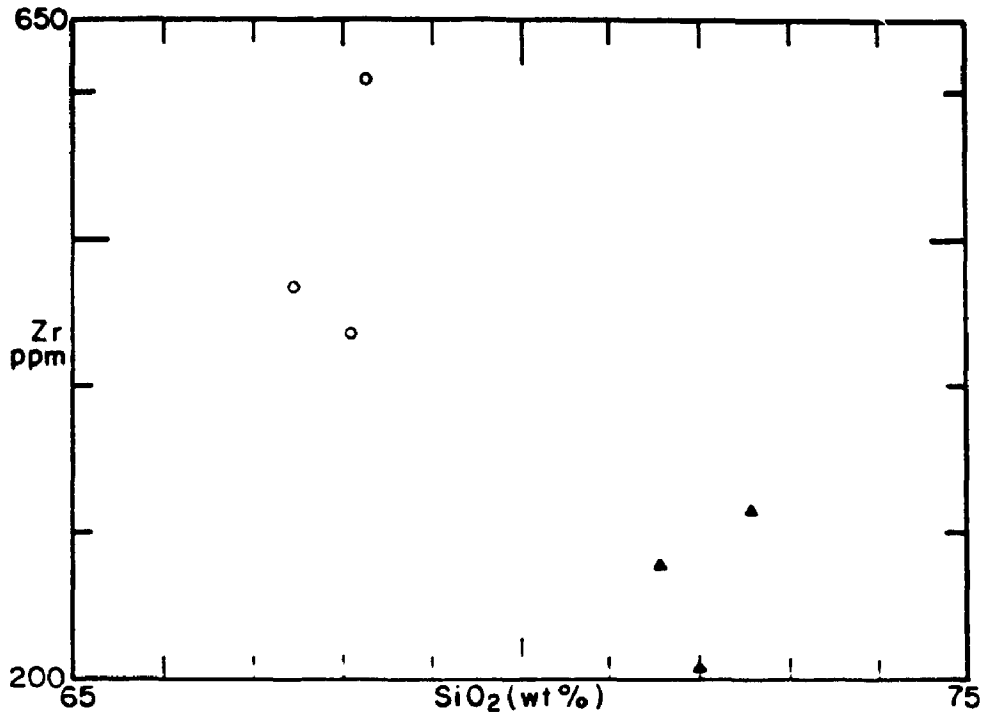
650
Zr
ppm
200
65
SiO2 (wt %)
75

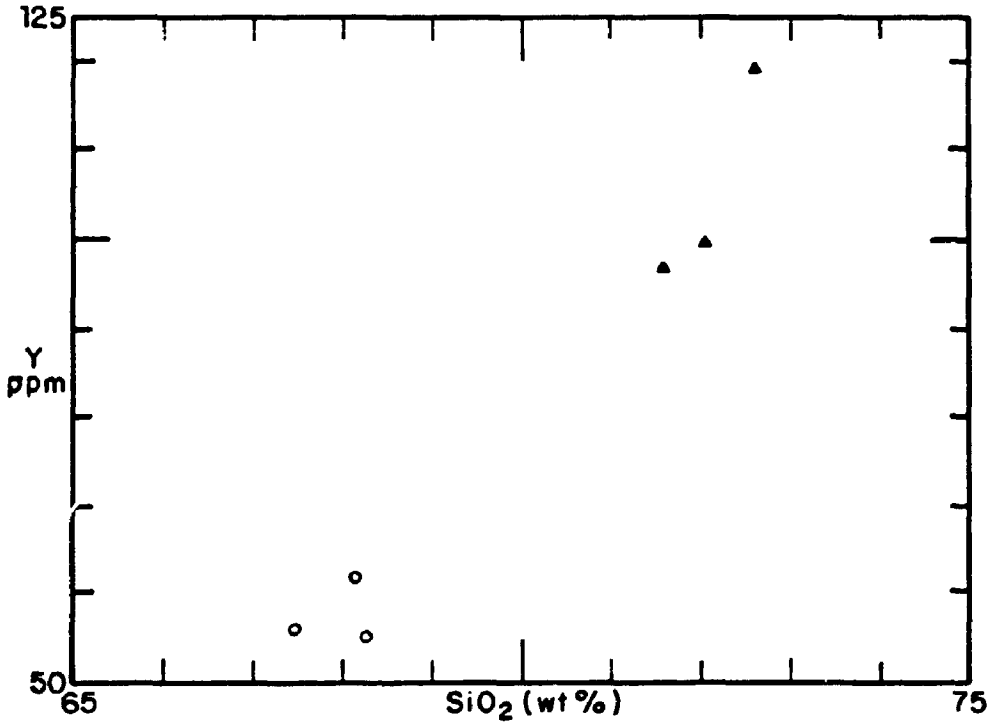
125
Y
ppm
50
65
SiO2 (wt %)
75

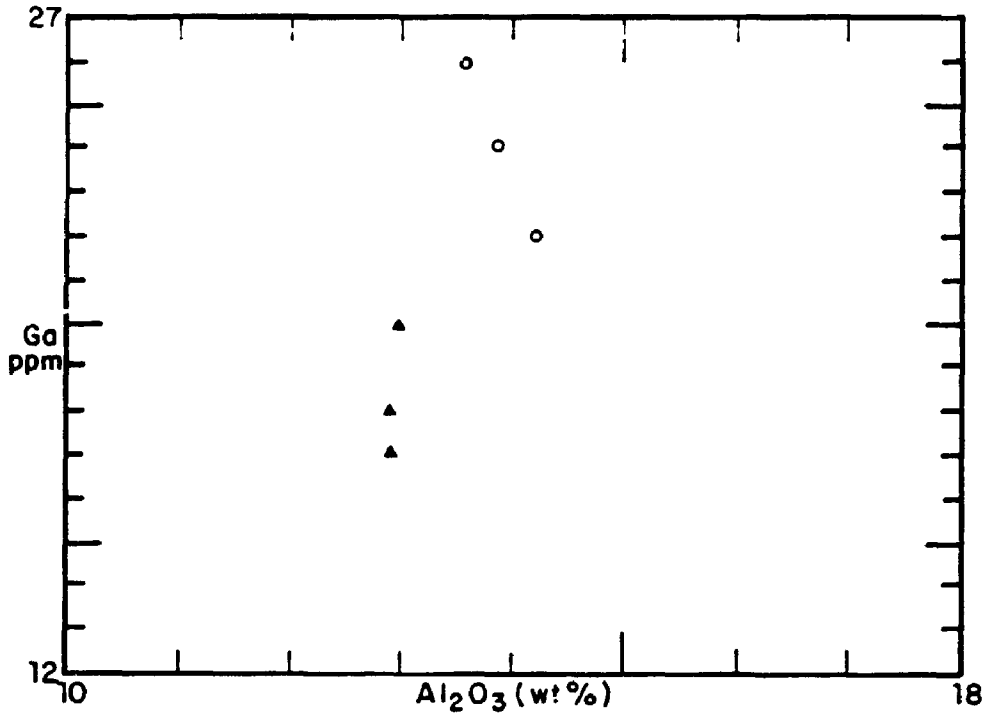

FIGURE 5.37. Al_2O_3 versus Ga for OSG (triangle) and YSG (circle).

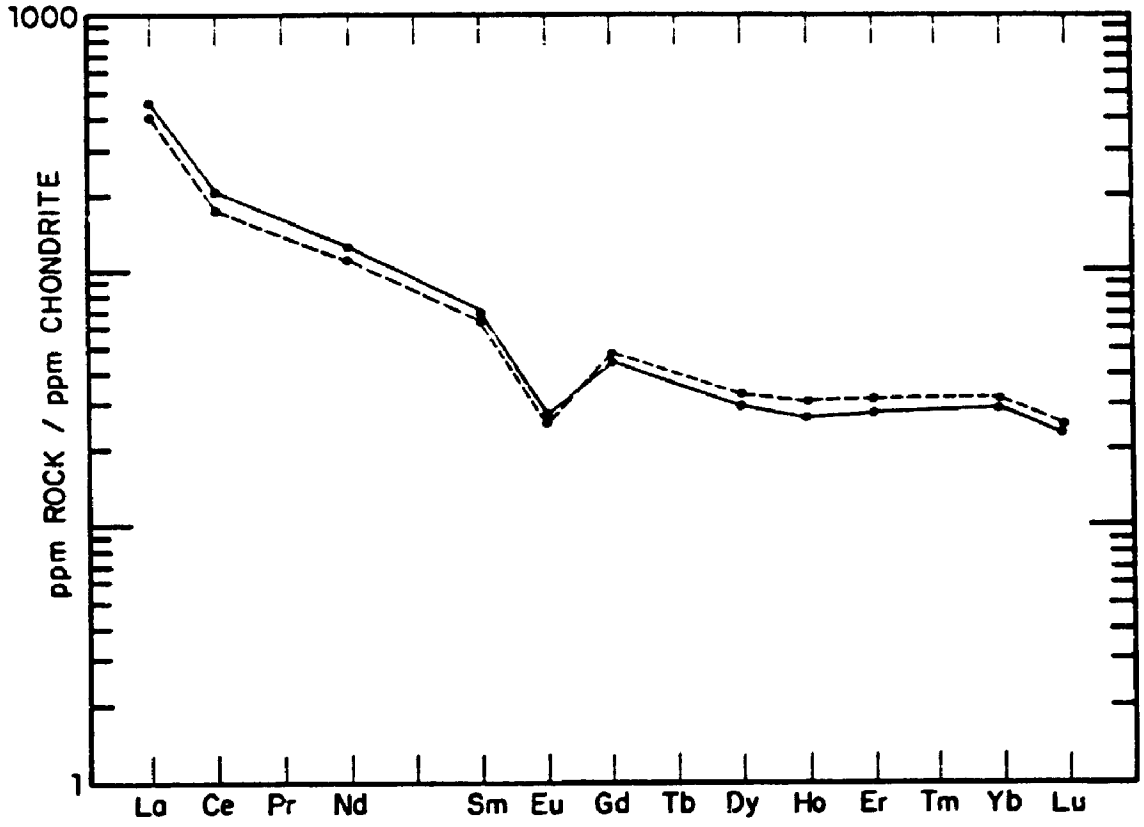

FIGURE 5.38. Chondrite-normalized REE patterns o. OSG.

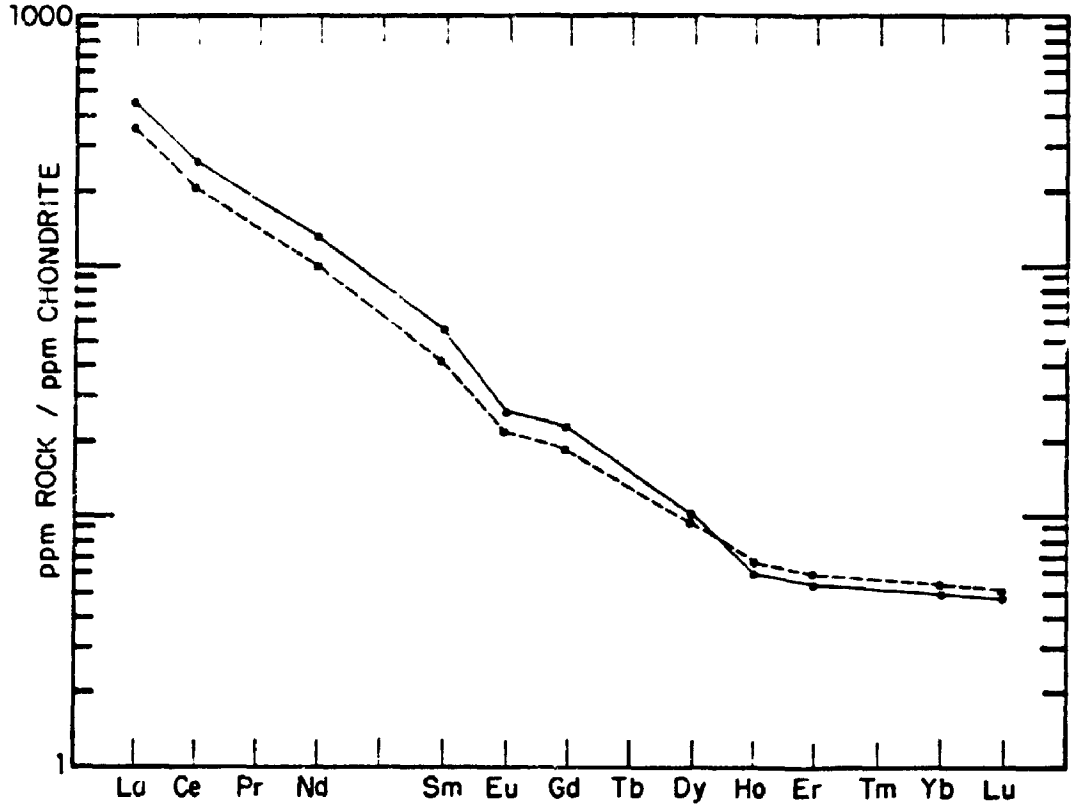

FIGURE 3.39. Chondrite-normalized REE patterns or YSG.

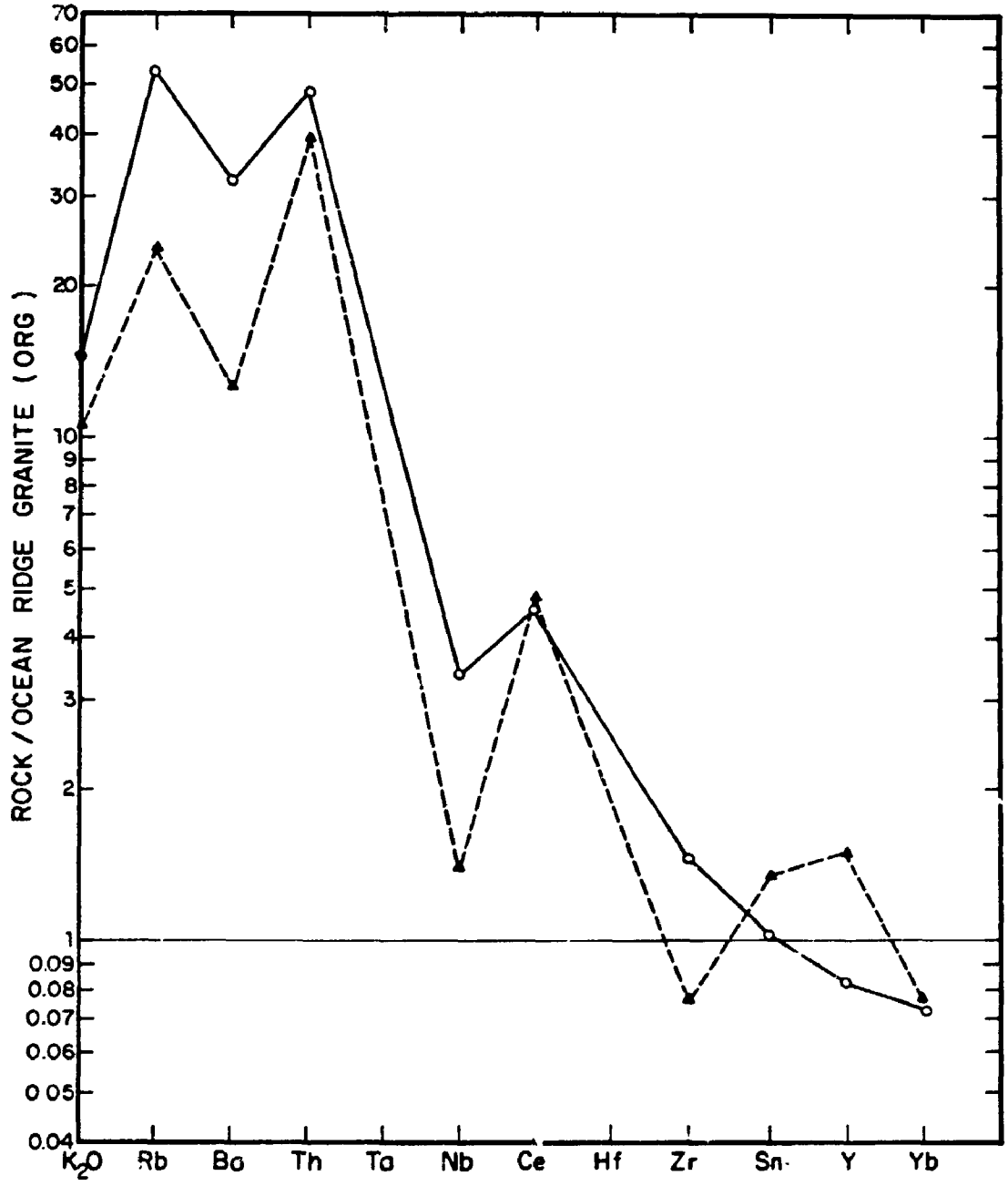

FIGURE 5.40. Ocean Ridge Granite-normalized geochemical patterns for Salobo granitoids (OSG triangle and YSG circle). Note that they are analogous to Pearce and Cann's (1984) within plate pattern.

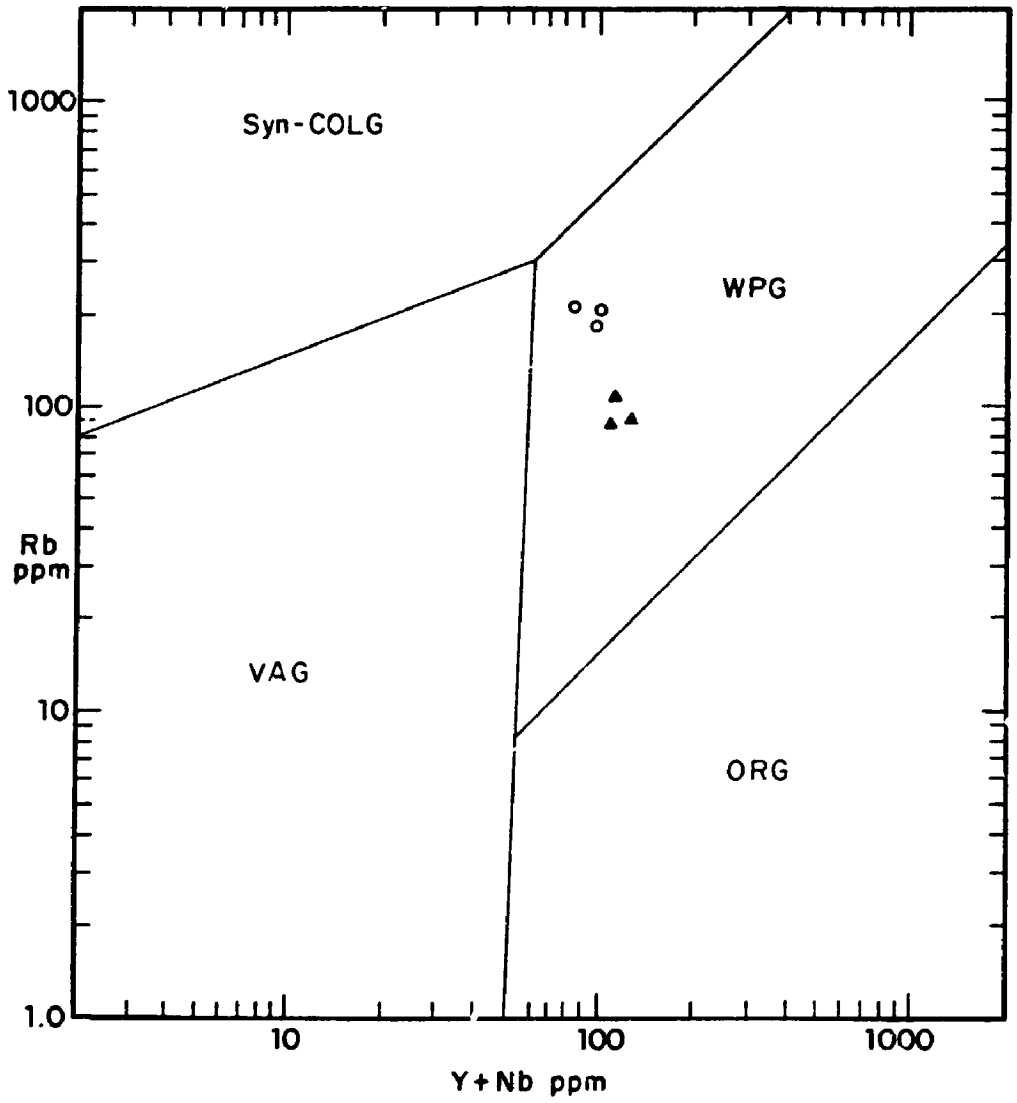

FIGURE 5.41. OSG (triangle) and YSG (circle) plotted on Pearce et al., (1984) discriminant diagram for: Syn-collision (SYN-COLG), volcanic arc (VAG), within plate (WPG) and Ocean ridge granites (ORG).

FIGURE 5.42. Diabase composition plotted on Winchester and Floyd's (1976) discriminant diagram of magma types.

FIGURE 5.43. Diabase composition plotted on Zr-(Ti/100)-(Yx3) Pearce and Cann's (1973) discriminant diagram. Low-K tholeiites (A and B), ocean floor basalts (B), calc-alkali basalts (C,B) and within plate basalts (D). Note that the fresh samples of Salobo dyke plot in the field of within plate basalts. The altered sample plots in calc-alkali basalts field.

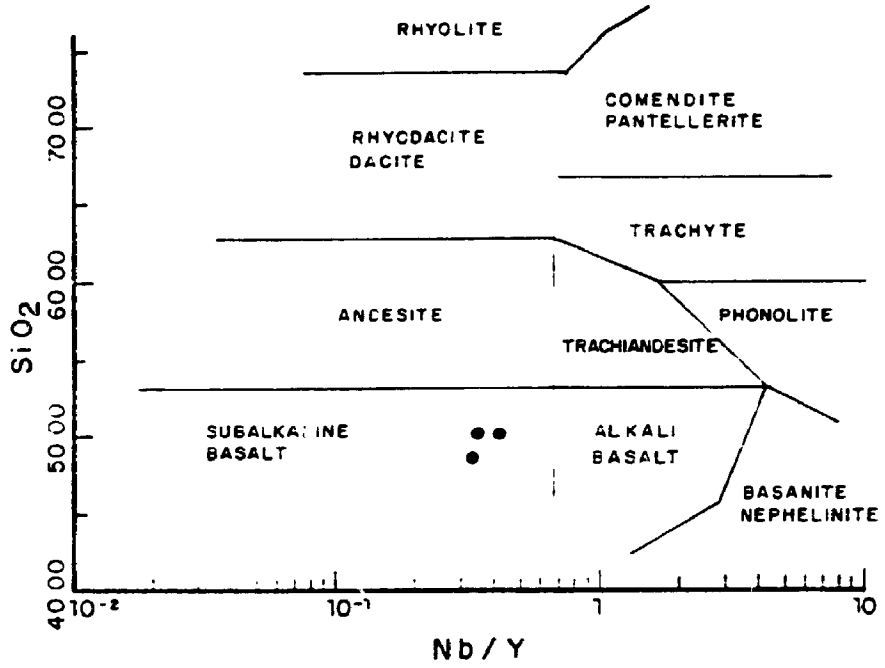
RHYOLITE
COMENDITE
PANTELLERITE
RHYODACITE
DACITE
TRACHYTE
ANDESITE
PHONOLITE
TRACHIANDESITE
SUBALKALINE
BASALT
ALKALI
BASALT
BASANITE
NEPHELINITE
70 00
60 00
50 00
40 00
Si O2
10-2
10-1
1
10
Nb / Y

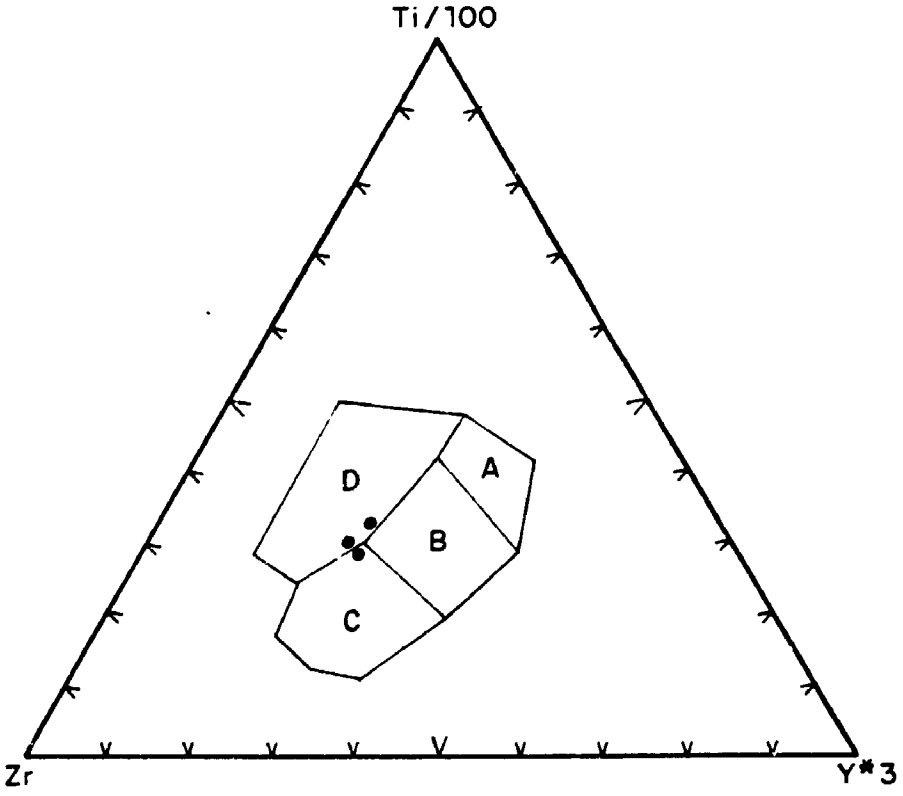
Ti/100
D
A
B
C
Zr
Y*3

CHAPTER 6

MINERAL CHEMISTRY

6.1 Introduction

This chapter summarizes the chemical composition of all silicate, carbonate and oxide minerals identified in the study area.

A total of 450 mineral analyses were carried out by electron microprobe, including fayalite, garnet, amphibole, biotite, muscovite, feldspar, chlorite, tourmaline, epidote, allanite, stilpnomelane, greenalite, carbonate and oxides.

Analytical techniques, and tables of mineral compositions are presented in Appendices B and A, respectively.

6.2. Fayalite

Fayalite occurs exclusively in iron formations. It is almost pure end-member with 94.85 to 99.75 mol % Fa (Table 6.1 and Figure 6.1). The Fe molar fraction (X_{Fe}) ranges from 0.923 to 0.965.

Fe^t/Fe^t+Mg ionic ratios of the fayalites and their host rocks show a good correlation (Figure 6.2) indicating equilibrium between them. One sample (50-127-1), with altered fayalite is an exception.

The range of the Fe molar ratios is controlled by the composition of the host rock, indicating minor chemical variations of the iron formation.

6.3. Garnet

Garnet occurs in iron formation, metagraywackes and quartzites (Figure 6.3).

Two types of garnet were distinguished in iron formation, zoned (type I) and unzoned (type II) garnet described in chapter 4. The zoned garnet is xenoblastic exhibiting inclusions of magnetite and hastingsite, whereas the unzoned one is sub idioblastic to idioblastic, showing inclusions of grunerite, quartz and tourmaline. Garnet in metagraywackes and quartzites is garnet II.

6.3.1. Garnet in iron formation

Both garnet types are almandine with minor molecular proportions of spessartine, grossular and pyrope (Table 6.2).

Fe^t/Fe^t+Mg ionic ratios of garnets and their host rocks show good correlation (Figure 6.4) indicating equilibrium.

The range of the Fe molecular proportion in the garnet (X_{Fe} 0.02 to 0.2) reflects the composition of the original microlayer where the mineral was formed (see chapter 5, table 5.8), and indicates chemical variation within the iron formation.

Type I garnet presents what has been commonly described as "normal" zoning, with Fe and Mg increasing and Ca and Mn decreasing from core to rim (Tracy, 1982), whereas Type II garnet is chemically, as well as optically, unzoned.

Garnet I composition is:

	Core	Rim
Almandine	56-77%	75-87%
Spessartine	14-32%	4-7%
Grossular	6-10%	3-8%
Pyrope	1-1.5%	1-2.5%

Type II garnet is richer in almandine than Type I. When both garnet types occur in the same rock, garnet II and the rims of garnet I have similar almandine contents (Figure 6.5).

Garnet II composition is:

Almandine	72-87%
Spessartine	3-19%
Grossular	5-10%
Pyrope	0.5-6%

6.3.2. Garnet in metagraywackes and quartzites

Garnet II in metagraywackes and quartzites is almandine, (Tables 6.3 and 6.4) whose composition varies according to the type of their host rock.

	Metagraywackes	Quartzites
Almandine	87.5-90%	91-93%
Spessartine	1.9-5%	2.4-3.2%
Grossular	1.7-2.9%	2.0-3.1%
Pyrope	3.3-7.4%	1.8-2.7%

6.4. Amphibole

Amphibole is found in all rock types of the study area, except quartzites. Hastingsite, grunerite, cummingtonite and gedrite were identified optically. According to Leake's (1968) amphibole classification, the first is a calcium amphibole and the last three are Fe-Mg-Mn amphiboles.

The green hastingsitic amphiboles prove to have the chemical compositions of hastingsite, pargasite, Fe-pargasite and less commonly Fe-tschermakite. The colorless, polysynthetically twinned "gruneritic" amphiboles are grunerite (an Fe-Mg-Mn amphibole) and the calcic amphiboles subcalcic-silicic hastingsites, with less common tschermakite and Mg-kaersutite. Other colorless Fe-Mg-Mn amphiboles are cummingtonite and rarer gedrite.

Therefore, the substitution of hastingsite by grunerite or cummingtonite, described in chapter 4 (Petrography), corresponds chemically to a two step substitution of hastingsite, Fe-pargasite and pargasite by subcalcic-silicic hastingsite, at the first step and to grunerite or cummingtonite at the second step.

Nevertheless, as a simplification, the petrographic classification of the amphiboles will be maintained in the next sections, unless otherwise stated.

Calcic and Fe-Mg-Mn amphiboles occur in gneisses, amphibolites and iron formation, while the latter are also found in metagraywacke. The calcic amphiboles in the study area always show higher Fe/Mg ratios than the associated Fe-Mg-Mn amphiboles.

6.4.1. Amphibole in Gneisses and Amphibolites

Calcic amphiboles in gneisses and amphibolites are hastingsite and Fe-pargasite, while cummingtonite is the only Fe-Mg-Mn amphibole (Tables 6.5 and 6.6).

In amphibolites, minor subcalcic-silicic hastingsite, Fe-tschermakite, Mg-hastingsite, tschermakite and Mg-kaersutite also occur.

Substitution relationships between calcic and Fe-Mg amphiboles are commonly observed in amphibolites, where hastingsite and Fe-pargasite are replaced by subcalcic-silicic hastingsite and cummingtonite.

In amphibolites, the two-stage substitution of Ca-amphiboles is present. The silica gap between calcic and Fe-Mg-Mn amphibole groups is over the interval 43.4 - 50.7 % SiO_2, which corresponds also to the color change, from green to colorless, between hastingsite and subcalcic-silicic hastingsite (Table 6.6).

Amphibole compositions in gneisses and amphibolites are represented in figure 6.6. The Fe^t/Fe^t+Mg ionic ratios of Ca-amphiboles in amphibolites are 0.512 to 0.697, always higher than their associated Fe-Mg-Mn amphiboles (0.461-0.544). In gneisses, they are 0.736 - 0.656 and 0.534 - 0.488 respectively.

Fe^t/Fe^t+Mg ionic ratios of Ca amphiboles in gneisses and amphibolites and their host rocks (figure 6.7) show one out of seven points with good correlation, indicating equilibrium relationships. The three points off the line correspond to rocks submitted to a late chloritization, their position in the diagram indicates that Fe or Mg, or both elements were mobilized in that alteration event.

6.4.2. Amphibole in iron formation and metagraywackes

Both calcic-amphiboles and Fe-Mg-Mn amphiboles occur in the iron formation, while metagraywackes present only Fe-Mg-Mn amphiboles (Tables 6.7, 6.8, 6.9 and Figure 6.8).

The calcic-amphiboles in iron formation are hastingsite, Fe-pargasite, subcalcic-silicic hastingsite and

subcalcic-silicic Fe-pargasite. The Fe-Mg-Mn amphiboles are mostly grunerite with subordinate Fe-gedrite.

Fe-Mg-Mn amphiboles in metagraywackes are cummingtonites.

Fe^t/Fe^t+Mg ionic ratios of amphiboles in iron formation are: hastingsite/Fe-pargasite 0.899 - 0.949; subcalcic-silicic hastingsite and subcalcic-silicic Fe-pargasite 0.718 - 0.770 and grunerite 0.722 - 0.843. Fe-gedrite from sample 61-120-2 shows an anomalously high Fe^t/Fe^t+Mg ratio, equals to 0.995. This mineral occurs in rims of fibrous Fe-gedrite around magnetite, in a quartz- rich rock, a texture not commonly seen in the study area.

Cummingtonites in metagraywackes have Fe^t/Fe^t+Mg ionic ratios 0.397 - 0.457.

The Fe^t/Fe^t+Mg ionic ratios of amphiboles in iron formation were plotted together with the ratios of their respective host rocks, in Figure 6.9. The points in the diagram do not indicate correlation between any one of the amphibole types and their host rocks, indicating disequilibrium and mobility of Fe and/or Mg during or after the episode of amphibole formation. Although, if all amphibole types are observed together in the same diagram, a weak correlation is suggested among them and their host rocks.

Subcalcic-silicic hastingsite and subcalcic-silicic Fe-pargasite show compositions (expressed as Fe molar fraction) varying from X_{Fe} = 0.547 - 0.512 and grunerite from 0.505 to

0.569. This small variation in X_{Fe} of 6 and 12%, respectively may indicate that these minerals formed in rocks of homogeneous composition or that these hydrated minerals formed under influence of an externally controlled fluid source, according to Frost (1982).

The absence of equilibrium relationships between grunerite, subcalcic-silicic hastingsite and subcalcic-silicic Fe-pargasite and their host rocks, shown above, along with their compositions, seems to suggest that an externally controlled fluid source played an important role during the formation of these hydrated minerals.

6.5 Biotite

The composition of biotite in the rocks of the study area is strongly influenced by the rock composition in which the biotite occurs.

Biotite is observed in all rock types, and is classified as Fe-biotite in iron formation, Fe-rich metagraywacke layers and quartzites and biotite in gneisses, amphibolites and Mg-rich metagraywacke layers, according to Foster's (1960) biotite classification.

The composition of the biotites may be seen in figure 6.10.

The biotite composition expressed in Fe molar proportion X_{Fe}, is: 0.465-0.470 in gneisses; 0.306-0.311 in amphibolites; 0.439-0.489 in iron formation; 0.384-0.429 in

Fe-rich metagraywacke and 0.229-0.275 in Mg-rich metagraywacke. It may be observed that these values, in each rock type, have a tendency to cluster around a point. This may indicate that every rock type has a very homogeneous composition or that the formation of these hydrated minerals took place under an externally controlled fluid source, as stated by Frost (1982).

Biotites show also Fe^t/Fe^t+Mg ionic ratios varying from 0.461 to 0.475 in gneisses, 0.521 to 0.565 in amphibolites; 0.685 to 0.903 in iron formation, 0.210 to 0.824 in metagraywacke and 0.908 in quartzite.

6.5.1. Biotite in gneisses and amphibolites

Biotite in gneisses (two analyzed samples, table 6.10) show octahedral Ti = 0.162 and Al^{vi} = 0.430 in a chloritized cummingtonite-bearing sample (19-191), and Ti = 0.132 and Al^{vi} = 0.834 in a biotite-tourmaline gneiss sample (31-311). Biotites in gneisses also have $Mg/Mg+Fe^t$ ionic ratios of 0.530 and 0.535.

Biotite in amphibolites (two analyzed samples, table 6.11) have Ti = 0.258 and Al^{vi} = 0.306 in a chloritized rock (49-526) and Ti = 0.243 and Al^{vi} = 0.215 in a sheared albite-rich amphibolite (20-505). They have $Mg/Mg+Fe^t$ ionic ratios of 0.465 and 0.461, respectively.

Biotite in the chloritized gneiss sample has lower Al^{vi} and higher Ti than that in the biotite-tourmaline-bearing

gneiss. The behavior of Al^{vi} agrees with literature discussions which show that the amount of Al^{vi} in biotites increases with the metamorphic grade (Guidotti, 1984; Engel and Engel, 1960), although the behavior of octahedral Ti is different The chloritized amphibolite sample (49-526) displays higher Ti and Al than the hastingsite-albite-bearing rock, exactly the contrary of the above author's observations.

6.5.2. Biotite in Iron Formation

Fe-biotites in iron formation are reddish brown minerals presenting Ti = 0.026 - 0.238, Al^{vi} = 0.228 - 0.487 and $Mg/Mg+Fe^t$ ionic ratio of 0.122 - 0.323 (Table 6.12).

Metamorphic biotites with $Mg/Mg+Fe^t$ less than 0.3, as found in Fe-biotites of Salobo iron formation are almost absent in literature surveys (Hewitt and Wones, 1975; Guidotti, 1984). This fact may be due to the bulk rock composition controls of the biotite analyses available in the literature (Guidotti, 1984).

Most biotites, as may be seen in figure 6.11, display a good correlation between Fe^t/Fe^t+Mg ratios and their host rocks indicating equilibrium. The exception are samples 49-351-4 and 49-351-5 where fayalite is replaced by subcalcic-silicic hastingsite with about 8% MgO, indicating Mg mobility.

According to petrographic descriptions (chapter 4) grunerite is an alteration product of fayalite, probably formed at a lower temperature than fayalite. On the other hand, biotites in fayalite-bearing rocks show lower Al^{vi} and Ti than biotites in grunerite-bearing rocks, exactly the opposite of the observations of Engel and Engel (1960) and Guidotti (1984).

This inverse correlation of low Ti-Al^{vi} Fe-biotites accompanying high temperature mineral assemblages in iron formation, may be tentatively interpreted as a result of a lower temperature equilibration (or reequilibration) of Fe-biotites.

6.5.3. Biotite in metagraywackes

There are Fe-biotites and biotites in metagraywackes. Fe-biotites present Al^{vi} 0.550 - 0.736, Ti 0.206 - 0.255 and $Mg/Mg+Fe^t$ ionic ratio of 0.175 - 0.261. Biotites show Al^{vi} 0.485 - 0.550, Ti 0.135 - 0.150 and $Mg/Mg+Fe^t$ ionic ratio of 0.595 - 0.673 (See table 6.13).

Fe-biotites in metagraywackes made up of quartz, garnet, plagioclase and sillimanite *q* muscovite, display high Al^{vi} and Ti, while biotites with lower Al^{vi} and Ti are found in rocks composed of quartz, garnet, tourmaline and plagioclase.

Fe-biotites are therefore, in higher metamorphic grade rocks than biotite, which agrees with Engel and Engel

(1960), Guidotti (1984) and Guidotti et al., (1988) observations about compositional variations of biotites in function of metamorphic grade.

It also seems to indicate that biotites in metagraywackes equilibrated (or reequilibrated) at the same temperatures as did the mineral assemblages of their host rocks.

6.3.4. Biotite in quartzite

Despite many attempts, only one biotite analysis of reasonable quality was obtained in quartzites (Table 6.14), since biotites in these rocks are almost totally pseudomorphically replaced by chlorite.

The analysis show a Fe-biotite with Ti 0.13 and Al^{vi} 0.771, presenting the lowest $Mg/Mg+Fe^{t}$ ionic ratio of the area: 0.092.

6.6. Muscovite

Muscovite is observed in metagraywackes, quartzites and quartz-albite veins (Tables 6.15, 6.16 and 6.17). It is mainly muscovite-paragonite solid solution (Figure 6.12). The point off the line at the figure cited above, corresponds to a mineral with 0.958% of Ba-muscovite.

The observed chemical variation of muscovites, expressed in muscovite-paragonite end members, are:

muscovite 88 to 97 % and paragonite 3 to 12 % in metagraywackes; muscovite 92 to 96 % and paragonite 2 to 8% in quartzites and muscovite 97% and paragonite 3% in the analyzed quartz-albite vein.

Muscovites in quartzites show Ti values varying from 0.03 to 0.07 in sillimanite-bearing rocks and 0.001 in a sample (20-190) where muscovite and chlorite are intergrown along cleavage planes.

6.7. Feldspar

Feldspar occurs in all rock types of the study area, except iron formation. The feldspars in deformed rocks are mainly plagioclase, which is albite-rich in protomylonitic to mylonitic rocks, as already cited in chapter 4. They also have orthoclase molecular proportions of less than 2.5%. In undeformed rocks there are K-feldspars and plagioclase.

6.7.1. Feldspar in Gneisses and amphibolites

Feldspar in gneisses is plagioclase varying in composition from $An_{32.6}$ to $An_{1.9}$ (Table 6.18 and Figure 6.13). It is mostly orthoclase-free, except for three analyses which correspond to the points off the line in figure 6.16, presenting 1.1 to 4.8 mol % of orthoclase. Plagioclase in gneisses is mostly chemically unzoned, except for two samples (15-212 and 31-311) out of the 11 analyzed

ones, where plagioclase show albite-rich rims. Compositional variation of plagioclase within the same rock was observed in two samples (56-257A and 56-288B), with plagioclase composition varying from An 2.4 to 10.9 and from 2.0 to 9.4, respectively.

Feldspar in amphibolites is plagioclase, with composition of andesine ($An_{31.4}$) to albite ($An_{4.2}$). Samples with composition of oligoclase to andesine are chemically unzoned, although the sheared albite-rich sample (20-505) shows core and rim composition of $An_{9.4}$ and $An_{4.2}$, respectively.

6.7.2. Feldspar in metagraywackes and quartzites

Plagioclase was analyzed in two undeformed metagraywacke samples and one extremely sheared (mylonitic) quartzite sample (Tables 6.20; 6.21 and Figure 6.13).

Plagioclase in granoblastic polygonal-textured metagraywacke (sample 31-283-B) is labradorite ($An_{64.5}$ to $An_{69.8}$) and in schistose metagraywacke (sample 17-350-7) is oligoclase ($An_{18.9}$ to $An_{23.2}$).

In the sheared quartzite sample, the plagioclase is albite, showing An $_{1.0}$ to An $_{2.1}$.

6.7.3. Feldspar in YSG and undeformed veins

Alkali-feldspar quartz syenite, with rapakivi texture shows albite ($An_{1.5}$) in the core of feldspar porphyrocrysts rimmed by orthoclase ($Or_{97.36}$) (Table 6.22).

An undeformed feldspar vein, in amphibolite near YSG contact, contains orthoclase, showing Or $_{98.3-99.0}$, Ab $_{1.0-1.7}$ and An $_{0-0.1}$. Albite in undeformed druses has composition of $An_{0.0-0.2}$; $Or_{0.1-0.2}$ and $Ab_{99.6-99.8}$ (Table 6.23).

6.8. Chlorite

Chlorite is observed in all rock types of the study area and its composition reflects the composition of the host rock. Mg-chamosite occurs in gneiss (except for sample 15-212, containing chamosite) and amphibolites, chamosite in iron formation, metagraywacke with Fe-rich microlayers and quartzite; and Fe-clinochlore in metagraywacke with Mg-rich microlayer , according to Bayliss' (1975) chlorite classification (Tables 6.24 to 6.29).

The composition of chlorites in terms of total Al and Mg/Mg+Fe may be visualized in figure 6.14. The analyses plotted in the diagram show that chlorites in quartzites, metagraywackes and iron formation are the richest in iron and Al.

It may be observed in figure 6.15, where all chlorite analyses are plotted, that except for two samples, more Fe-rich chlorites are also more aluminous. This same correlation was also observed by Steward and Flohr (1984) in chlorites from metamorphosed silicic volcanics and pelitic rocks in Maine.

6.8.1. Chlorite in gneisses and amphibolites

The compositions of chlorite in gneisses and amphibolites is:

	Gneisses		Amphibolites
	Mg-chamosite	Chamosite	Mg-chamosite
Fe^t/Fe^t+Mg	0.370-0.683	0.757	0.579-0.659
X_{Fe}	0.415-0.474	0.523	0.411-0.478

Chlorite within individual gneiss samples shows a wide variation in composition (see table 6.24). This feature has been observed in chlorites of very low metamorphic grade rocks or where prograde and retrograde chlorite occur (Laird, 1988). Chlorite in Salobo gneisses is however, only retrograde, replacing hastingsite, Fe-pargasite or biotite.

Chlorite within individual amphibolite samples is less heterogeneous than in gneisses.

6.8.2. Chlorite in Iron Formation metagraywackes and quartzites

Chamosite in iron formations, metagraywacke and quartzite and Mg-chamosite in metagraywacke have Fe^t/Fe^t+Mg ionic ratios proportional to the same ratios of their host rocks. They also have Fe molecular proportion (X_{Fe}) varying according to their host rock composition.

The composition of chlorites in iron formation, metagraywackes and quartzites is:

	Iron Formation	Metagraywacke	Quartzite
Fe^t/Fe^t+Mg	0.738-0.811	0.846-0.347	0.919
X_{Fe}	0.531-0.569	0.551-0.259	0.591

6.8.3. Chlorite in veins

Chlorite veins are made up of: chamosite in iron formation and Mg-chamosite in amphibolites (Table 6.29).

Chamosite in veins transecting iron formation have Fe^t/Fe^t+Mg ionic ratios varying from 0.641 to 0.747, whereas the ratios in Mg-chamosites in veins cutting through amphibolites vary from 0.525 to 0.630.

6.9. Tourmaline

Tourmaline is observed in all rock types of the study area. It occurs mainly in metagraywackes, gneisses and amphibolites and less frequently in quartzites and iron formations (Tables 6.30 and 6.31).

Ca-Fe^t-Mg molecular proportions for tourmalines from all rock types are plotted in figure 6.16, along with common tourmaline end members for reference (according to Henry and Guidotti (1985) tourmaline classification). The position of the mineral analyses in the figure shows that tourmaline composition is schorlitic in iron formation and Fe-rich metagraywacke microlayers, dravitic in gneiss and Mg-rich metagraywacke microlayers and has 50% dravite and 50% schorlite molecular proportions in amphibolite.

It may be observed in figure 6.17 that there is a very good correlation between Fe^t/Mg ionic ratios of tourmalines and their host rocks, except for the gneiss sample 29-658, which was chloritized after tourmaline formation. It may be also inferred, by observing figure 6.17, that the Fe^t/Mg ratio of sample 29-658 increased with chloritization.

6.10. Oxides

Magnetites were analyzed in iron formation and amphibolite; ilmenite was analyzed in one amphibolite sample (Table 6.32).

Magnetites in Salobo iron formation are almost pure iron oxides as it has been described in other iron formations (Annersten, 1968; Klein, 1983), except for one sample containing 2.14% Al_2O_3.

Magnetite in amphibolite presents up to 1.51 % Al_2O_3. whereas ilmenite in the same rock has 1.11 MnO.

6.11. Other Minerals

Minerals occurring in veins, common accessories and minor alteration products are here referred as "other" minerals.

They are epidotes, allanites, carbonates, greenalite and stilpnomelane.

Epidotes are observed in optically zoned crystals, lining the walls of undeformed veins. They are iron-rich epidotes (almost pure pistacite end members) with Ps from 30.7 to 32.9% (Ps is the mole fraction of component $Ca_2Fe_3Si_3O_{12}$, pistacite, in the clinozoisite-epidote series, calculated from the ratio 100 $Fe^{3+}/(Fe^{3+}+Al)$: Holdaway, 1972). Ps varies from 15 to 33 mol %). As may be seen in table 6.34, the epidotes are not chemically zoned.

Allanite is a common accessory in most rock types of the study area. They show up to 7.15% La_2O_3 and 11.57% Ce_2O_3. Allanite analyses are in table 6.34.

Carbonates usually occupy the inner part of undeformed veins. They are almost pure calcite showing up to 0.15% $MgCO_3$, 0.19% $FeCO_3$ and 0.53% $MnCO_3$ (Table 6.35).

Greenalite is observed replacing fayalite and subcalcic silicic-hastingsite, and in veins crosscutting iron formation. Greenalite analyses are in table 6.36 and its composition is plotted in the Mg-Al-Fe+Mg diagram of figure 6.22.

Stilpnomelane occurs in undeformed veins. The color variation described in chapter 4 (brownish to greenish, from the wall to centre of the veins) indicates the presence of ferri-stilpnomelane at the margins grading to ferro-stilpnomelane at the inner part of the veins (according to Miyano (1982), reporting stilpnomelane analyses in iron formations of Hamersley Group, in western Australia). Stilpnomelane analyses are in table 6.37 and its composition may be seen, together with greenalite, in the Mg-Al-Fe+Mg diagram of figure 6.18.

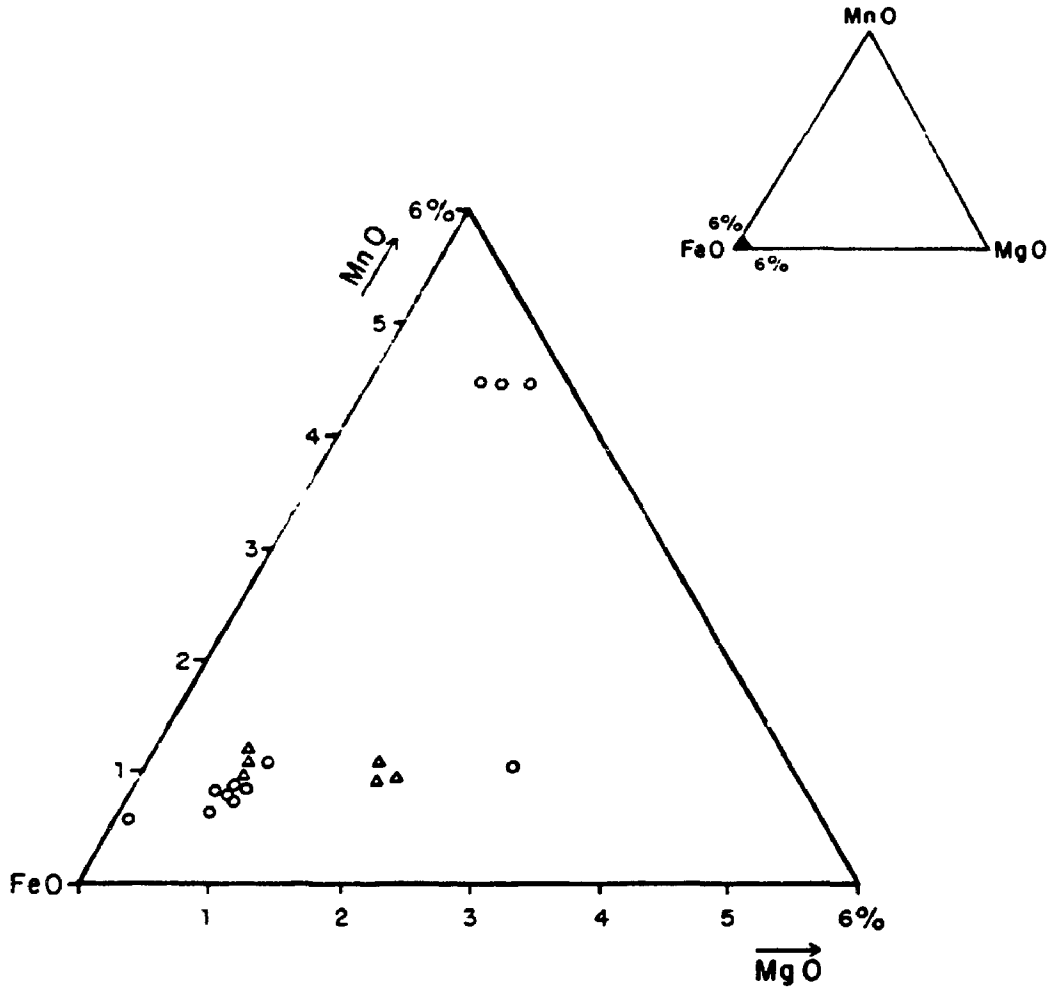

FIGURE 6.1. Fayalite FeO-MgO-MnO composition-diagram. (triangles) fayalite in Type I and (circles) fayalite in Type II iron formation.

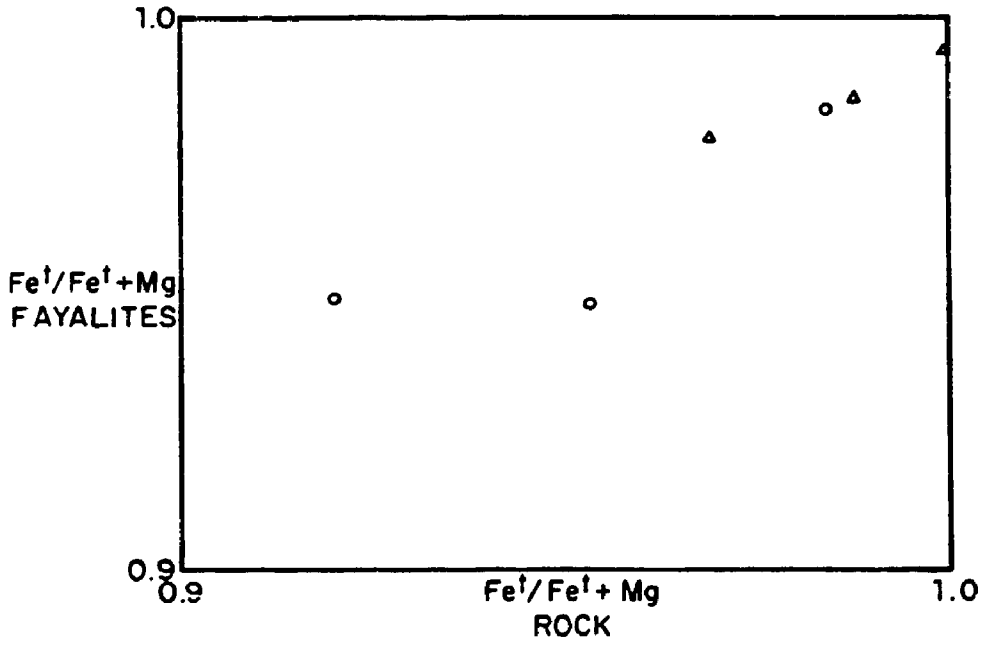

FIGURE 6.2. Fe^t/Fe^t+Mg ionic ratios of fayalites and their host rocks, showing Type I iron formation in triangles and Type II iron formation in circles.

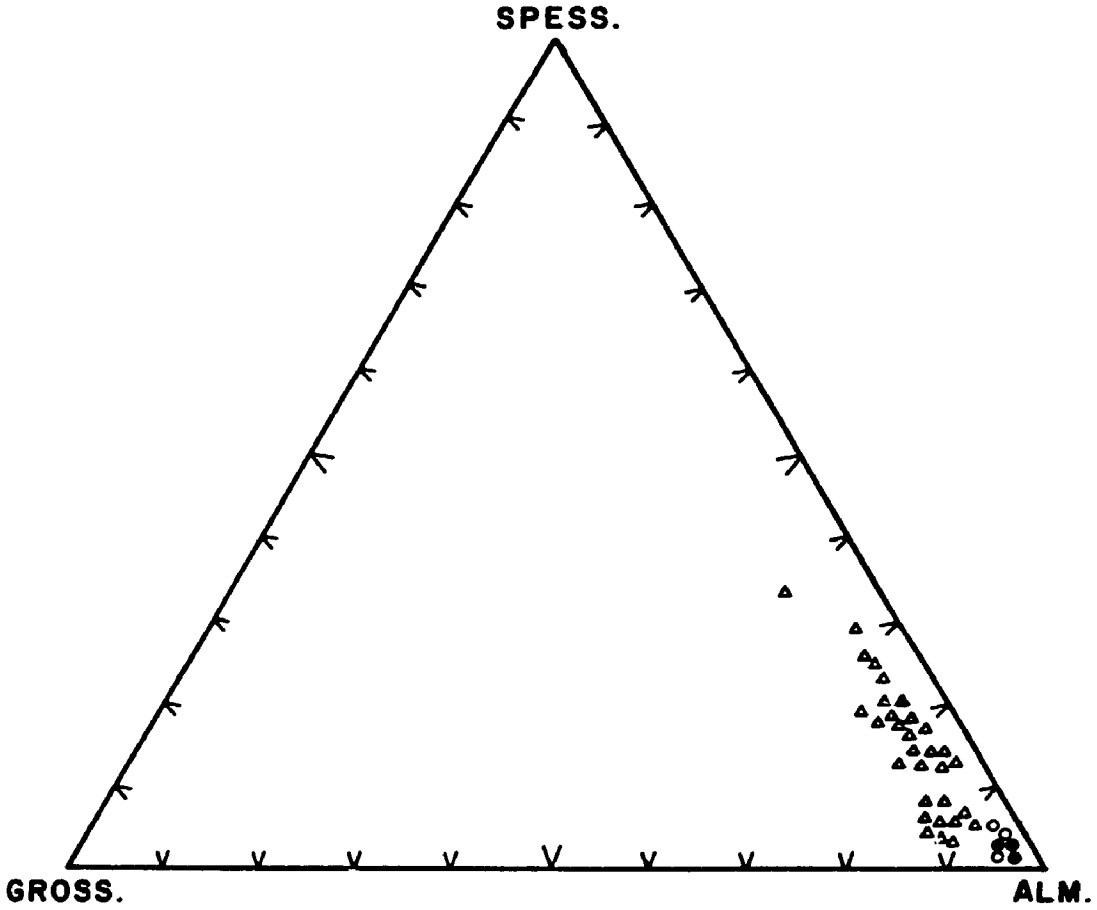

FIGURE 6.3. Chemical variation of garnets expressed as end-members almandine, grossular and spessartine.
Iron formation (triangles), metagraywackes (circ'es), and quartzites (dots).

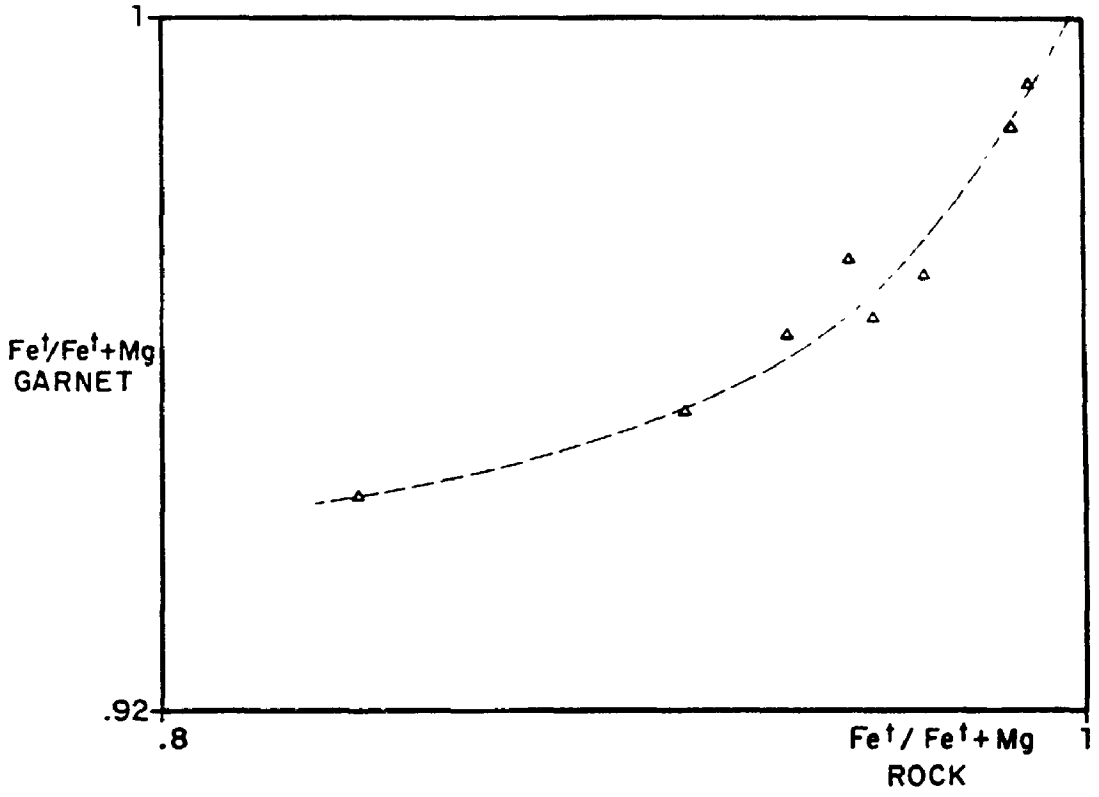

FIGURE 6.4. Fe^t/Fe^t+Mg ionic ratios of iron-formation garnets and their host rocks.

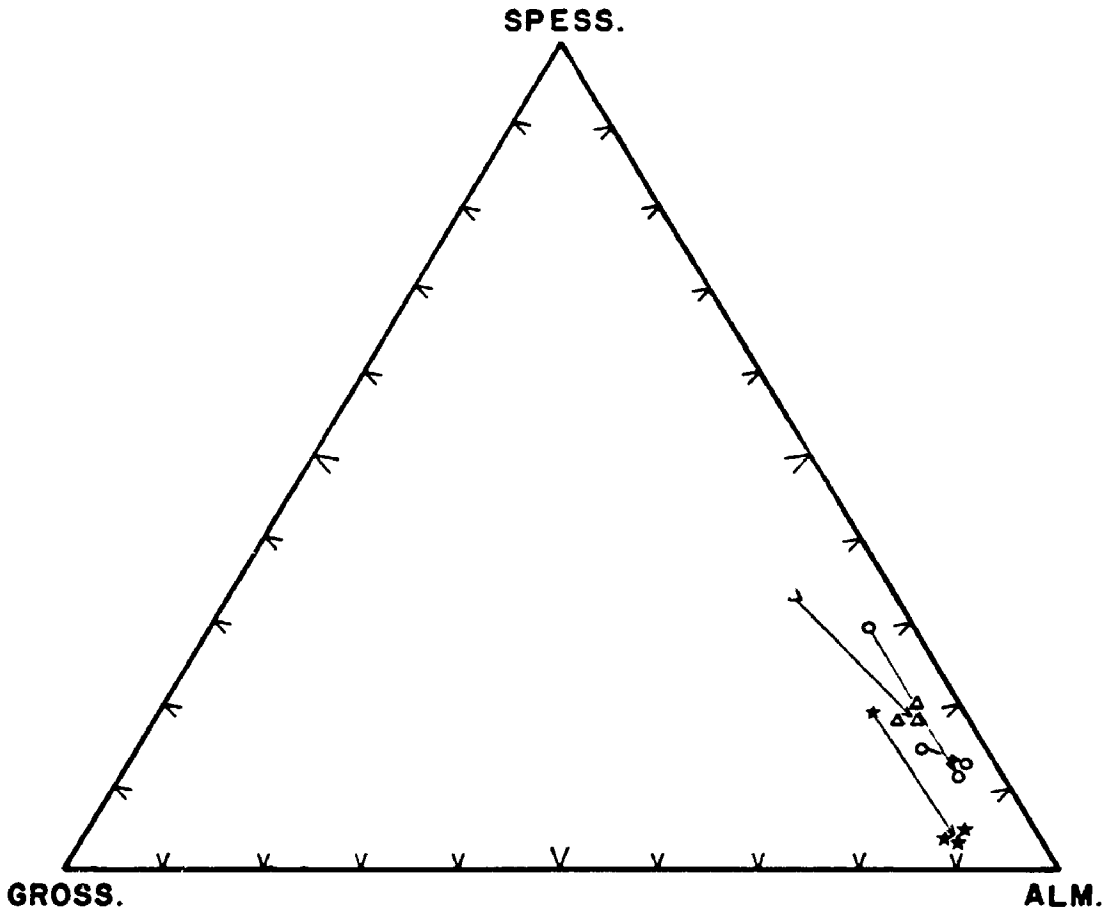

FIGURE 6.5. Chemical variation of Zoned garnet I in iron formation and their associated garnet II, expressed as end-members almandine, spessartine and grossular.
Arrows point to the rim of garnet I.

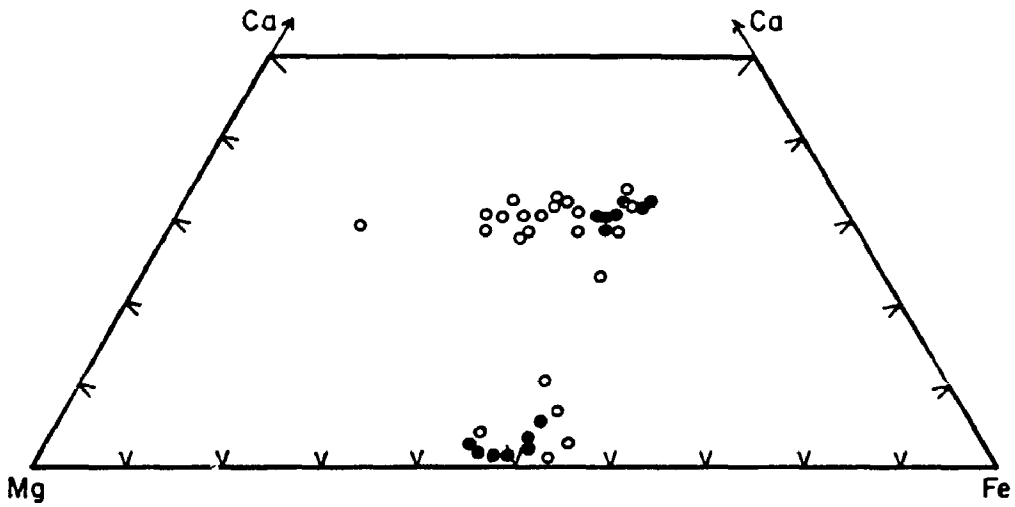

FIGURE 6.6. Mg-Ca-Fe molecular-proportion diagram for amphiboles from gneisses (dots) and amphibolites (circles).

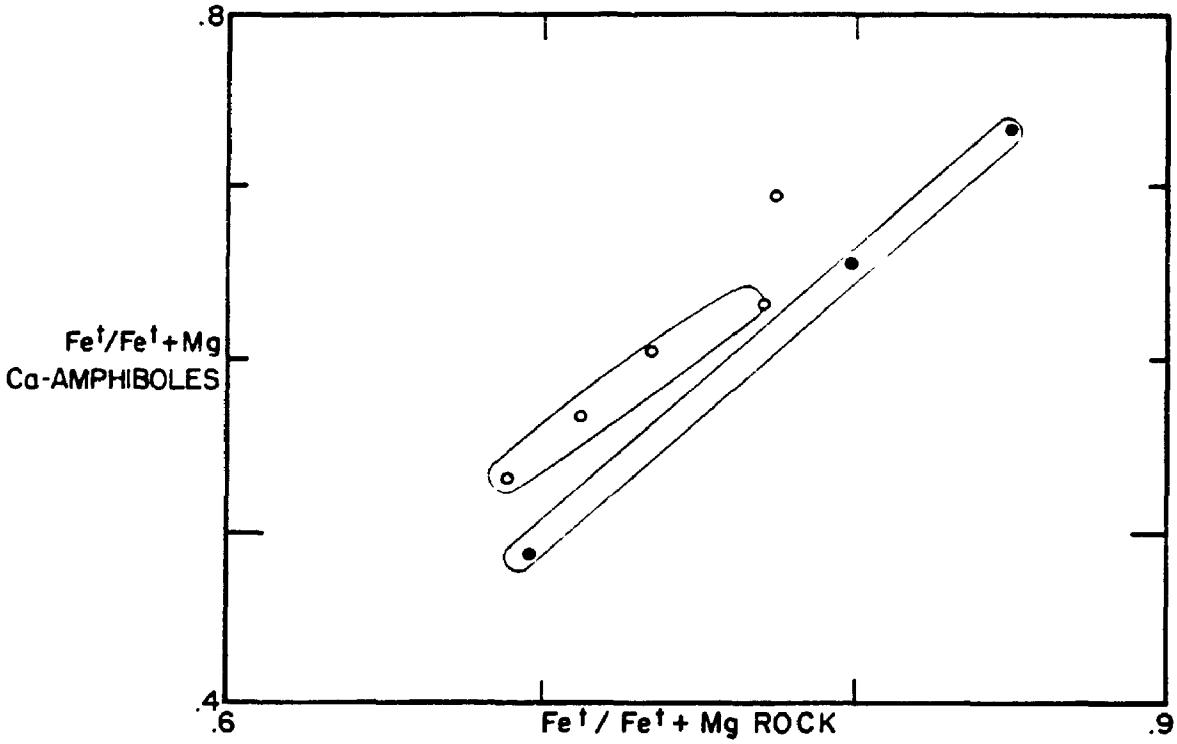

FIGURE 6.7. Fe^t/Fe^t+Mg ionic ratios of calcic amphiboles and their host rocks. Gneisses (dots) and amphibolites (circles).

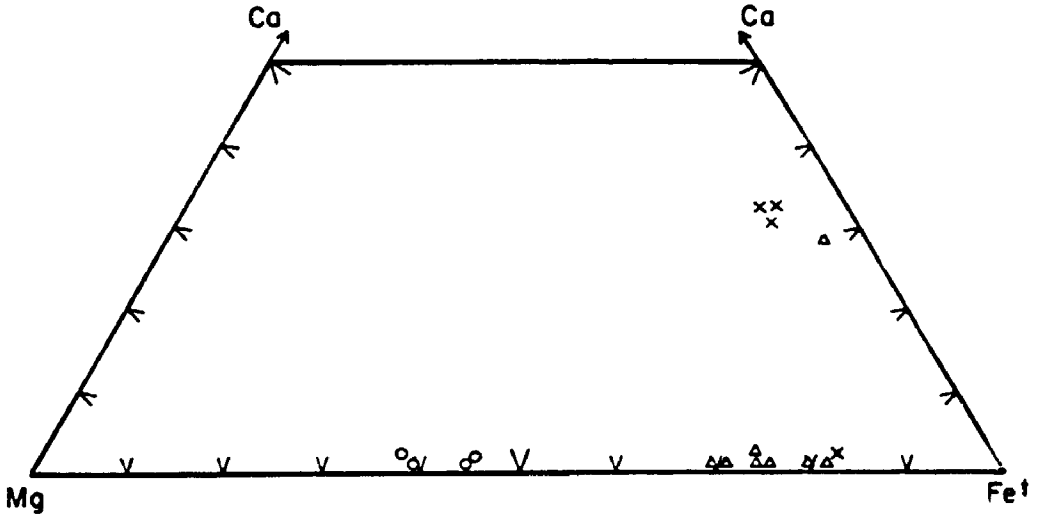

FIGURE 6.8. Fe*-Mg-Ca molecular-proportion diagram for amphiboles from metagraywackes (circles), Type I (X) and Type II iron formation (triangles).

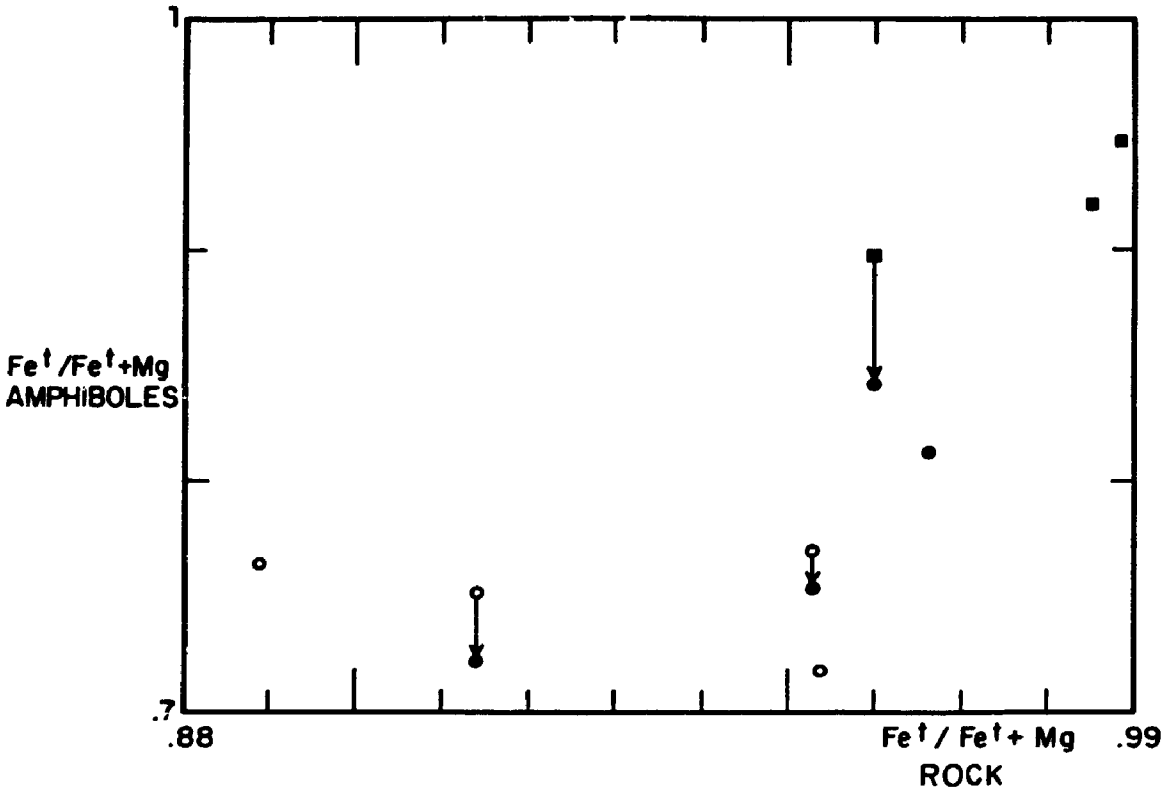

FIGURE 6.9. Fe^t/Fe^t+Mg ionic ratios of amphiboles in iron formation and their host rocks. Arrows point to the rim of altered amphiboles. Green calcic amphiboles (squares), colorless calcic amphiboles (circles), and Fe-Mg-Mn amphiboles (dots).

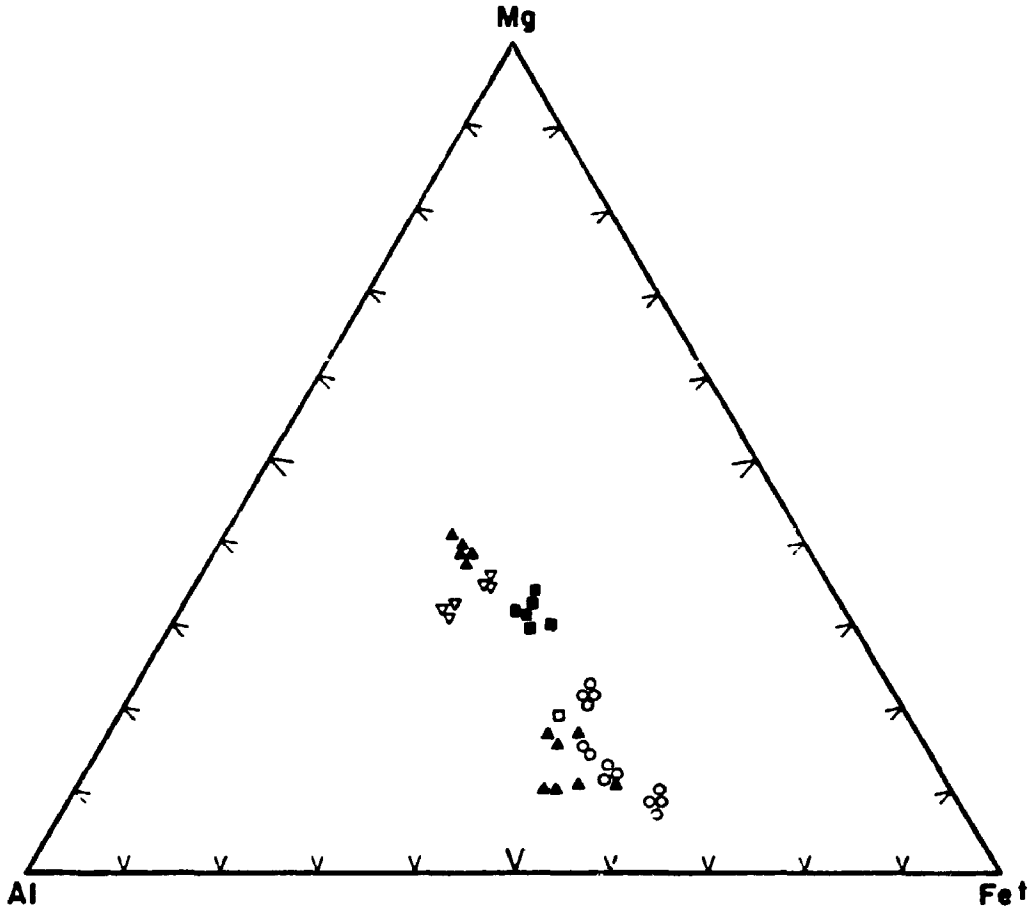

FIGURE 6.10. Al-Fe^t-Mg molecular-proportion diagram for biotites from: Iron formations (circles), quartzite (hollow square), amphibolites (solid squares), gneisses (triangles), and metagraywackes (solid triangles).

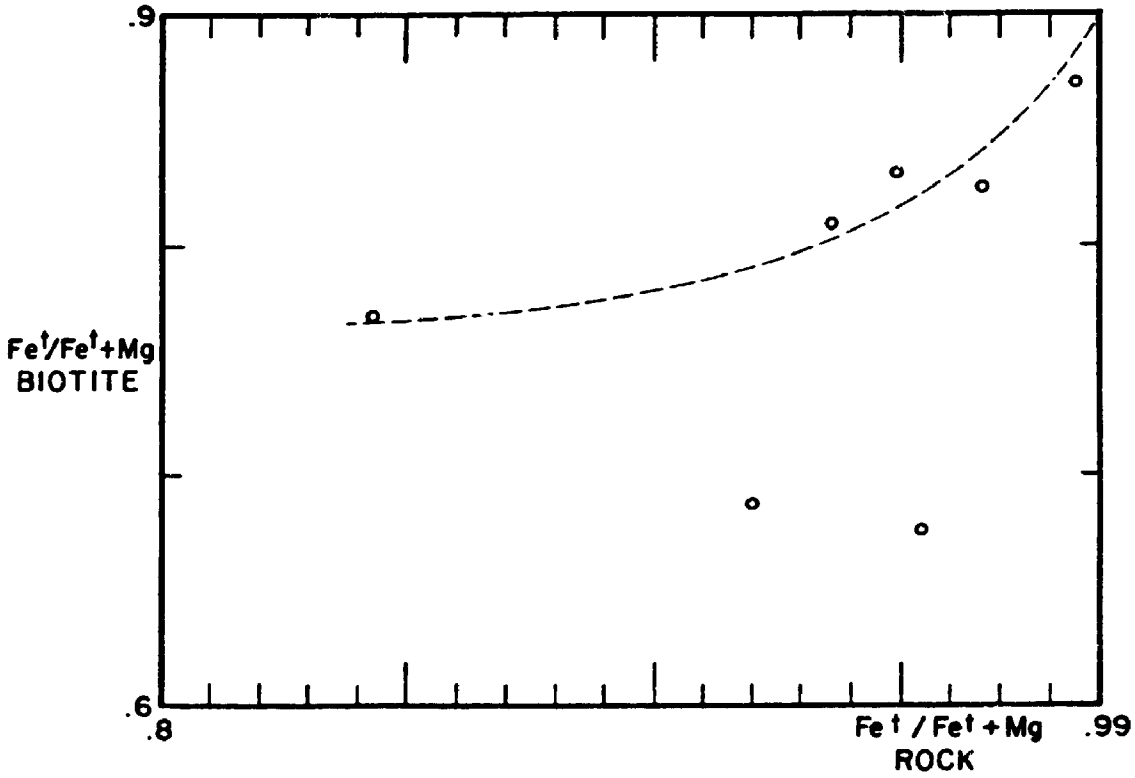

FIGURE 6.11. Fe^t/Fe^t+Mg ionic ratios in iron-formation biotites and their host rocks.

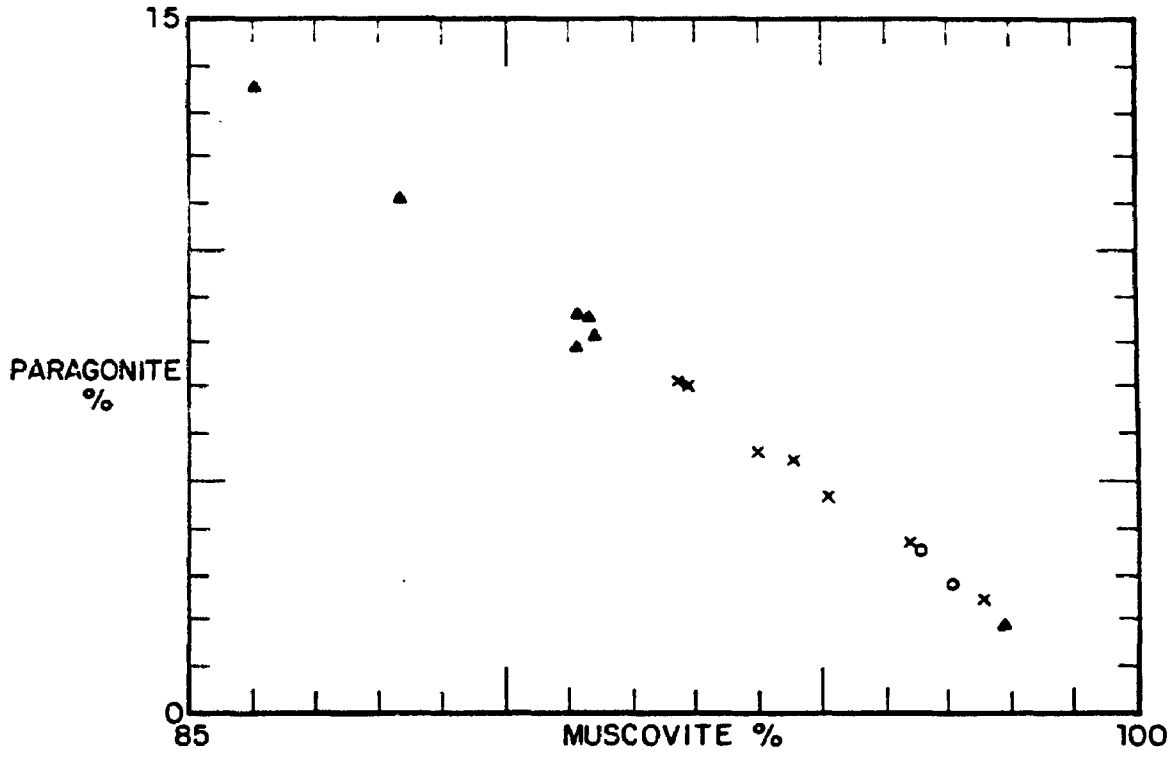

FIGURE 6.12. Chemical variation of muscovite expressed as end-members muscovite and paragonite, including: metagraywackes (triangles), quartzites (X), and albite-quartz vein (circles).

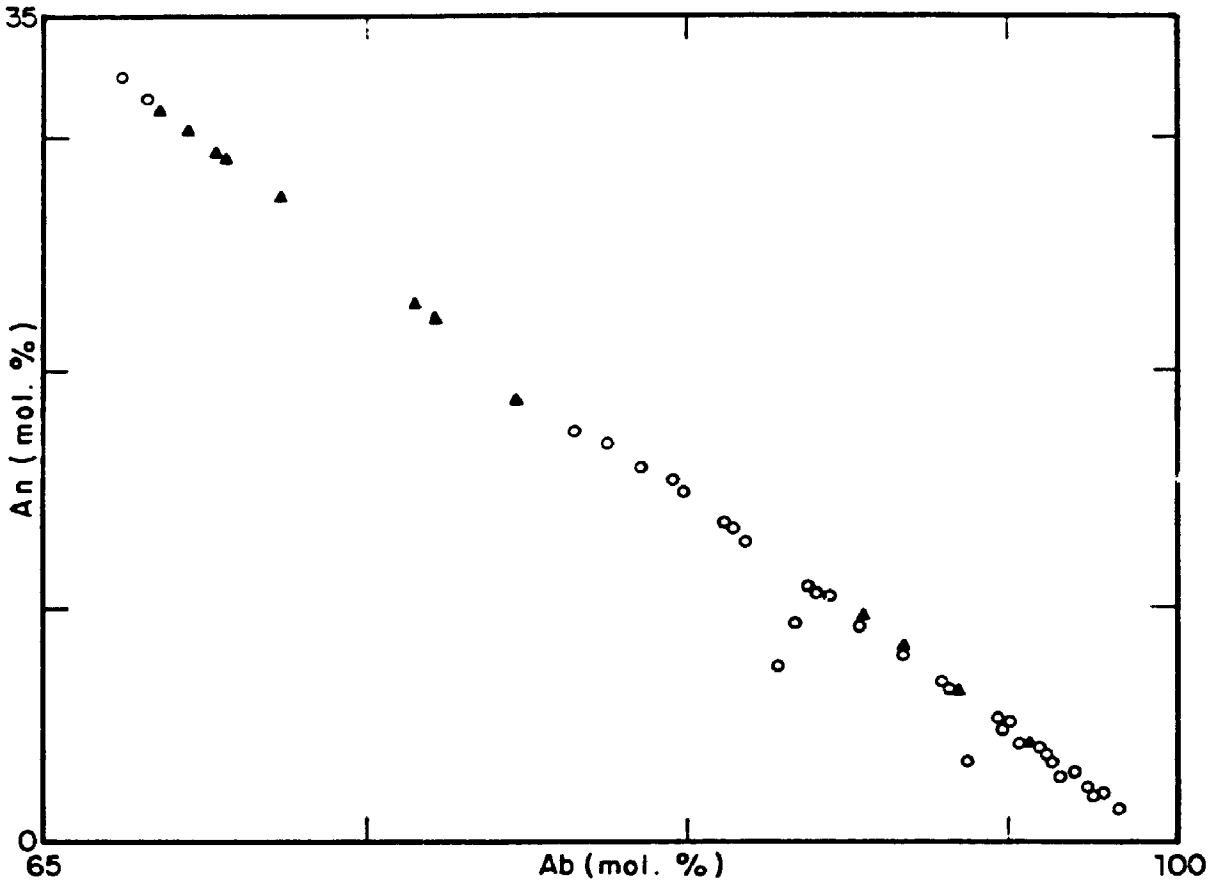

FIGURE 6.13. Chemical variation of plagioclase expressed as end-members albite and anortite, including analyses from gneisses (circles) and amphibolites (triangles).

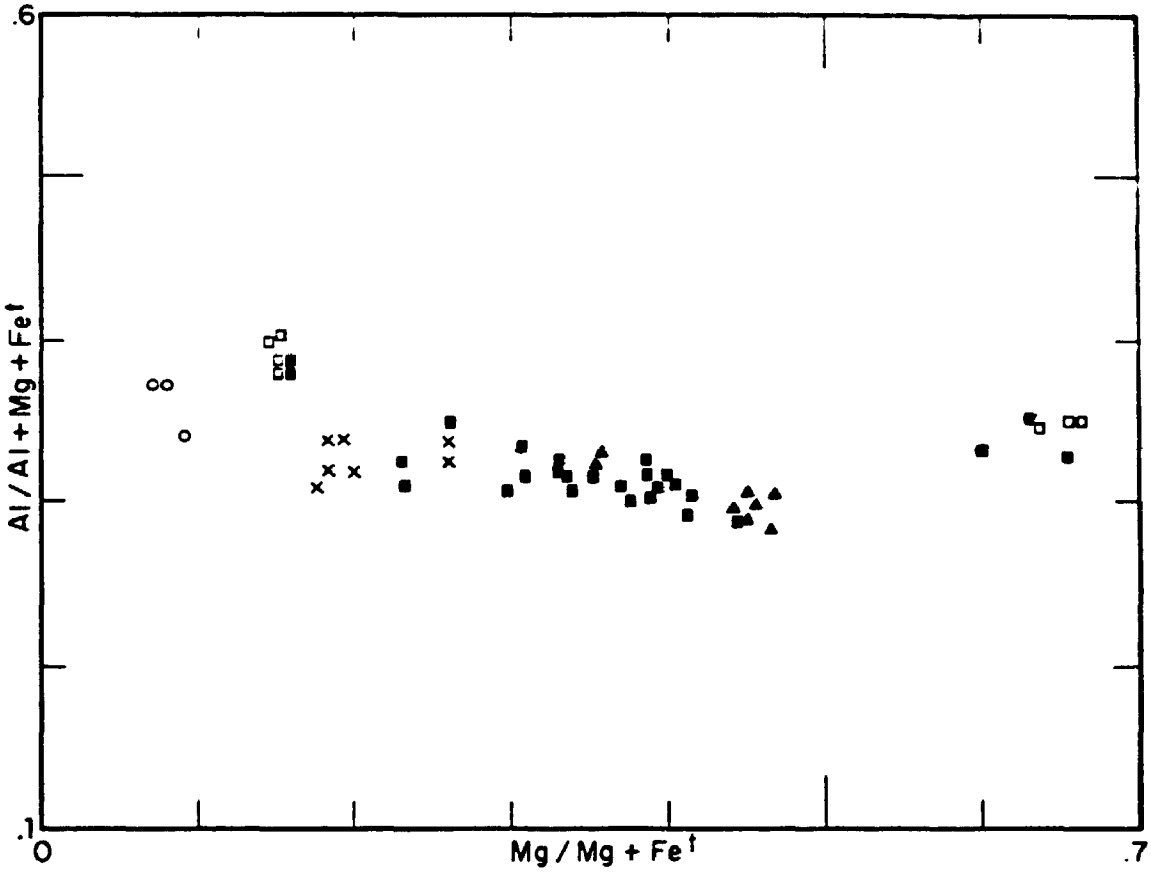

FIGURE 6.14. Al/Al+Mg+Fe versus Mg/Mg+Fe^t atomic ratios for chlorites from quartzites (circles), metagraywackes (hollow squares), iron formations (X), gneisses (solid squares) and amphibolites (triangles).

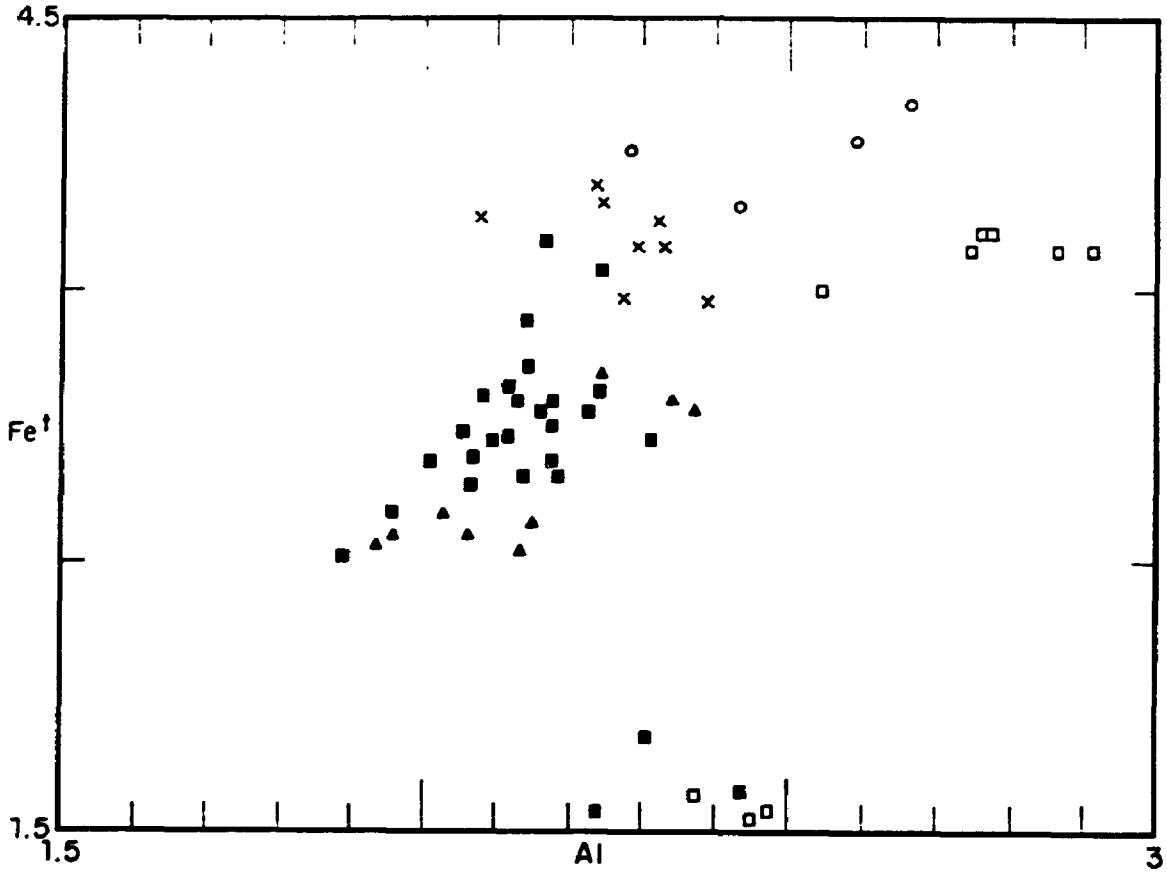

FIGURE 6.15. Al versus Fe^t for chlorites from quartzites (circles), metagraywackes (hollow squares), iron formation (X), gneisses (solid squares) and amphibolites (triangles).

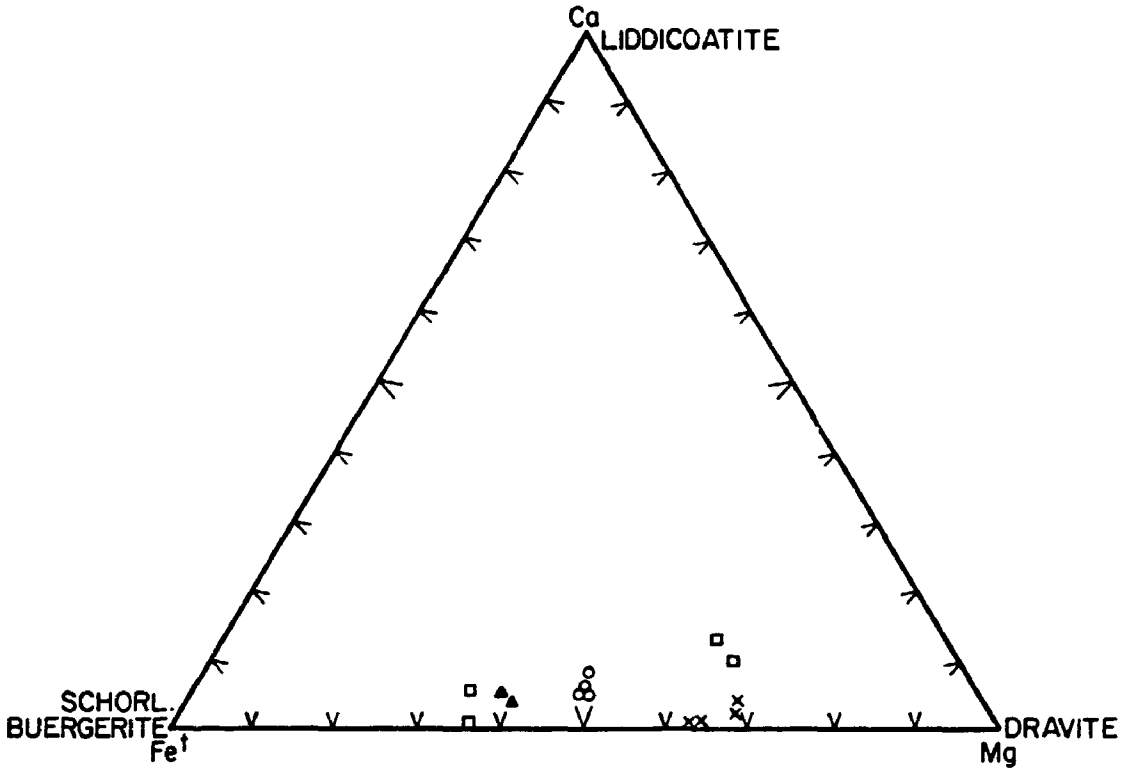

FIGURE 6.16. Ca-Fe^t-Mg molecular-proportion diagram for tourmalines from gneisses (x), amphibolite (circles), iron formation (triangles) and metagraywackes (squares).

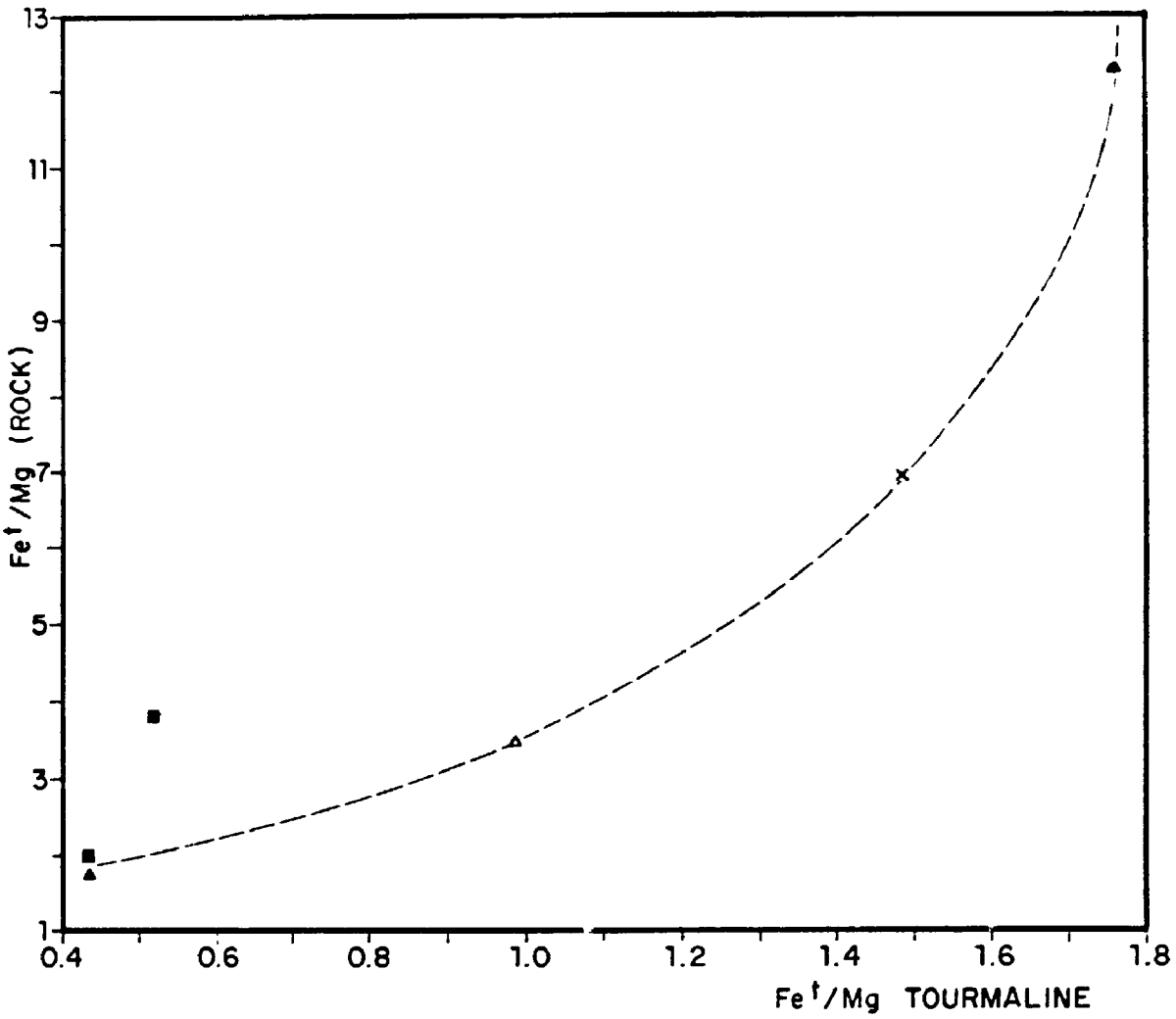

FIGURE 6.17. Fe^t/Mg ionic ratios of tourmalines and their host rocks. Gneisses (squares), amphibolite (hollow triangle), iron formation (X) and metagraywackes (solid triangles).

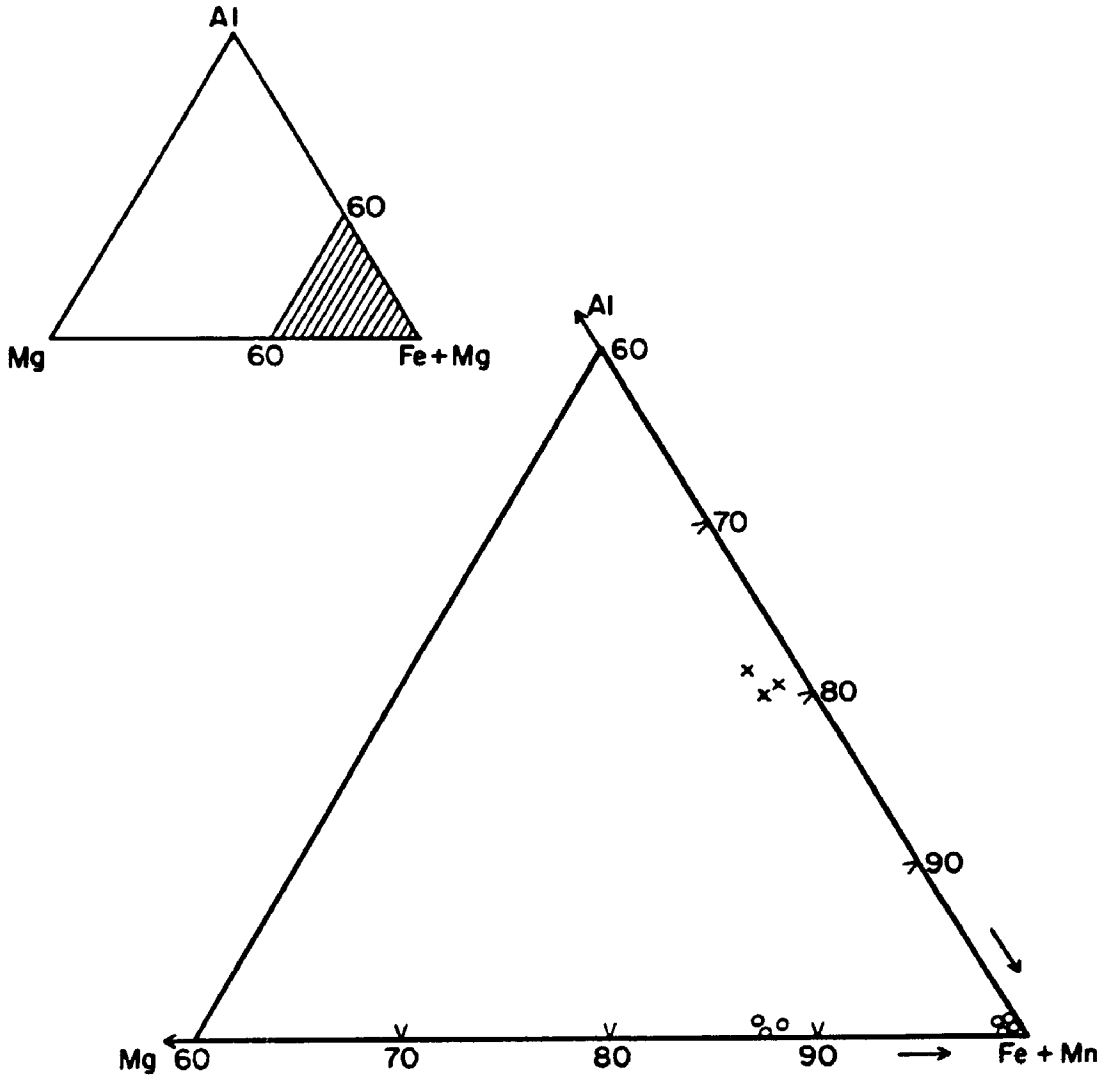

FIGURE 6.18. (Fe+Mn)-Mg-Al molecular proportions for greenalite (circles) and stilpnomelane (x).

CHAPTER 7

METAMORPHISM

7.1. Introduction

This chapter describes the metamorphic history of the study area based on geological, petrographic and geochemical data, previously presented and discussed in chapters 4 to 6.

7.2. Metamorphic events

The studied rocks show evidence of three successive metamorphic events: an older progressive episode followed by two younger retrogressive ones.

The first metamorphic episode is represented in rocks with granoblastic to hornfelsic textures, whereas the later two events are observed in foliated to mylonitic rocks.

The rocks formed during the first metamorphic episode occur as lens-shaped relicts, observed mostly close to the contact between the iron formation and the basement gneisses, although there are also high grade metamorphosed lenses near the Southern Shear Zone (SSZ).

The rocks affected by the second metamorphic event have extensive distribution in the study area and are observed from basement gneisses at north, to quartzites at south. They are characterized by two different textural types: foliated/schistose and protomylonitic. The first type dominates in amphibolites, iron formation, metagraywackes and quartzites, whereas the second is more frequently observed in the basement gneisses.

The third metamorphic episode is restricted to zones of intensive brittle deformation, the SSZ and surrounding rocks. It is represented in shear zones occurring mainly in quartzites, although it is also present in iron formation, metagraywackes, and basement gneisses.

In iron formations the characteristic mineral assemblages of the three metamorphic events are:

1st.- Fayalite (Fa 95-99%)-hastingsite-almandine garnet (Alm. 56-82% Spess. 12-32%)-magnetite$_q$-biotite$_q$ chalcopyrite$_q$ graphite.

2nd.- Grunerite-almandine-magnetite-biotite-quartz$_q$ bornite$_q$ chalcocite$_q$ graphite.

3rd.- Greenalite-chlorite-quartz.

The approximate proportion of rocks representing each one of the three metamorphic episodes in the iron formation is 10-15% of the first, 80-85% of the second and 5% of the third.

The three characteristic mineral assemblages in amphibolites are:

1st.- Hastingsite-plagioclase (An_{30})-magnetite-ilmenite$q$ biotite.

2nd.- Cummingtonite-plagioclase (An_{4})- magnetite-ilmenite-biotite-quartz.

3rd.- Chlorite-epidote-calcite-quartz-titanite.

The proportion of amphibolites representing the metamorphic events is about 5-10% (first), 80-85% (second) and 10-15% (third).

In basement trondhjemitic gneisses the representative mineral assemblages of the three metamorphic episodes are:

1st.-Plagioclase (An_{16-32})-quartz-hastingsite$q$ biotite$q$ magnetite.

2nd.-Plagioclase (An_{5-2})-quartz$q$ cummingtonite$q$ tourmaline$q$ biotite$q$ magnetite$q$ ilmenite.

3rd.-Albite-chlorite-quartz-epidote-calcite-magnetite-titanite.

The approximate proportion of rocks representing each one of the metamorphic events in trondhjemitic gneisses is: 5-10% (first), 80-85% (second) and 10-15% (third).

In metagraywackes and quartzites there are solely characteristic mineral assemblages of the second and third metamorphic episodes.

These two metamorphic events in metagraywackes are represented by the mineral assemblages listed below:

2nd.- Quartz-plagioclase (An_{21-65})-almandine (Alm.65%)q tourmaline$q$ cummingtonite$q$ sillimanite$q$ muscovite q magnetite$q$ ilmenite.

3rd.-Quartz-chlorite-muscovite.

About 80-85% of the metagraywackes are affected by the second metamorphic episode, whereas only about 15-20% show effects of the third one.

The representative mineral assemblages of the last two metamorphic events in quartzites are:

2nd. - Quartz-biotite-almandine-sillimanite-muscovite$_q$ tourmaline$_q$ plagioclase$_q$ K-feldspar$_q$ magnetite.

3rd. - Quartz-chlorite-muscovite-rutile.

The proportion of quartzites representing each metamorphic episode is about 60% of the second and 40% of the third metamorphic event.

7.3. Metamorphic Reactions

7.3.1. Introduction

The mineral reactions observed in thin sections (Chapter 4), representing the two retrometamorphic events of the study area will be presented here by means of molar chemical reactions, permitting an estimation of the fluid composition.

The coefficients of the molar reactions shown here correspond to the number of moles of each mineral involved in the reaction. This number of moles was obtained by dividing the modal percentage of each mineral by its respective molar volume (Table 7.1). The mineral

compositions presented in the reactions were obtained by electron microprobe analyses (Chapter 6). A detailed description of the methodology for writing the reactions is located in appendix B.

The reactions were written without taking into account changes in Fe oxidation state. It was also considered that the reactions took place in an Fe and Si saturated system.

Therefore, the molar reactions are semi-quantitative mass balance calculations of the chemical elements involved in mineral substitutions, petrographically observed.

7.3.2. Second metamorphic event

The second metamorphic event is defined in iron formations by the substitution of fayalite and hastingsite by grunerite; by biotite formation and by the disappearance of zoned garnet, with consequent formation of unzoned almandine. This episode is marked in gneisses and amphibolites by the albitization of plagioclase and by partial destruction of Ca-amphibole, with cummingtonite formation.

The molar reaction (1) representing the replacement of fayalite, hastingsite and Mn-zoned garnet by grunerite, biotite and almandine corresponds to sample 61-230-2 data (Tables 7.1 and 7.2).

$$0.65\ [(Fe_{1.99}Mg_{0.02}Mn_{0.01})SiO_4] +$$

$$0.05\ [(Na_{0.5}K_{0.18}Ca_{1.5})(Fe_{4.5}Mg_{0.24}Mn_{0.21})Si_8Al_{2.34}O_{22}(OH)_2]$$

$$+ 0.11[(Fe_{2.17}Mg_{0.024}Mn_{0.588}Ca_{0.273})Si_3Al_2O_{12}] + 0.017\ Mg^{2+} +$$

$$0.099\ K^+ + 0.752\ SiO_2 + 0.193\ H_2O + 0.154\ H^+ + 0.014\ O_2$$

$$<=>$$

$$0.2\ [(Fe_{6.73}Mg_{0.025}Mn_{0.22})\ Si_8Al_{0.04}O_{22}(OH)_2] +$$

$$0.03\ [(Fe_{2.62}Mg_{0.03}Mn_{0.09}Ca_{0.05})\ Si_3Al_{1.99}O_{12}] +$$

$$0.12\ [K_{0.9}(Fe_{2.4}Mg_{0.33}Mn_{0.033})\ Si_{2.85}Al_{2.46}O_{10}(OH)_2] +$$

$$0.013\ Fe_3O_4 + 0.028\ Mn^{2+} + 0.025\ Na^+ + 0.103\ Ca^{2+} \qquad (1)$$

Or, simplifying:

13 fayalite + 1 hastingsite + 2 garnet I + 2 K^+ + 15 SiO_2 + 0.3 Mg^{2+} + 4 H_2O + 3 H^+ + 0.3 O_2 <=> 4 biotite + 1 grunerite + 2 garnet II + 0.3 magnetite + 0.5 Mn^{2+} + 0.5 Na^+ + 2 Ca^{2+} (1a)

The silicification reaction (2) observed in gneisses, producing the albitization of plagioclase and cummingtonite after hastingsite, is theoretical because it is impossible to determine the modal percentage of albite and oligoclase in the same thin section.

$$[NaCa_2(Fe_{2.5}Mg_{2.5})\ Si_8Al_2O_{22}(OH)_2] + 8\ SiO_2 + Na^+ + 4.5\ Mg^{2+}$$

$$+ 3\ H_2O + 0.16\ O_2 \quad <=>$$

$$[Mg_7Si_8O_{22}(OH)_2] + 2\ NaAlSi_3O_8 + 0.83\ Fe_3O_4 + 2\ Ca^{2+} + 6\ H^+ \qquad (2)$$

Or, simplifying:

1 hastingsite + 8 SiO_2 + Na^+ + 4.5 Mg^{2+} + 3 H_2O + 0.1 O_2 <=> 1 cummingtonite + 2 albite + 1 magnetite + 2 Ca^{2+} + 6 H^+ (2a)

Reaction (1) shows that the fluid originating the mineral assemblage of the second metamorphic event in iron formation was acidic and slightly oxidizing. It was also Si and K saturated, being responsible for a strong silicification, along with biotite formation. Roughly 50% of K necessary to form biotite came from Ca-amphibole and 50% from external source, indicating K mobility during this event. There was also a significant Ca, along with a slight Mn and Na leaching. The amount of introduced Mg is insignificant and may be credited to local compositional variations of Fe-Mg bearing minerals.

Reactions (1) and (2) are analogous as far as silicification and Ca leaching are concerned. It is not possible to make a detailed comparison between them because reaction (2) is theoretical.

In metagraywackes the reaction of biotite and sillimanite forming muscovite and tourmaline is observed. This is a late reaction in the second metamorphic episode, what is shown by the outer rims of tourmaline inclusions in garnet II crystals (Chapter 4).

The molar reaction (3) representing the replacement of biotite and sillimanite by muscovite and tourmaline corresponds to the data of sample 17-350-7 (Tables 7.1 and 7.2).

$$0.54\ [K_{0.8}(Fe_{2.2}Mg_{0.47})Al_{1.7}Si_{2.58}O_{10}(OH)_2] + 0.383\ Al_2SiO_5 + 0.21\ BO_3^{3-} + 0.03\ Na^+ + 0.05\ Ca^{2+} + 1.034\ H^+ + 0.235\ O_2$$

<=>

$0.07\ [(Na_{0.43}Ca_{0.08})(Mg_{0.8}Fe_{1.4})\ Al_{6.7}Si_{5.8}\ O_{18}(BO_3)_3\ (OH)_4]$

$+\ 0.45\ [K_{0.85}Na_{0.1}Al_{2.7}\ Si_3O_{10}\ (OH)_2] + 0.36\ Fe_3O_4 + 0.05\ K^+$

$+\ 0.197\ Mg^{2+} + 0.009\ SiO_2 + 0.467\ H_2O$ (3)

Or, simplifying:

8 biotite + 5 sillimanite + 3 BO_3^{3+} + 0.4 Na^+ + 0.1 Ca^{2+} +

+ 15 H^+ + 3 O_2 <=> 1 tourmaline + 6 muscovite + 5 magnetite

+ 0.5 K^+ + 3 Mg^{2+} + 7 H_2O (3a)

Reaction (3) shows volatile substitution with H_2O being replaced by BO_3. It demonstrates that the fluid penetrating metagraywackes was oxidizing and extremely acidic, boron-bearing and with a Ca/Na ratio of 0.25. There was also Mg and K leaching (6 Mg to 1 K).

In summary, reaction (1) shows that the second metamorphic event is retrometamorphic and corresponds to a hydrothermal alteration. The fluids percolating the iron formation produced hydration of an almost anhydrous metamorphic assemblage. The fluid responsible for the second metamorphic event was acidic and slightly oxidizing, as can be observed in reactions (1), (2) and (3). This event is characterized by strong silicification and Ca leaching.

7.3.3. Third metamorphic event

The third metamorphic event corresponds to chloritization occurring in localized zones of intensive ductile deformation. The chloritization is observed in all

rock types of the study area. In iron formation greenalitization predominates over chloritization.

The molar reaction (4) representing the replacement of fayalite and grunerite by greenalite was written based on sample 49-351-4 data (Tables 7.1 and 7.2).

$$0.66\ [(Fe_{1.7}Mg_{0.1}Mn_{0.02})\ SiO_4] + 0.15\ [(Fe_{4.8}Mg_{2.0}Mn_{0.08})\ Si_8O_{22}(OH)_2 + 0.23\ Fe_3O_4 + 0.38\ SiO_2 + 0.003\ Mn^{2+} + 1.493\ H_2O + 0.335\ O_2 + 1.194\ H^+ \ <=>$$
$$0.56\ [(Fe_{4.8}Mg_{0.85}Mn_{0.05})\ Si_4O_{10}\ (OH)_8] + 0.6\ Mg^{2+} \qquad (4)$$

Or, simplifying:

$$4\ \text{fayalite} + 1\ \text{grunerite} + 1.5\ \text{magnetite} + 2.5\ SiO_2 + 10\ H_2O + 2\ O_2 + 8\ H^+ <=> 4\ \text{greenalite} + 4\ Mg^{2+} \qquad (4a)$$

The replacement of almandine and biotite by chlorite corresponds to reaction (5), which was written based on data of sample 56-280-5 (Tables 7.1 and 7.2).

$$0.2\ [(Fe_{2.0}Mg_{0.07}Mn_{0.57}Ca_{0.17})\ Al_{1.8}Si_3O_{12}] + 0.26\ \{K_{0.8}(Fe_{2.5}\ Mg_{0.48})\ Al_{1.3}Si_3O_{10}\ (OH)_2 + 0.091\ Mg^{2+} + 0.002\ Fe_3O_4 + 0.726\ H_2O + 0.348\ H^+ \ <=>$$
$$0.29\ [(Fe_{3.6}Mg_{0.8})(Al_{2.3}\ Si_3O_{10})(OH)_8] + 0.234\ K^+ + 0.034\ Ca^{2+} + 0.114\ Mn^{2+} + 0.29\ SiO_2 + 0.877\ O_2 \qquad (5)$$

Or, simplifying:

$$1\ \text{garnet} + 1.5\ \text{biotite} + 3.5\ H_2O + 2\ H^+ + 0.5\ Mg^{2+} \ <=> 1.5\ \text{chlorite} + 1.5\ SiO_2 + 1\ K^+ + 0.15\ Ca^{2+} + 5\ Mn^{2+} + 4\ O_2 \qquad (5a)$$

In quartzites chlorite-muscovite intergrowths with inclusions of rutile needles are observed, replacing biotite

and sillimanite. (Chapter 4). This substitution corresponds to molar reaction (6), written with the data of sample 20-221 (Tables 7.1 and 7.2).

$$0.5\ [K_{0.9}(Mg_{0.95}Fe_{2.2}Ti_{0.06})\ Si_{2.56}Al_{1.181}O_{10}(OH)_2] +$$
$$0.4\ [Al_2\ SiO_5] + 0.073\ Fe_3O_4 + 0.495\ SiO_2 + 0.472\ H_2O +$$
$$1.082\ H^+ \quad <=> \quad 0.203\ [K_{0.9}Al_{2.8}Si_3\ O_{10}\ (OH)_2] +$$
$$0.33\ [(Fe_4Mg_{0.34}Ti_{0.02})\ Si_{2.88}Al_{2.49}O_{10}(OH)_2] +$$
$$0.026\ TiO_2 + 0.268\ K^+ + 0.407\ Mg^{2+} + 0.663\ O_2 \qquad (6)$$

Or, simplifying:

2.5 biotite + 2 sillimanite + 0.35 magnetite + 2.5 SiO_2 + 2.4 H_2O + 5.4 H^+ <=> 1 muscovite + 1.5 chlorite + 0.1 rutile +1 K^+ + 2 Mg^{2+} + 3 O_2 (6a)

Reaction (6) is analogous to reaction (13) described by Miyashiro and Shido (1984) defining the biotite isograd. It is also analogous to the the reaction defining the same isograd in low-pressure metamorphic series of Japan proposed by Wang et al., (1986). But, as opposed to the progressive reactions presented by the authors above, reaction (6) is regressive.

The replacement of hastingsite by chlorite commonly observed in gneisses and amphibolites, corresponds to the theoretical reaction (7) below:

$$[NaCa_2(MgFe)_5Si_6Al_2O_{22}(OH)_2] + 0.5\ H_2O + 5\ H^+ \quad <=>$$
$$[(FeMg)_5Si_3Al_2O_{10}(OH)_8] + Na^+ + 2\ Ca^{2+} + 3\ SiO_2 + 0.25\ O_2$$
$$(7)$$

Or. simplifying:

1 hastingsite + 0.5 H_2O + 5 H^+ <=> 1 chlorite + Na^+ + 2 Ca^{2+} + 3 SiO_2 + 0.25 O_2 (7a)

Reaction (4) shows that the fluid, which formed greenalite in the iron formation was acidic and oxidizing, whereas reactions (5), (6) and (7) demonstrate that the fluid responsible for chlorite formation was acidic. Quartz produced by the chloritization of Fe-Mg minerals is in accordance with the close association of chlorite and quartz observed in thin sections. Ca, Na, K and Mn are leached during the third metamorphic event. Mg introduction or leaching depends on the chemical composition of the mineral assemblage involved. The chlorite-producing reactions yield oxygen-rich fluids.

7.4. Geothermometry and geobarometry

7.4.1. Introduction

Geothermometers and geobarometers were applied to samples with mineral assemblages representative of each one of the metamorphic events.

The garnet-hornblende (Graham and Powell, 1984), garnet-biotite (Ferry and Spear, 1978) and biotite-muscovite (Hoisch, 1989) geothermometers and the garnet-plagioclase geobarometer (Ghent,1976) were applied.

Microprobe analyses of mineral pairs used in calculations were always carried out in minerals with sharp and direct contacts. The rims of zoned garnets were analyzed for garnet-biotite geothermometer calculations, whereas the cores of zoned garnet with inclusions of hastingsite were analyzed for the garnet-hornblende geothermometer.

Mineral analyses are in tables 7.3 to 7.9 and the summary of temperatures and pressure are in tables 7.10 and 7.11.

7.4.2. Geothermometry

a) First metamorphic event

The temperature of the first metamorphic event was obtained by the application of garnet-hornblende Fe-Mg exchange geothermometer calibrated by Graham and Powell (1984). The analyzed mineral pairs (hastingsite-garnet I) are in coarse granoblastic iron formation composed of fayalite-hastingsite-garnet I-magnetite.

Calculations were performed by using the equation below, empirically calibrated by Graham and Powell (1984).

$$T^{o}(K) = 2880 + 3280X_{Ca\ gn} / \ln K_D + 2.426$$

Were: $X_{Ca\ gn}$ = Ca molar proportion in garnet

$$K_D = (X_{Fe\ gn} / X_{Mg\ gn}) / (X_{Fe\ hb} / X_{Mg\ hb})$$

Three mineral pairs analyzed in two different samples yielded the temperatures of 738, 742 and 767°C (Table 7.10), with an average of 750°C which corresponds to the maximum temperature attained by the iron formation during the progressive metamorphic event.

b) Second and third metamorphic events

Two different geothermometers, garnet-biotite geothermometer calibrated by Ferry and Spear (1978) and biotite-muscovite geothermometer calibrated by Hoisch (1989) were applied and three groups of samples were analyzed: a) foliated metagraywacke composed of quartz-biotite-garnet-plagioclase-muscovite-tourmaline-sillimanite, b) mylonitic iron formation made up of garnet-biotite-grunerite-quartz and c) greenalitized iron formation.

The equation empirically calibrated by Ferry and Spear (1978) is:

$$\ln K = -2109 / T(^{\circ}K) + 0.782$$

where:

$$K = (Mg/Fe)_{gn} / (Mg/Fe)_{biot}$$

The equation empirically calibrated by Hoisch (1989), corresponding to a geothermometer based on the exchange of Mg-Tschermak's component between muscovite and biotite, is:

$$T = \frac{500.110 + 0.0147890P - 878.745(X^{B}_{Mg} - X^{B}_{[6]Al}) - 4532.67[X^{M}_{Mg}(X^{M}_{Mg} - 2)]}{1 + 0.0237527\ R\ \ln K}$$

Where: P is pressure in bars

T is Kelvin temperature

R = 8.3144 J/K

X_q^m = mole fraction q in the octahedral site for mineral m (M muscovite, B biotite)

$K = 27[(Mg/[^6]Al)^M / (Mg/[^6]Al)^B]$

Note: the pressure used in these calculations were obtained by applying the garnet-plagioclase geobarometer (Ghent, 1976), presented in the next item.

As expected, the application of these geothermometers yielded three groups of temperatures (Tables 7.10 and 7.11).

The highest temperature of 650°C corresponds to the second metamorphic event and was obtained in the foliated metagraywacke. The temperature of 550°C yielded by the mylonitic iron formation, probably reflects the ductile event which took place late in the second metamorphic episode. The lowest temperature of 370°C, obtained in the greenalitized rock, represents the last metamorphic event.

7.4.3. Geobarometry

a) First metamorphic event

Pressure estimate

Ca-amphiboles in the study area occur in mineral assemblages defining the first metamorphic event. In these minerals the edenitic $[(Na^A+K),Al^{iv}[],Si]$ and tschermakitic substitutions $[(Al^{vi}+Fe^{3+}+Ti+Cr), Al^{iv} (Fe^{2+}+Mg+Mn), Si]$ predominate over the glaucophanitic ones $[(Na^{M4}$,

$(Al^{vi}+Fe^{3+}+Ti+Cr)$ Ca, $(Fe^{2+}+Mg+Mn)$] as may be observed in figures 7.2 to 7.5.

This feature, according to Liou et al.,(1974), Laird and Albee (1981) and Moody et al., (1983) characterizes low pressure metamorphic terranes as in the Abukuma region of Japan, whose amphiboles plot in the same field of Salobo Ca-amphiboles.

Pressure may be estimated at 2 to 3 kbar by comparing the mineral assemblage of the study area with the isobaric diagrams of phase relations f_{O_2} -T, calculated by Miyano and Klein (1983) (Figures 7.6 and 7.7).

b) Second metamorphic event

The metagraywackes are the only rock type of the study area displaying mineral associations suitable for application of presently existing calibrated geobarometers.

The garnet-plagioclase geobarometer, empirically calibrated by Ghent (1976), was applied to the same metagraywacke sample, composed of quartz-biotite-garnet-tourmaline-plagioclase-sillimanite-muscovite, where the temperature of 650°C was determined.

The equation (Ghent, 1976) for sillimanite-plagioclase-garnet-quartz bearing-rocks is:

$$0=[-3272 / T°C] + 8.3969 - [0.3448\ (P-1)/T°C] + \log KD$$

where:

$$\log KD = 3 \log X_{Ca_3Al_2Si_3O_{12}}^{(garnet)} - 3 \log X_{CaAl_2Si_2O_8}^{(plagioclase)}$$

The calculation yielded 2.6 kbar, as the pressure for the second metamorphic episode.

7.5.Discussion

7.5.1. First metamorphic event

The mineral assemblage of the iron formation, consisting of fayalite-garnet I-hastingsite-magnetite qbiotiteqgraphite in rocks with granoblastic to hornfelsic textures, represents the highest metamorphic grade attained by the rocks of the study area. This metamorphic mineral assemblage is indicative of high temperature (Miyano and Klein, 1983), which is in accordance with the determined temperature of 750°C and compatible with the pyroxene hornfels metamorphic facies. On the other hand, the estimated low- metamorphic pressure agrees with the presence of hornfelsic textures.

This metamorphic event is progressive as indicated by: chemical zoning of garnet, where Mn-Ca enriched-cores have higher crystallization temperatures than the Fe-Mg enriched-rims, such as described by Laird and Albee (1981) and Tracy (1982); association of this garnet with fayalite, magnetite and hastingsite forming an almost anhydrous mineral assemblage.

The crystallization sequence of these minerals is suggested by the position of hastingsite inclusions in garnet, where the former is distributed mid-way between core and rim, indicating that garnet started forming before

hastingsite. It is further confirmed by higher X_{Fe} in garnet (0.2 to 0.02) than in hastingsite (0.0022 to 0.0085). In addition to that, Mn enrichment in garnet cores indicates that garnet formed before hastingsite and also that P_{H2O} was very low. According to Hall (1985) Mn has a preference for being incorporated in pyroxene, hornblende or garnet, in this order. Thus, the formation of an anhydrous mineral, such as garnet before hastingsite indicates a very low P_{H2O}.

The predominance of Fe^{2+}-bearing minerals in the studied mineral association, along with the presence of graphite, suggest that this metamorphic episode took place under low oxygen fugacity, in accordance with the absence of coexisting quartz and fayalite. This also suggests that the oxygen fugacity conditions, prevailing during this metamorphic event, were compatible to those defined by the QFM buffer (Figure 7.6).

Similar assemblages occur under dry conditions and high temperatures, such those of contact metamorphism (Miyano and Klein, 1983).

Despite being metamorphosed at conditions close to the pyroxene hornfels facies, Salobo iron formation does not show pyroxene. In high grade metamorphosed iron formations (high T - low P), such as Mesabi Range (USA), Biwabik (USA-Canada) and Gunflint (Canada),(Bonnichsen, 1975; Miyano and Klein, 1983; Floran and Papike, 1978 and Gole and Klein, 1981), the presence of fayalite or pyroxene is principally determined by pressure, chemical composition of the host

rock and oxygen fugacity. Fayalite is favored over pyroxene under conditions of high Fe/Fe+Mg ratios, low pressure and low oxygen fugacity (Haase, 1982; Miyano and Klein, 1983), characteristic of the study area.

The mineral assemblage of granoblastic amphibolites, composed of Ca-amphibole, Ca-plagioclase and ilmenite, is also typical of progressive metamorphism of rocks of basaltic composition, according to Miyashiro, 1972 and Winkler, 1976.

Therefore, the first metamorphic episode took place at low pressure, high temperature and under low oxygen fugacity. It was also shown that the iron formations display mineral assemblages and textures analogous to contact metamorphosed iron formations, such as Biwabik (USA-Canada) and Gunflint (Canada) (Miyano and Klein, 1983). However, in Salobo there is not an intrusion responsible for such metamorphism, as opposed to the areas mentioned. But, if is taken into account the rift-related tectonic setting of Carajas, with voluminous flood basalts (Gibbs et al., 1986) where the Salobo sequence is, it is possible to suggest that magma underplating could have originated a high heat flow, where this thermal metamorphic event could have developed (see discussion in chapter 8).

7.5.2. Second metamorphic event

The second metamorphic event, or first hydrothermal episode, is marked by fluid penetration and hydration of previously dehydrated mineral assemblages.

This episode is characterized in iron formation by pseudomorphic substitution of fayalite and hastingsite by grunerite, biotite formation and by the appearance of fine unzoned-almandine, giving place to foliated/schistose to protomylonitic rocks composed of grunerite-almandine-magnetite-biotite-quartz. The textures of the rocks formed during this metamorphic episode indicate that fluid penetration took place under conditions of shearing stress.

Fluid/rock ratios may have been remarkably high during this episode, because the hydrated minerals formed, such as grunerite and biotite, show chemical composition (expressed in X_{Fe}) restricted to a very narrow interval (grunerite 0.505-0.559, biotite 0.439-0.489). This indicates that the formation of these hydrated minerals took place under the influence of an externally controlled fluid source, as observed by Frost (1982) in the iron formation of Montana (USA). The same feature is not observed in garnet II, which is the anhydrous mineral characteristic of this episode, whose chemical composition is strongly controlled by that of the host rock (X_{Fe} 0.02 to 0.2).

The distinct mineral assemblage of the second metamorphic event in metagraywackes, consisting of quartz-biotite-garnet-plagioclase-tourmaline-sillimanite-

cummingtonite+magnetite+ilmenite, is equivalent to the assemblages formed either in the iron formation or in gneisses and amphibolites, during the same metamorphic event.

The lack of vestiges of the first metamorphic episode in metagraywackes is probably due to high intensity of the second metamorphic event in these rocks. Nevertheless, evidences of the first episode are observed from base to top of the iron formation-metagraywacke unit.(See figure 3.1 and tables 4.1 and 4.2).

7.5.3. Temperature and Pressure

The temperature of 750°C was obtained through the application of garnet-hornblende geothermometer to three analyzed mineral pairs in iron formation, displaying granoblastic texture and mineral assemblage representative of the first metamorphic event (garnet-fayalite-hastingsite-magnetite+biotite).

This value is in the temperature range of iron formations exhibiting mineral assemblages analogous to that of Salobo, and which were also submitted to thermal metamorphism (Montana (USA)- 830°C (Vaniman et al., 1980) and Biwabik (USA-Canada) 650-750°C (Bonnichsen, 1975)).

As it was seen in chapter 6, Fe^t/Fe^t+Mg ionic ratios in iron-formation garnets and their host rocks show good positive correlation, indicating equilibrium.
Fe^t/Fe^t+Mg ionic ratios of amphiboles and their host rocks

do not present correlation, indicating disequilibrium between them.

Analyzed mineral pairs show microscopic features of textural equilibrium, along with chemical equilibrium relationships between garnet and host rocks. Besides, as 750°C temperature is compatible with similar world-wide iron formation mineral assemblages, one is led to assume that 750°C is the maximum temperature attained by iron formation during progressive metamorphism.

Granoblastic gneisses and amphibolites, with mineral assemblages composed of Ca-amphibole, Ca-plagioclase and ilmenite (plus quartz in the gneisses), indicate that these rocks were also submitted to a high temperature and low pressure metamorphism, as well as the iron formation.

The lack of epidote, associated with the presence of ilmenite instead of titanite, implies a metamorphic temperature higher than 500-550°C (Liou et al., 1974; Moody et al., 1983), since titanite coexists with ilmenite up to 500-550°C, under oxygen fugacity conditions compatible with either IM or HM buffer. On the other hand, epidote is stable up to 600°C under oxygen fugacity defined by the QFM buffer, which seems to represent the prevailing conditions in amphibolites during the first metamorphic episode, as indicated by their mineralogy.

The upper stability of Ca-amphiboles, established by Spear (1981) at f_{O_2}=QFM, is 768q8°C at 1 kbar and 788q2°C at 2 kbar. Moreover, high Ti, Al and Na contents in Ca-

amphiboles, as well as high Ti content in biotites, also indicate high metamorphic temperatures (Leake, 1965; Raase, 1974; Spear, 1981), as observed in gneisses and amphibolites of the study area. Therefore, the data suggest that amphibolites and gneisses attained a temperature higher than 600°C during the first metamorphic episode but, based on experimental data on Ca-amphiboles stability, it is possible that they had attained the same temperature as did the iron formation: 750°C.

If the basement gneisses attained a temperature of 750°C they should have undergone partial melting (Fyfe, 1987). The percentage of this possible melt should also have been function of pressure and of the amount of water available in the system (Brown and Fyfe, 1970; Fyfe, 1987). Then it is possible to speculate that trondhjemitic rocks, if they were originally water poor, at low pressure would yield a very small percentage of melt.

Common physical evidence for partial melting are migmatites (Fyfe, 1987). The lack of migmatitic structures or quartz-feldspar deformed veins in the trondhjemitic gneisses seems to suggest that, if there was melt, the granitic component was separated from the gneisses, and these rocks, as they are observed today, would correspond to a melting residue. If so, the granitic bands intercalated with trondhjemitic gneisses could represent the crystallization product of this possible melt.

By any means, trondhjemitic gneisses should probably have undergone a small degree of partial melt, if they attained the same temperature as did the iron formation. However, the lack of data does not permit further speculations about its possible partial melt.

The temperature of 650°C was obtained through the application of the garnet-biotite and biotite-muscovite geothermometer on the same metagraywacke sample, where two garnet-biotite pairs (average temperature 643°C) and one muscovite-biotite pair (652°C) were analyzed.

It was shown in chapter 6 that Al^{vi} and Ti contents in metagraywacke biotites indicate that these minerals equilibrated (or reequilibrated) at the same temperature as did the mineral assemblages of their host rocks. On the other hand, garnets in metagraywackes also show equilibrium relationships with their host rocks.

Therefore, despite the small number of analyzed mineral pairs, the coincidence of values obtained through two different geothermometers, along with the equilibrium relationships presented by the analyzed minerals and their host rocks, indicate 650°C as the representative temperature of the second metamorphic or first hydrothermal event.

The temperature of 650°C determined for the second metamorphic event is coincident with the upper stability temperature of muscovite (640*q*10°C), experimentally determined by Day (1973) for $P_{H_2O} = P_{fluid} = 2$ kbar. However, this is the highest of the experimentally

determined temperatures for the upper stability limit of muscovite, since most experiments showed temperatures between 600 and 620°C (Evans, 1965; Kerrick, 1972). Nevertheless, the incipient muscovitization observed in metagraywackes (w 1-3% modal proportion), related to retrogressive metamorphism due to penetration of very acidic fluids, seems to show that muscovite was forming near its upper stability temperature.

A temperature of 625-675°C was estimated for Salobo grunerites (70-99 mole % $Fe_7Si_8O_{22}(OH)_2$), using the condensed T-X section of the phase diagram, defined by the QFM buffer and P_{Total}= 2 kbar (Popp et al., 1977). This temperature is also in accordance with that determined by geothermometry calculations.

In gneisses and amphibolites the second metamorphic event is principally represented by albitization of plagioclase. Albitization without concomitant epidote formation, along with partial substitution of hastingsite by cummingtonite (associated to ilmenite as the only Ti phase), indicate that this process took place at high temperature, compatible with amphibolitic facies rocks. According to experimental data from Liou et al., (1974) and Moody et al., (1983) either titanite or epidote are stable in metabasite up to a temperature of 500-550°C. Above this temperature ilmenite is the only stable Ti phase and epidote reacts with albite and quartz to produce calcic plagioclase (Miyashiro, 1973; Winkler, 1977;Liou et al., 1974; Moody et al., 1983).

Therefore, it can be inferred that albite and grunerite formation took place at a temperature higher than 550°C, possibly as high as 650°C.

The temperature of 550°C was obtained by garnet-biotite geothermometry calculations in mylonite-textured metagraywackes and iron formations.

It was seen in chapter 6 that either biotites or garnets show chemical equilibrium relationships with their respective host rocks. This chemical feature, along with the mylonitic textures and the mineral assemblages presented by the analyzed rocks (quartz-biotite-garnet-grunerite ±tourmaline), indicate that 550°C reflects the ductile deformation which occurred late in the second metamorphic event, still under conditions within amphibolitic facies.

The temperature of 370°C was determined in an iron formation sample, where 5% of fayalite and hastingsite are replaced by greenalite and chlorite, respectively. The equilibrium relationships presented by garnet and biotite and their respective host rocks (chapter 6) suggest that this temperature represents the third metamorphic event, reflecting a possible reequilibration between garnet and biotite during this metamorphic episode.

The low percentage of greenalite+chlorite (5%) suggests that 370°C reflects the maximum temperature for this event, which is in the transition zone between amphibolite and greenschist facies. This is consistent with the transition temperature between greenschist and

amphibolite facies, experimentally determined in metabasalts by Moody et al. (1983) and Liou and al. (1974).

The analyzed mineral pairs yielding this temperature are about 2 cm apart from the analyzed garnet-hastingsite pairs which produced 750°C. As seen above, both temperatures are consistent either with the Salobo mineralogy or with data in the literature, leading to the conclusion that the diffusion rates of Fe and Mg in these rocks during the last metamorphic event should have been restricted to zones of shearing.

In the SSZ where chloritization was intense, the temperature should have been lower and compatible with greenschist facies.

The first metamorphic event took place under low pressure (2-3 kbar), which is indicated by the mineralogy (compared to the data presented by Miyano and Klein (1983), hornfelsic texture and by the predominance of edenitic and tschermakitic substitutions over glaucophanitic ones, in Ca-amphiboles.

These data, along with the calculated pressure of 2.5 kbar for the second metamorphic event, suggest that the pressure conditions were maintained during the first and second metamorphic episodes. Thus, both events took place at about 8.5 km depth. The thermal gradient was 85°C/km for the first and of 75°C/km for the second metamorphic episode. In other words, under high heat flow regime.

7.5.4. Estimate of oxygen fugacity conditions

The highest temperature assemblage of the iron formation, composed of fayalite (almost pure end member), almandine, hastingsite and magnetite, indicate that these rocks were formed under very low oxygen fugacity conditions, compatible with those defined by the QFM buffer.

According to experimental data hastingsite is stable at 750°C (QFM buffer, $P_t = P_{tot} = 1500$ bars) up to log $f_{O_2} = -18$ (Thomas, 1982) and the association fayalite-magnetite-hastingsite, at the same conditions above, is stable up to log $f_{O_2} = -22$ (Ferry and Burt, 1982). These data constrain the oxygen fugacity in the first metamorphic event to the interval of log $f_{O_2} = -18$ to -22.

The silicate mineral assemblages formed in the iron formation during the second metamorphic event (reaction 1) s gest that oxidation was minor. This is confirmed by transformation of chalcopyrite into bornite according to the reaction:

$$15\ CuFeS_2 + 8\ O_2 \iff 3\ Cu_5FeS_4 + 4\ Fe_3O_4 + 9\ S_2$$

Thus, this episode is still compatible with conditions defined by the QFM buffer, where grunerite (the dominant mineral of this episode in Salobo iron formation) attains its maximum thermal stability Forbes (1977). Grunerite, according to Miyano and Klein, (19832) and Popp et al., (1977), is stable at log $f_{O_2} = -18$ to -19 at QFM buffer, 650°C and 2.5 kbar. Therefore, this oxygen fugacity may be

considered as representative of this event in the iron formation.

The oxygen fugacity during the second metamorphic episode in amphibolites was also low, what is demonstrated by ilmenite composition, where molecular proportion of the component $FeTiO_3$ (0.95) indicates (according to experimental data from Spear (1981)) crystallization under oxygen fugacity conditions compatible with QFM buffer.

The third metamorphic episode took place under more oxidizing conditions than the previous ones. This is shown by: reaction (4), epidote and rutile formation, disappearance of graphite, and replacement of bornite by chalcocite, according to the oxidation reaction:

$$2\ Cu_5FeS_4 + 4/3\ O_2 \iff 5\ Cu_2S + 2/3\ Fe_3O_4 + 1\ 1/2\ S_2$$

7.5.5. Fluid compositions

The composition of fluids, originating the mineral assemblages formed in each metamorphic event, is discussed below, taking into account the mineral compositions in the studied assemblages and the semi-quantitative mass balance calculation.

The first metamorphic event in the iron formation originated an almost anhydrous mineral assemblage. Thus, the fluids in equilibrium with this rock probably had $P_{CO_2} > P_{H_2O}$. The presence of graphite along with fayalite-magnetite indicates low f_{O_2}, log f_{O_2} about -18 to -22 given by the stability of the assemblage fayalite-magnetite-hastingsite

(Ferry and Burt, 1982). Hence, graphite controls f_{O_2} through the equilibria C (graphite) + O_2 (fluid) <=> CO_2 (fluid) (Fyfe et al., 1978). The presence of graphite at a temperature above 500°C also indicates that CO as well as CH_4 should be present in the fluid (Fyfe et al., 1978) (Figure 7.10). Copper sulphides still indicate H_2S in the fluid phase.

The dominating fluids in the second metamorphic or first hydrothermal event were acidic and slightly more oxidizing than those involved in the formation of the higher temperature assemblage, with log f_{O_2} between -18 and -19, compatible with grunerite stability. They were also Cl^- rich, i.e. highly saline in order to leach Ca and Na in the proportion of 4 to 1, and to fix Si and K in the rock. Moreover, the fluid at a temperature of 650°C should have had high CO-CH_4 concentration, besides CO_2, due to the presence of graphite (Fyfe et al., 1978). Copper sulphides indicate the presence of H_2S in the fluid and tourmaline and biotite its enrichment in B and K. The fluid was still saturated in Si, Fe and Na and sub saturated in Ca.

The fluid in equilibrium with metagraywackes, which formed tourmaline and muscovite, was extremely acidic, oxidizing and saturated in Si and B. It was capable of leaching Mg and K in the proportion of 6 to 1 and fixing Ca and Na in the proportion of 1 to 4, indicating its subsaturation in Mg and Ca and saturation in Ca and Na. This is also indicative of a moderate chlorine content i.e.

moderate salinity, according to the experimental data of Popp and Franz, (1979).

The fluid in equilibrium with gneisses and amphibolites was acidic, saturated in Si, Na and B, forming quartz, albite and tourmaline, and subsaturated in Ca which was leached.

To leach Ca and precipitate Si and Na the fluid should have had a very high salinity with high concentration of chlorine. According to Popp and Franz's (1979) experimental data, high Cl concentration favors Si deposition in the rock, whereas the fluid becomes enriched in Ca. In high salinity hydrothermal fluids, the ratios Na/Ca and K/Ca are low (Barnes, 1979), in accordance with observations in the study area.

The fluid should also have had: a) low f_{O_2}, possibly buffered by the rock, due to the absence of oxidized minerals, such as hematite or rutile (since the theoretical reaction (2) of albite formation produces O_2) and b) $P_{H_2O} >> P_{CO_2}$ to prevent Ca precipitation as carbonat

Fluids of the third metamorphic event, or second hydrothermal episode, penetrate zones of intense deformation at a temperature of 370°C. The absence of graphite along with the presence of calcite, epidote, rutile and titanite indicate that the fluid had higher P_{CO_2} and f_{O_2} than those of the previous event. At high f_{O_2} graphite is oxidized to CO_2.

The fluid forming greenalite and chlorite in the iron formation was acidic, oxidizing, Si saturated and Mg subsaturated. It should have had $XCO_2 < 0.25$, indicated by the coexistence of chlorite and greenalite (Haase, 1982).

The fluid responsible for chlorite formation in all rock types of the study area was acidic and saline, leaching Na, Ca, K and Mn. Mg and Si behavior was ambiguous: they were introduced in some reactions and leached in others.

The composition of the fluids in equilibrium with metamorphic assemblages, characterizing the discussed metamorphic events, in the study area, are summarized in the next page:

Progressive metamorphism	1st Hydrothermal alteration	2nd Hydrothermal alteration
T = 750°C	T = 650 - 550°C	T = 370°C
log f_{O_2} -18 to -22	log f_{O_2} -18 to -19	high f_{O_2}
pH	acidic	acidic
$P_{CO_2} > P_{H_2O}$	$P_{H_2O} > P_{CO_2}$	
	high salinity	moderate salinity
$CO > CH_4$	CH_4-CO	CO_2
H_2S	H_2S	
	<u>iron formation</u>	<u>iron formation</u>
	Mn -	greenalite
	Na -	Si +
	Ca ----	Mg --
	Mg +	chlorite
	K ++++	Mg +
	<u>metagraywackes</u>	Si ---
	Mg ------	K --
	K -	Mn ------
	BO_3^{3-} +++	<u>quartzites</u>
		Si +++++
		K --
		Mg ----

7.6. Interpretation of geochronological data

Taking into account the data presented and discussed in previous chapters it is possible to reinterpret the available geochronological data, obtained by studies carried out in the Carajas area (Machado et al., 1990). These studies yielded the following U-Pb ages:

-Xingu Complex	(zircon)		2859+/-2 Ma
			2851+/-4 Ma
-Salobo trondhjemitic		core	2851+/-4 Ma
gneiss	(zoned zircon)	overgrowth	2739-2742 Ma
-Grao Para rhyolite	(zircon)		2759+/-2 Ma
-Pojuca metagraywacke (Salobo Sequence)	(zircon)		2732+/-2 Ma
-Mirim amphibolite	(zircon)	overgrowth	2761+/-3 Ma
-Granitic vein in amphibolite	(zoned zircon)	core	2758 Ma
		overgrowth	2732 Ma
-Old Salobo Granite (OSG)	(zircon)		2573+/-2 Ma
-Salobo amphibolite	(zircon)		2555+4/-3Ma
-Pojuca iron formation (Salobo Sequence)	(monazite)		2551+/-2 Ma
-Vein in Mirim	(titanite)		2584+/-5 Ma
amphibolite	(titanite)		2581+/-5 Ma
-Xingu Complex	(titanite)		2519+/-5 Ma
-Mirim amphibolite	(titanite)		2497+/-5 Ma

The analyzed zircon core of Salobo trondhjemite indicates that it is part of the Xingu Complex, and the age of 2851+/-4 Ma probably represents its emplacement.

The sample denominated Mirim amphibolite by Machado et al. (1990) corresponds to a finely banded and mixed contact zone between an amphibolite lens and its host trondhjemitic gneiss. The obtained age of 2761+/-3 Ma strongly suggests that the zircon, where the overgrowth was dated, was extracted from a thin band of the trondhjemitic basement, and not from the amphibolite itself.

It was seen in chapter 5 that the composition of Salobo amphibolites strongly suggests that they are related to the same magmatic event which formed the volcanic rocks of Grao Para Group. It was also seen that these latter rocks are the source for volcaniclastic contaminants in Salobo Type I iron formation, indicating that Salobo is coeval to Grao Para Group.

Therefore, the age of Grao Para rhyolite (2759+/-2Ma), which occurs intercalated in the top basaltic unit of Parauapebas Formation, also corresponds to the deposition age of Salobo iron formation. The dated deformed granitic-vein (2758 Ma), cutting the amphibolites.
represents this felsic magmatic event at Salobo area.

The age interval of 2732-2742 Ma, yielded by samples of Pojuca metagraywacke (denominated amphibolite by Machado et al., 1990); of zircon overgrowth in Salobo trondhjemitic gneiss and of overgrowth of zoned zircon in a granitic vein,

probably represents the first and second metamorphic events in the study area.

The emplacement of OSG at 2573+/-2 Ma corresponds to a period of tectonic reactivation of the area (Machado et al., 1990) reflected by shearing, which took place still under amphibolitic-facies conditions. The Salobo mylonitic amphibolite dated at 2555+4/-3 Ma probably represents the ductile stage of the second metamorphic episode. This tectonic reactivation seems to have regional extent, being also reflected by the monazite age in a sheared and silicified Pojuca iron-formation, which yielded 2551+/-2 Ma, as well as by a titanite analyzed in a sample of the Xingu Complex, collected 100 km east of Salobo, which yielded 2519+/-5 Ma.

The ages of 2584+/-5 Ma and 2581+/-5 Ma, obtained in titanites from granitic vein in Mirim amphibolite, reflect basement uplift. Whereas mylonitized amphibolites were at a crustal level compatible with amphibolitic facies metamorphism (2555+4/-3 Ma, 550°C, ductile stage of the second metamorphic event), the basement gneisses were forming titanite (2584+/-5 Ma; 2581+/-5 Ma), along with chlorite in shallower crustal levels, compatible with greenschist facies metamorphism. This facies is characteristic of the third metamorphic event (<370°C) at Salobo area.

The age of 2497+/- Ma obtained in titanite from Mirim amphibolite also represents the third metamorphic episode,

where chlorite and titanite formed after Fe-Mg minerals (Photomicrographs 26 and 27).

Thus, chlorite-titanite formation which occurred at 2581+/-5 Ma, 2584+/-5 Ma and 2497+/-5 Ma reflects different periods of shearing, corresponding to the uplift of the basement and of Salobo supracrustal rocks.

Table 7.1. Molar volumes of minerals used in semi-quantitative mass balance calculations

MINERAL	MOLAR VOLUME (cm^3)
Fayalite	46.389
Hastingsite	272.500*
Magnetite	44.524
Flogopite	149.910
Annite	154.300
Grunerite	277.960
Almandine	115.270
Spessartine	118.150
Grossular	125.300
Pyrope	113.270
Muscovite	140.710
Dravite	319.190
Schorlite	319.450
Chlorite	210.900
Greenalite	115.000
Quartz	23.718
Titanite	55.650
Sillimanite	49.899

Molar volumes from CRC Handbook of Chemistry and Physics (1984), except for chlorite (Chernosky et al., 1988) and greenalite (Miyano & Klein, 1983).
* Hastingsite molar volume is the average of amphiboles of similar structure. From: CRC Handbook of Chemistry and Physics (1984).

Table 7.2. Modal composition of iron formations, metagraywackes and quartzite

Sample no.	1 49-351 /4	2 56-280 /5	3 61-230 /3	4 61-230 /2	5 61-230 /1	6 50-127 /1	7 56-217 /2-3	8 20-221	9 17-350 /7	10 17-350 /4
Fayalite(%)	26.50	----	46.60	22.36	4.85	26.00	----	----	----	----
Hastingsite	----	----	----	9.70	4.80	----	4.36	----	----	----
Grunerite	35.90	2.00	----	11.65	7.86	32.00	28.42	----	----	----
Garnet I	----	22.00	----	9.90	18.34	----	----	----	----	----
Garnet II	----	----	----	3.70	6.86	----	----	1.76	----	3.93
Biotite	1.70	38.00	----	4.85	36.90	----	----	7.07	33.23	28.93
Magnetite	21.40	2.00	28.15	32.00	15.50	17.00	29.17	----	1.20	2.52
Quartz	----	28.00	----	----	----	25.00	36.65	70.79	34.61	34.83
Chlorite	----	8.00	----	----	----	----	----	11.50	7.84	10.39
Greenalite	9.40	----	13.60	5.85	2.90	----	----	----	----	----
Allanite	0.85	----	----	----	----	----	1.37	----	0.15	0.56
Apatite	4.20	----	----	----	----	----	----	----	----	----
Fluorite	----	----	11.65	----	2.00	----	----	----	----	----
Muscovite	----	----	----	----	----	----	----	5.30	10.46	6.17
Sillimanite	----	----	----	----	----	----	----	2.65	7.84	1.90
Tourmaline	----	----	----	----	----	----	----	----	3.69	7.30
Plagioclase	----	----	----	----	----	----	----	0.88	0.92	3.37

1 to 7 - iron formation 8 - quartzite 9 and 10 - metagraywackes

Table 7.3. Biotite analyses used for garnet-biotite geothermometry calculations

Sample no.	1 56-280-1 a	2 idem b	3 idem c	4 idem d	5 idem e	6 12-214
SiO_2(wt%)	33.92	33.62	33.68	34.33	34.08	34.88
TiO_2	1.90	1.87	2.11	2.20	1.89	2.46
Al_2O_3	14.56	14.08	14.64	14.58	14.90	16.16
FeO^t	33.02	32.71	32.35	32.99	32.74	28.47
Cr_2O_3	0.02	0.01	0.42	0.01	0.01	0.05
MnO	0.30	0.38	0.32	0.24	0.34	0.18
MgO	3.60	3.73	3.66	3.65	3.76	5.25
CaO	0.01	0.01	0.01	0.01	0.01	0.01
Na_2O	0.07	0.05	0.14	0.01	0.04	0.01
K_2O	8.96	8.92	9.11	9.48	8.81	9.61
Total	96.15	95.17	96.21	97.26	96.37	96.61
	number of ions on the basis of 24 oxygens					
Si	5.511	5.525	5.465	5.514	5.504	5.490
Ti	0.233	0.232	0.258	0.267	0.230	0.292
Al	2.788	2.727	2.800	2.760	2.836	2.998
Fe	4.486	4.496	4.390	4.431	4.422	3.721
Cr	0.003	0.001	0.054	0.001	0.001	0.006
Mn	0.041	0.053	0.044	0.033	0.047	0.024
Mg	0.872	0.914	0.885	0.874	0.905	1.232
Ca	0.002	0.002	0.002	0.002	0.002	0.002
Na	0.022	0.016	0.044	0.003	0.013	0.003
K	1.857	1.870	1.886	1.943	1.815	1.930
Fe^t/Mg	5.140	4.919	4.960	5.069	4.886	3.020
Fe^t/Fe^t+Mg	.837	.831	.832	.835	.830	.751

FeO calculated as total iron (FeO^t)

Table 7.4. Biotite analyses used for geothermometry calculations

Sample no.	1 50-682-1 a	2 idem b	3 61-230-1 a	4 idem b	5 17-350-4 a	6 idem b	7 idem I
SiO_2(wt%)	32.44	33.41	34.89	35.58	31.70	33.20	30.42
TiO_2	1.46	1.31	1.00	1.05	1.58	1.87	1.51
Al_2O_3	15.58	15.82	12.65	12.57	17.86	18.69	16.59
FeO*	31.71	31.54	35.64	34.04	32.82	30.22	31.60
Cr_2O_3	0.09	0.05	0.01	0.01	0.10	0.12	0.10
MnO	0.10	0.14	0.09	0.12	0.26	0.14	0.48
MgO	5.21	5.27	2.76	2.73	3.75	3.61	3.78
CaO	0.00	0.00	0.01	0.01	0.00	0.00	0.00
Na_2O	0.04	0.08	0.16	0.25	0.06	0.16	0.00
K_2O	8.89	8.98	8.63	8.97	8.66	9.62	8.41
Total	95.53	96.61	95.73	95.22	96.73	97.63	93.22
	number of ions on the basis of 24 oxygens						
Si	5.290	5.361	5.758	5.861	5.117	5.236	5.122
Ti	0.180	0.159	0.125	0.131	0.192	0.222	0.191
Al	2.995	2.992	2.461	2.441	3.398	3.474	3.293
Fe	4.325	4.233	4.919	4.689	4.430	3.986	4.450
Cr	0.012	0.006	0.001	0.001	0.013	0.015	0.013
Mn	0.014	0.019	0.013	0.017	0.036	0.019	0.068
Mg	1.267	1.261	0.679	0.670	0.902	0.849	0.949
Ca	0.000	0.000	0.002	0.002	0.000	0.000	0.000
Na	0.013	0.025	0.051	0.080	0.019	0.049	0.000
K	1.850	1.838	1.817	1.885	1.783	1.935	1.914
Fe*/Mg	3.413	3.356	7.244	6.998	4.911	4.694	4.689
Fe*/Fe*+Mg	.773	.770	.878	.874	.830	.824	0.824

FeO calculated as total iron (FeO*)
1 to 6 - garnet-biotite geothermometer
7 - muscovite-biotite geothermometer

Table 7.5. Garnet analyses used for garnet-biotite geothermometry calculations

Sample no.	1 56-280-1 a	2 idem b	3 idem c	4 idem d	5 idem e	6 12-214
SiO_2(wt%)	35.76	36.74	36.40	36.49	36.70	37.03
Al_2O_3	20.34	20.38	20.65	20.49	20.18	20.92
FeO^t	34.81	34.69	34.39	34.36	34.21	39.16
MnO	6.00	5.98	5.98	6.38	6.51	0.84
MgO	0.66	0.59	0.63	0.59	0.72	1.29
CaO	1.35	1.46	1.11	1.54	1.54	0.78
Total	98.92	99.44	99.16	99.85	99.86	100.02
number of ions on the basis of 24 oxygens						
Si	5.995	6.038	6.013	6.003	6.039	6.034
Al	3.992	3.947	4.021	3.973	3.914	4.018
Fe	4.848	4.768	4.751	4.727	4.708	5.337
Mn	0.846	0.832	0.836	0.889	0.907	0.116
Mg	0.163	0.144	0.155	0.144	0.176	0.313
Ca	0.240	0.257	0.196	0.271	0.255	0.136
Fe^t/Mg	29.586	32.982	30.621	32.668	26.653	17.028
Fe^t/Fe^t+Mg	.967	.970	.968	.970	.963	.944
End members (mol.%)						
Pyr.	2.6	2.4	2.6	2.4	2.9	5.3
Alm.	79.4	79.4	79.9	78.3	77.8	90.4
Gross.	3.9	4.2	3.3	4.5	4.2	2.3
Spess.	13.8	13.8	14.0	14.7	15.0	1.9

FeO calculated as total iron (FeO^t)

Table 7.6. Garnet analyses used for geothermometry and geobarometry calculations

Sample no.	1 50-682 /1a	2 idem b	3 61-230 /1a	4 idem b	5 170-350 /4a	6 idem b	7 61-230 /2	8 61-230 /1A	9 61-230 /1B	10 17-350 /4
SiO_2(%)	36.37	36.20	35.72	36.63	36.34	36.35	36.09	35.72	36.40	36.34
Al_2O_3	20.71	20.66	20.23	20.34	20.63	20.65	20.10	20.13	20.45	20.63
FeO*	36.53	36.66	36.69	35.77	38.99	39.09	37.80	36.69	36.20	38.99
MnO	2.22	2.48	1.98	2.46	2.11	2.17	1.88	1.98	1.93	2.11
MgO	1.08	1.02	0.23	0.24	0.82	1.05	0.15	0.23	0.23	0.82
CaO	2.35	2.01	3.20	3.24	0.84	0.61	2.71	3.20	3.19	0.84
Total	99.26	99.03	98.05	98.68	99.21	100.22	98.73	97.95	98.40	99.73
				number of ions on the basis of 24 oxygens						
Si	5.982	5.976	5.988	5.973	5.987	5.977	6.012	5.988	6.040	5.987
Al	4.015	4.020	3.977	4.019	4.006	4.002	3.947	3.977	4.000	4.006
Fe	5.025	5.062	5.144	5.015	5.372	5.375	5.267	5.144	5.023	5.372
Mn	0.309	0.346	0.281	0.349	0.294	0.302	0.265	0.281	0.271	0.294
Mg	0.264	0.251	0.057	0.060	0.201	0.257	0.037	0.057	0.056	0.201
Ca	0.414	0.355	0.574	0.600	0.148	0.107	0.483	0.574	0.567	0.148
Fe^t/Mg	18.974	20.161	89.485	83.606	26.673	20.883	141.36	89.485	88.290	26.673
Fe^t/Fe^t+Mg	.949	.952	.988	.988	.963	.954	.993	.988	.988	.963
					End members (mol%)					
Pyr.	4.4	4.1	0.8	1.0	4.3	4.2	0.6	0.8	0.9	3.3
Alm.	83.5	84.1	84.9	83.2	89.1	88.9	87.0	84.9	84.8	89.2
Gross.	6.8	5.9	9.4	9.9	1.7	1.7	7.9	9.3	9.5	2.4
Spess.	5.1	5.7	4.6	5.8	4.7	5.0	4.3	4.6	4.5	4.8

FeO calculated as total iron (Fe_2O^*)
1 to 3 hornblende-garnet geothermometer 4 - garnet plagioclase geobarometer

Table 7.7. Amphibole analyses used for geothermometry calculations

Sample no.	1 61-230 /2	2 61-230 /1A	3 61-230 /1B
SiO_2(wt%)	38.60	40.86	40.25
TiO_2	0.15	0.18	0.17
Al_2O_3	12.51	10.44	9.99
FeO*	33.55	29.97	32.68
MnO	0.16	0.58	0.75
MgO	1.02	1.79	1.96
CaO	8.99	10.91	10.29
Na_2O	2.54	1.11	1.23
K_2O	0.93	1.31	1.36
Total	98.45	97.15	98.68
number of ions on the basis of 24 oxygens			
Si	6.2387	6.5750	6.4142
Al	2.3837	1.9805	1.8780
Fe	4.5340	4.0332	4.3582
Mg	0.2457	0.4293	0.4658
Mn	0.0219	0.0791	0.1013
Ti	0.0182	0.0218	0.0204
Ca	1.5569	1.8811	1.7582
Na	0.7960	0.3463	0.3803
K	0.1918	0.2689	0.2767

Table 7.8. Muscovite analysis used for geothermometry calculations

Sample no.	1 17-350-4 I
SiO_2(%)	47.49
TiO_2	0.14
Al_2O_3	36.47
FeO*	1.63
MnO	0.07
MgO	0.33
CaO	0.00
Na_2O	0.84
K_2O	10.09
BaO	0.18
Total	97.55
number of ions on the basis of 22 oxygens	
Si	6.202
Ti	0.014
Al	5.579
Fe	0.177
Mn	0.008
Mg	0.064
Na	0.211
K	1.671
Ba	0.006
musc.%	88.330
parag.%	11.176
Ba musc.%	0.494

Table 7.9. Plagioclase analysis used for geobarometry calculations

Sample no.	17-350-4
SiO_2(%)	63.02
Al_2O_3	23.06
CaO	4.37
Na_2O	9.25
K_2O	0.05
Total	99.75
number of ions on the basis of 32 oxygens	
Si	11.173
Al	4.819
Na	3.180
Ca	0.830
K	0.011
An.(mol%)	20.60
Ab.	79.10
Or.	0.30

Table 7.10. GARNET-HORNBLENDE GEOTHERMOMETRY

Sample	K_D^{GR-HB}	$\ln K_D$	T°C	Average
61-230-2	7.714	2.0430	767	
61-230-1A	9.606	2.2624	742	
61-230-1B	9.571	2.2587	738	
				=749°C

Graham and Powell (1984) temperatures

MUSCOVITE-BIOTITE GEOTHERMOMETRY

Sample	K	lnK	T°C
17-350-4-I	0.19977	-1.61058	652

Hoisch (1989) temperature

GARNET-PLAGIOCASE GEOBARometry

Sample	$X_{Ca}^{(garnet)}$ $_{Ca_3Al_2Si_3O_{12}}$	$X_{CaAl_2Si_2O_8}^{(plagioclase)}$	logKD	Pressure (bars)
17-350-4	0.00351	0.02061	-1.85829	2.6

Ghent (1976) pressure

Table 7.11. GARNET-BIOTITE GEOTHERMOMETRY

Sample	K_D^{gr-bi}	$\ln K_D$	x	y	T°C	AVERAGE
56-280-1a	0.1739	-1.749	0.17	0.09	560	
56-280-1b	0.1492	-1.902	0.17	0.08	512	
56-280-1c	0.1618	-1.821	0.16	0.08	537	
56-280-1d	0.1552	-1.862	0.18	0.09	524	
56-280-1e	0.1831	-1.697	0.18	0.09	578	
12-214	0.1785	-1.722	0.03	0.13	569	
50-682-1a	0.1798	-1.715	0.11	0.12	571	
50-682-1b	0.1663	-1.793	0.11	0.11	546	
						=550°C
61-230-1a	0.0809	-2.513	0.12	0.05	367	
61-230-1b	0.0836	-2.480	0.13	0.06	373	
						=370°C
17-350-4a	0.2123	-1.549	0.06	0.11	632	
17-350-4b	0.2247	-1.492	0.06	0.15	654	
						=643°C

Ferry & Spear (1978) temperature (valid only when x < 0.2 and y < 0.15 where: x= (Ca+Mn)/(Ca+Mn+Mg+Fe) garnet, y= (Al_{VI}+Ti)/(Al_{VI}+Ti+Fe+Mg) biotite.

FIGURE 7.1. Graphical representation of the intensity and areal distribution of the three metamorphic events at Salobo area. (The ductile second event is also represented).

METAMORPHIC EVENTS AT SALOBO AREA

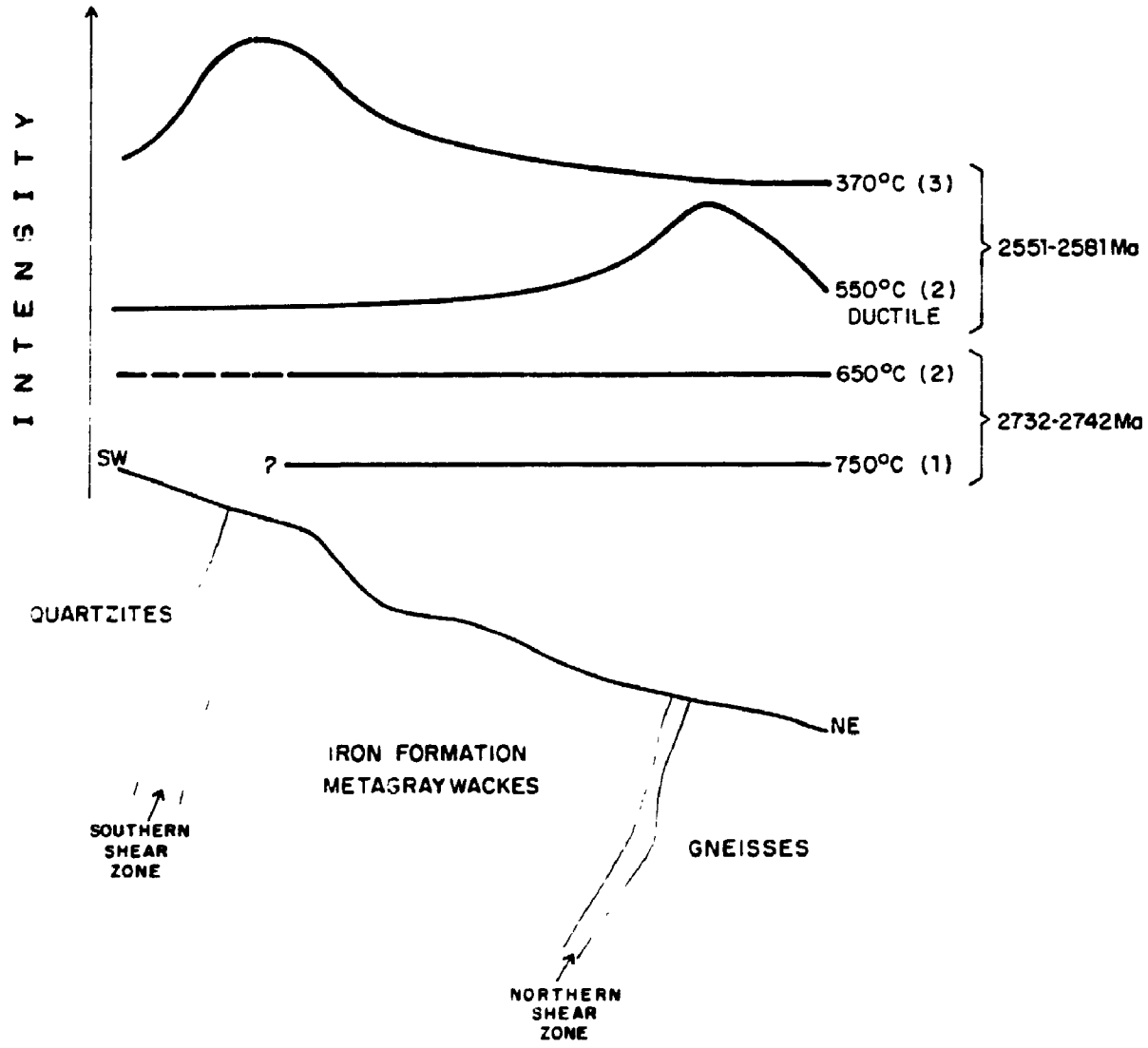

FIGURE 7.2. Al^{IV} versus $Al^{VI}+Fe^{3+}+Ti$ formula-proportion diagram for Salobo calcic amphiboles. (X) iron formations, (squares) amphibolites, and (triangles) gneisses. Note that the tschermakitic substitutions predominate over the glaucophanitic ones. Fields from high-pressure facies Sanbagawa (Japan) and Franciscan (California), medium-pressure Dalradian (Scotland) and Haast River Schist Group (New Zealand), and low-pressure Abukuma terrane (Japan) from Laird and Albee (1981).

FIGURE 7.3. $(Na^{A}+K)$ versus Na^{M4} formula-proportion diagram for Salobo calcic amphiboles. Note that the edenitic substitution predominate over the glaucophanitic one. (See figure 7.3 for symbols and for the field references).

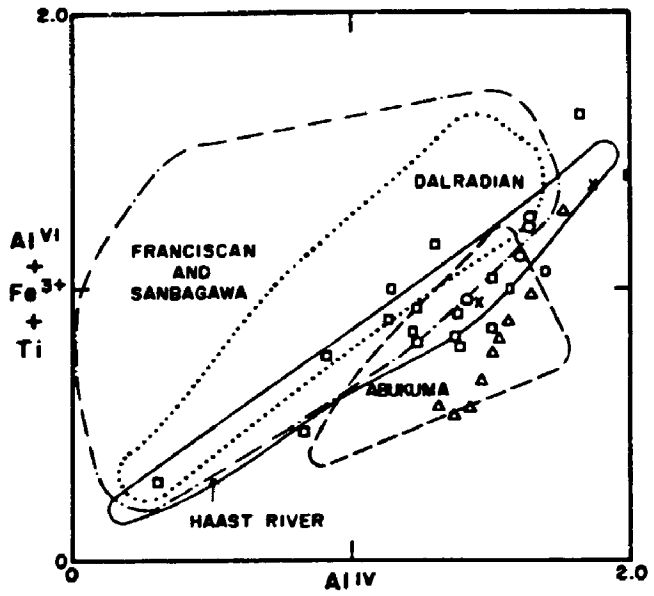
2.0
$Al^{VI} + Fe^{3+} + Ti$
FRANCISCAN AND SANBAGAWA
DALRADIAN
ABUKUMA
HAAST RIVER
0
0
AlIV
2.0

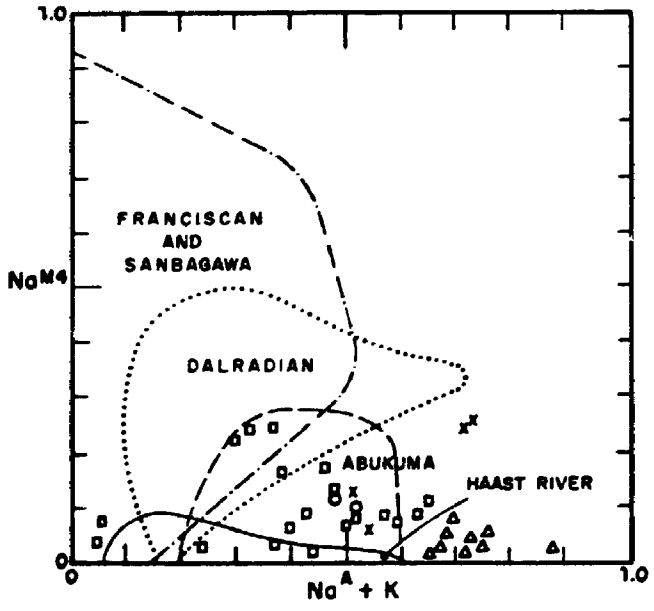
1.0
Na^{M4}
FRANCISCAN AND SANBAGAWA
DALRADIAN
ABUKUMA
HAAST RIVER
0
0
$Na^{A} + K$
1.0

FIGURE 7.4. $(Al^{VI}+Fe^{3+}+Ti)$ versus Na^{M4} formula-proportion diagram for Salobo calcic amphiboles.
Note that the tschermakitic substitution predominates over the glaucophanitic one. (See figure 7.3 for symbols and for the field references).

FIGURE 7.5. (100 Al/Al+Si) versus (100 Na/Ca+Na) formula-proportion diagram for Salobo calcic amphiboles. Note that the edenitic plus tschermakitic substitutions predominate over the edenitic plus tschermakitic ones. (See figure 7.3 for symbols and for the field references).

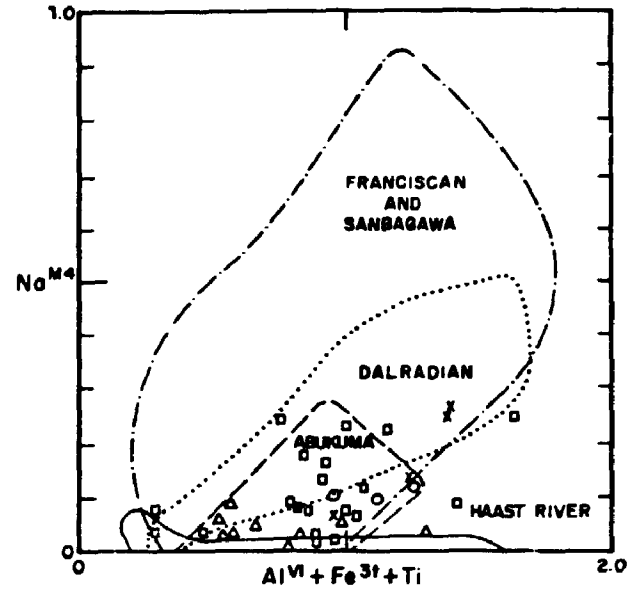
1.0
FRANCISCAN
AND
SANBAGAWA
Na^{M4}
DALRADIAN
ABUKUMA
HAAST RIVER
0
0
2.0
$Al^{VI} + Fe^{3+} + Ti$

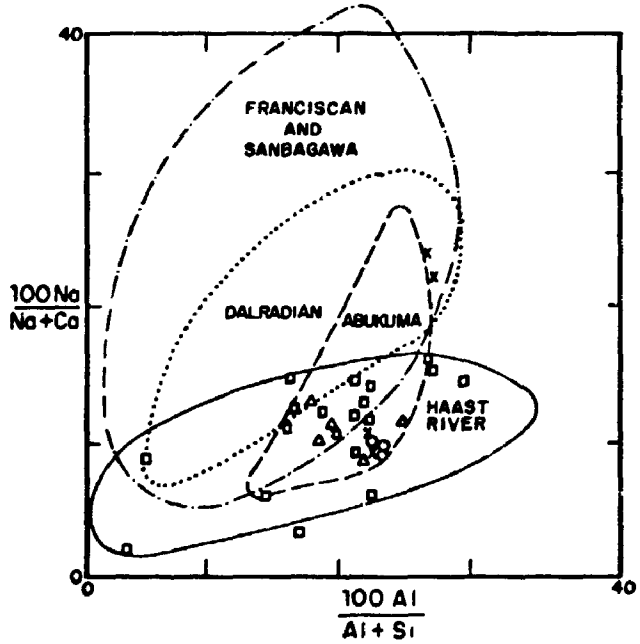
40
FRANCISCAN
AND
SANBAGAWA
$\frac{100\,Na}{Na+Ca}$
DALRADIAN
ABUKUMA
HAAST
RIVER
0
0
40
$\frac{100\,Al}{Al+Si}$

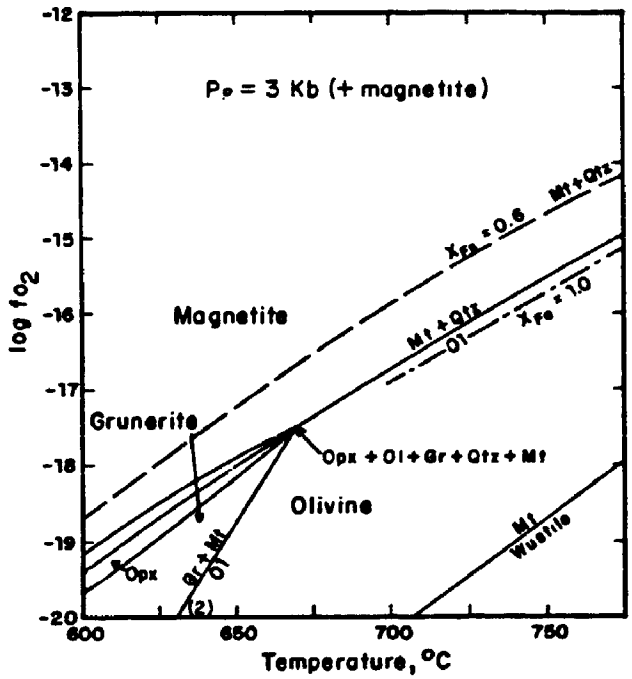

FIGURE 7.6. log f_{O_2} - T diagram of phase relations in low pressure regionally-metamorphosed iron formations (From Miyano and Klein, 1983).

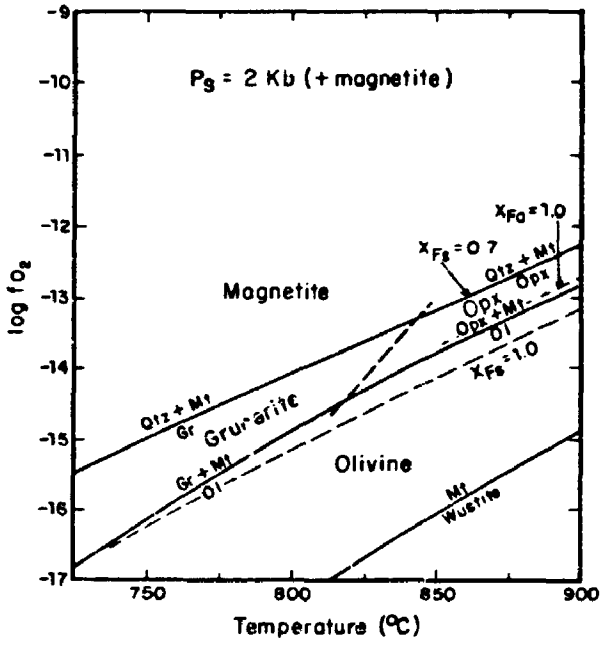

FIGURE 7.7. log f_{O_2} - T diagram of phase relations in low pressure contact-metamorphosed iron formations. (Diagram from Miyano and Klein, 1983).

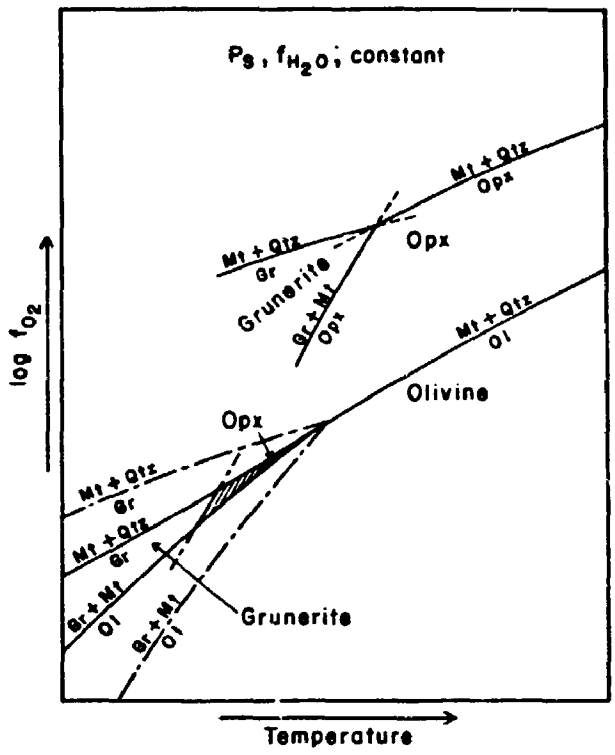

FIGURE 7.8. log f_{O_2} - T diagram of phase relations in high-grade metamorphic iron formations. Phase relations in the first and second metamorphic events at Salobo area reflect relatively low f_{O_2}. (Diagram from Miyano and Klein, 1983).

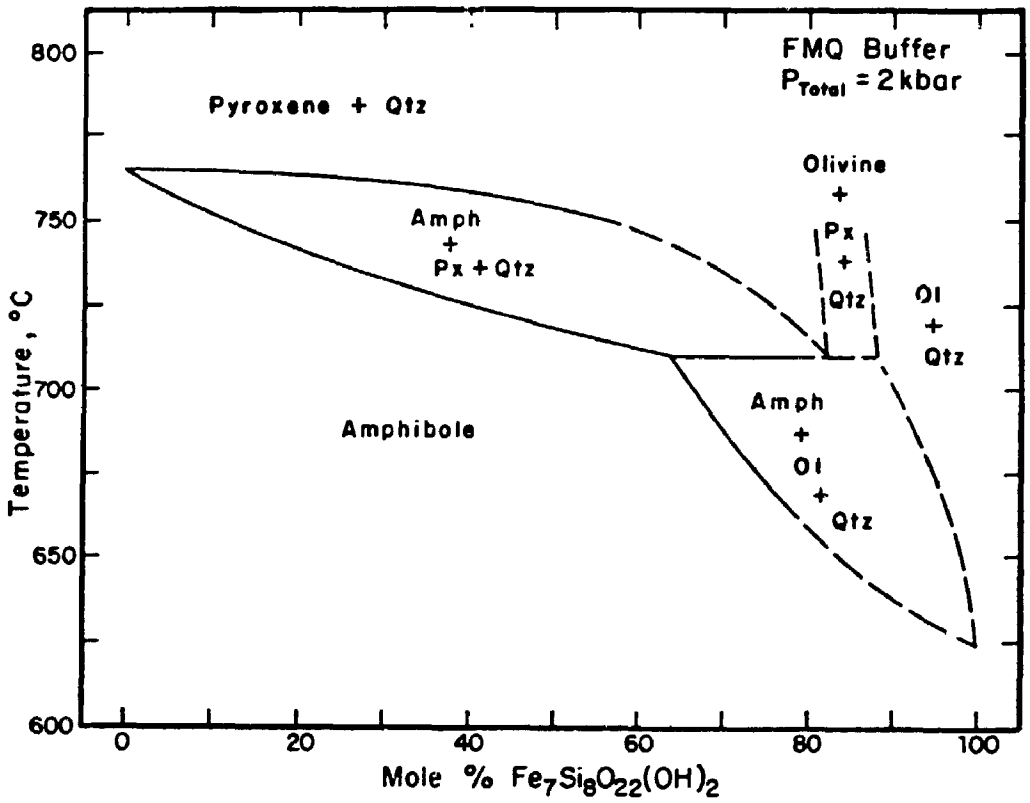

FIGURE 7.9. Temperature versus mole % $Fe_7Si_8O_{22}(OH)_2$ diagram of phase relations in Fe-Mg amphiboles (From Popp et al., 1977).

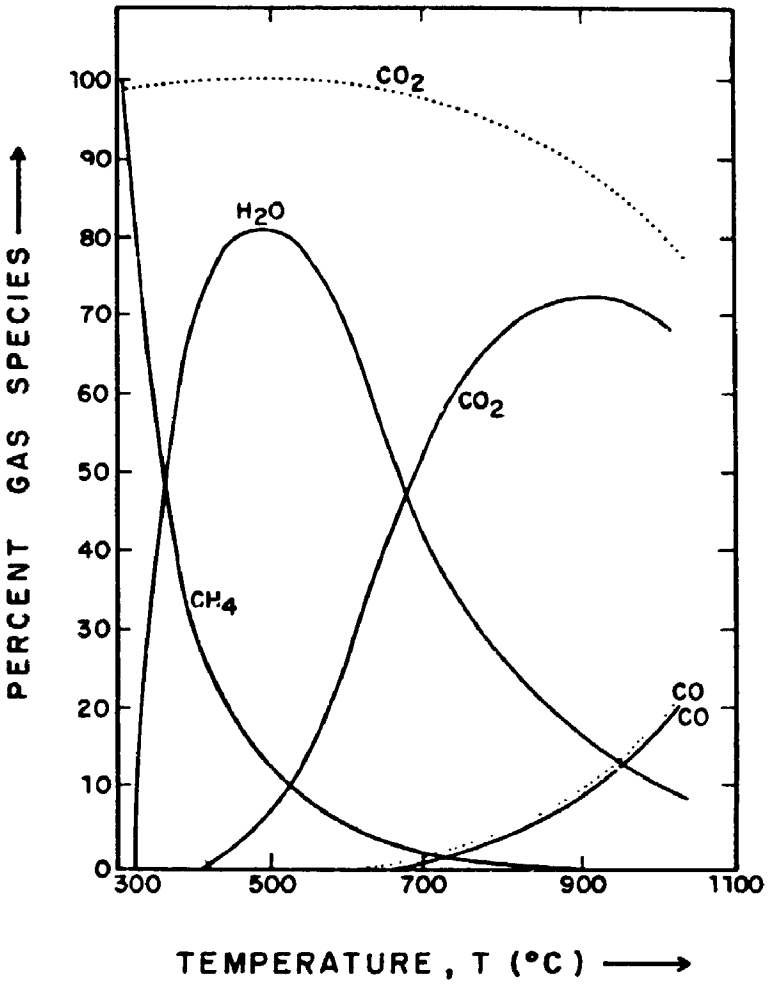

FIGURE 7.10. Compositions of C-O-H gas at 2 kbar pressure in the presence of graphite. The curves indicate f_{H_2} buffered by hematite-magnetite (dotted) and quartz-fayalite-magnetite (solid). (From Eugster and Skippen, 1967, in Fyfe et al., 1978)

CHAPTER 8

THE SALOBO SEQUENCE IN THE CARAJAS BASIN: GEOLOGICAL EVOLUTION AND COMPARISON WITH SIMILAR GEOLOGICAL ENVIRONMENTS

1.8. Introduction

The data obtained in this study, along with the available literature on the Carajas area, will be summarized in this chapter with the aim of building a schematic geological evolution of the area. A brief comparison between Carajas and similar late-Archean basins will also be presented.

8.2. Summary

The rocks of the Grao Para Group were deposited on an extensional continental crust, during Archean time (Gibbs et al., 1986; Olszewski et al., 1989), into a rift basin (Hutchinson, 1979), developed on the gneissic basement of the Xingu Complex (Beisiegel et al., 1973; Docegeo, 1988).

(Beisiegel et al., 1973; Gibbs et al., 1986; Olszewski et al., 1989).

The Salobo sequence, consisting of metamorphosed basaltic rocks, iron formations, graywackes and quartzites at the study area, may probably be included in the Upper Volcanic Sequence, because this Sequence is the only one, at the present stage of knowledge of the area, including rock types similar to the Salobo area.

8.3. Schematic geological evolution

Despite the lack of detailed information, it is possible to suggest a schematic evolution for the Carajás basin and the Salobo sequence, taking into account the data summarized above and in previous chapters.

The initial rift related activity in the Carajas basin was subsidence, possibly associated with the uplift of the southern granite-greenstone terrains of the Amazon craton, and eruption of flood-basalt lavas, rich in incompatible elements, dated at 2759+/-2 Ma by Machado et al., (1988). The flood volcanism was probably preceded by underplating of the continental crust by dense primary magma from the mantle (Cox, 1979; Herzberg et al., 1983; Walker, 1989). Crustal extension probably took place through dyke injections from the ponded magma, into incipient vertical fractures under a high heat flow regime. Mafic-ultramafic layered complexes

were emplaced at this time, particularly the Luanga Complex (2763+/-6 Ma, Machado et al., 1988) (Figure 8.1).

As volcanism waned, a period of exceptional stability in the basin began with the deposition of the 100 to 400 m thick finely banded iron formation. The almost total absence of clastic rocks associated with iron formations indicates that the deposition took place in an environment protected from clastic debris and dominated by intense hydrothermal activity, under high heat flow conditions (Figure 8.2).

The transition between the Carajas Formation and the Upper Volcanic Sequence was marked by the end of the stable period and possibly by more active subsidence, with the start of a continuing supply of terrigenous material. This is shown by the deposition of clastic sediments intercalated with volcanic flows and tuffs, although stable conditions could have prevailed in localized area to permit the precipitation of thin layers of iron formation (Figure 8.3).

At this time, at the north-northwestern margin of the basin, the deposition of the Salobo sequence took place, in a zone of high heat flow, intense hydrothermal activity and tectonic instability. This is shown by iron formations with highly fractioned REE patterns and strong Eu positive anomalies, indicating a hydrothermal source. Tectonic instability is indicated by iron formations showing gradual increase in Al, K, Ti and Zr and decrease in Si and Fe, which characterize volcaniclastic contaminants, intercalated with and grading to graywackes. The sedimentation at Salobo

area culminated with an increasing supply of basement-derived material, which gave origin to mature quartzites, whose trace elements indicate source rocks of principally trondhjemitic-granitic-basaltic origin.

The Salobo rocks were deposited in an highly unstable tectonic environment, being rapidly taken to a depth of 8.5 km, where progressive metamorphism (750°C) followed by hydrothermal alteration (650°C) took place at a time interval of 20 to 25 Ma after deposition (2732-2742 Ma). The thermal gradient during these two events varied from 85°C/km in the first metamorphic episode to 75°C/km in the second, showing that the high heat flow regime persisted.

After that, the area experienced a period of stability which lasted for 140 Ma.

A new instability epoch, represented by tectonic reactivation of regional extent affecting the basin as well as the gneissic basement, initiated at 2581+/-5 Ma lasting over a time span of 30 Ma. This period was marked by intense shearing and granite emplacement. Evidences of this tectonic reactivation were obtained through geochronological studies carried out by Machado et al., (1990) in: Salobo albitized and mylonitized amphibolite (2555+4/-3 Ma); sheared and silicified Pojuca iron formation (2531+/-2 Ma); Mirim vein (titanite, 2584+/-5 Ma and 2581+/-5 Ma) and Xingu Complex (titanite, 2519+/-5 Ma).

In the rocks of Salobo area, this period of 30 Ma corresponds to reactivations of the NSZ, with basement

ascent and emplacement of the OSG at 2573+/-2 Ma (Machado et al., 1988). The basement ascent is shown by the same age interval obtained in zircon analyzed in mylonitized amphibolite (2555+4/-3 Ma) and in titanite of Mirim vein (2584+/-5 Ma and 2581+/-5 Ma). These ages show that whereas amphibolites were at a depth compatible with amphibolite facies metamorphism, the trondhjemitic gneisses were at higher crustal levels, compatible with greenschist facies metamorphic condition.

Another stabilization period lasted about 50 Ma, being followed at the Salobo area by the reactivation of SSZ, with intensive chloritization of Fe-Mg minerals and titanite production at 2497+/-5 Ma (Machado et al., 1990).

A long stable period of 700 Ma ended with the widespread emplacement of anorogenic granites associated with felsic volcanic rocks, which extended all over the Amazon craton. In the Carajas basin this episode was marked by the intrusions of Carajas (1880+/-2 Ma), Cigano (1883+/-2 Ma), Pojuca (1874+/-2 Ma), and Salobo (YSG) granites (1880+/-80 Ma)(Machado et al.,(1988); Cordani, 1981).

The last record of Salobo geological history is registered by diabase dykes, emplaced 1300 Ma later than the granite, during Cambrian time (560+/-32 Ma, Cordani, 1981).

8.4. Comparison with similar Archean basins

Archean rift basins developed on continental basement include the Transvaal and Pongola basins in South Africa (Armstrong et al., 1986; Marsh et al., 1989), the Hamersley basin, in Western Australia and Carajas in Brazil.

The Transvaal, Hamersley and Carajas basins are of the same age: Carajas volcanic rocks are 2759+/-2 Ma (Machado et al., 1988), Hamersley volcanic rocks are 2768+/-16 Ma (Pidgeon, 1984) and Transvaal rocks are ~ 2720 Ma (Marsh et al., 1989), whereas Pongola is older ~3000 Ma (Marsh et al., 1989).

The three younger basins show roughly the same stratigraphy, with a basal unit consisting of a bimodal suite of continental volcanic rocks, a chemical sedimentary unit and an upper clastic unit (Button, 1976; Trendall, 1983; Marsh et al, 1989; Gibbs et al., 1986). In addition to that, the Pongola basin shows a different stratigraphic succession, with a basal unit made up of clastic sedimentary and acid to intermediate volcanic rocks overlain by a volcanic unit, which exhibits a complete spectrum of chemical compositions, from basalt to rhyolite. The top unit consists of volcanic and clastic sedimentary rocks (Armstrong et al., 1986).

The three younger basins also have in common the same tectonic setting. They are preserved within the limits of Archean tectonic units, such as the Kaapvaal Block

(Transvaal), Pilbara Block (Hamersley) and Amazon Craton (Carajas) and they developed on Archean gneiss-greenstone basements, with ages in excess of 3000 Ma (Button, 1976).

The basins have some important mineral deposits in common as such as, Mn in Transvaal, Carajas and Hamersley; gold in Transvaal and Carajas and crocidolite in Transvaal and Hamersley basins (Button, 1976; Trendall, 1983; Docegeo, 1988). Two of them, Hamersley and Carajas, host the two largest iron ore deposits of the planet. This fact seems to point to a greater similarity between Hamersley and Carajas, despite the lack of detailed information on the latter, preventing more lengthy comparisons.

The summarized comparison of the stratigraphy of the Carajas and Hamersley basins is shown in table 8.1.

The three Archean intracratonic basins are very similar in age, tectonic setting and stratigraphic successions. They are early representatives of what is commonly interpreted as a major change in tectonic style, from Archean to Proterozoic times (Button, 1976; Marsh et al., 1989; Armstrong et al., 1986).

FIGURE 8.1. Initial rift related activity in Carajas basin, with eruption of continental basaltic lavas, dyke injections and emplacement of mafic-ultramafic Complexes.

FIGURE 8.2. Intermediate depositional stage in Carajas basin. Deposition of iron formation at a period of basin stability.

FIGURE 8.3. Final depositional stage in Carajas basin. Deposition of clastic sedimentary rocks intercalated with volcanic flows and iron formations, at a period of basin instability.

SCHEMATIC EVOLUTION OF CARAJAS BASIN

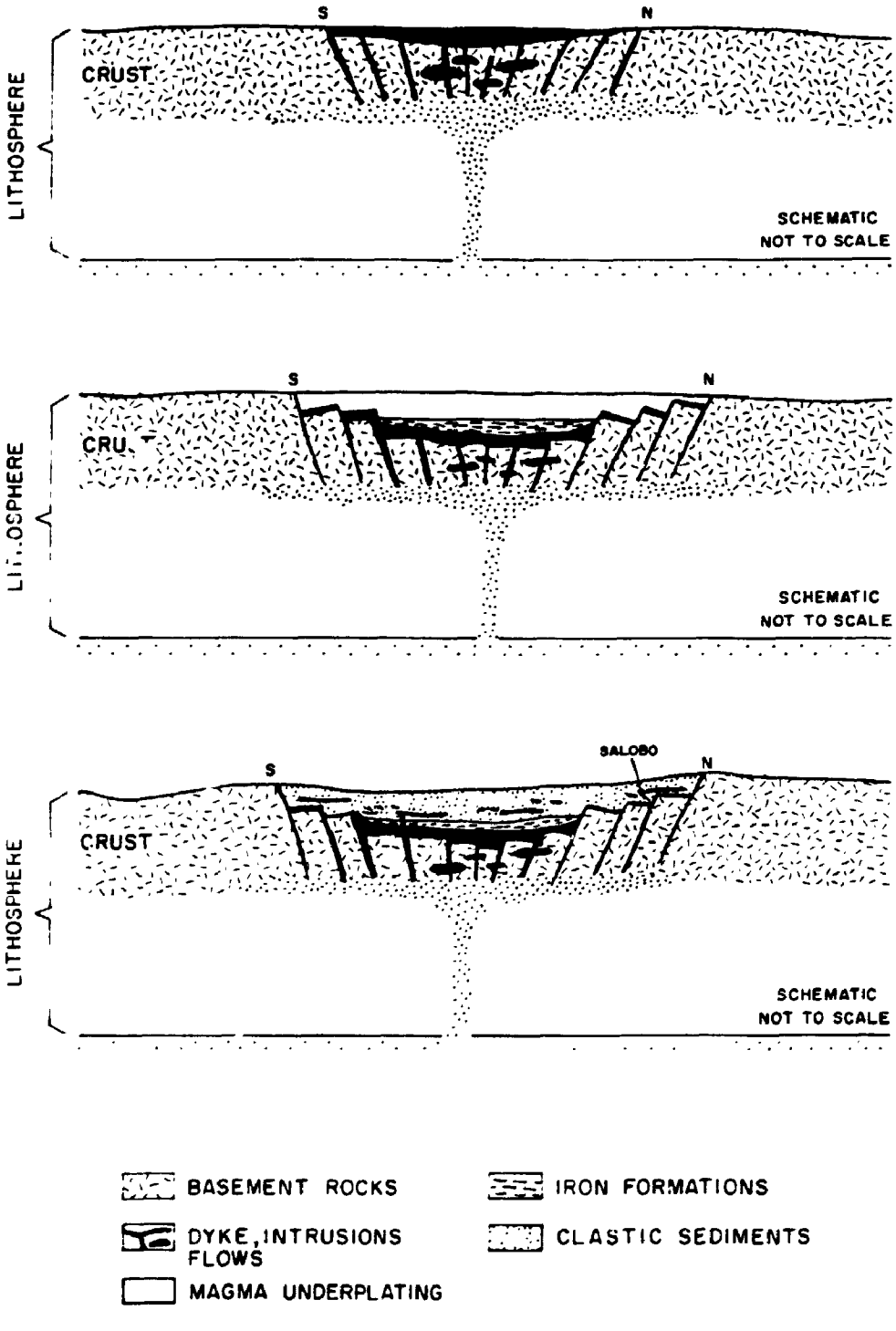

Table 8.1. Comparison between the Stratigraphy of Carajas and Hamersley Basins

CARAJAS	HAMERSLEY
Upper Volcanic Sequence	Wyloo Group
- 1000 to 3000 m thick - clastic sediments: graywackes, phyllites, tuffaceous sandstones, mafic flows, tuffs, cherts, iron formations, conglomerates, quartzites. (Beisiegel et al., 1973; Gibbs et al., 1986; Olszewski et al., 1989)	- 9000 m thick - clastic sediments: graywacke, dolomite, basalts. (Trendall, 1983)
Carajas Formation	Hamersley Group
- 100 to 400 m thick - iron formation Beisiegel et al., (1973)	- 2500 m thick - major units of iron formation, shales, dolomite, volcanic rocks. (Trendall, 1983)
Parauapebas Formation	Fortescue Group
- 4000 to 6000 m thick - volcanic rocks: basalts, basaltic andesites, rhyolites (Gibbs et al., 1986; Olszewski et al., 1989)	- 3000 m thick - volcanic rocks: basaltic flows, tuffs, sandstones, siltstones, shales. (Richards and Blockley, 1984)

CHAPTER 9

CONCLUSIONS

As stated in Chapter 1, this work was carried out with the objective of contributing to a better understanding of the Salobo Sequence stratigraphy, its metamorphic history and geological evolution.

The principal conclusions reached in this study, based on the interpretation of data collected for this research, are the following:

1. The Salobo sequence comprises metamorphosed basaltic rocks, iron formations, graywackes, and arkoses to arkosic arenites, resting on a basement composed of trondhjemitic and less frequently granitic gneisses.

2. Salobo amphibolites show tholeiitic basaltic composition, with Fe, LIL and LREE enrichment characterizing continental basaltic rocks, similar to the volcanic rocks of Grao ParàGroup.

3. The quartzites are metamorphosed mature clastic-sedimentary rocks, whose source area, indicated mainly by less mobile element contents such as Ti and Cr, was probably granitic to trondhjemitic.

4. There are two types of iron formations at the study area, one Fe-Si rich (Type I), and the other aluminous (Type II). Both types together with metagraywackes form sedimentary cycles, where Type I grades to Type II and the latter to metagraywackes towards the top.

5. There is a continuous compositional variation between Type I and Type II iron formations, with a gradual Al, K, Ti and Zr increase and Fe and Si decrease. This compositional variation defines a mixing line between chemical iron formation and volcanic rocks of Grao Parà Group, indicating that the latter are the volcaniclastic contaminants of Salobo Type II iron-formation.

6. The gradation between Type II iron formation and metagraywackes is chemically represented by Si, Ti, Al, Na and K increase and Fe, Mn and Mg decrease.

7. The highly fractionated REE chondrite-normalized pattern of Type I iron formation, together with strong positive Eu anomaly, indicate a hydrothermal origin for Fe-Si in this rock type.

8. The positive correlations between Fe-Cu and Fe-REE indicate a common hydrothermal origin for Fe-Cu-REE.

9. The Salobo sequence is part of Grao ParàGroup and was deposited at 2759+/- 2 Ma.

10. Two granitoid bodies intrude Salobo sequence at the study area:

a. OSG is an alkalic, sodic and metaluminous granite. It is deformed and emplaced in mesozonal conditions,

presenting chemical characteristics similar to I-type granites. It is analogous to Phanerozoic within plate granites, emplaced in attenuated continental crust.

b. YSG is an alkalic, potassic and metaluminous alkali-feldspar quartz syenite, post tectonically emplaced in epizonal conditions. It shows chemical, mineralogical and textural features analogous to A-type Phanerozoic granitoids, within plate emplaced.

11. The Salobo sequence was submitted to a progressive metamorphism of thermal character, at conditions close to pyroxene hornfels facies. This was followed by two episodes of hydrothermal alteration, at conditions compatible with amphibolitic and greenschist metamorphic facies, respectively.

12. The progressive metamorphic episode is distinguished by almost anhydrous mineral assemblages, such as fayalite, hastingsite, almandine and magnetite in iron formation; hastingsite and calcic plagioclase in amphibolites and calcic plagioclase, quartz and hastingsite in trondhjemitic gneisses.

13. The first hydrothermal event is marked by the destruction of fayalite and hastingsite, as well as by the albitization of plagioclase. The resulting mineral assemblages are: grunerite, almandine, magnetite, biotite and quartz in iron formation; cummingtonite and albite in amphibolites; albite, quartz and cummingtonite in

trondhjemitic gneiss; and quartz, almandine, biotite and sillimanite in metagraywackes and quartzites.

14. The second hydrothermal event corresponds to intensive chloritization of Fe-Mg minerals occurring in all rock types of the study area, except Type I iron formation where greenalitization took place.

15. Fe/Mg ratios in minerals and their respective host rocks indicate that near-equilibrium conditions were attained in the three metamorphic/hydrothermal episodes.

16. The first metamorphic episode of thermal character originated granoblastic to hornfelsic-textured rocks. It took place at a temperature of 750°C, given by garnet-hornblende geothermometer in iron formation.

17. The first hydrothermal alteration event, originating foliated-schistose rocks, attained a temperature of 650°C evidenced by biotite-garnet and biotite-muscovite geothermometer.

18. Both metamorphic/hydrothermal episodes took place at low pressure - 2.5 kbar - during the time interval of 2732-2742 Ma. This is indicated by the garnet-plagioclase geobarometer and by the predominance of tschermakitic and edenitic substitutions over glaucophanitic, in Ca-amphiboles.

19. During the first hydrothermal alteration event, but at lower temperature (550°C, garnet-biotite geothermometer), a ductile episode occurred. It is demonstrated by mylonitic-

textured mineral assemblages, characteristic of amphibolitic facies rocks.

20. The second hydrothermal alteration episode occurred at 370°C (garnet-biotite geothermometer), being represented by mylonitized and chloritized zones, cutting all rock types of the study area.

21. Hydrothermal episodes at temperatures between 550 and 370°C occurred over a time interval of 2581-2551 Ma, which also corresponds to a tectonic reactivation of regional extent, when Salobo basement rocks ascended. This is evidenced by the presence of zircon ages in mylonitized amphibolite (2555 Ma) in the same age interval of those obtained in titanites in mylonitized and chloritized trondhjemitic gneiss (2554-2581). Whereas amphibolites were at a depth compatible with amphibolite facies metamorphism, the trondhjemitic gneisses were at higher crustal levels, compatible with conditions of greenschist facies metamorphism.

22. The culmination of the second hydrothermal alteration event took place at 2497 Ma, together with activation/reactivation of SSZ, and intense chloritization.

23. Fluids in equilibrium with the first metamorphic event (at 750°C) had low oxygen fugacity, with log f_{O_2} -18 to -22. They had $P_{CO_2} > P_{H_2O}$, and were H_2S and $CO > CH_4$-bearing.

24. Fluids in equilibrium with the first hydrothermal alteration episode (at 650-550°C) also had low oxygen

fugacity (log f_{O_2} -18 to -19), $P_{H_2O} > P_{CO_2}$, were CO-CH_4-bearing, acidic and highly saline. These fluids are responsible for an extensive strong Ca leaching from gneisses, amphibolites and iron formations.

25. Fluids responsible for the second hydrothermal alteration episode were acidic, oxidizing and moderately saline. They percolated along shear zones at a temperature of 370°C.

26. The Salobo sequence was formed under a high heat flow regime and tectonic instability. Intense volcanism and submarine hydrothermal activity prevailed during the sedimentation time. After deposition, it was rapidly taken to a depth of 8.5 km, with a thermal gradient of 85°C/km. This was followed by cooling, still under high heat flow regime, which is demonstrated by hydrothermal activities at 650 and 370°C. Subsequently, the area underwent reheating, related to the emplacement of the post tectonic granitoid body.

27. The Carajásbasin has many features in parallel to other late Archean continental basins, such as Transvaal (South Africa) and Hamersley (Western Australia) basins, i. e., a basal unit mainly composed of bimodal continental volcanic flows, an intermediate unit of major iron formations and a chiefly clastic top unit. Of these, Carajás and Hamersley exhibit remarkable similarities with respect to the huge Fe ore deposits they host and to the age of

their basal volcanic flows: Carajàs2759+/-2 Ma and Hamersley 2768+/-16 Ma.

APPENDIX A

CHEMICAL ANALYSES

Table 5.1 Whole rock analyses in gneisses

Sample no.	1 12-490	2 25-512	3 31-311	4 57-112	5 15-159	6 15-212	7 15-223
SiO2(wt%)	75.40	71.50	71.00	78.10	72.00	74.40	70.50
TiO2	.15	.17	.20	.18	.11	.12	.20
Al203	12.40	13.60	14.10	11.30	12.30	12.00	13.20
Fe203	2.55	4.19	3.38	2.28	5.33	6.07	3.25
MnO	.02	.02	.02	.01	.05	.03	.04
MgO	1.06	1.47	1.97	2.04	2.60	1.08	.67
CaO	.70	.76	1.95	1.23	.39	.60	1.75
Na20	6.52	5.55	4.42	3.32	4.58	3.68	4.76
K20	.24	1.51	1.76	.38	.87	1.07	2.09
P205	.05	.04	.05	.04	.07	.04	.05
LOI	1.08	1.23	.93	1.39	1.85	1.39	1.93
Total	100.17	100.04	99.78	100.27	100.15	100.48	98.44
Co(ppm)	4	15	10	3	24	27	9
Ni	12	14	14	9	19	14	4
Cu	248	13	4	154	669	472	160
Zn	25	22	19	18	25	23	22
Mo	10	nd	nd	nd	nd	20	nd
Pb	6	17	15	11	7	7	8
Th	nd	60	80	30	30	70	110
U	nd	10	20	10	30	20	20
Cr	9	4	16	nd	1	nd	nd

nd = not detected 1 to 7 trondhjemitic gneisses

Table 5.1 Whole rock analyses in gneisses (continued)

	1	2	3	4	5	6	7
Sample no.	12-490	25-512	31-311	57-112	15-159	15-212	15-223
Rb(ppm)	nd	58	79	4	34	44	91
Sr	50	30	50	39	25	33	65
Y	18	17	33	22	19	18	25
Zr	55	182	212	48	86	116	290
Nb	4	19	18	8	8	16	22
Ba	38	129	117	27	54	155	217
Ga	8	20	22	18	21	17	17
La	43	92	123	21	58	53	148
V	3	1	4	14	73	1	22

nd = not detected 1 to 7 trondhjemitic gneisses

Table 5.1 Whole rock analyses in gneisses (continued)

Sample no.	1 16-135	2 16-186	3 49-505	4 57-122	5 16-246	6 15-440
SiO2(wt%)	72.40	75.00	67.60	75.30	70.40	65.70
TiO2	.10	.10	.07	.09	.12	.14
Al2O3	11.80	10.70	11.00	13.80	11.00	12.20
Fe2O3	6.58	6.44	10.20	.33	7.71	10.70
MnO	.07	.09	.16	.01	.06	.10
MgO	1.47	1.58	3.07	.12	4.18	1.75
CaO	.26	.27	1.43	.93	.17	1.99
Na2O	4.54	3.33	1.95	4.35	1.50	2.03
K2O	1.64	1.32	2.27	4.68	1.61	2.54
P2O5	.06	.04	.07	.03	.06	.12
LOI	1.39	1.62	2.08	.54	3.00	2.31
Total	100.31	100.49	99.90	100.18	99.81	99.58
Co(ppm)	26	31	29	nd	40	156
Ni	16	18	21	1	19	29
Cu	217	833	561	308	740	2125
Zn	38	46	24	nd	32	29
Mo	nd	10	20	nd	nd	nd
Pb	14	13	16	44	12	20
Th	70	70	20	20	50	nd
U	20	20	50	20	20	nd
Cr	nd	nd	nd	nd	nd	nd

nd = not detected 1-2 trondhjemitic gneisses 3-4-5 granitic gneisses
6- monzonitic gneiss

Table 5.1 Whole rock analyses in gneisses (continued)

Sample no.	1 16-135	2 16-186	3 49-505	4 57-122	5 16-246	6 15-440
Rb(ppm)	45	48	42	134	54	92
Sr	33	41	20	39	25	74
Y	10	22	33	15	nd	42
Zr	145	156	79	13	155	144
Nb	16	20	23	14	21	28
Ba	259	292	91	397	131	714
Ga	11	10	18	18	13	15
La	191	112	148	1	237	314
V	30	nd	nd	nd	4	nd

nd = not detected 1-2 trondhjemitic gneisses 3-4-5- granitic gneisses
6- monzonitic gneiss

Table 5.2 Normative composition of gneisses

Sample no.	1 25-512	2 31-311	3 15-233	4 12-490	5 57-112	6 15-159	7 15-212
Quartz	29.73	31.58	30.20	33.62	51.77	37.52	46.12
Orthoclase	8.92	10.40	12.35	1.42	2.25	5.14	6.32
Albite	46.96	37.40	40.28	55.17	28.09	38.76	31.14
Anortite	3.51	9.35	8.36	3.15	5.84	1.48	2.72
Corundum	1.55	1.50	.05	.26	3.29	3.28	3.79
Hypersthene	3.66	4.91	1.67	2.64	5.08	6.47	2.69
Ilmenite	.04	.04	.09	.04	.02	.11	.06
Hematite	4.19	3.38	3.25	2.55	2.28	5.33	6.07
Apatite	.09	.12	.12	.12	.09	.16	.09
Rutile	.15	.18	.15	.13	.17	.05	.09

1 to 7 trondhjemitic gneisses

Table 5.2 Normative composition of gneisses (continued)

Sample no.	1 16-135	2 16-186	3 49-505	4 57-122	5 16-246	6 15-440
Quartz	37.14	47.76	45.91	30.02	49.47	37.64
Orthoclase	9.69	7.80	13.42	27.66	8.92	15.01
Albite	38.42	28.18	16.50	36.81	12.69	17.18
Anortite	.90	1.08	---	4.31	.45	9.09
Corundum	2.23	3.40	7.72	---	6.73	2.78
Hypersthene	3.66	3.93	7.65	.30	10.41	4.36
Magnetite	---	---	.32	---	---	---
Ilmenite	.15	.19	.13	.02	.13	.21
Hematite	6.58	6.44	9.98	.33	7.71	10.70
Titanite	---	---	---	.08	---	---
Apatite	.14	.09	.16	.07	.14	.28
Rutile	.02	---	---	.05	.05	.03
Acmite	---	---	4.73	---	---	---

1-2 - trondhjemitic gneisses 3-4-5 - granitic gneisses
6 - monzonitic gneiss

Table 5.3 Average composition of trondhjemites selected from the literature

Sample no.	1	2	3	4	4	6	7	8	9
SiO2(wt%)	73.95	71.38	71.14	73.85	71.20	78.03	70.07	72.80	73.36
TiO2	.59	.22	.33	.59	.18	.28	.23	.34	.14
Al2O3	11.27	15.25	15.65	11.27	17.00	12.21	16.47	14.16	12.37
FeO	4.45	1.93	2.35	4.45	1.18	2.52	1.41	2.61	4.00
MnO	.05	.03	.03	.05	.02	0.04	.03	.03	.03
MgO	1.32	.93	.99	1.32	.36	.69	.80	.91	1.54
CaO	2.10	3.78	4.47	2.10	3.00	1.78	3.14	2.91	.87
Na2O	4.00	4.87	4.64	4.00	5.50	2.73	5.50	4.46	4.52
K2O	1.89	.85	.35	1.89	.95	.19	1.34	1.06	1.20
P2O5	.08	.06	.07	.08			.07	.07	.04
Total	99.86	99.52	100.03	99.76	99.45	98.60	99.12	99.46	98.52
V(ppm)	17	--	--	17	--	--	--	17	16
Cr	8	--	4	8	1.2	6.38	--	5.4	4
Ni	15	7.9	6	15	--	--	--	11	13
Cu	7	--	--	7	--	--	--	7	308
Zn	42	22.5	28	42	--	--	--	33.75	26
Ga	17	20.5	21.5	17	--	--	--	19.25	16
Rb	22	6	1.5	22	17	3.5	27.96	14.42	45
Sr	132	480	369.5	132	711	328	613	395	41

1- Average of undepleted trondhjemites from Antarctic (Sheraton et al., 1985)
2- Mean trondhjemite from Scourie, Scottland (Rollinson and Windley, 1980)
3- Average of trondjemites from Scourie Badcall, Scottland (Rollinson and Windley, 1980)
4- Average of trondhjemitic gneisses from Napier Complex, Antarctic (Sheraton and Black, 1983)
5- Average of trondhjemitic gneisses from Wind River, Wyoming (USA) (Barker et al., 1979)
6- Average of trondhjemites from southern Massif Central, France (Nicollet et al., 1979)
7- Average of trondhjemite-type, Norway (Barker and Millard Jr., 1979)
8- Average of 1 to 7
9- Average of Salobo trondhjemitic gneisses

Table 5.3 Average composition of trondhjemites selected from the literature (continued)

Sample no.	1	2	3	4	5	6	7	8	9
Y	41	1.4	2.55	41	--	--	--	21.5	20
Nb	14	1.8	3	14	--	--	--	8.25	14
Ba	792	518	166.5	792	477	335	328	487	143
La	60	15.6	12	60	7	28.43	8.2	27.31	93.44
Ce	97	28.2	23	97	11	60.25	16.2	47.52	255
Pb	10	7.4	4.5	10	--	--	--	8	11
Th	14	.9	--	14	.8	11.28	--	8.2	59
U	1.4	--	--	1.4	.36	--	--	.93	17.70
Zr	379	117	188	379	87	--	--	230	143

See last page for samples location.

Table 5.3 Average composition of granitic gneisses selected from the literature

Sample no.	1	2	3	4	5	6	7	8
SiO2	71.10	67.70	68.40	72.70	70.00	74.89	70.79	71.10
TiO2	.25	.42	.42	.18	.85	.05	.36	.09
Al2O3	15.90	16.80	14.70	14.60	12.35	15.07	14.90	11.93
FeO*	1.91	3.15	4.78	1.40	5.03	.58	5.61	5.38
MnO	.05	.06	----	.03	.08	.02	.04	.07
MgO	.70	1.30	2.23	.40	1.01	.29	.98	2.45
CaO	1.60	2.70	2.89	1.90	2.13	1.25	2.07	.84
Na2O	3.80	4.30	2.68	4.10	2.70	4.23	3.63	2.60
K2O	4.50	3.20	3.17	3.70	4.82	4.60	3.99	2.85
P2O5	.09	.17	----	.07	.22	.01	.11	.05
Total	99.99	99.95	99.27	99.08	99.37	100.99	100.48	97.96
Ni	5	7	15	3	6	1	6	14
Cu	10	22	22	--	7	--	15	536
Zn	--	--	--	--	62	7	34	19
Pb	--	--	29	29	23	18	25	24
Cr	7	13	34	23	13	2	15	1

1- Average of granitic gneisses, Manitoba, Canada (Ermanovics et al., 1979)
2- Average of granodioritic gneiss, Manitoba, Canada (Ermanovics et al., 1979)
3- Average of Australian and South Africa granitic gneiss (Collerson and Bridgwater, 1979)
4- Average of Amitsoq granodioritic gneiss, Greenland (Collerson and Bridgwater, 1979)
5- Average of undepleted granitic gneiss, Antarctic (Sheraton and Black, 1983)
6- Average of granitic gneiss, Scotland (Rollinson and Windley, 1980)
7- Average of 1 to 6, this table
8- Average of Salobo granitic gneiss

Table 5.3 Average composition of granitic gneisses selected from the literature (continued)

Sample no.	1	2	3	4	5	6	7	8
Th	--	--	--	--	24	2	13	30
U	--	--	--	--	1	--	1	30
Rb	140	99	121	122	102	47	105	77
Sr	386	574	190	252	130	267	140	28
Y	--	--	37	2	26	3	17	16
Zr	183	214	195	136	586	46	226	82
Nb	--	--	--	4	19	--	8	19
Ba	883	839	500	607	2310	596	955	206
Ga	--	--	20	--	16	18	18	16
V	39	74	65	--	27	--	51	2

See last page for samples location

Table 5.4 REE analysis in trondhjemitic gneiss

Sample no.	31-311
La(ppm)	192.00
Ce	255.00
Pr	23.00
Nd	73.80
Sm	8.70
Eu	1.97
Gd	7.30
Tb	1.00
Dy	5.00
Ho	.87
Er	1.60
Tm	.20
Yb	1.30
Lu	.24
ΣLREE	552.50
ΣHREE	17.51
ΣL/ΣH	31.55
ΣH/ΣL	.03
ΣREE	571.98
Eu/Eu*	.77
La/Sm_c	12.65
La/Yb_c	95.56
La/Lu_c	80.00
Ce/Yb_c	47.41
Gd/Lu_c	3.97

Table 5.5 Whole rock analyses in amphibolites

Sample no.	1 20-505	2 56-135	3 56-107 /2	4 56-138	5 56-154	6 56-224	7 56-121	8 AV-AMP.
SiO2(wt%)	48.50	49.30	50.60	49.20	49.70	49.90	44.70	48.84
TiO2	1.90	1.82	2.06	1.89	2.02	1.83	2.03	1.85
Al2O3	12.90	12.80	13.50	12.50	12.80	13.20	13.2	12.98
Fe2O3	17.40	17.70	17.90	18.90	18.40	16.80	19.50	18.08
MnO	0.09	.33	.32	.30	.24	.15	.30	.24
MgO	5.69	4.82	4.81	4.71	4.79	4.81	5.09	4.96
CaO	6.53	7.57	4.66	7.15	7.65	8.49	7.78	7.11
Na2O	3.83	2.76	3.16	2.52	2.59	2.71	2.46	2.86
K2O	1.22	1.30	1.58	1.75	1.40	1.56	1.31	1.44
P2O5	.19	.22	.23	.22	.22	.19	.14	.20
LOI	1.31	1.47	1.23	.93	.70	.62	3.85	1.44
Total	99.56	100.09	100.05	100.07	100.51	100.26	100.36	100.00
Nb(ppm)	10	9	11	8	8	9	7	9
Zr	169	159	178	165	150	129	136	155
Y	55	36	47	44	46	42	28	42
Sr	56	109	79	78	109	120	56	87
Rb	61	58	52	52	34	41	29	46
Ba	79	386	692	531	296	241	428	379
Ga	22	22	16	14	9	12	16	16
Zn	32	74	59	65	53	42	290	88
Cu	253	115	225	156	148	192	310	200
Ni	78	52	57	51	53	66	110	66
Co	46	46	44	46	46	46	140	59
Cr	103	103	81	83	76	92	130	95
V	321	275	255	305	314	272	nd	290
S	nd	901	459	673	494	688	nd	803

nd = not detected 8 - average of Salobo amphibolites

Table 5.6 Normative composition of amphibolites

Sample no.	20-505	56-135	56-1072	56-138	56-154	56-224	56-121
Orthoclase	7.21	7.68	9.34	10.34	8.27	9.22	7.74
Albite	31.95	23.35	26.74	21.32	24.45	22.93	20.82
Anortite	14.41	18.70	17.99	17.63	17.82	19.25	21.11
Nepheline	.25	-----	-----	-----	-----	-----	-----
Diopside	14.14	14.80	3.08	13.98	15.90	18.41	14.10
Hypersthene	-----	-----	30.21	19.63	15.80	14.20	6.10
Olivine	24.51	28.94	5.22	10.24	11.67	10.11	24.98
Ilmenite	3.61	3.46	3.91	3.59	3.84	3.48	3.86
Apatite	.44	.51	.53	.51	.51	.44	.32

Table 5.7 REE analyses in amphibolites

Sample no.	1 20-505	2 49-526	3 56-107 /2
La(ppm)	26.40	23.80	15.40
Ce	56.00	39.70	29.60
Pr	6.20	4.30	3.80
Nd	25.30	16.50	16.50
Sm	5.20	3.00	3.40
Eu	2.28	1.02	.82
Gd	6.60	3.80	6.10
Tb	1.30	.80	1.10
Dy	8.40	5.20	7.90
Ho	2.23	1.16	1.87
Er	5.70	3.50	5.00
Tm	.90	.50	.80
Yb	6.80	3.50	5.20
Lu	.86	.60	.83
ΣREE	154.17	107.38	98.32
ΣLREE	119.10	87.30	68.70
ΣHREE	32.79	19.06	28.80
ΣL/ΣH	3.63	4.58	2.38
La/Yb_c	2.51	4.40	1.91
La/Lu_c	1.04	1.34	.63
Ce/Yb_c	1.99	2.74	1.37
La/Sm_c	2.91	4.55	2.59
Gd/Lu_c	1.00	.82	.96
Eu/Eu*	1.21	.93	.56

Table 5.8 Whole rock analyses in Type I iron formation

Sample no.	1 50-92	2 50-135 /1	3 50-135 /3	4 56-217 /1	5 56-217 /2	6 56-217 /4	7 56-217 /5	8 61-230 /4	9 49-351 /4
SiO2(wt%)	38.10	50.00	56.50	87.80	48.20	46.20	68.90	8.43	28.00
TiO2	.05	.04	.06	.02	.04	.02	.04	.07	.12
Al2O3	.72	.95	.65	.11	.49	.20	.37	.83	1.88
Fe2O3	60.70	47.50	41.30	7.39	50.20	53.20	27.20	83.00	64.00
MnO	.18	1.40	1.26	.40	.25	.30	.58	.21	.49
MgO	.12	.48	.53	.26	.36	.28	1.31	.03	2.77
CaO	.33	.42	.39	1.88	1.26	.82	2.43	4.45	1.53
Na2O	<.01	<.01	<.01	<.01	<.01	.01	.01	<.01	.08
K2O	.11	.06	.11	.02	.06	.05	.06	.03	.26
P2O5	.11	.06	.06	.01	.06	.03	.05	.07	1.03
LOI	-1.00	-.77	-.46	1.54	-.92	-.77	-.61	-1.00	-.15
Total	99.50	100.20	100.40	99.44	100.00	100.40	100.40	96.13	100.10
Nb(ppm)	8	6	7	10	6	12	4	nd	68
Zr	nd	nd	nd	nd	nd	nd	nd	nd	nd
Y	nd	24	nd	nd	21	17	13	nd	163
Sr	27	nd	nd	12	nd	nd	nd	nd	35
Rb	82	1	8	nd	11	5	nd	nd	179
Ba	65	nd	nd	nd	nd	nd	nd	nd	59
Ga	nd	nd	nd	nd	nd	nd	nd	51	nd
La	1587	153	289	nd	674	240	59	na	3403

nd = not detected
na = not analyzed

Table 5.8 Whole rock analyses in Type I iron formation (continued)

Sample no.	1 50-92	2 50-135 /1	3 50-135 /3	4 56-217 /1	5 56-217 /2	6 56-217 /4	7 56-217 /5	8 61-230 /4	9 49-351 /4
Pb(ppm)	nd	nd	nd	nd	31	184	nd	14	nd
Zn	61	189	139	25	37	29	65	91	20
Cu	1998	315	1905	50	2374	1765	547	25719	4321
Ni	16	15	34	4	15	12	15	202	93
Co	44	66	79	251	53	56	59	nd	64
Cr	nd	nd	12	nd	nd	1	9	99	74
V	nd	nd	nd	nd	nd	nd	30	108	1
S	424	nd	449	nd	771	775	nd	3681	11057
Au	na	.1	.1	.1	.1	.1	.1	.6	.6
Ag	na	nd	nd	nd	nd	nd	1	3	nd

nd = not detected
na = not analyzed

Table 5.9 Whole rock analyses in iron formation

Sample no.	1 61-120 /2	2 61-230 /3	3 17-312 /2	4 49-337 /1	5 50-86	6 56-217 /3	7 17-312 /3	8 49-243 /3	9 49-337 /3
SiO2(wt%)	47.90	12.14	22.20	11.90	43.60	65.00	34.70	53.90	22.70
TiO2	.14	.10	.34	.25	.12	.08	.57	1.05	.54
Al203	1.97	1.26	4.71	3.56	2.07	2.26	9.14	9.56	6.68
Fe203	49.30	80.88	67.70	79.00	52.70	29.40	47.90	29.80	61.30
MnO	.81	.34	.15	.19	.88	.63	.39	.59	.40
MgO	.10	.01	1.12	2.36	.17	1.13	2.17	1.67	3.75
CaO	.59	4.56	.64	.49	.51	1.56	1.02	1.01	.76
Na20	.05	.00	.02	.05	<.01	.11	.04	.14	.09
K20	.08	.00	2.19	.95	.12	.30	3.73	1.81	2.07
P205	.09	.04	.29	.10	.10	.12	.25	.11	.12
LOI	-.77	0.00	-.38	-.69	.00	-.38	.23	.08	.62
Total	100.30	99.32	99.10	98.20	100.30	100.20	100.30	99.80	99.10
Nb(ppm)	5	nd	17	15	8	7	27	11	7
Zr	nd	nd	346	nd	30	nd	442	153	32
Y	46	nd	350	144	26	22	nd	30	nd
Sr	nd	nd	nd	22	17	28	20	19	48
Rb	6	nd	nd	nd	27	20	573	131	1992
Ba	nd	nd	1116	322	nd	22	1120	346	694
Ga	nd	36	4	nd	nd	nd	16	4	nd
La	353	nd	7296	2286	306	370	1653	114	772

1-2-5-6- Type I iron formation 3-4-7-8-9- Type II iron formation
nd = not detected
na = not analyzed

Table 5.9 Whole rock analyses in iron formation (continued)

	1	2	3	4	5	6	7	8	9
Sample no.	61-120 /2	61-230 /3	17-312 /2	49-337 /1	50-86	56-217 /3	17-312 /3	49-243 /3	49-337 /3
Pb(ppm)	nd	10	nd	nd	nd	nd	nd	23	nd
Zn	nd	72	nd	nd	46	42	nd	35	19
Cu	7270	12307	10093	7575	2106	3155	7364	1783	4833
Ni	19	162	42	102	11	14	59	40	137
Co	65	nd	54	50	44	80	66	105	60
Cr	nd	66	nd	130	nd	nd	nd	4	307
V	7	86	3	19	nd	3	24	202	78
S	2739	2695	6896	6103	638	1434	3145	430	3068
Au	1.1	.3	.5	.6	.1	.1	na	.1	na
Ag	2.0	1.0	7.0	3.0	nd	1.0	na	nd	1.0

1-2-5-6- Type I iron formation 3-4-7-8-9- Type II iron formation
nd = not detected
na = not analyzed

Table 5.9 Whole rock analyses in Type II iron formation (continued)

Sample no.	1 49-337 /2	2 49-351 /5	3 50-135 /2	4 50-470 /1	5 50-470 /2	6 50-470 /3	7 50-470 /4	8 50-470 /5	9 50-569 /1
SiO2(wt%)	30.00	36.70	45.10	37.60	41.40	37.50	37.90	45.50	32.20
TiO2	.41	.59	.39	.66	.56	.72	.78	.43	.63
Al2O3	8.71	5.94	9.11	9.29	8.69	9.88	10.00	9.36	8.92
CaO	.87	.80	1.13	.72	.61	.47	1.36	.82	.69
MgO	4.21	4.02	.86	5.05	6.04	5.48	4.34	4.02	4.37
Na2O	.02	.21	.07	.15	.44	.17	.26	1.93	.15
K2O	1.81	.59	1.50	2.01	1.99	2.96	2.34	1.68	2.03
Fe2O3	53.00	50.50	38.50	43.90	39.00	38.80	42.20	35.50	50.50
MnO	1.19	.66	3.34	.66	.24	.25	.51	.32	.74
P2O5	.09	.15	.23	.07	.06	.07	.60	.05	.10
LOI	-.23	-.92	.08	.08	.77	3.08	.08	-.07	-.38
Total	100.10	99.40	100.40	100.30	99.90	99.60	100.50	99.70	100.10
Nb(ppm)	9	26	25	12	9	3	11	nd	nd
Zr	34	61	457	66	49	49	75	99	51
Y	14	152	40	19	nd	nd	nd	nd	nd
Sr	nd	16	22	nd	40	30	34	66	19
Rb	504	106	310	314	299	389	414	154	367
Ba	515	82	305	630	524	891	901	483	1012
Ga	nd	nd	nd	nd	6	15	13	7	10
La	596	804	338	221	22	89	3	217	81

nd = not detected

Table 5.9 Whole rock analyses in Type II iron formation (continued)

	1	2	3	4	5	6	7	8	9
Sample no.	49-337 /2	49-351 /5	50-135 /2	50-470 /1	50-470 /2	50-470 /3	50-470 /4	50-470 /5	50-569 /1
Pb(ppm)	nd	nd	11	29	9	nd	nd	nd	nd
Zn	21	38	92	24	34	35	30	33	20
Cu	4827	1562	2998	1577	126	348	1219	199	3318
Ni	138	198	33	299	242	287	223	156	372
Co	61	63	69	71	80	75	79	85	68
Cr	56	633	1	387	390	527	498	234	506
V	59	55	11	86	81	106	148	97	107
S	1919	2032	924	404	nd	nd	153	nd	1996
Au	.4	.1	.1	.1	.1	.1	.1	.1	.1
Ag	1.0	nd	nd	nd	nd	nd	nd	nd	nd

nd = not detected

Table 5.9 Whole rock analyses in Type II iron formation (continued)

Sample no.	1 50-682 /2	2 50-682 /4	3 50-682 /5	4 50-682 /6	5 56-280 /2	6 56-280 /5	7 61-109 /1	8 61-120 /3	9 61-124 /2
SiO2(wt%)	41.90	41.30	43.90	43.10	32.96	55.26	44.90	31.40	46.20
TiO2	.32	.44	.46	.52	.56	.50	.70	.43	.65
Al2O3	7.22	8.74	9.34	9.48	9.38	9.56	9.87	8.38	8.52
Fe2O3	44.70	43.80	38.90	39.50	49.12	26.46	36.10	56.40	37.40
MnO	.88	.85	.70	.84	3.76	1.82	.42	1.75	.41
MgO	3.58	3.60	3.21	3.46	1.70	1.76	1.10	.43	1.13
CaO	1.04	1.10	1.34	1.23	.80	.58	1.10	1.11	1.02
Na2O	.06	.10	.52	.14	0.00	0.00	.16	.04	.14
K2O	.22	.63	1.45	1.25	.16	2.20	4.21	.84	3.86
P2O5	.25	.30	.38	.28	0.01	.06	.09	.11	.09
LOI	-1.00	-.69	0.00	-.46	0.00	0.00	1.08	-.69	.77
Total	99.20	100.20	100.30	99.40	98.44	98.40	99.80	100.20	100.20
Nb(ppm)	32	64	72	74	6	2	7	7	9
Zr	20	50	32	57	45	48	78	59	81
Y	146	170	183	41	nd	3	nd	121	nd
Sr	14	16	16	nd	nd	nd	24	29	31
Rb	45	161	199	172	nd	50	453	258	444
Ba	62	283	544	479	nd	33	525	349	532
Ga	nd	nd	nd	nd	25	14	nd	nd	nd
La	1568	1278	847	996	nd	nd	448	903	583

nd = not detected

Table 5.9 Whole rock analyses in Type II iron formation (continued)

Sample no.	1 50-682 /2	2 50-682 /4	3 50-682 /5	4 50-682 /6	5 56-280 /2	6 56-280 /5	7 61-109 /1	8 61-120 /3	9 61-124 /2
Pb(ppm)	1003	199	88	114	6	4	8	nd	15
Zn	nd	nd	nd	nd	107	58	37	nd	54
Cu	9411	8891	6351	6467	4766	3967	2391	8253	151
Ni	69	86	103	108	147	109	42	21	34
Co	69	71	76	73	40	107	81	60	73
Cr	nd	4	9	16	84	62	25	16	27
V	57	77	90	112	204	165	128	81	100
S	8512	7726	3384	4060	922	708	393	4488	nd
Au	.5	.5	.5	.5	.1	na	.1	1.8	.1
Ag	nd	nd	nd	nd	nd	nd	nd	4.0	nd

nd = not detected
na = not analyzed

Table 5.9 Whole rock analyses in Type II iron formation (continued)

	1	2	3	4	5	6	7	8	9
Sample no.	61-230 /2	17-312 /1b	17-312 /4	36-277 /1	36-277 /2	36-277 /3	36-277 /4	36-277 /5	49-243 /1
SiO2(wt%)	22.78	52.40	58.30	43.10	42.69	46.92	48.30	41.39	50.30
TiO2	.60	.81	.74	.82	.78	.61	.81	.78	.99
Al2O3	7.34	11.80	11.20	13.18	12.04	12.66	12.00	11.98	10.70
Fe2O3	62.26	26.60	23.00	34.04	35.66	31.98	30.10	36.96	32.40
MnO	.40	.67	.69	.98	1.88	.98	.98	1.46	1.16
MgO	.66	1.87	1.28	2.04	2.30	.84	2.24	2.32	1.59
CaO	1.64	1.33	1.32	.70	.86	.32	.44	.46	1.20
Na2O	0.00	.07	.05	0.00	0.00	0.00	.11	0.00	.11
K2O	2.42	3.96	2.88	3.40	2.56	3.00	3.95	3.06	1.43
P2O5	.06	.34	.30	.08	.08	0.01	.09	.08	.15
LOI	1.59	.31	.31	.39	.00	.99	.62	.70	.00
Total	99.75	100.30	100.20	98.73	98.85	98.30	99.64	99.16	100.10
Nb(ppm)	3	25	22	6	4	4	10	8	8
Zr	10	472	366	82	65	78	83	77	134
Y	38	29	24	37	18	5	15	1	33
Sr	nd	26	25	nd	nd	nd	nd	nd	19
Rb	35	255	147	67	48	85	84	66	112
Ba	166	788	548	274	126	297	227	130	390
Ga	25	7	6	27	21	21	27	23	3
La	nd	403	240	nd	nd	nd	nd	nd	228

nd = not detected

Table 5.9 Whole rock analyses in Type II iron formation (continued)

	1	2	3	4	5	6	7	8	9
Sample no.	61-230 /2	17-312 /1b	17-312 /4	36-277 /1	36-277 /2	36-277 /3	36-277 /4	36-277 /5	49-243 /1
Pb(ppm)	9	5	nd	6	4	4	6	5	10
Zn	62	26	37	60	65	66	73	70	22
Cu	6476	2699	31	2607	7058	758	2070	1224	4063
Ni	223	50	39	232	180	161	180	164	37
Co	17	75	74	140	175	157	56	112	84
Cr	71	4	nd	76	90	72	67	82	10
V	197	60	66	260	249	321	268	266	193
S	2163	662	585	445	1071	247	337	329	1543
Au	na	.1	.1	na	na	na	.1	na	.3
Ag	na	1.0	nd	na	na	na	na	na	2.0

na = not analyzed
nd = not detected

Table 5.9 Whole rock analyses in Type II iron formation (continued)

Sample no.	1 49-366 /1	2 50-582 /3	3 50-682 /1	4 50-682 /3	5 56-280 /1	6 61-109 /2	7 61-124 /1	8 61-230 /1	9 61-230 /5
SiO2(wt%)	53.20	37.80	54.30	46.10	38.68	36.50	37.40	25.65	43.20
TiO2	.75	1.03	.41	.41	.80	.92	.37	.60	.73
Al2O3	12.20	11.50	10.30	10.70	14.04	12.40	12.80	12.92	10.40
Fe2O3	26.00	37.80	23.70	36.00	38.06	40.60	42.30	53.18	35.00
MnO	.32	1.13	.33	.82	2.32	.44	2.96	1.80	.67
MgO	1.58	3.86	4.02	3.66	1.96	1.35	.52	.76	1.09
CaO	1.04	1.32	1.45	.95	.62	1.50	1.72	2.30	2.88
Na2O	.43	.44	2.13	.10	0.00	.19	.12	0.00	.46
K2O	2.97	3.67	1.58	1.76	3.10	5.02	1.56	1.78	3.00
P2O5	.30	.28	.05	.08	.04	.10	.11	.02	.09
LOI	.47	1.47	1.08	-.38	0.00	1.39	.16	0.00	1.77
Total	99.40	100.40	99.40	100.30	99.82	100.50	100.10	98.99	99.30
Nb(ppm)	22	27	12	74	nd	6	7	9	5
Zr	429	181	26	31	53	120	25	53	49
Y	43	10	33	49	nd	nd	83	278	51
Sr	27	35	53	13	nd	45	nd	nd	nd
Rb	227	382	135	210	51	553	176	37	78
Ba	906	907	316	629	130	663	367	96	137
Ga	15	nd	nd	2	22	4	nd	26	15
La	440	515	83	145	0	554	531	nd	nd

nd = not detected

Table 5.9 Whole rock analyses in Type II iron formation (continued)

	1	2	3	4	5	6	7	8	9
Sample no.	49-366 /1	50-582 /3	50-682 /1	50-682 /3	56-280 /1	61-109 /2	61-124 /1	61-230 /1	61-230 /5
Pb(ppm)	11	nd	nd	nd	4	nd	7	7	4
Zn	20	31	24	19	83	34	nd	46	55
Cu	2569	1995	980	1420	1448	2566	7034	2083	2298
Ni	83	117	101	104	157	60	19	272	167
Co	85	73	87	89	115	88	73	31	158
Cr	nd	68	18	12	71	25	19	64	52
V	59	97	112	86	247	156	60	175	307
S	990	722	174	376	353	343	4269	591	414
Au	.4	.1	.1	.1	na	.1	.6	.1	.1
Ag	nd	nd	nd	nd	nd	nd	2.0	nd	nd

na = not analyzed
nd = not detected

Table 5.10 REE analyses in iron formation

	1	2	3	4
Sample no.	50-682 /1	56-217 /3	49-351 /5	61-230 /2
La(ppm)	73.40	295.00	343.00	706.00
Ce	99.40	357.00	488.00	986.00
Pr	9.00	26.60	46.90	86.20
Nd	29.20	80.40	163.00	280.00
Sm	3.20	8.90	24.50	40.60
Eu	2.24	17.60	4.02	14.50
Gd	3.30	8.30	23.50	37.40
Tb	.60	1.10	3.80	6.00
Dy	4.00	3.20	21.30	29.40
Ho	1.27	.48	5.21	5.74
Er	3.40	.90	18.00	13.50
Tm	.50	.10	2.50	1.50
Yb	3.00	.40	11.20	8.20
Lu	.32	.06	.96	.85
ΣREE	232.83	800.04	1155.80	2215.80
ΣLREE	214.20	767.90	1065.40	2098.80
ΣHREE	16.39	14.54	86.46	102.59
ΣL/ΣH	13.06	52.81	12.32	20.45
La/Lu_c	22.93	491.80	35.70	83.04
La/Sm_c	13.15	19.00	8.02	9.97
Gd/Lu_c	1.34	18.09	3.20	5.75
Sm/Nd	.10	.11	.15	.14
Eu/Eu^*	2.13	6.34	.51	1.16

1-2-3- Type II iron formation
4- Type I iron formation

Table 5.11 Whole rock analyses in volcanic rocks of Grao Para Group

Sample no.	1 GB-82A	2 GB-82B	3 GB-81	4 GB-86	5 GB-90	6 GB-87	7 GB-93	8 GB-67	9 GB-102
SiO2(wt%)	50.54	49.51	50.29	54.34	48.70	49.06	53.36	53.82	54.77
TiO2	1.33	1.52	1.55	.76	.81	.83	.84	.76	.84
Al2O3	14.31	14.96	14.96	15.17	15.89	15.97	15.09	14.47	15.02
Fe2O3	17.39	15.23	15.71	11.45	13.46	13.00	13.38	12.21	10.53
MnO	.39	.17	.19	.19	.19	.19	.22	.52	.58
MgO	6.22	5.60	5.75	6.30	7.74	7.75	5.45	6.58	5.96
CaO	7.74	9.86	9.66	7.13	10.84	10.80	8.78	7.14	6.35
Na2O	2.85	2.84	2.60	4.17	1.92	3.17	2.48	2.91	3.48
K2O	.78	.59	.75	1.46	1.08	1.02	1.17	2.30	2.73
P2O5	.09	.12	.15	.05	.08	.09	0.08	.07	.06
H2O	.81	.43	.68	1.07	1.91	1.95	1.62		2.05
Total	100.06	99.02	100.19	99.98	99.49	100.70	99.64	99.67	99.37
Sr(ppm)	79	112	---	127	---	131	146	---	---
Rb	20	18	---	36	---	41	43	---	---
Ba	376	151	290	522	213	636	594	1847	1736
La	9	8	8	13	3	12	15	---	12
Ni	59	57	66	66	133	78	82	63	61
Co	57	56	56	45	62	47	57	50	44
Cr	202	180	178	259	308	167	70	141	137
Sc	45	43	45	36	38	34	37	37	38

From: Gibbs et al., (1986) Volcanic rocks of Parauapebas Group, 1 to 3 lower unit 4 to 7 intermediate unit, 8 and 9 upper unit.

Table 5.11 Whole rock analyses in volcanic rocks of Grao Para Group (continued)

	1 GB-74	2 GB-72	3 GB-104	4 GB-96	5 4-293	6 8-390	7 4-288	8 9-188	9 9-175
SiO2(wt%)	54.07	57.69	54.40	54.39	49.50	47.80	49.10	48.80	48.10
TiO2	.86	.86	.88	.97	1.00	1.10	1.10	1.40	2.10
Al2O3	14.93	13.91	14.51	14.00	14.70	12.90	14.30	12.80	13.10
Fe2O3	13.69	11.57	11.20	13.00	9.90	13.20	11.44	14.30	13.42
MgO	7.17	4.84	5.81	5.57	5.20	5.60	6.60	4.80	5.20
CaO	4.10	5.05	6.50	7.14	9.20	9.20	9.40	6.80	7.10
Na2O	2.72	2.66	2.60	3.08	2.70	2.10	1.90	.86	2.00
K2O	2.39	3.16	3.22	2.56	1.70	1.30	1.80	2.80	3.00
MnO	.32	.36	.62	.21	.33	.28	.28	.23	.24
P2O5	.06	.07	.04	.07	.10	.10	.11	.12	.36
H2O	----	2.58	2.15	1.67	----	----	----	----	----
Total	99.07	99.12	98.77	99.81	99.69	100.31	99.86	99.86	100.25
Ba(ppm)	1499	1759	---	1367	---	---	---	---	---
La	---	16	---	17	---	---	---	---	---
Ni	29	59	---	81	---	---	---	---	---
Co	45	50	---	51	---	---	---	---	---
Cr	121	77	---	79	---	---	---	---	---
Sc	41	37	---	40	---	---	---	---	---

1 to 4 Parauapebas Group volcanic rocks (upper unit) From: Gibbs et al., (1986)
5 to 9 "Upper volcanic Sequence". From: Ferreira Filho and Danni (1985)

Table 5.12 Whole rock analyses in metagraywackes

	1	2	3	4	5	6
Sample no.	12-214	17-350 /2	17-350 /3	17-350 /4	17-350 /6	17-350 /7
SiO2(wt%)	65.90	60.00	57.10	59.50	59.00	60.00
TiO2	.81	.85	.93	.86	.92	.88
Al2O3	11.20	14.30	14.20	13.30	14.70	13.90
Fe2O3	13.50	15.40	17.60	17.30	15.90	16.50
MnO	.18	.14	.16	.17	.11	.19
MgO	1.77	1.68	2.14	1.71	1.42	1.47
CaO	.84	.92	.80	.79	.81	.86
Na2O	1.34	.52	.34	.20	.24	.37
K2O	2.46	4.06	4.53	3.96	4.14	4.28
P2O5	.11	.37	.35	.34	.35	.34
LOI	1.16	1.54	1.85	1.77	2.23	1.62
Total	99.27	99.78	100.00	99.90	99.82	100.41
Nb(ppm)	18	10	24	24	25	26
Zr	274	417	440	418	500	460
Y	26	18	37	28	24	nd
Sr	62	45	25	26	23	33
Rb	89	123	144	130	117	148
Ba	164	311	338	342	396	416
Ga	6	20	25	24	26	21
La	135	97	125	169	101	145

nd = not detected

Table 5.12 Whole rock analyses in metagraywackes (continued)

Sample no.	1 12-214	2 17-350 /2	3 17-350 /3	4 17-350 /4	5 17-350 /6	6 17-350 /7
Pb(ppm)	9	6	6	7	5	nd
Zn	nd	31	30	29	30	25
Cu	3419	18	112	347	19	1083
Ni	31	42	54	47	40	40
Co	45	107	83	88	82	95
Cr	187	11	4	10	17	8
V	143	66	89	74	84	85
S	1140	nd	nd	nd	nd	297

nd = not detected

Table 5.13 REE analyses in metagraywackes

Sample no.	1 12-214	2 17-350 /4
La(ppm)	150.00	240.00
Ce	196.00	347.00
Pr	19.60	29.40
Nd	63.40	95.80
Sm	9.40	11.80
Eu	5.45	6.00
Gd	8.50	9.60
Tb	1.40	1.50
Dy	8.10	6.20
Ho	1.46	1.20
Er	4.10	2.40
Tm	.70	.20
Yb	4.00	2.10
Lu	.69	.38
ΣEE	472.80	753.58
ΣLREE	438.40	724.00
ΣHREE	28.95	23.58
ΣL/ΣH	15.14	30.70
La/Lu_c	21.74	63.19
La/Sm_c	9.15	11.66
Gd/Lu_c	1.61	3.30
Sm/Nd	.14	.12
Eu/Eu*	1.86	1.73

Table 5.14 Whole rock analyses in quartzites

Sample no.	1 20-162	2 20-184	3 20-190	4 28-202	5 28-214	6 28-400	7 28-417	8 28-449
SiO2(wt%)	95.30	93.50	92.90	86.70	83.00	75.10	91.70	96.30
TiO2	.06	.06	.08	.12	.21	.24	.11	.06
Al2O3	3.06	3.11	3.36	6.32	10.80	10.50	4.60	1.32
Fe2O3	.29	1.03	1.89	3.38	.78	6.13	.29	.26
MnO	.01	.01	.03	.05	.01	.09	.02	.02
MgO	.04	.05	.12	.74	.40	1.75	.09	.12
CaO	.02	.03	.03	.06	.05	.09	.29	.22
Na2O	.08	.32	.15	.19	.39	.07	.12	.08
K2O	.83	.78	.77	1.46	3.06	3.21	1.32	.32
P2O5	.02	.02	.02	.03	.03	.03	.02	.02
LOI	.70	.93	.93	1.39	1.54	2.16	.93	.70
Total	100.41	99.84	100.28	100.44	100.27	99.37	99.49	99.42
Co(ppm)	nd	nd	1	20	nd	24	nd	nd
Ni	3	11	11	8	4	12	3	4
Cu	649	1034	387	855	103	305	601	603
Zn	17	22	22	18	18	26	20	20
Mo	10	10	10	10	10	10	10	10
Pb	nd	nd	9	nd	6	nd	nd	nd
Th	10	10	10	10	10	10	10	10
U	10	10	10	10	10	10	10	10
Cr	12	10	12	31	57	63	31	30

nd = not detected

Table 5.14 Whole rock analyses in quartzites (continued)

Sample no.	1 20-162	2 20-184	3 20-190	4 28-202	5 28-214	6 28-400	7 28-417	8 28-449
Rb(ppm)	11	21	23	26	85	70	38	nd
Sr	nd	13	nd	13	13	19	13	nd
Y	9	8	8	8	nd	11	nd	9
Zr	19	13	25	34	83	102	51	17
Nb	nd	3	3	4	6	6	4	nd
Ba	25	24	30	29	93	244	46	nd
Ga	nd	nd	nd	nd	9	4	nd	nd
La	nd	nd	nd	14	12	12	13	nd
V	nd	nd	nd	6	21	44	11	1
S	491	1742	131	nd	nd	nd	nd	nd

Table 5.15 REE analyses in quartzites

Sample no.	1 20-184	2 28-214	3 28-449
La(ppm)	6.00	11.10	5.20
Ce	10.30	19.00	9.20
Pr	1.20	2.00	.90
Nd	4.50	6.60	3.60
Eu	.32	.29	.21
Sm	.60	.90	.30
Gd	0.40	.40	<.10
Tb	0.10	<.10	<.10
Dy	0.20	.30	<.10
Ho	<0.50	.14	.11
Er	<0.01	.20	<.10
Tm	<0.01	<.10	<.10
Yb	<0.01	.40	<.10
Lu	<0.05	.10	<.05
ΣREE	23.62	41.43	19.52
ΣLREE	22.60	39.60	19.41
ΣHREE	.70	1.54	.11
ΣL/ΣH	32.28	25.71	176.45
La/Lu_c	----	11.43	----
La/Sm_c	5.49	6.76	9.54
Gd/Lu_c	----	.54	----
Sm/Nd	.13	.13	.08
Eu/Eu*	2.01	1.50	2.06

<.10 below the detection limit

Table 5.16 Normative composition of "quartz-free" quartzites

Sample no.	1 20-184	2 28-202	3 20-162	4 20-190	5 28-214	6 28-417	7 28-449
Quartz	47.28	51.94	45.21	24.40	39.79	40.13	.34
Orthoclase	21.57	19.21	30.55	30.20	34.10	32.80	34.87
Albite	12.61	3.55	4.15	8.38	6.18	4.23	12.44
Anortite	.11	.25	----	.09	.12	5.53	17.74
Corundum	8.11	9.77	12.25	15.15	12.87	10.49	9.04
Hypersthene	.57	4.11	.60	1.97	.45	.92	5.50
Ilmenite	.09	.24	.13	.41	.02	.17	.77
Hematite	4.82	7.52	1.80	12.56	1.47	1.22	4.79
Apatite	.21	.14	.28	.30	.12	.19	.83
Rutile	.23	.14	.30	.32	.92	.37	.69

Table 5.17 Whole rock analyses in granitoid rocks

Sample no.	1 12-477	2 19-199	3 19-206	4 KA6-88	5 KA6A-88	6 KA6B-88	7 AV12-19	8 AV-KA
SiO2(wt%)	67.40	67.20	66.40	72.50	71.90	71.40	67.00	71.93
TiO2	.65	.61	.61	.30	.29	.30	.62	.29
Al203	13.60	13.80	14.20	13.00	12.80	12.90	13.86	12.90
Fe203	2.50	2.50	2.50	1.20	1.60	2.00	2.50	1.60
FeO	2.00	2.00	2.20	1.70	1.40	1.60	2.06	1.56
MnO	.04	.04	.04	.04	.04	.04	.04	.04
MgO	.73	.80	.76	.23	.20	.20	.76	.21
CaO	1.20	1.50	1.20	1.40	1.40	1.40	1.30	1.40
Na20	4.30	4.50	4.50	6.00	5.10	5.30	4.33	5.46
K20	6.10	5.50	5.80	3.40	5.00	4.50	5.80	4.30
P205	.20	.19	.19	.07	.08	.06	.19	.07
LOI	.84	1.03	1.13	.16	.14	.10	1.00	.13
Total	99.56	99.67	99.53	100.00	99.95	99.80	99.46	99.89
Cu(ppm)	1084	40	63	22	22	18	395	17
Pb	10	13	16	11	20	17	13	16
Zn	19	31	23	7	60	5	21	24
Ni	32	16	16	10	5	5	21	6
Cr	16	6	11	<5	<5	<5	11	5
V	108	62	47	80	72	63	72	72

< 5 = below the detection limit
1 to 3 - alkali feldspar quartz-syenite (YSG)
4 to 6 - granite (OSG)
7 - YSG average composition 8 - OSG average composition

Table 5.17 Whole rock analyses in granitoid rocks (continued)

Sample no.	1 12-477	2 19-199	3 19-206	4 KA6-88	5 KA6A-88	6 KA6B-88	7 AV12-19	8 AV-KA
Zr(ppm)	610	440	470	320	210	280	506	270
Nb	62	20	20	24	10	8	34	14
Y	55	62	56	120	100	97	57	105
Ga	26	25	22	20	19	17	24	18
F	1800	2200	2200	100	100	500	2066	233
Cl	230	240	270	1520	940	740	246	1066
Ba	1580	1620	1610	540	700	620	1603	620
Rb	200	220	220	80	120	96	213	98
Sr	150	200	200	73	110	96	183	93
Th	37	46	34	28	40	29	39	32
B	31	<10	<10	36	42	18	17	32

< 10 = below the detection limit 1 to 3 - YSG, 4 to 6 - OSG
7 - average YSG 8 - average OSG

Table 5.18 Normative composition of granitoid rocks

Sample no.	1 12-477	2 19-199	3 19-206	4 KA6-88	5 KA6A-88	6 KA6B-88
Quartz	16.72	16.87	15.09	22.39	21.62	21.65
Orthoclase	36.05	32.50	34.28	20.09	29.55	26.59
Albite	35.99	38.08	38.08	47.94	38.00	41.30
Diopside	3.74	1.21	1.42	5.61	5.10	4.38
Hypersthene	.73	4.00	2.67	.09	.22	.61
Acmite	.34	.75	1.64	2.49	4.54	3.12
Magnetite	3.45	3.62	3.62	.49	.05	1.33
Ilmenite	1.23	1.16	1.16	.57	.55	.57
Apatite	.46	.44	.44	.16	.19	.14

1 -2 -3- Alkali feldspar quartz-syenite (YSG)
4 -5 -6- Granite (OSG)

Table 5.19 REE analyses in granitoid rocks

Sample no.	1 12-477	2 19-199	3 19-206	4 KA6A88	5 KA6B88	6 AV12-14	7 AV-KA
La(ppm)	120.50	140.20	150.60	160.30	145.60	137.10	152.95
Ce	182.50	277.20	231.40	183.60	155.80	161.03	169.70
Nd	60.50	76.81	79.27	75.39	70.29	72.14	72.84
Sm	7.70	9.70	10.00	12.70	11.80	9.13	12.25
Eu	1.51	1.80	1.76	1.88	1.85	1.69	1.86
Gd	4.66	5.53	5.64	11.37	11.74	5.27	11.55
Dy	2.97	3.06	3.10	9.53	10.40	3.04	9.96
Ho	.47	.46	.43	1.93	2.24	.45	2.08
Er	1.21	1.13	1.08	5.69	6.34	1.14	6.01
Yb	1.07	1.03	1.01	6.01	6.46	1.03	6.23
Lu	.17	.17	.16	.80	.87	.16	.83
ΣLREE	371.20	503.90	471.20	431.90	383.40	448.76	407.65
ΣHREE	12.06	13.18	13.18	37.21	39.90	12.80	38.55
ΣL/ΣH	30.77	38.23	35.75	11.60	9.60	34.91	10.60
ΣREE	383.20	517.00	484.30	469.10	423.30	461.50	446.20
Eu/Eu*	.76	.74	.72	.48	.48	.74	.48
La/Yb_c	67.96	82.49	90.36	16.03	13.65	80.27	14.84
La/Lu_c	73.02	84.96	96.98	20.65	17.24	88.28	18.98
Eu/Sm	.19	.18	.17	.14	.15	.18	.15

1 - 2 - 3 - YSG 4 - 5 - OSG 6 - Average YSG 7 - Average OSG

Table 5.20 Whole rock analyses in diabases

Sample no.	1 24-179	2 24-190	3 24-195
SiO2(wt%)	48.80	50.30	50.10
TiO2	3.23	2.83	2.94
Al2O3	12.20	12.50	12.30
Fe2O3	17.50	16.20	16.30
MnO	.31	.24	.24
MgO	4.77	4.24	4.14
CaO	7.01	8.42	8.35
Na2O	1.97	4.45	2.52
K2O	.54	1.19	1.21
P2O5	.40	.46	.48
LOI	2.31	1.31	1.39
Total	99.10	100.20	100.10
Nb(ppm)	18	19	18
Zr	263	261	281
Y	55	46	54
Sr	204	284	282
Rb	13	44	32
Ba	282	405	488
Ga	18	26	18
La	15	11	243
Pb	10	nd	9
Zn	81	125	123
Cu	3452	162	55
Ni	42	23	24
Co	49	46	45
Cr	43	18	29
V	327	277	288
S	2012	1110	843

nd = not detected

Table 5.21 Diabase normative composition

Sample no.	1 24-179	2 24-190	3 24-195
Quartz	58.22	0.00	2.08
Orthoclase	3.19	7.03	7.15
Albite	16.67	32.99	21.32
Anortite	22.85	10.62	18.68
Nepheline	0.00	2.53	0.00
Diopside	7.89	23.89	16.65
Hypersthene	32.04	0.00	24.37
Olivine	0.00	15.72	0.00
Ilmenite	6.13	5.37	5.58
Apatite	0.93	1.07	1.11

1 - chilled margin
2 - hydrothermally altered sample
3 - centre of the dyke

Table 6.1. Fayalite analyses in iron formations (continued)

Sample no.	1 49-3515A	2 idem	3 idem	4 61-2303	5 49-3514	6 idem	7 61-2301	8 idem	9 idem
SiO_2(wt%)	29.11	29.88	29.84	30.02	29.44	29.96	29.45	28.23	29.21
TiO_2	0.01	0.00	0.02	0.00	0.02	0.02	0.01	0.02	0.02
FeO*	66.60	67.79	67.58	69.53	68.34	67.12	69.30	69.06	67.71
Cr_2O_3	0.00	0.05	0.00	0.03	0.00	0.08	0.00	0.00	0.00
MnO	0.70	0.61	0.68	0.40	0.78	0.77	0.80	0.64	0.87
MgO	1.99	1.97	2.04	0.10	2.09	1.98	0.55	0.54	0.49
CaO	0.04	0.01	0.00	0.04	0.00	0.00	0.00	0.00	0.01
K_2O	0.00	0.00	0.01	0.01	0.02	0.00	0.01	0.01	0.00
Total	98.45	100.31	100.17	100.13	100.69	99.93	100.12	99.00	98.31
	number of ions on the basis of 4 oxygens								
Si	0.991	0.996	0.996	1.011	0.983	1.001	.995	.986	1.002
Cr	0.000	0.001	0.000	0.001	0.000	0.002	0.000	0.000	0.000
Ti	0.000	0.000	0.001	0.000	0.001	0.001	0.000	0.001	0.001
Mg	0.101	0.098	0.101	0.005	0.104	0.099	0.028	0.028	0.025
Fe	1.896	1.890	1.886	1.958	1.904	1.874	1.958	1.981	1.943
Mn	0.020	0.017	0.019	0.011	0.022	0.022	0.023	0.019	0.025
Ca	0.001	0.000	0.000	0.001	0.000	0.000	0.000	0.000	0.000
Fe*/Mg	18.97	19.48	18.77	392.38	18.55	19.24	71.52	72.42	78.54
Fe* /Fe*+Mg	.950	.951	.949	.997	.949	.951	.986	.986	.987
Fo	5.06	4.42	5.11	.26	5.17	5.00	1.39	1.37	1.27
Fa	94.94	95.08	94.89	99.74	94.83	95.00	98.61	98.63	98.73

FeO calculated as total iron (FeO*)
1 to 3 & 7 to 9 - Type II iron formation
4 to 6 - Type I iron formation

Table 6.1. Fayalite analyses in iron formations

Sample no.	1 61-2302	2 idem	3 idem	4 idem	5 idem	6 idem	7 50-1271	8 idem	9 idem
SiO_2(wt%)	28.87	28.98	28.90	29.09	29.03	29.29	28.98	28.98	29.00
TiO_2	0.05	0.05	0.03	0.00	0.03	0.00	0.02	0.04	0.00
FeO*	70.48	70.32	69.30	69.55	69.12	69.39	66.02	67.30	66.27
Cr_2O_3	0.09	0.00	0.02	0.01	0.01	0.00	0.01	0.02	0.11
MnO	0.59	0.44	0.56	0.53	0.61	0.54	3.13	3.20	3.16
MgO	0.48	0.50	0.53	0.49	0.52	0.56	0.60	0.78	0.89
CaO	0.00	0.04	0.01	0.01	0.00	0.01	0.00	0.00	0.00
K_2O	0.00	0.02	0.01	0.00	0.00	0.00	0.00	0.00	0.00
Total	100.56	100.35	99.36	99.68	99.32	99.79	98.76	100.32	99.43
number of ions on the basis of 4 oxygens									
Si	0.978	0.982	0.987	0.990	0.991	0.994	0.993	0.981	0.987
Cr	0.002	0.000	0.001	0.000	0.000	0.000	0.000	0.001	0.003
Ti	0.001	0.001	0.001	0.000	0.001	0.000	0.001	0.001	0.000
Mg	0.024	0.025	0.027	0.025	0.026	0.028	0.031	0.039	0.045
Fe	1.997	1.993	1.980	1.979	1.973	1.969	1.891	1.905	1.886
Mn	0.017	0.013	0.016	0.015	0.018	0.016	0.091	0.092	0.091
Ca	0.000	0.001	0.000	0.000	0.000	0.000	0.000	0.000	0.000
Fe*/Mg	83.08	79.41	73.96	80.25	75.24	70.07	64.70	50.74	43.79
Fe*/Fe*+Mg	.988	.988	.987	.988	.987	.986	.985	.981	.978
Fo	1.20	1.25	1.34	1.24	1.32	1.42	1.59	2.02	2.34
Fa	98.80	98.75	98.66	98.76	98.68	98.58	98.41	97.98	97.66

FeO calculated as total iron (FeO*)
1 to 3 - Type I iron formation
4 to 6 - Type II iron formation

Table 6.2. Garnet analyses in Type II iron formation

Sample no.	1 56-2805	2 idem	3 idem	4 idem	5 idem	6 idem	7 idem	8 idem	9 idem	10 idem
SiO_2(wt%)	36.82	36.61	36.95	36.47	35.88	37.29	37.77	36.88	36.91	36.54
Al_2O_3	20.57	20.81	20.35	20.64	20.39	20.77	20.77	20.51	20.57	20.42
FeO*	24.66	30.32	30.37	31.43	32.03	32.63	33.05	31.54	32.84	32.41
MnO	14.24	11.04	10.66	10.00	8.38	8.08	7.59	7.46	7.94	8.06
MgO	0.37	0.65	0.52	0.61	0.52	0.71	0.66	0.42	0.50	0.45
CaO	3.35	2.00	1.68	1.71	1.57	1.50	1.36	2.66	1.56	1.94
Total	100.01	101.43	100.53	100.86	98.77	100.98	100.20	99.47	100.32	99.82
				number of ions on the basis of 24 oxygens						
Si	6.018	5.943	6.037	5.957	5.973	6.042	6.012	6.054	6.034	6.012
Al	3.962	3.982	3.919	3.973	4.001	3.967	4.003	3.968	3.964	3.960
Fe	3.370	4.116	4.150	4.293	4.459	4.422	4.519	4.330	4.490	4.459
Mn	1.971	1.518	1.475	1.383	1.181	1.109	1.051	1.037	1.099	1.123
Mg	0.090	0.157	0.126	0.148	0.129	0.171	0.160	0.102	0.121	0.110
Ca	0.586	0.347	0.294	0.299	0.280	0.260	0.238	0.467	0.273	0.342
Fe*/Mg	37.387	26.166	32.762	28.903	34.553	25.780	28.900	42.125	36.843	40.401
Fe*/Fe*+Mg	0.973	0.963	0.970	0.966	0.971	0.962	0.965	0.976	0.973	0.995
				End members (mol.%)						
Alm.	56.0	67.0	68.6	70.1	73.7	74.1	75.7	72.9	75.0	73.8
Spess.	32.7	24.7	24.4	22.5	19.5	18.6	17.6	17.4	18.3	18.6
Gross	9.7	5.6	4.8	4.8	4.6	4.3	4.6	7.8	4.5	5.6
Pyr.	1.5	2.5	2.1	2.4	2.1	2.8	2.1	1.7	2.0	1.8

FeO calculated as total iron (Feo*)
1 to 7- same crystal of type I garnet, 1- centre, 2 to 6 towards the margin, 7- margin.
8 to 10- type II garnet, 3 different crystals.

Table 6.2. Garnet analyses in Type II iron formation (continued)

Sample no.	1 56-2801	2 idem	3 idem	4 idem	5 idem	6 idem	7 idem	8 idem	9 idem	10 idem
SiO_2(wt%)	35.83	36.63	36.41	36.73	35.64	36.20	36.21	36.41	36.05	35.68
Al_2O_3	20.08	20.33	20.48	20.42	20.50	20.67	20.14	20.57	20.57	20.36
FeO*	28.36	30.14	35.16	35.00	35.40	34.13	34.43	34.57	35.37	35.78
MnO	12.29	10.95	5.54	5.32	5.10	6.22	5.36	5.93	5.84	5.30
MgO	0.31	0.39	0.67	0.68	0.54	0.41	0.36	0.44	0.70	0.66
CaO	1.62	1.75	1.42	1.34	1.19	2.08	2.08	1.46	1.18	1.00
Total	98.49	100.19	99.68	99.49	98.37	99.71	98.58	99.38	99.71	98.78
				number of ions on the basis of 24 oxygens						
Si	5.992	6.015	5.999	6.046	5.959	5.967	6.029	6.012	5.954	5.953
Al	3.958	3.935	3.977	3.962	4.040	4.016	3.953	4.003	4.004	4.004
Fe	3.967	4.139	4.845	4.812	4.950	4.705	4.794	4.774	4.885	4.993
Mn	1.741	1.523	0.773	0.741	0.722	0.868	0.756	0.829	0.817	0.749
Mg	0.077	0.095	0.164	0.166	0.134	0.100	0.089	0.108	0.172	0.164
Ca	0.290	0.307	0.250	0.236	0.213	0.367	0.371	0.258	0.208	0.178
Fe*/Mg	51.318	43.352	29.437	28.873	36.774	46.696	53.649	44.073	28.344	30.410
Fe*/Fe*+Mg	0.980	0.977	0.967	0.966	0.973	0.979	0.981	0.977	0.965	0.968
				End members (mol.%)						
Alm.	65.2	68.2	80.3	80.8	82.2	77.8	79.7	79.9	80.3	82.0
Spess.	28.6	25.1	12.8	12.4	12.0	14.3	12.5	13.8	13.4	12.3
Gross.	4.7	5.0	4.1	3.9	3.5	6.0	6.1	4.3	3.4	2.9
Pyr.	1.2	1.5	2.7	2.8	2.2	1.6	1.4	1.8	2.8	2.7

FeO calculated as total iron (FeO*)
1 to 5- same crystal of type I garnet, 1- core , 2 to 4- towards the rim , 5- rim
6 to 10- same crystal of type I garnet, 6- core , 7 to 9- towards the rim , 10- rim.

Table 6.2. Garnet analyses in Type II iron formation (continued)

Sample no.	1 61-2301	2 idem	3 idem	4 idem	5 idem	6 idem	7 idem	8 idem	9 idem	10 idem
SiO_2(wt%)	36.75	36.51	36.42	35.97	36.23	36.64	36.53	37.00	36.44	36.82
Al_2O_3	20.91	20.97	20.79	20.78	20.66	20.83	20.83	20.81	20.39	20.71
FeO*	32.05	34.05	36.65	36.72	37.20	36.48	38.16	37.73	38.22	38.48
MnO	8.29	5.52	3.51	2.94	2.71	2.80	1.68	1.85	1.58	1.43
MgO	0.20	0.20	0.23	0.23	0.34	0.26	0.20	0.23	0.23	0.25
CaO	3.15	2.87	2.79	2.89	2.69	2.93	2.79	2.98	2.53	2.94
Total	100.35	100.12	100.39	99.53	99.83	99.94	100.19	100.60	99.39	100.63
				number of ions on the basis of 24 oxygens						
Si	5.960	5.976	5.964	5.940	5.964	6.001	5.983	6.022	6.019	6.004
Al	3.997	4.045	4.013	4.045	4.009	4.021	4.021	3.992	3.970	3.980
Fe	4.347	4.661	5.019	5.071	5.121	4.997	5.227	5.136	5.280	5.248
Mn	1.138	0.765	0.486	0.411	0.377	0.388	0.223	0.255	0.221	0.197
Mg	0.048	0.048	0.056	0.056	0.083	0.063	0.048	0.055	0.056	0.060
Ca	0.547	0.503	0.489	0.511	0.474	0.514	0.489	0.519	0.447	0.513
Fe^t/Mg	89.893	95.503	89.387	89.558	61.375	78.707	107.03	92.020	93.217	86.340
Fe^t/Fe^t+Mg	0.989	0.989	0.988	0.989	0.983	0.987	0.990	0.989	0.989	0.988
					End members (mol%)					
Alm.	71.4	77.9	82.9	83.8	84.5	83.8	87.1	86.0	87.9	87.1
Spess.	18.7	12.8	8.0	6.8	6.2	6.5	3.8	4.2	3.6	3.2
Gross.	9.0	8.4	8.0	8.4	7.8	8.6	8.1	8.7	7.4	8.5
Pyr.	0.8	0.8	0.9	0.9	1.3	1.0	0.8	0.9	0.9	1.0

FeO calculated as total iron (FeO*)
1 to 7- same crystal of type I garnet, 1- core , 2 to 6- towards the rim , 7- rim .
8 to 10- type II garnet, 3 different crystals

Table 6.2. Garnet analyses in Type II iron formation (continued)

Sample no.	1 56-2802	2 idem	3 idem	4 idem	5 50-6821	6 idem	7 idem	8 idem	9 idem	10 idem
SiO_2(wt%)	36.10	36.79	36.89	36.16	36.69	36.37	36.20	36.19	36.60	35.98
Al_2O_3	20.48	20.73	20.86	20.72	20.93	20.71	20.66	20.52	20.53	21.00
FeO*	34.01	33.63	34.55	33.80	37.35	36.53	36.66	35.93	36.82	36.53
MnO	7.19	7.16	7.26	6.84	2.23	2.22	2.48	2.32	2.34	2.09
MgO	0.52	0.56	0.62	0.56	1.24	1.08	. 02	0.98	1.24	1.45
CaO	1.30	1.38	1.57	1.80	1.57	2.35	2.01	2.43	2.16	1.33
Total	99.60	100.25	100.75	99.88	100.01	99.26	99.03	98.37	99.69	98.38
				number of ions on the basis of 24 oxygens						
Si	5.970	6.017	5.969	5.953	5.988	5.982	5.976	6.000	5.998	5.955
Al	3.992	3.996	3.978	4.020	4.026	4.015	4.020	4.010	3.966	4.097
Fe	4.704	4.600	4.675	4.653	5.098	5.025	5.062	4.982	5.046	5.056
Mn	1.007	0.992	0.995	0.953	0.308	0.309	0.346	0.325	0.324	0.293
Mg	0.128	0.136	0.149	0.137	0.301	0.264	0.251	0.242	0.303	0.357
Ca	0.230	0.241	0.272	0.317	0.274	0.414	0.355	0.431	0.379	0.235
Fe^*/Mg	36.689	33.687	31.260	33.858	16.896	18.974	20.161	20.566	16.656	14.132
Fe^*/Fe^*+Mg	0.973	0.971	0.969	0.971	0.944	0.949	0.952	0.953	0.943	0.933
					End members (mol%)					
Alm.	77.5	77.0	76.7	76.7	85.2	83.5	84.1	83.2	83.3	85.0
Spess.	16.5	16.6	16.3	15.7	5.1	5.1	5.7	5.4	5.3	4.9
Gross.	3.8	4.0	4.4	5.2	4.5	6.8	5.9	7.2	6.2	3.9
Pyr.	2.1	2.2	2.4	2.2	0.5	4.4	4.1	4.0	5.0	6.0

FeO calculated as total iron (Feo^*)

Table 6.2. Garnet analyses in Type II iron formation (continued)

Sample no.	1 61-230 /2	2 idem	3 idem	4 50-569 /1	5 49-331 /5A	6 61-230 /1	7 idem	8 idem	9 56-280 /5	10 idem
SiO_2(wt%)	35.74	36.09	36.42	36.17	36.56	35.72	36.40	35.63	36.02	36.07
Al_2O_3	20.55	20.10	20.40	20.68	20.64	20.13	20.45	20.34	20.63	20.32
FeO*	36.50	37.80	38.31	36.14	37.91	36.69	36.20	35.77	32.13	30.98
MnO	1.93	1.88	1.43	3.68	2.84	1.98	1.93	2.46	7.73	8.34
MgO	0.14	0.15	0.17	0.94	0.73	0.23	0.23	0.24	0.72	0.57
CaO	3.19	2.71	2.97	1.95	1.72	3.20	3.19	3.34	1.83	2.00
Total	98.05	98.73	99.70	99.56	100.40	97.95	98.40	98.78	99.06	98.28
				number of ions on the basis of 24 oxygens						
Si	5.973	6.012	6.003	5.956	5.983	5.988	6.040	5.973	5.963	6.010
Al	4.048	3.947	3.963	4.014	3.981	3.977	4.000	4.019	4.025	3.990
Fe	5.101	5.267	5.281	4.977	5.188	5.144	5.023	5.015	4.448	4.317
Mn	0.273	0.265	0.199	0.513	0.393	0.281	0.271	0.349	1.084	1.177
Mg	0.034	0.037	0.041	0.230	0.178	0.057	0.056	0.060	0.177	0.141
Ca	0.571	0.483	0.524	0.344	0.301	0.574	0.567	0.600	0.324	0.357
Fe^t/Mg	146.25	141.36	126.41	21.567	29.131	89.485	88.290	83.606	25.032	30.488
Fe^t/Fe^t+Mg	0.993	0.993	0.992	0.955	0.966	0.988	0.988	0.998	0.961	0.968
					End members (mol%)					
Alm.	85.3	87.0	87.3	82.0	85.5	84.9	84.8	83.2	73.7	72.0
Spess.	4.5	4.3	3.3	8.4	6.4	4.6	4.5	5.8	17.9	19.6
Gross.	9.5	7.9	8.8	5.6	4.9	9.3	9.5	9.9	5.3	5.9
Pyr.	0.5	0.6	0.6	3.8	2.9	0.8	0.9	1.0	2.9	2.3

FeO calculated as total iron (FeO^t)

Table 6.3. Garnet analyses in metagraywackes

Sample no.	1 17-3504	2 idem	3 idem	4 idem	5 idem	6 12-214	7 idem	8 idem	9 idem	10 idem
SiO_2(wt%)	36.12	36.34	36.30	36.35	36.30	36.21	36.32	36.63	37.03	36.93
Al_2O_3	20.54	20.63	20.71	20.65	20.77	21.02	21.11	20.67	20.92	20.85
FeO^t	38.86	38.99	38.89	39.09	39.15	38.42	37.97	38.37	39.16	38.71
MnO	2.05	2.11	2.18	2.17	2.19	0.97	0.91	0.96	0.84	0.84
MgO	1.06	0.82	0.98	1.05	0.82	1.57	1.80	1.76	1.29	1.50
CaO	0.58	0.84	0.62	0.61	0.91	0.71	1.00	0.81	0.78	0.59
Total	99.21	99.73	99.68	100.22	100.14	98.81	99.11	99.20	100.02	98.92
				number of ions on the basis of 24 oxygens						
Si	5.978	5.987	5.978	5.977	5.962	5.967	5.960	6.013	6.034	6.042
Al	4.007	4.006	4.020	4.002	4.021	4.082	4.083	3.999	4.018	4.021
Fe	5.379	5.372	5.357	5.375	5.378	5.295	5.211	5.267	5.337	5.297
Mn	0.287	0.294	0.304	0.302	0.304	0.135	0.126	0.133	0.116	0.116
Mg	0.261	0.201	0.240	0.257	0.200	0.385	0.440	0.430	0.313	0.365
Ca	0.102	0.148	0.109	0.107	0.160	0.125	0.175	0.142	0.136	0.103
Fe^t/Mg	20.565	26.673	22.261	20.883	26.782	13.727	11.833	12.229	17.078	14.476
Fe_t/Fe^t+Mg	0.953	0.963	0.957	0.954	0.964	0.932	0.922	0.924	0.944	0.935
				End members (mol.%)						
Alm.	89.1	89.2	89.1	88.9	88.9	89.1	87.5	88.1	90.4	90.0
Spess.	4.7	4.8	5.0	5.0	5.0	2.2	2.1	2.2	1.9	1.9
Gross.	1.7	2.4	1.8	1.7	2.6	2.1	2.9	2.3	2.3	1.7
Pyr.	4.3	3.3	4.0	4.2	3.3	6.4	7.4	7.2	5.3	6.2

FeO calculated as total iron (FeO^t)
1 - core 2 - rim

Table 6.4. Garnet analyses in quartzites

Sample no.	1 20-190	2 idem	3 idem	4 idem	5 20-143
SiO_2(wt%)	36.02	36.12	36.41	36.03	36.08
Al_2O_3	20.77	20.79	20.88	20.96	20.14
FeO*	40.40	39.87	40.42	40.17	40.43
MnO	1.38	1.29	1.41	1.27	1.03
MgO	0.55	0.47	0.63	0.69	0.46
CaO	0.71	0.91	1.00	1.07	0.78
Total	99.83	99.45	100.75	100.19	98.92
number of ions on the basis of 24 oxygens					
Si	5.949	5.973	5.954	5.592	6.014
Al	4.043	4.052	4.025	4.062	3.957
Fe	5.580	5.514	5.528	5.523	5.636
Mn	0.193	0.180	0.195	0.176	0.145
Mg	0.135	0.115	0.153	0.169	0.114
Ca	0.125	0.161	0.175	0.188	0.139
Fe*/Mg	41.205	47.586	35.990	32.657	49.303
Fe*/Fe*+Mg	0.976	0.979	0.973	0.970	0.980
End members (mol.%)					
Alm.	92.4	92.3	91.3	91.1	93.3
Spess.	3.2	3.0	3.2	2.9	2.4
Gross.	2.0	2.7	2.9	3.1	2.3
Pyr.	2.2	1.9	2.5	2.7	1.8

FeO calculated as total iron (FeO*)

Table 6.5 Amphibole analyses in gneisses

Sample no.	1 56-1081	2 idem	3 idem	4 idem	5 idem	6 19-191	7 idem	8 idem	9 idem
SiO_2(wt%)	41.25	39.57	40.76	41.37	41.43	53.20	53.36	53.03	53.38
TiO_2	0.45	0.40	0.29	0.57	0.40	0.09	0.09	0.11	0.05
Al_2O_3	10.13	11.37	10.86	10.15	9.80	1.43	1.03	1.45	1.07
Fe_2O_3	4.52	4.05	5.12	3.52	3.61	0.32	0.58	0.88	0.37
FeO	21.23	23.22	21.94	22.29	22.57	25.87	24.83	26.67	26.65
MnO	0.03	0.16	0.16	0.16	0.26	0.40	0.38	0.30	0.39
MgO	5.88	4.59	5.09	5.43	5.28	15.45	16.43	15.37	15.58
CaO	11.66	11.45	11.31	11.55	11.83	0.39	0.71	0.48	0.52
Na_2O	1.12	1.52	1.25	1.13	1.18	0.15	0.20	0.26	0.14
K_2O	1.73	2.25	1.83	1.81	1.67	0.00	0.02	0.00	0.01
Total	98.00	98.58	98.61	97.99	98.03	97.80	97.63	98.55	98.17
	number of ions on the basis of 24 oxygens								
Si	6.436	6.234	6.355	6.472	6.495	7.857	7.874	7.818	7.886
Al^{IV}	1.564	1.766	1.645	1.528	1.505	0.143	0.126	0.182	0.114
Al^{VI}	0.299	0.346	0.351	0.343	0.306	0.106	0.053	0.070	0.072
Ti	0.053	0.474	0.034	0.067	0.047	0.010	0.010	0.012	0.006
Fe^{3+}	0.531	0.480	0.601	0.415	0.426	0.036	0.064	0.098	0.041
Mg	1.367	1.078	1.183	1.266	1.234	3.511	3.613	3.377	3.430
Fe^{2+}	2.770	3.059	2.861	2.917	2.959	3.195	3.064	3.288	3.293
Mn	0.004	0.021	0.021	0.021	0.034	0.050	0.475	0.037	0.049
Ca	1.949	1.933	1.889	1.936	1.987	0.062	0.112	0.076	0.082
Na	0.321	0.429	0.319	0.309	0.352	0.012	0.021	0.032	0.014
K	0.344	0.452	0.364	0.361	0.334	0.000	0.004	0.000	0.002
Fe^*/Mg	2.417	3.303	2.944	2.649	2.772	0.934	0.879	1.014	0.986
Fe^*/Fe^*+Mg	0.707	0.768	0.746	0.726	0.735	0.483	0.468	0.503	0.497

1 to 5 - hastingsite 6 to 9 - cummingtonite

Table 6.5 Amphibole analyses in gneisses (continued)

Sample no.	1 56-289	2 idem	3 idem	4 idem	5 idem	6 56-1071	7 idem
SiO_2(wt%)	42.31	42.04	41.86	42.12	43.30	52.30	51.65
TiO_2	1.16	1.14	1.09	1.18	1.19	0.06	0.08
Al_2O_3	8.23	8.34	8.85	9.04	8.18	1.05	1.16
Fe_2O_3	1.83	1.89	3.13	1.55	2.14	0.79	0.13
FeO	21.94	20.99	20.82	22.21	22.09	26.34	26.48
MnO	0.12	0.18	0.21	0.18	0.28	0.73	0.66
MgO	6.99	7.19	7.04	6.60	7.01	13.89	13.06
CaO	11.23	11.48	11.30	11.54	11.11	1.52	2.34
Na_2O	1.55	1.30	1.43	1.40	1.63	0.36	0.17
K_2O	1.73	1.76	1.77	1.80	1.52	0.06	0.05
Total	97.08	96.31	97.50	97.61	98.45	97.10	95.78
	number of ions on the basis of 24 oxygens						
Si	6.643	6.633	6.538	6.582	6.689	7.872	7.894
Al^{iv}	1.357	1.367	1.462	1.418	1.311	0.128	0.106
Al^{vi}	0.167	0.184	0.168	0.248	0.179	0.058	0.103
Ti	0.137	0.135	0.128	0.139	0.138	0.007	0.009
Fe^{3+}	0.216	0.224	0.368	0.182	0.249	0.090	0.015
Mg	1.636	1.691	1.639	1.537	1.614	3.116	2.975
Fe^{2+}	2.880	2.770	2.720	2.902	2.855	3.315	3.385
Mn	0.016	0.024	0.028	0.024	0.037	0.093	0.085
Ca	1.889	1.941	1.891	1.932	1.839	0.245	0.383
Na	0.413	0.366	0.375	0.388	0.398	0.030	0.005
K	0.346	0.354	0.353	0.359	0.299	0.011	0.010
Fe^t/Mg	1.902	1.785	1.901	2.022	1.945	1.123	1.171
Fe^t/Fe^t+Mg	0.655	0.641	0.655	0.669	0.660	0.529	0.539

1 to 3 and 5 - hastingsite 4 - Fe pargasite 6 - 7 cummingtonite

Table 6.6 Amphibole analyses in amphibolites

Sample no.	1 56-135	2 idem	3 idem	4 20-544	5 idem	6 idem	7 20-505	8 idem	9 idem
SiO_2(wt%)	42.69	42.54	42.86	47.71	45.46	43.73	44.95	45.26	45.13
TiO_2	1.19	1.29	1.23	0.30	0.32	0.43	0.83	0.98	1.02
Al_2O_3	10.03	10.60	10.76	7.08	8.71	11.12	7.83	7.63	7.55
Fe_2O_3	5.36	4.79	2.65	0.00	3.73	3.14	5.92	5.44	1.44
FeO	18.20	17.85	19.79	19.42	16.36	18.24	17.33	17.58	21.16
MnO	0.33	0.45	0.33	0.17	0.29	0.23	0.06	0.05	0.00
MgO	7.32	7.77	7.38	9.22	9.05	7.76	9.06	9.46	6.41
CaO	11.48	11.52	11.37	12.19	12.00	12.10	10.45	10.35	10.18
Na_2O	1.18	1.48	1.86	0.80	0.46	0.84	1.47	1.77	1.26
K_2O	0.60	0.72	0.67	0.91	0.70	1.15	0.63	0.66	0.68
Total	98.38	99.01	98.89	97.80	98.07	98.74	98.52	99.18	94.53
			number of ions on the basis of 24 oxygens						
Si	6.494	6.424	6.493	7.135	6.871	6.580	6.759	6.773	7.097
Al^{IV}	1.506	1.576	1.507	0.825	1.129	1.420	1.231	1.227	0.903
Al^{VI}	0.293	0.312	0.414	0.430	0.423	0.553	0.159	0.119	0.497
Ti	0.136	0.146	0.140	0.034	0.036	0.049	0.094	0.110	0.121
Fe^{3+}	0.613	0.544	0.302	0.000	0.424	0.355	0.670	0.613	0.135
Mg	1.659	1.749	1.666	2.066	2.068	1.740	2.033	2.110	1.502
Fe^{2+}	2.315	2.257	2.507	2.443	2.068	2.296	2.182	2.200	2.783
Mn	0.042	0.058	0.042	0.022	0.037	0.029	0.008	0.006	0.000
Ca	1.871	1.864	1.846	1.964	1.943	1.951	1.686	1.659	1.715
Na	0.279	0.361	0.464	0.198	0.105	0.219	0.261	0.331	0.138
K	0.116	0.139	0.129	0.175	0.135	0.221	0.121	0.127	0.186
Fe^t/Mg	1.790	1.633	1.711	1.192	1.240	1.540	1.406	1.336	1.942
Fe^t/Fe^t+Mg	0.642	0.620	0.631	0.544	0.554	0.606	0.584	0.572	0.660

1 - 2 - 5 - 7 - 8 - hastingsite 3 - 4 - 6 - 9 - Fe pargasite

Table 6.6 amphibole analyses in amphibolites (continued)

Sample no.	1 56-1072	2 idem	3 idem	4 idem	5 idem	6 idem	7 idem	8 idem	9 idem
SiO_2(wt%)	38.61	40.41	40.41	43.41	50.72	51.32	52.05	52.84	52.10
TiO_2	0.45	0.90	0.59	0.62	0.13	0.19	0.09	0.07	0.11
Al_2O_3	14.03	13.06	12.80	10.21	2.13	2.49	1.13	1.13	1.11
Fe_2O_3	5.88	2.19	9.42	4.52	2.05	1.07	0.52	0.74	0.16
FeO	19.03	20.86	16.87	20.54	25.71	25.04	28.66	26.90	27.97
MnO	0.24	0.26	0.14	0.27	0.86	0.88	0.90	0.82	0.86
MgO	5.03	5.40	6.52	7.14	12.27	12.13	12.63	14.28	13.65
CaO	10.96	10.82	8.84	7.78	2.72	4.16	1.14	1.05	0.38
Na_2O	1.89	1.98	1.69	1.33	0.50	0.39	0.31	0.30	0.25
K_2O	0.79	0.86	0.58	0.63	0.10	0.11	0.06	0.03	0.03
Total	97.52	96.74	97.86	96.45	98.18	97.78	97.48	98.16	96.53
			number of ions on the basis of 24 oxygens						
Si	5.996	6.301	6.179	6.701	7.648	7.704	7.880	7.864	7.906
Al^{IV}	2.004	1.699	1.820	1.299	0.352	0.296	0.120	0.135	0.094
Al^{VI}	0.674	0.701	0.487	0.559	0.027	0.145	0.081	0.063	0.105
Ti	0.053	0.105	0.068	0.072	0.015	0.021	0.010	0.008	0.013
Fe^{3+}	0.688	0.256	1.084	0.526	0.233	0.121	0.059	0.083	0.019
Mg	1.164	1.255	1.486	1.643	2.757	2.714	2.850	3.167	3.087
Fe^{2+}	2.472	2.720	2.158	2.652	3.368	3.144	3.628	3.349	3.537
Mn	0.032	0.034	0.018	0.035	0.110	0.112	0.115	0.103	0.110
Ca	1.824	1.807	1.448	1.287	0.439	0.669	0.185	0.167	0.062
Na	0.475	0.479	0.251	.172	0.095	0.040	0.019	0.027	0.006
K	0.156	0.171	0.113	0.124	0.019	0.021	0.012	0.006	0.006
Fe^*/Mg	2.741	2.399	2.194	1.955	1.345	1.244	1.334	1.116	1.188
Fe^*/Fe^*+Mg	0.733	0.706	0.687	0.662	0.574	0.554	0.572	0.527	0.543

1- hastingsite 2- 4- Fe pargasite 3- Fe tschermakite
5- 7- 8- 9- cummingtonite 6- silicic subcalcic-hastingsite 1 to 4- green amphiboles
5 to 9- colorless amphiboles

Table 6.6 Amphibole analyses in amphibolites (continued)

Sample no.	1 49-526	2 idem	3 idem	4 idem	5 idem	6 idem	7 idem	8 idem	9 idem
SiO_2 (wt%)	44.00	44.19	53.04	45.66	45.02	53.19	53.36	44.30	53.64
TiO_2	0.96	1.10	0.10	0.68	0.93	0.19	0.09	1.07	0.09
Al_2O_3	10.28	10.30	1.89	9.26	9.70	1.57	0.47	10.79	0.53
Fe_2O_3	2.18	2.14	2.30	3.73	1.87	0.16	0.08	2.27	0.23
FeO	17.44	16.35	10.93	15.09	15.60	24.45	24.92	16.14	24.61
MnO	0.00	0.00	0.00	0.00	0.00	0.26	0.26	0.00	0.30
MgO	9.29	9.85	15.88	9.95	10.27	15.91	16.75	9.57	16.64
CaO	11.41	11.48	12.38	10.23	11.46	1.78	0.95	11.16	1.38
Na_2O	1.56	1.59	0.27	1.43	1.37	0.11	0.15	1.65	0.21
K_2O	1.08	0.74	0.04	0.63	0.63	0.03	0.06	0.69	0.00
Total	98.19	97.73	96.83	96.66	96.87	97.65	97.09	97.54	97.63
			number of ions on the basis of 24 oxygens						
Si	6.617	6.629	7.695	6.858	6.765	7.840	7.918	6.626	7.912
Al^{IV}	1.383	1.371	0.305	1.142	1.235	0.160	0.082	1.373	0.088
Al^{VI}	0.439	0.450	0.018	0.498	0.483	0.113	0.000	0.533	0.004
Ti	0.109	0.124	0.011	0.077	0.105	0.021	0.010	0.120	0.010
Fe^{3+}	0.247	0.241	0.251	0.422	0.211	0.018	0.009	0.256	0.025
Mg	2.082	2.202	3.434	2.227	2.300	3.495	3.704	2.138	3.658
Fe^{2+}	2.193	2.051	1.326	1.896	1.960	3.014	3.092	2.024	3.036
Mn	0.000	0.000	0.000	0.000	0.000	0.032	0.033	0.000	0.037
Ca	1.839	1.845	1.925	1.646	1.845	0.281	0.151	1.793	0.218
Na	0.354	0.376	0.041	0.182	0.304	0.006	0.042	0.345	0.049
K	0.207	0.142	0.007	0.121	0.121	0.006	0.011	0.132	0.000
Fe^t/Mg	1.172	1.041	0.459	1.040	0.944	0.877	0.846	1.066	0.847
Fe^t/Fe^t+Mg	0.540	0.510	0.315	0.510	0.486	0.467	0.458	0.516	0.459

1 to 3 - same crystal 1. green core (Fe pargasite), 2. towards the rim (green) pargasite 3. colorless rim (silicic tschermakite). 4 to 7 - same crystal 4. green half (pargasite), 5. green (pargasite), 6. colorless half (cummingtonite), 7. colorless (silicic subcalcic-Mg kaersutite). 8 & 9 - same crystal 8. green (pargasite), 9. colorless (silicic subcalcic-Mg hastingsite).

Table 6.7 Amphibole analyses in Type I iron formation

Sample	1	2	3	4	5	6	7	8	9	10
no.	61-120 /2	idem	56-217 /2-3	idem	idem	idem	49-351 /4	idem	idem	idem
SiO_2(wt%)	48.29	47.21	40.32	41.35	40.35	49.57	47.74	45.57	48.01	47.52
TiO_2	0.10	0.08	0.22	0.23	0.24	0.04	0.10	0.07	0.09	0.09
Al_2O_3	0.05	0.23	10.29	10.36	10.74	0.79	2.65	3.98	2.99	2.76
Fe_2O_3	0.00	0.13	6.59	3.24	7.44	0.77	2.22	4.66	2.78	2.56
FeO	48.65	42.68	25.46	26.65	25.59	40.31	34.66	33.16	34.25	34.57
MnO	1.43	1.57	0.69	0.52	0.64	1.96	0.65	0.62	0.48	0.52
MgO	0.15	0.10	2.13	2.13	1.67	4.49	8.53	4.84	8.25	8.34
CaO	0.05	0.06	10.68	10.59	10.50	0.80	0.41	0.49	0.39	0.43
Na_2O	0.05	0.00	1.20	0.99	1.09	0.25	0.66	0.53	0.93	0.63
K_2O	0.05	0.04	1.49	1.56	1.34	0.00	0.05	0.04	0.04	0.05
Total	98.82	97.10	99.08	97.61	99.54	98.97	97.67	96.96	98.21	97.47
	number of ions on the basis of 24 oxygens									
Si	7.986	7.952	6.386	6.594	6.355	7.883	7.511	7.250	7.498	7.494
Al^{IV}	0.010	0.046	1.614	1.406	1.645	0.117	0.489	0.747	0.502	0.506
Al^{VI}	0.000	0.000	0.307	0.542	0.349	0.031	0.003	0.000	0.048	0.007
Ti	0.012	0.010	0.026	0.027	0.028	0.004	0.012	0.008	0.011	0.011
Fe^{3+}	0.000	0.017	0.786	0.388	0.881	0.092	0.263	0.558	0.326	0.304
Mg	0.037	0.025	0.502	0.506	0.392	1.064	2.000	1.859	1.920	1.960
Fe^{2+}	6.729	6.717	3.373	3.554	3.370	5.361	4.561	4.413	4.473	4.560
Mn	0.200	0.224	0.093	0.070	0.085	0.264	0.087	0.084	0.063	0.069
Ca	0.008	0.011	1.812	1.809	1.772	0.136	0.069	0.083	0.066	0.073
Na	0.003	0.000	0.268	0.204	0.211	0.030	0.195	0.163	0.190	0.177
K	0.010	0.008	0.301	0.317	0.269	0.000	0.010	0.008	0.008	0.010
Fe^*/Mg	187.39	277.11	8.455	7.925	11.063	5.371	2.455	2.719	2.532	2.517
Fe^*/Fe^*+Mg	0.995	0.996	0.894	0.888	0.917	0.843	0.711	0.731	0.717	0.716

1- 2 Fe gedrite, 4- Fe pargasite 6- grunerite 7 to 10 - subcalcic silicic-hastingsite
3 and 5 - hastingsite 3 to 5 - green 1 - 2 and 6 to 10 colorless

Table 6.8 Amphibole analyses in Type II iron formation

Sample no.	1 49-351 /2-3	2 idem	3 idem	4 idem	5 61-230 /1	6 idem	7 idem	8 61-230 /2	9 50-470 /5
SiO_2(wt%)	46.20	46.61	48.13	46.63	40.86	40.25	38.54	38.60	48.22
TiO_2	0.12	0.10	0.08	0.13	0.18	0.17	0.15	0.15	0.10
Al_2O_3	3.91	4.05	2.80	4.31	10.44	9.99	12.08	12.51	2.06
Fe_2O_3	4.05	4.48	2.87	4.83	3.46	8.86	8.18	7.38	2.28
FeO	33.66	33.80	34.95	33.59	26.84	25.07	26.89	26.90	36.72
MnO	0.53	0.52	0.65	0.62	0.58	0.75	0.28	0.16	0.43
MgO	6.30	6.46	6.91	6.45	1.79	1.96	0.96	1.02	6.58
CaO	0.79	0.59	0.46	0.81	10.91	10.29	8.80	8.99	0.45
Na_2O	1.09	1.23	0.88	1.25	1.11	1.23	2.76	2.54	0.60
K_2O	0.03	0.07	0.02	0.03	1.31	1.36	0.72	0.93	0.00
Total	96.68	97.91	97.75	98.64	97.49	99.52	99.36	99.19	97.45
	number of ions on the basis of 24 oxygens								
Si	7.380	7.353	7.581	7.303	6.545	6.359	6.129	6.134	7.661
Al^{IV}	0.620	0.647	0.418	0.697	1.454	1.640	1.870	1.866	0.338
Al^{VI}	0.116	0.105	0.101	0.099	0.516	0.219	0.394	0.478	0.047
Ti	0.014	0.011	0.009	0.015	0.021	0.020	0.018	0.018	0.012
Fe^{3+}	0.487	0.532	0.340	0.568	0.418	1.005	0.979	0.883	0.273
Mg	1.499	1.518	1.622	1.505	0.427	0.461	0.227	0.242	1.558
Fe^{2+}	4.497	4.460	4.605	4.399	3.597	3.313	3.576	3.576	4.879
Mn	0.071	0.069	0.087	0.082	0.078	0.100	0.037	0.215	0.058
Ca	0.135	0.099	0.077	0.135	1.872	1.742	1.499	1.530	0.076
Na	0.159	0.174	0.111	0.186	0.277	0.239	0.583	0.532	0.089
K	0.006	0.014	0.004	0.006	0.267	0.274	0.146	0.188	0.000
Fe^*/Mg	3.371	3.332	3.102	3.354	9.578	9.573	20.183	18.544	3.344
Fe^*/Fe^*+Mg	0.771	0.769	0.756	0.770	0.905	0.905	0.953	0.949	0.770

1 - 2 - 4 - 9 - subcalcic silicic hastingsite 3 - grunerite 5 - Fe pargasite
6 - 7 - 8 - hastingsite (5 to 8 green, 1 to 4 and 9 colorless)

Table 6.8 Amphibole analyses in Type II iron formation (continued)

Sample no.	1 50-4705	2 idem	3 idem	4 idem	5 idem	6 50-5691	7 idem	8 idem	9 idem
SiO_2(wt%)	49.01	48.84	48.40	49.34	49.48	49.31	50.20	49.02	48.72
TiO_2	0.15	0.07	0.06	0.08	0.07	0.80	0.12	0.21	0.18
Al_2O_3	2.06	1.77	1.67	1.69	1.57	0.74	0.87	1.95	2.06
Fe_2O_3	2.06	1.45	1.22	1.83	1.65	0.74	0.00	1.33	1.76
FeO	37.27	38.98	38.07	37.86	38.03	37.77	38.68	35.04	34.99
MnO	0.34	0.31	0.36	0.34	0.38	0.83	0.30	0.28	0.40
MgO	9.93	6.30	7.00	6.71	6.94	7.04	7.45	7.86	7.97
CaO	0.36	0.30	0.34	0.35	0.30	0.11	0.10	0.26	0.25
Na_2O	0.54	0.46	0.54	0.53	0.48	0.22	0.11	0.60	0.54
K_2O	0.00	0.00	0.00	0.00	0.00	0.00	0.23	0.02	0.01
Total	98.72	99.10	97.66	98.73	98.90	96.84	98.06	96.57	96.88
	number of ions on the basis of 24 oxygens								
Si	7.672	7.667	7.694	7.735	7.744	7.876	7.898	7.752	7.695
Al^{iv}	0.327	0.327	0.306	0.264	0.256	0.124	0.101	0.248	0.305
Al^{vi}	0.053	0.000	0.007	0.048	0.033	0.015	0.059	0.116	0.079
Ti	0.017	0.008	0.007	0.009	0.008	0.009	0.014	0.025	0.023
Fe^{3+}	0.243	0.171	0.146	0.216	0.194	0.089	0.000	0.158	0.209
Mg	1.617	1.621	1.658	1.568	1.618	1.676	1.747	1.852	1.876
Fe^{2+}	4.879	5.117	5.061	4.964	4.978	5.045	5.089	4.635	4.622
Mn	0.045	0.041	0.048	0.045	0.050	0.112	0.040	0.037	0.054
Ca	0.060	0.050	0.058	0.058	0.050	0.018	0.017	0.044	0.042
Na	0.079	0.000	0.152	0.071	0.079	0.034	0.000	0.052	0.068
K	0.000	0.000	0.000	0.000	0.000	0.000	0.046	0.004	0.002
Fe^t/Mg	3.196	3.287	3.169	3.333	3.226	3.131	2.936	2.607	2.603
Fe^t/Fe^t+Mg	0.762	0.767	0.760	0.769	0.763	0.758	0.746	0.723	0.722

1 to 6- subcalcic silicic-hastingsite 7- subcalcic silicic-Fe pargasite
8- 9- grunerite (1 to 9 colorless)

Table 6.8 amphibole analyses in Type II iron formation (continued)

Sample no.	1 56-2802	2 idem	3 idem
SiO_2(wt%)	49.61	48.87	48.94
TiO_2	0.14	0.14	0.13
Al_2O_3	0.56	0.73	0.76
Fe_2O_3	0.00	0.28	0.32
FeO	39.65	40.23	40.04
MnO	1.66	1.49	1.53
MgO	5.70	5.18	5.15
CaO	0.19	0.16	0.20
Na_2O	0.05	0.20	0.11
K_2O	0.01	0.20	0.01
Total	97.57	97.12	97.18
number of ions on the basis of 24 oxygens			
Si	7.938	7.894	7.896
Al^{IV}	0.062	0.106	0.104
Al^{VI}	0.044	0.033	0.040
Ti	0.017	0.017	0.016
Fe^{3+}	0.000	0.034	0.038
Mg	1.359	1.247	1.238
Fe^{2+}	5.306	5.434	5.402
Mn	0.225	0.204	0.209
Ca	0.033	0.027	0.035
Na	0.000	0.003	0.013
K	0.002	0.004	0.002
Fe^t/Mg	4.068	4.548	4.562
Fe^t/Fe^t+Mg	0.803	0.820	0.820

1 to 3 - grunerite

Table 6.9 Amphibole analyses in metagraywackes

Sample no.	1 20-520	2 idem	3 idem	4 idem	5 31-283B	6 idem	7 idem	8 idem	9 idem
SiO_2(wt%)	54.08	53.79	54.03	54.54	53.13	53.06	53.20	53.24	52.38
TiO_2	0.05	0.02	0.05	0.03	0.04	0.07	0.09	0.05	0.09
Al_2O_3	1.27	1.40	1.30	1.16	0.85	1.47	1.23	0.82	1.80
Fe_2O_3	0.09	0.20	0.00	0.04	1.07	0.0[illegible]	1.42	0.01	1.69
FeO	20.44	21.32	21.36	21.40	24.23	24.56	24.29	24.56	23.90
MnO	0.73	0.64	0.68	0.77	0.17	0.13	0.14	0.13	0.13
MgO	18.68	18.46	18.62	18.92	17.09	16.58	17.14	17.02	16.69
CaO	1.10	0.55	0.54	0.47	0.46	0.71	0.53	0.48	0.50
Na_2O	0.16	0.18	0.07	0.12	0.05	0.08	0.15	0.01	0.18
K_2O	0.10	0.03	0.00	0.01	0.01	0.01	0.02	0.00	0.00
Total	96.60	96.59	96.65	97.46	97.09	96.73	98.21	96.32	97.35
			number of ions on the basis of 24 oxygens						
Si	7.899	7.881	7.902	7.909	7.861	7.869	7.723	7.923	7.739
Al^{IV}	0.101	0.119	0.098	0.091	0.139	0.131	0.207	0.077	0.261
Al^{VI}	0.117	0.123	0.126	0.108	0.009	0.126	0.005	0.067	0.053
Ti	0.005	0.002	0.005	0.003	0.004	0.008	0.010	0.006	0.010
Fe^{3+}	0.009	0.022	0.000	0.005	0.119	0.006	0.156	0.001	0.188
Mg	4.066	4.030	4.058	4.089	3.768	3.664	3.742	3.775	3.675
Fe^{2+}	2.497	2.612	2.612	2.596	2.998	3.046	2.976	3.057	2.953
Mn	0.090	0.079	0.084	0.095	0.021	0.016	0.017	0.016	0.016
Ca	0.172	0.086	0.085	0.073	0.073	0.113	0.083	0.076	0.079
Na	0.003	0.007	0.000	0.002	0.007	0.002	0.032	0.001	0.026
K	0.002	0.005	0.000	0.002	0.002	0.002	0.004	0.000	0.000
Fe^*/Mg	0.639	0.673	0.664	0.659	0.833	0.837	0.842	0.814	0.854
Fe^*/Fe^*+Mg	0.390	0.402	0.399	0.397	0.454	0.456	0.457	0.449	0.462

1 to 9 - cummingtonite

Table 6.10 Biotite analyses in gneisses

Sample no.	1 31-311	2 idem	3 idem	4 idem	5 19-191	6 idem	7 idem	8 idem	9 idem
SiO_2(wt%)	37.00	36.55	37.14	37.27	36.82	36.38	37.25	37.61	36.52
TiO_2	1.11	1.46	1.01	1.09	1.39	1.37	1.49	1.43	1.44
Al_2O_3	18.89	18.43	18.64	18.67	16.35	15.48	16.10	15.95	16.02
FeO^t	17.45	18.31	18.05	17.79	19.29	19.48	19.39	19.59	19.80
Cr_2O_3	0.11	0.11	0.13	0.13	0.08	0.00	0.04	0.21	0.00
MnO	0.07	0.05	0.05	0.04	0.11	0.06	0.10	0.02	0.08
MgO	11.30	11.78	11.17	11.14	12.39	12.61	12.71	12.48	12.71
CaO	0.02	0.01	0.07	0.00	0.01	0.04	0.01	0.00	0.02
Na_2O	0.00	0.00	0.01	0.00	0.10	0.00	0.36	0.09	0.06
K_2O	9.97	9.37	9.18	9.71	9.04	9.14	9.19	9.70	9.07
BaO	0.00	0.00	0.00	0.00	0.16	0.15	0.13	0.17	0.04
Total	95.80	95.90	95.34	95.72	95.75	94.72	96.77	97.25	95.77
	number of ions on the basis of 22 oxygens								
Si	5.536	5.475	5.573	5.577	5.572	5.586	5.583	5.622	5.541
Ti	0.126	0.165	0.115	0.124	0.159	0.159	0.168	0.162	0.165
Al^{iv}	0.867	0.730	0.870	0.870	0.488	0.388	0.428	0.432	0.406
Al^{vi}	2.464	2.525	2.427	2.423	2.248	2.414	2.417	2.378	2.459
Fe	2.183	2.294	2.265	2.226	2.441	2.501	2.431	2.449	2.512
Cr	0.013	0.013	0.015	0.015	0.010	0.000	0.005	0.025	0.000
Mn	0.009	0.006	0.006	0.005	0.014	0.002	0.013	0.003	0.010
Mg	2.521	2.631	2.499	2.485	2.795	2.887	2.840	2.781	2.875
Ca	0.003	0.002	0.011	0.000	0.002	0.007	0.002	0.000	0.003
Na	0.000	0.000	0.003	0.000	0.029	0.000	0.105	0.026	0.018
K	1.903	1.791	1.757	1.854	1.745	1.790	1.757	1.850	1.756
Ba	0.000	0.000	0.000	0.000	0.010	0.009	0.008	0.010	0.003
Fe^t/Mg	0.865	0.871	0.906	0.895	0.873	0.866	0.855	0.880	0.873
Fe^t/Fe^t+Mg	0.469	0.465	0.475	0.472	0.466	0.464	0.461	0.468	0.466

FeO calculated as total iron (FeO^t)

Table 6.11 Biotite analyses in amphibolites

Sample no.	1 20-505	2 idem	3 idem	4 idem	5 idem	6 49-526	7 idem	8 idem	9 idem
SiO_2 (wt%)	37.36	37.43	36.65	36.57	37.57	37.24	37.08	37.68	36.96
TiO_2	2.37	2.04	2.47	1.59	2.03	2.23	2.39	2.19	2.23
Al_2O_3	13.63	13.54	14.49	13.33	13.74	14.93	14.66	14.96	14.80
FeO^t	21.46	22.20	22.61	23.53	22.49	21.45	22.57	21.34	23.00
Cr_2O_3	0.15	0.23	0.11	0.27	0.15	0.00	0.10	0.00	0.11
MnO	0.11	0.16	0.14	0.06	0.07	0.09	0.17	0.04	0.15
MgO	11.00	11.43	10.06	10.13	11.16	11.02	10.80	10.99	10.14
CaO	0.00	0.00	0.00	0.00	0.00	0.04	0.04	0.03	0.02
Na_2O	0.16	0.01	0.13	0.00	0.05	0.03	0.01	0.08	0.00
K_2O	9.24	9.40	9.31	9.45	9.44	9.65	9.45	9.16	9.83
BaO	0.00	0.00	0.00	0.00	0.00	0.12	0.18	0.12	0.16
Total	95.22	96.21	95.70	94.75	96.47	96.80	97.46	96.54	97.40
			number of ions on the basis of 22 oxygens						
Si	5.749	5.726	5.648	5.738	5.733	5.652	5.623	5.702	5.630
Ti	0.275	0.235	0.287	0.188	0.234	0.255	0.273	0.249	0.256
Al^{vi}	0.222	0.168	0.280	0.203	0.205	0.323	0.243	0.371	0.288
Al^{iv}	2.251	2.274	2.352	2.262	2.267	2.348	2.377	2.298	2.370
Fe	2.762	2.840	2.914	3.088	2.870	2.723	2.862	2.701	2.930
Cr	0.018	0.028	0.013	0.033	0.018	0.000	0.012	0.000	0.013
Mn	0.014	0.021	0.018	0.008	0.009	0.012	0.022	0.005	0.019
Mg	2.521	2.607	2.311	2.370	2.539	2.494	2.442	2.480	2.303
Ca	0.000	0.000	0.000	0.000	0.000	0.007	0.006	0.005	0.003
Na	0.048	0.003	0.039	0.000	0.015	0.009	0.003	0.023	0.000
K	1.814	1.835	1.830	1.892	1.838	1.869	1.828	1.769	1.910
Ba	0.000	0.000	0.000	0.000	0.000	0.007	0.011	0.008	0.010
Fe^t/Mg	1.094	1.089	1.260	1.302	1.130	1.091	1.171	1.089	1.272
Fe^t/Fe^t+Mg	0.522	0.521	0.557	0.565	0.530	0.521	0.539	0.521	0.559

FeO calculated as total iron (FeO^t)

Table 6.12 Biotite analyses in iron formation

Sample no.	1 50-6821	2 idem	3 49-3515	4 idem	5 idem	6 49-3514	7 idem
SiO_2(wt%)	32.44	33.41	35.23	35.49	36.14	36.06	36.32
TiO_2	1.46	1.31	0.84	0.65	0.62	0.23	0.21
Al_2O_3	15.58	15.82	13.80	13.57	13.76	14.05	14.70
FeO^t	31.71	31.54	28.87	29.50	28.29	29.70	29.33
Cr_2O_3	0.09	0.05	0.11	0.15	0.14	0.00	0.01
MnO	0.10	0.14	0.16	0.13	0.06	0.18	0.21
MgO	5.21	5.27	7.14	7.46	7.29	8.08	7.68
CaO	0.00	0.00	0.00	0.00	0.00	0.02	0.02
Na_2O	0.04	0.08	0.07	0.00	0.16	0.18	0.24
K_2O	8.89	8.98	8.60	8.85	9.09	9.08	9.15
BaO	0.22	0.29	0.00	0.00	0.00	0.11	0.15
Total	95.75	96.90	94.73	95.73	95.48	97.69	97.03
	number of ions on the basis of 22 oxygens						
Si	5.290	5.361	5.670	5.672	5.752	5.651	5.727
Ti	0.180	0.159	0.102	0.079	0.075	0.027	0.026
Al^{vi}	0.285	0.353	0.287	0.228	0.334	0.247	0.274
Al^{iv}	2.710	2.639	2.330	2.328	2.248	2.349	2.273
Fe	4.325	4.233	3.886	3.943	3.766	3.893	3.868
Cr	0.012	0.006	0.014	0.019	0.018	0.000	0.001
Mn	0.014	0.019	0.022	0.018	0.008	0.024	0.028
Mg	1.267	1.261	1.713	1.777	1.730	1.888	1.806
Ca	0.000	0.000	0.000	0.000	0.000	0.003	0.003
Na	0.013	0.025	0.022	0.000	0.049	0.055	0.073
K	1.850	1.838	1.766	1.804	1.846	1.815	1.841
Ba	0.015	0.018	0.000	0.000	0.000	0.007	0.010
Fe^t/Mg	3.413	3.356	2.268	2.218	2.176	2.060	2.141
Fe^t/Fe^t+Mg	0.773	0.770	0.694	0.689	0.685	0.673	0.681

FeO calculated as total iron (FeO^t) 1 to 5- type II iron formation
6-7 - type I iron formation

Table 6.12 Biotite analyses in Type II iron formation

Sample no.	1 56-2801	2 idem	3 idem	4 idem	5 idem	6 56-2805	7 idem	8 idem	9 idem
SiO_2(wt%)	33.92	33.62	33.68	34.33	34.12	34.48	35.15	34.57	34.72
TiO_2	1.90	1.87	2.11	2.20	1.64	1.49	1.34	1.30	1.57
Al_2O_3	14.56	14.08	14.64	14.58	14.52	14.46	14.10	14.46	14.37
FeO^t	33.02	32.71	32.35	32.99	32.73	32.17	32.48	32.17	32.03
Cr_2O_3	0.02	0.01	0.42	0.01	0.01	0.01	0.01	0.01	0.32
MnO	0.30	0.38	0.32	0.24	0.27	0.18	0.25	0.20	0.19
MgO	3.60	3.73	3.66	3.65	3.57	4.19	4.12	4.41	4.05
CaO	0.01	0.01	0.01	0.01	0.01	0.01	0.01	0.01	0.01
Na_2O	0.07	0.05	0.14	0.01	0.08	0.07	0.04	0.01	0.03
K_2O	8.96	8.92	9.11	9.48	9.31	9.16	8.90	8.92	8.68
BaO	0.00	0.00	0.00	0.00	0.00	0.00	0.00	0.00	0.00
Total	96.15	95.17	96.21	97.26	96.08	96.03	96.25	95.91	95.79
			number of ions on the basis of 22 oxygens						
Si	5.511	5.525	5.465	5.514	5.549	5.581	5.668	5.593	5.613
Ti	0.233	0.232	0.258	0.267	0.201	0.179	0.163	0.158	0.191
Al^{IV}	0.489	0.475	0.535	0.486	0.451	0.340	0.347	0.351	0.351
Al^{VI}	2.299	2.252	2.265	2.274	2.332	2.419	2.332	2.407	2.387
Fe	4.486	4.496	4.390	4.431	4.452	4.355	4.380	4.353	4.331
Cr	0.003	0.001	0.054	0.001	0.001	0.001	0.001	0.001	0.041
Mn	0.041	0.053	0.044	0.033	0.037	0.025	0.034	0.027	0.026
Mg	0.872	0.914	0.885	0.874	0.866	1.011	0.990	1.064	0.976
Ca	0.002	0.002	0.002	0.002	0.002	0.002	0.002	0.002	0.002
Na	0.022	0.016	0.044	0.003	0.025	0.022	0.013	0.003	0.009
K	1.857	1.870	1.886	1.943	1.932	1.892	1.831	1.841	1.790
Ba	0.000	0.000	0.000	0.000	0.000	0.000	0.000	0.000	0.000
Fe^t/Mg	5.140	4.919	4.960	5.069	5.140	4.307	4.424	4.091	4.437
Fe^t/Fe^t+Mg	0.837	0.831	0.832	0.835	0.837	0.811	0.815	0.803	0.816

FeO calculated as total iron (FeO^t)

Table 6.12 Biotite analyses in Type II iron formation (continued)

Sample no.	1 61-2301	2 idem	3 idem	4 idem	5 idem	6 56-2802	7 idem	8 idem	9 idem
SiO_2(wt%)	34.89	35.58	35.07	34.89	33.81	34.98	34.18	35.60	32.63
TiO_2	1.00	1.05	1.15	0.81	0.69	2.01	2.03	1.98	1.99
Al_2O_3	12.65	12.57	12.32	13.12	13.25	14.57	13.78	14.09	14.54
FeO*	35.64	34.04	35.05	35.11	36.41	33.00	31.92	32.44	33.34
Cr_2O_3	0.01	0.01	0.02	0.00	0.02	0.01	0.01	0.04	0.10
MnO	0.09	0.12	0.02	0.12	0.23	0.23	0.26	0.21	0.31
MgO	2.76	2.73	3.07	2.82	2.10	3.83	4.01	3.82	3.61
CaO	0.01	0.01	0.01	0.04	0.05	0.01	0.01	0.01	0.00
Na_2O	0.16	0.25	0.07	0.15	0.09	0.05	0.05	0.07	0.04
K_2O	8.63	8.97	8.64	8.71	8.71	8.99	8.64	9.39	9.25
BaO	0.00	0.00	0.00	0.14	0.21	0.00	0.00	0.00	0.13
Total	95.73	95.22	95.30	95.92	95.65	97.46	94.66	97.43	95.94
	number of ions on the basis of 22 oxygens								
Si	5.758	5.861	5.795	5.742	5.644	5.578	5.604	5.670	5.[illegible]3
Ti	0.125	0.131	0.144	0.101	0.087	0.242	0.251	0.238	0.2[illegible]6
Al^{vi}	0.242	0.139	0.205	0.258	0.356	0.422	0.396	0.330	0.627
Al^{iv}	2.219	2.302	2.195	2.287	2.251	2.316	2.267	2.315	2.195
Fe	4.919	4.689	4.844	4.832	5.083	4.401	4.377	4.321	4.591
Cr	0.001	0.001	0.003	0.000	0.003	0.001	0.001	0.005	0.013
Mn	0.013	0.017	0.003	0.017	0.033	0.031	0.036	0.028	0.043
Mg	0.679	0.670	0.756	0.692	0.543	0.910	0.980	0.907	0.886
Ca	0.002	0.002	0.002	0.007	0.009	0.002	0.002	0.002	0.000
Na	0.051	0.080	0.022	0.048	0.029	0.015	0.016	0.022	0.013
K	1.817	1.885	1.821	1.829	1.855	1.829	1.807	1.908	1.943
Ba	0.000	0.000	0.000	0.010	0.014	0.000	0.000	0.000	0.009
Fe^*/Mg	7.244	6.998	6.407	6.982	9.360	4.836	4.466	4.764	5.181
Fe^*/Fe^*+Mg	0.878	0.874	0.865	0.874	0.903	0.828	0.817	0.826	0.838

FeO calculated as total iron (FeO*)

Table 6.13 Biotite analyses in metagraywackes

Sample no.	1 12-214	2 idem	3 idem	4 17-3504	5 idem	6 31-298	7 idem	8 idem	9 idem
SiO_2(wt%)	34.88	35.26	35.60	30.42	33.20	38.76	38.73	38.39	37.82
TiO_2	2.46	1.62	2.38	1.51	1.87	1.37	1.57	1.14	1.07
Al_2O_3	16.16	16,21	16.02	16.59	18.69	16.23	16.00	16.11	16.09
FeO*	28.47	27.21	27.44	31.60	30.22	16.98	16.60	16.39	16.23
Cr_2O_3	0.05	0.01	0.01	0.10	0.12	0.10	0.11	0.21	0.10
MnO	0.18	0.03	0.04	0.48	0.14	0.03	0.05	0.40	0.02
MgO	5.25	5.63	5.48	3.78	3.61	13.50	13.39	13.98	13.48
CaO	0.01	0.01	0.01	0.00	0.00	0.00	0.00	0.00	0.00
Na_2O	0.01	0.09	0.05	0.00	0.16	0.18	0.06	0.10	0.11
K_2O	9.61	9.32	9.45	8.41	9.62	9.13	9.56	9.74	9.44
BaO	0.00	0.00	0.00	0.00	0.09	0.00	0.00	0.00	0.00
Total	96.61	95.21	96.22	93.22	97.72	96.12	95.89	96.34	94.24
			number of ions on the basis of 22 oxygens						
Si	5.490	5.590	5.584	5.122	5.236	5.735	5.749	5.692	5.715
Ti	0.292	0.193	0.282	0.191	0.222	0.153	0.176	0.128	0.123
Al^{VI}	0.488	0.618	0.545	0.445	0.710	0.565	0.548	0.507	0.580
Al^{IV}	2.510	2.410	2.416	2.848	2.764	2.265	2.251	2.308	2.285
Fe	3.721	3.607	3.599	4.450	3.986	2.101	2.061	2.032	2.051
Cr	0.006	0.001	0.001	0.013	0.015	0.012	0.013	0.025	0.012
Mn	0.024	0.004	0.005	0.068	0.019	0.004	0.006	0.005	0.003
Mg	1.232	1.331	1.281	0.949	0.849	2.978	2.963	3.090	3.037
Ca	0.002	0.002	0.002	0.000	0.000	0.000	0.000	0.000	0.000
Na	0.003	0.028	0.015	0.000	0.049	0.052	0.017	0.029	0.032
K	1.930	1.885	1.891	1.914	1.935	1.723	1.810	1.842	1.820
Ba	0.000	0.000	0.000	0.000	0.006	0.000	0.000	0.000	0.000
Fe^*/Mg	3.020	2.709	2.809	4.689	4.694	0.705	0.695	0.657	0.675
Fe^*/Fe^*+Mg	0.751	0.730	0.737	0.824	0.824	0.413	0.410	0.396	0.403

FeO calculated as total iron (FeO*)

Table 6.13 Biotite analyses in metagraywackes (continued)

Sample no.	1 31-283	2 idem	3 idem	4 17-3507	5 idem	6 20-520	7 idem	8 idem	9 idem
SiO_2(wt%)	37.66	37.79	36.79	34.49	34.09	38.15	37.80	37.81	38.33
TiO_2	1.17	1.26	1.19	1.57	1.87	1.34	1.52	1.28	1.42
Al_2O_3	16.89	16.61	16.50	17.14	17.50	16.38	16.21	15.63	16.40
FeO*	16.72	17.08	16.57	29.38	29.53	15.12	15.68	16.66	14.72
Cr_2O_3	0.00	0.00	0.00	0.05	0.04	0.17	0.08	0.05	0.04
MnO	0.09	0.31	0.04	0.08	0.14	0.10	0.09	0.12	0.11
MgO	14.46	14.32	14.41	3.47	3.50	14.65	14.74	13.90	14.72
CaO	0.01	0.01	0.03	0.00	0.00	0.00	0.00	0.00	0.00
Na_2O	0.14	0.09	0.27	0.01	0.01	0.23	0.11	0.06	0.20
K_2O	9.65	9.40	9.00	9.35	9.65	9.35	9.69	9.69	9.44
BaO	0.12	0.06	0.10	0.00	0.00	0.00	0.00	0.00	0.00
Total	96.92	96.94	94.90	95.36	96.12	95.34	95.75	95.05	95.22
			number of ions on the basis of 22 oxygens						
Si	5.564	5.585	5.544	5.521	5.430	5.664	5.618	5.690	5.684
Ti	0.130	0.141	0.135	0.189	0.225	0.150	0.170	0.145	0.159
Al^{VI}	0.505	0.478	0.474	0.756	0.716	0.531	0.457	0.463	0.551
Al^{IV}	2.436	2.415	2.456	2.479	2.570	2.336	2.382	2.310	2.316
Fe	2.066	2.111	2.088	3.933	3.934	1.877	1.949	2.097	1.867
Cr	0.000	0.000	0.000	0.006	0.005	0.020	0.009	0.006	0.005
Mn	0.011	0.039	0.005	0.011	0.019	0.013	0.011	0.015	0.014
Mg	3.185	3.155	3.237	0.828	0.831	3.243	3.266	3.119	3.255
Ca	0.002	0.002	0.005	0.000	0.000	0.000	0.000	0.000	0.000
Na	0.040	0.026	0.079	0.003	0.003	0.066	0.032	0.018	0.058
K	1.819	1.772	1.730	1.910	1.961	1.771	1.837	1.861	1.786
Ba	0.008	0.004	0.006	0.000	0.000	0.000	0.000	0.000	0.000
Fe^t/Mg	0.648	0.669	0.645	4.750	4.734	0.578	0.596	0.672	0.560
Fe^t/Fe^t+Mg	0.393	0.400	0.392	0.826	0.825	0.366	0.373	0.210	0.359

FeO calculated as total iron (FeO*)

Table 6.14 biotite analysis in quartzite

Sample no.	1 20-143
SiO_2(wt%)	31.74
TiO_2	1.06
Al_2O_3	19.04
FeO^t	33.83
Cr_2O_3	0.14
MnO	0.07
MgO	1.91
Na_2O	0.13
K_2O	8.84
BaO	0.61
Total	96.82
number of ions on the basis of 22 oxygens	
Si	5.138
Ti	0.130
Al^{IV}	0.771
Al^{VI}	2.862
Fe	4.580
Cr	0.018
Mn	0.010
Mg	1.910
Na	0.041
K	1.826
Ba	0.004
Fe^t/Mg	9.930
Fe^t/Fe^t+Mg	.908

FeO calculated as total iron (FeO^t)

Table 5.15 Muscovite analyses in metagraywackes

Sample no.	1 17-3504	2 17-3506	3 idem	4 idem	5 17-3507	6 idem	7 idem	8 20-520
SiO_2(wt%)	47.79	46.55	46.28	46.17	45.30	45.65	46.58	46.81
TiO_2	0.14	0.21	0.21	0.20	0.35	0.33	0.36	0.05
Al_2O_3	36.47	35.85	35.49	35.57	36.25	36.45	37.03	35.18
FeO^t	1.63	1.71	2.31	1.91	1.78	1.64	1.74	1.11
Cr_2O_3	0.00	0.00	0.00	0.00	0.04	0.03	0.09	0.00
MnO	0.07	0.00	0.02	0.00	0.00	0.00	0.00	0.06
MgO	0.33	0.29	0.25	0.21	0.22	0.20	0.27	0.07
CaO	0.00	0.00	0.00	0.00	0.00	0.00	0.00	0.00
Na_2O	0.84	1.05	0.61	0.58	0.63	0.63	0.61	0.13
K_2O	10.09	10.07	10.28	10.14	10.20	10.08	9.88	10.11
BaO	0.18	0.11	0.14	0.34	0.05	0.05	0.04	0.06
Total	97.55	95.84	95.60	95.13	94.82	95.06	96.90	93.54
	number of ions on the basis of 22 oxygens							
Si	6.202	6.164	6.164	6.170	6.060	6.086	6.098	6.298
Ti	0.014	0.021	0.022	0.021	0.036	0.034	0.036	0.001
Al^{iv}	1.798	1.836	1.836	1.830	1.932	1.914	1.902	1.702
Al^{vi}	3.781	3.759	3.736	3.774	3.792	3.814	3.811	3.877
Fe	0.177	0.189	0.257	0.213	0.199	0.183	0.190	0.125
Cr	0.000	0.000	0.000	0.000	0.004	0.003	0.009	0.000
Mn	0.008	0.000	0.002	0.000	0.000	0.000	0.000	0.007
Mg	0.064	0.057	0.050	0.042	0.044	0.040	0.053	0.014
Ca	0.000	0.000	0.000	0.000	0.000	0.000	0.000	0.000
Na	0.211	0.270	0.158	0.150	0.164	0.163	0.155	0.034
K	1.671	1.701	1.747	1.729	1.743	1.714	1.650	1.735
Ba	0.009	0.006	0.008	0.018	0.003	0.003	0.003	0.004
musc.%	88.330	86.056	91.363	91.120	91.292	91.191	91.293	97.881
parag.%	11.176	13.638	8.240	7.921	8.570	8.662	8.567	1.913
Ba musc.%	0.494	0.306	0.397	0.958	0.139	0.146	0.140	0.207
Fe^t/Fe^t+Mg	0.831	0.855	0.902	0.900	0.890	0.891	0.865	0.940

FeO calculated as total iron (FeO^t)

Table 6.16 Muscovite analyses in quartzites

Sample no.	1 20-224	2 idem	3 20-233	4 idem	5 idem	6 20-190	7 idem	8 idem
SiO_2(wt%)	46.87	46.19	46.38	45.80	46.47	46.89	46.70	47.43
TiO_2	0.33	0.35	0.65	0.73	0.51	0.01	0.01	0.01
Al_2O_3	35.01	35.12	36.30	35.67	36.22	36.07	36.00	36.04
FeO*	1.54	1.56	1.14	1.38	1.09	1.16	1.34	1.34
Cr_2O_3	0.04	0.05	0.13	0.09	0.02	0.00	0.00	0.00
MgO	0.29	0.36	0.41	0.43	0.52	0.14	0.17	0.17
CaO	0.00	0.00	0.00	0.00	0.00	0.00	0.00	0.00
Na_2O	0.41	0.34	0.54	0.42	0.55	0.27	0.17	0.26
K_2O	10.41	10.66	10.73	11.00	10.82	11.13	10.41	10.57
BaO	0.13	0.09	0.05	0.03	0.03	0.00	0.00	0.00
Total	95.03	94.72	96.34	95.49	94.51	95.66	94.79	95.81
	number of ions on the basis of 22 oxygens							
Si	6.250	6.194	6.109	6.104	6.126	6.210	6.217	6.250
Ti	0.033	0.036	0.065	0.073	0.051	0.001	0.001	0.001
Al^{iv}	1.752	1.806	1.891	1.896	1.874	1.790	1.783	1.750
Al^{vi}	3.752	3.744	3.744	3.707	3.754	3.841	3.867	3.847
Fe	0.172	0.175	0.126	0.154	0.120	0.128	0.149	0.148
Cr	0.007	0.005	0.014	0.009	0.002	0.000	0.000	0.000
Mg	0.058	0.072	0.081	0.085	0.102	0.028	0.034	0.033
Ca	0.000	0.000	0.000	0.000	0.000	0.000	0.000	0.000
Na	0.106	0.088	0.138	0.109	0.141	0.069	0.044	0.066
K	1.771	1.824	1.803	1.870	1.820	1.881	1.768	1.777
Ba	0.007	0.005	0.003	0.002	0.002	0.000	0.000	0.000
musc.%	94.003	95.139	92.754	94.594	92.919	96.447	97.581	96.399
parag.%	5.627	4.612	7.095	5.406	7.081	3.553	2.419	3.601
Ba musc.%	0.370	0.249	0.151	0.000	0.000	0.000	0.000	0.000
Fe^t/Fe^t+Mg	0.747	0.708	0.608	0.644	0.540	0.820	0.814	0.817

FeO calculated as total iron (FeO*)

Table 6.17 Muscovite analyses in albite vein

Sample no.	1 27-242	2 idem	3 idem
SiO_2(wt%)	46.16	47.72	45.61
TiO_2	0.33	0.27	0.24
Al_2O_3	35.68	36.62	35.84
FeO*	1.38	2.64	1.59
Cr_2O_3	0.09	0.08	0.11
MnO	0.07	0.00	0.02
MgO	0.41	1.66	0.46
CaO	0.00	0.00	0.00
Na_2O	0.25	0.20	0.21
K_2O	10.32	10.63	11.07
BaO	0.03	0.03	0.06
Total	94.73	93.86	95.21
ions on the basis of 22 oxygens			
Si	6.167	6.490	6.103
Ti	0.034	0.028	0.025
Al^{IV}	1.833	1.510	1.897
Al^{VI}	3.785	3.399	3.756
Fe	0.154	0.300	0.178
Cr	0.010	0.009	0.012
Mn	0.008	0.000	0.002
Mg	0.082	0.337	0.092
Ca	0.000	0.000	0.000
Na	0.065	0.053	0.054
K	1.759	1.844	1.890
Ba	0.002	0.002	0.003
musc.%	96.539	97.113	97.033
parag.%	3.548	2.777	2.798
Ba musc.%	0.093	0.110	0.169
Fe^*/Fe^*+Mg	0.652	0.470	0.659

Table 6.18. Plagioclase analyses in gneisses

Sample no.	1 56-1071	2 idem	3 56-289	4 idem	5 idem	6 idem	7 19-191	8 idem	9 idem
SiO_2(wt%)	64.77	64.90	67.91	68.32	68.31	68.80	59.97	60.59	60.55
Al_2O_3	22.23	22.15	19.87	20.03	20.32	20.00	24.84	24.55	24.87
CaO	2.88	3.22	0.87	0.62	1.06	0.30	6.84	6.70	7.10
Na_2O	10.01	10.07	11.05	11.52	11.25	11.59	8.08	8.08	8.10
K_2O	0.01	0.01	0.06	0.01	0.01	0.01	0.02	0.01	0.01
Total	99.90	100.35	99.76	100.50	100.95	100.70	99.75	99.80	100.63
	number of ions on the basis of 32 oxygens								
Si	11.411	11.400	11.899	11.889	11.842	11.931	10.719	10.798	10.732
Al	4.616	4.586	4.104	4.108	4.152	4.088	5.233	5.157	5.196
Ca	0.544	0.606	0.163	0.116	0.197	0.056	1.310	1.279	1.348
Na	3.419	3.430	3.754	3.887	3.781	3.897	2.800	2.775	2.784
K	0.002	0.002	0.013	0.002	0.002	0.002	0.005	0.002	0.002
An(mol%)	13.7	15.0	4.2	2.9	4.9	1.4	31.8	31.5	32.6
Ab	86.2	84.9	95.5	97.1	95.0	98.5	68.1	68.4	67.3
Or	0.1	0.1	0.3	0.0	0.1	0.1	0.1	0.1	0.1

Table 6.18. Plagioclase analyses in gneisses (continued)

Sample no.	1 29-659	2 56-257B	3 idem	4 56-288B	5 idem	6 idem	7 idem	8 56-1071	9 idem
SiO_2(wt%)	66.40	67.84	68.82	66.00	68.00	67.13	68.08	65.52	64.71
Al_2O_3	21.29	19.44	19.83	21.04	19.45	20.42	20.17	21.38	22.16
CaO	2.31	0.48	0.41	2.02	0.43	1.14	0.83	1.54	3.29
Na_2O	10.83	11.52	11.40	10.73	11.50	11.44	11.28	10.06	9.99
K_2O	0.10	0.02	0.07	0.01	0.01	0.01	0.01	0.83	0.01
Total	100.93	99.30	100.53	99.80	99.39	100.14	100.37	99.33	100.16
	number of ions on the basis of 32 oxygens								
Si	11.581	11.945	11.953	11.619	11.956	11.759	11.862	11.598	11.389
Al	4.377	4.034	4.060	4.366	4.031	4.216	4.142	4.461	4.597
Ca	0.432	0.091	0.076	0.381	0.081	0.214	0.155	0.292	0.620
Na	3.662	3.933	3.839	3.663	3.921	3.886	3.811	3.453	3.409
K	0.022	0.004	0.016	0.002	0.002	0.003	0.002	0.187	0.002
An(mol%)	10.5	2.2	1.9	9.4	2.0	5.2	3.9	7.4	15.4
Ab	89.0	97.6	97.7	90.5	97.9	94.7	96.0	87.8	84.6
Or	0.5	0.2	0.4	0.1	0.1	0.1	0.1	4.8	0.1

Table 6.18 Plagioclase analyses in gneisses (continued)

Sample no.	1 56-257A	2 idem	3 idem	4 idem	5 idem	6 idem	7 56-1081	8 idem
SiO_2(wt%)	66.75	67.91	66.61	65.40	67.00	68.20	68.87	68.25
Al_2O_3	20.78	19.72	20.43	21.13	21.15	20.16	19.54	19.57
CaO	1.77	0.71	1.47	2.32	1.99	0.74	0.57	0.70
Na_2O	11.21	11.63	11.10	10.41	10.73	11.55	11.58	11.18
K_2O	0.05	0.05	0.04	0.05	0.07	0.04	0.14	0.02
Total	100.56	100.02	99.65	99.31	100.94	100.69	100.70	99.72
	number of ions on the basis of 32 oxygens							
Si	11.670	11.891	11.731	11.577	11.654	11.857	11.963	11.954
Al	4.282	4.070	4.241	4.409	4.336	4.131	4.001	4.040
Ca	0.332	0.133	0.277	0.440	0.371	0.138	0.106	0.131
Na	3.800	3.949	3.790	3.573	3.619	3.894	3.900	3.797
K	0.011	0.011	0.009	0.011	0.016	0.009	0.031	0.004
An(mol%)	8.0	3.3	6.8	10.9	9.3	3.4	2.6	3.3
Ab	91.7	96.5	93.0	88.8	90.4	96.4	96.6	96.5
Or	0.3	0.2	0.2	0.3	0.3	0.2	0.8	0.1

4-5 cloudy crystals 1-2-3-6 clean twinned crystals

yable 6.18. Plagioclase analyses in gneisses (continued)

Sample no.	1 15-212	2 idem	3 idem	4 31-311	5 idem	6 idem	7 idem	8 idem	9 idem
SiO_2(wt%)	67.63	66.64	65.57	65.12	65.59	64.45	63.63	64.96	63.87
Al_2O_3	20.47	21.05	21.08	21.83	21.70	22.30	22.86	22.07	23.28
CaO	1.42	2.25	2.15	3.60	2.94	3.75	3.73	3.38	2.86
Na_2O	11.29	10.80	11.23	9.63	10.45	10.02	9.63	9.75	10.74
K_2O	0.07	0.06	0.46	0.07	0.04	0.07	0.20	0.07	0.08
Total	100.88	100.80	100.29	100.25	100.72	100.59	100.05	100.23	100.83
	number of ions on the basis of 32 oxygens								
Si	11.764	11.626	11.535	11.445	11.478	11.325	11.241	11.418	11.204
Al	4.197	4.239	4.371	4.522	4.476	4.619	4.760	4.572	4.813
Ca	0.265	0.421	0.405	0.678	0.551	0.706	0.706	0.637	0.538
Na	3.800	3.654	3.831	3.282	3.546	3.414	3.299	3.323	3.653
K	0.016	0.013	0.103	0.016	0.009	0.016	0.045	0.016	0.018
An(mol%)	6.5	10.3	9.3	17.1	13.4	17.1	17.4	16.0	12.8
Ab	93.1	89.4	88.3	82.6	86.4	82.5	81.5	83.6	86.8
Or	0.4	0.3	2.4	0.3	0.2	0.4	1.1	0.4	0.4

1 - rim 2 - core 4 - core 5 - rim 8 - core 9 - rim

Table 6.18 Plagioclase analyses in gneisses (continued)

Sample no.	1 15-159	2 idem	3 idem
SiO_2(wt%)	67.14	68.42	68.60
Al_2O_3	20.48	20.05	20.45
CaO	0.67	0.74	0.97
Na_2O	10.58	10.86	10.61
K_2O	0.52	0.02	0.05
Total	99.39	100.09	100.68
number of ions on the basis of 32 oxygens			
Si	11.818	11.924	11.884
Al	4.249	4.118	4.176
Ca	0.126	0.138	0.180
Na	3.611	3.670	3.564
K	0.117	0.004	0.011
An(mol%)	3.3	3.6	4.8
Ab	93.7	96.3	94.9
Or	0.0	0.1	0.3

Table 6.19 Plagioclase analyses in amphibolites

Sample no.	1 20-505	2 idem	3 idem	4 idem	5 29-635	6 idem	7 idem
SiO_2(wt%)	66.95	66.49	68.13	66.80	63.67	63.54	63.27
Al_2O_3	20.55	20.47	20.04	20.89	22.57	23.04	22.85
CaO	1.85	2.11	0.93	1.38	4.20	4.87	4.94
Na_2O	11.16	11.27	11.77	10.98	9.71	9.23	9.05
K_2O	0.01	0.05	0.03	0.02	0.21	0.07	0.07
Total	100.52	100.39	100.90	100.07	100.40	100.75	100.18
	number of ions on the basis of 32 oxygens						
Si	11.704	11.665	11.841	11.702	11.237	11.170	11.183
Al	4.235	4.233	4.105	4.313	4.695	4.774	4.760
Na	0.374	0.397	0.173	0.259	0.794	0.917	0.936
Ca	3.783	3.834	3.967	3.730	3.323	3.146	3.102
K	0.002	0.011	0.007	0.004	0.056	0.016	0.016
An(mol%)	8.4	9.4	4.2	6.5	19.0	22.5	23.1
Ab	91.6	90.4	95.7	93.4	79.6	77.1	76.5
Or	0.2	0.2	0.1	0.1	1.3	0.4	0.4

2-3 same crystal 2- core, 3- rim
6-7 same crystal 6- core, 7- rim

Table 6.19 Plagioclase analyses in amphibolites (continued)

Sample no.	1 49-526	2 idem	3 56-1072	4 idem	5 idem	6 idem
SiO_2(wt%)	60.97	61.48	60.54	60.13	60.35	60.96
Al_2O_3	24.42	24.52	24.20	24.70	25.04	24.16
CaO	6.30	6.67	6.33	6.33	6.67	5.91
Na_2O	7.91	8.08	8.39	8.35	8.75	8.55
K_2O	0.02	0.03	0.02	0.04	0.01	0.02
Total	99.62	100.73	99.48	99.55	100.82	99.60
number of ions on the basis of 32 oxygens						
Si	10.866	10.854	10.835	10.759	10.693	10.881
Al	5.130	5.102	5.105	5.210	5.229	5.083
Ca	1.203	1.262	1.214	1.214	1.266	1.130
Na	2.734	2.749	2.912	2.897	3.006	2.959
K	0.005	0.007	0.005	0.009	0.002	0.005
An(mol%)	30.5	31.4	29.4	29.5	29.6	27.6
Ab	69.4	68.4	70.5	70.3	70.3	72.3
Or	0.1	0.2	0.1	0.2	0.1	0.1

Table 6.20 Plagioclase analyses in metagraywackes

Sample no.	1 21-283B	2 idem	3 idem	4 idem	5 17-3504	6 idem	7 idem	8 idem	9 idem
SiO_2(wt%)	51.84	52.68	52.98	52.44	62.84	61.78	63.49	64.03	62.76
Al_2O_3	31.13	30.38	30.27	30.66	23.68	23.40	22.47	22.60	23.68
CaO	13.48	13.71	13.57	13.23	4.85	4.98	3.98	4.03	4.89
Na_2O	3.21	4.13	4.12	4.00	9.13	8.99	9.41	9.40	8.94
K_2O	0.03	0.03	0.02	0.01	0.20	0.28	0.01	0.01	0.01
Total	99.69	100.93	100.96	100.34	100.52	99.43	99.36	100.17	100.28
				number of ions on the basis of 32 oxygens					
Si	9.410	9.482	9.523	9.473	11.073	11.034	11.281	11.292	11.077
Al	6.660	6.445	6.413	6.528	4.918	4.926	4.706	4.698	4.926
Ca	2.622	2.644	2.614	2.561	0.916	0.953	0.758	0.762	0.925
Na	1.130	1.441	1.436	1.401	3.119	3.113	3.242	3.214	3.060
K	0.007	0.003	0.005	0.002	0.004	0.064	0.002	0.002	0.002
An(mol%)	69.8	64.6	64.5	64.6	22.7	23.1	18.9	19.1	23.2
Ab	30.1	35.2	35.4	35.3	77.2	75.4	81.0	80.8	76.7
Or	0.1	0.2	0.1	0.1	0.1	1.5	0.1	0.1	0.1

3 - 4 same crystal 3- core, 4- rim

Table 6.21. Plagioclase analyses in Quartzites

Sample no.	1 20-244	2 idem	3 idem	4 idem
SiO_2(wt%)	68.57	68.50	68.93	68.69
Al_2O_3	19.07	19.28	19.37	19.23
CaO	0.35	0.28	0.23	0.47
Na_2O	11.83	11.76	11.99	11.94
K_2O	0.06	0.05	0.04	0.05
Total	100.42	99.87	100.56	100.38
number of ions on the basis of 34 oxygens				
Si	12.007	11.990	11.998	11.979
Al	3.936	3.978	3.971	3.953
Ca	0.066	0.053	0.043	0.088
Na	4.017	3.991	4.043	4.038
K	0.013	0.011	0.009	0.011
An(mol%)	1.6	1.3	1.0	2.1
Ab	98.0	98.4	98.7	97.6
Or	0.3	0.3	0.3	0.3

Table 6.22 Feldspar analyses in alkali-feldspar quartz syenite (YSG)

Sample no.	1 19-201	2 idem	3 idem	4 idem	5 idem
SiO_2(wt%)	69.18	67.71	64.64	64.42	63.63
Al_2O_3	19.01	18.64	17.64	17.70	17.80
CaO	0.29	0.39	0.02	0.00	0.00
Na_2O	10.42	12.06	0.39	0.22	0.29
K_2O	0.07	0.07	16.98	16.91	16.95
Total	98.97	98.87	99.67	99.25	98.67
number of ions on the basis of 32 oxygens					
Si	12.135	12.002	12.047	12.046	11.990
Al	3.930	3.894	3.875	3.901	3.953
Ca	0.055	0.074	0.004	0.000	0.000
Na	3.544	4.145	0.141	0.080	0.105
K	0.016	0.016	4.037	4.034	4.075
An(mol%)	1.5	1.7	0.1	0.0	0.0
Ab	98.1	97.9	3.4	1.9	2.5
Or	0.4	0.4	96.5	98.1	97.5

2- albite core 3- orthoclase rim

Table 6.23. Feldspar analyses in undeformed veins

Sample no.	1 20-544	2 idem	3 idem	4 idem	5 27-242	6 idem	7 idem
SiO_2(wt%)	64.85	63.54	63.91	64.43	69.25	68.61	68.77
Al_2O_3	18.03	18.20	17.95	18.08	18.91	19.37	18.96
CaO	0.00	0.00	0.02	0.00	0.01	0.04	0.04
Na_2O	0.18	0.12	0.14	0.20	12.05	11.71	12.36
K_2O	17.88	17.42	17.95	17.85	0.02	0.04	0.02
Total	100.94	99.28	99.97	100.56	100.24	99.97	100.15
	number of ions on the basis of 32 oxygens						
Si	11.984	11.926	11.948	11.959	12.067	12.005	12.019
Al	3.927	4.027	3.956	3.955	3.884	3.995	3.906
Ca	0.000	0.000	0.004	0.000	0.002	0.007	0.007
Na	0.065	0.044	0.051	0.072	4.071	3.973	4.189
K	4.216	4.171	4.281	4.227	0.004	0.009	0.004
An(mol%)	0.0	0.0	0.1	0.0	0.0	0.2	0.2
Ab	1.5	1.0	1.2	1.7	99.8	99.6	99.7
Or	98.5	99.0	98.7	98.3	0.2	0.2	0.1

1 to 4 microcline vein in amphibolite
5 to 7 albite in druse

Table 6.24 Chlorite analyses in gneisses

Sample no.	1 56-1071	2 idem	3 idem	4 idem	5 56-289	6 idem	7 idem	8 idem	9 idem
SiO_2(wt%)	28.29	28.88	27.78	27.61	27.44	26.25	26.43	27.38	27.92
TiO_2	3.66	0.17	0.25	0.18	0.09	1.49	0.07	0.31	0.12
Al_2O_3	14.63	15.55	16.73	17.10	16.42	16.54	16.19	16.69	16.41
FeO*	27.55	30.06	31.00	31.07	34.77	32.22	36.20	33.88	33.62
Cr_2O_3	0.05	0.11	0.04	0.04	0.10	0.07	0.07	0.04	0.02
MnO	0.25	0.25	0.16	0.30	0.18	0.28	0.11	0.12	0.20
MgO	10.98	13.44	11.82	11.64	8.77	8.00	8.65	9.23	9.38
CaO	2.79	0.00	0.06	0.05	0.00	3.05	0.00	0.19	0.00
Na_2O	0.00	0.00	0.00	0.00	0.00	0.17	0.00	0.00	0.01
K_2O	0.09	0.17	0.05	0.01	0.00	0.05	0.03	0.05	0.07
Total	88.29	88.63	87.89	88.00	87.77	88.12	87.75	87.39	87.75
			number of ions on the basis of 14 oxygens						
Si	3.096	3.086	3.011	2.989	3.039	2.927	2.962	3.028	3.070
Ti	0.301	0.013	0.020	0.014	0.007	0.125	0.005	0.025	0.009
Al	1.887	1.958	2.137	2.182	2.143	2.174	2.139	2.176	2.127
Fe	2.521	2.686	2.810	2.813	3.220	3.005	3.393	3.088	3.092
Cr	0.004	0.008	0.003	0.003	0.008	0.006	0.006	0.003	0.001
Mn	0.023	0.022	0.014	0.027	0.016	0.026	0.010	0.011	0.018
Mg	1.791	2.141	1.910	1.879	1.448	1.330	1.445	1.522	1.537
Ca	0.327	0.000	0.007	0.005	0.000	0.364	0.000	0.022	0.000
Na	0.000	0.000	0.000	0.000	0.000	0.036	0.000	0.000	0.002
K	0.012	0.023	0.006	0.001	0.000	0.007	0.004	0.007	0.009
Fe*/Mg	1.407	1.254	1.471	1.497	2.224	2.259	2.347	2.028	2.010
Fe*/Fe*+Mg	0.584	0.556	0.595	0.599	0.689	0.689	0.701	0.669	0.667

FeO calculated as total iron (FeO*)

Table 6.24 Chlorite analyses in gneisses (continued)

Sample no.	1 15-212	2 idem	3 idem	4 15-159	5 idem	6 idem	7 27-288	8 idem	9 idem
SiO_2(wt%)	26.89	29.69	26.63	28.07	27.75	27.57	28.44	28.83	30.04
TiO_2	0.40	0.16	0.11	0.16	0.04	0.18	0.01	0.07	0.01
Al_2O_3	17.44	17.60	16.63	16.28	17.05	16.53	18.93	20.32	18.84
FeO*	39.15	34.09	39.82	34.38	31.66	34.56	21.35	19.37	18.67
Cr_2O_3	0.0.	0.01	0.01	0.01	0.01	0.01	0.01	0.01	0.01
MnO	0.24	0.27	0.24	0.32	0.38	0.25	0.12	0.04	0.01
MgO	6.59	6.79	6.83	9.91	11.23	9.96	18.05	18.60	19.98
CaO	0.05	0.06	0.05	0.09	0.11	0.09	0.05	0.01	0.09
Na_2O	0.01	0.01	0.16	0.01	0.04	0.05	0.01	0.01	0.01
K_2O	0.76	1.28	0.12	0.16	0.03	0.23	0.03	0.01	0.07
Total	91.54	89.96	90.60	89.39	88.30	89.43	87.00	87.27	87.73
			number of ions on the basis of 14 oxygens						
Si	2.935	3.188	2.941	3.044	3.002	2.997	2.942	2.932	3.026
Ti	0.032	0.012	0.009	0.013	0.003	0.014	0.000	0.005	0.000
Al	2.244	2.227	2.165	2.081	2.174	2.118	2.308	2.436	2.237
Fe	3.574	3.061	3.679	3.119	2.864	3.142	1.847	1.647	1.573
Cr	0.000	0.000	0.000	0.000	0.000	0.000	0.000	0.000	0.000
Mn	0.022	0.024	0.022	0.029	0.034	0.023	0.010	0.003	0.000
Mg	1.072	1.086	1.124	1.602	1.811	1.614	2.783	2.820	3.000
Ca	0.005	0.006	0.005	0.010	0.012	0.010	0.005	0.001	0.008
Na	0.002	0.002	0.034	0.002	0.008	0.010	0.002	0.002	0.002
K	0.105	0.175	0.016	0.022	0.004	0.031	0.004	0.001	0.008
Fe*/Mg	3.333	2.816	3.270	1.946	1.581	1.946	0.663	0.584	0.524
Fe*/Fe*+Mg	0.769	0.738	0.765	0.660	0.612	0.660	0.398	0.368	0.343

FeO calculated as total iron (FeO*) 7-8-9 mylonitic matrix

Table 6.24 Chlorite analyses in gneisses (continued)

Sample no.	1 56-257	2 idem	3 idem	4 idem	5 29-658	6 idem	7 idem	8 idem	9 15-159
SiO_2(wt%)	28.25	27.67	27.69	27.68	27.55	29.05	28.01	28.43	27.05
TiO_2	0.09	0.06	0.04	0.07	0.05	0.07	0.06	0.10	0.13
Al_2O_3	16.20	16.39	17.06	17.87	16.35	16.36	16.08	16.03	18.82
FeO^t	33.13	32.38	33.92	35.07	32.41	31.09	31.61	32.32	33.87
Cr_2O_3	0.23	0.27	0.25	0.51	0.01	0.01	0.01	0.01	0.01
MnO	0.01	0.01	0.01	0.01	0.21	0.08	0.12	0.27	0.01
MgO	11.24	10.71	10.36	9.73	11.54	11.34	11.34	12.68	11.96
CaO	0.09	0.09	0.07	0.06	0.10	0.03	0.04	0.11	0.61
Na_2O	0.01	0.01	0.01	0.01	0.11	0.01	0.25	0.01	0.01
K_2O	0.19	0.12	0.16	0.03	0.17	0.98	0.07	0.21	0.01
Total	89.44	87.61	89.57	91.04	88.50	89.02	87.59	90.17	92.48
	number of ions on the basis of 14 oxygens								
Si	3.038	3.028	2.984	2.945	2.993	3.111	3.056	3.021	2.819
Ti	0.007	0.004	0.003	0.005	0.004	0.005	0.004	0.008	0.010
Al	2.053	2.114	2.167	2.241	2.093	2.065	2.068	2.008	2.312
Fe	2.979	2.963	3.057	3.121	2.944	2.784	2.885	2.873	2.952
Cr	0.019	0.023	0.021	0.042	0.000	0.000	0.000	0.000	0.000
Mn	0.000	0.000	0.000	0.000	0.019	0.007	0.011	0.024	0.000
Mg	1.801	1.747	1.664	1.543	1.868	1.810	1.844	2.009	1.858
Ca	0.010	0.010	0.008	0.006	0.011	0.003	0.004	0.012	0.068
Na	0.002	0.002	0.002	0.002	0.023	0.002	0.052	0.002	0.002
K	0.026	0.016	0.022	0.004	0.023	0.133	0.008	0.029	0.001
Fe^t/Mg	1.653	1.696	1.836	2.022	1.575	1.538	1.563	1.430	1.588
Fe^t/Fe^t+Mg	0.623	0.629	0.647	0.669	0.611	0.606	0.610	0.588	0.613

FeO calculated as total iron (FeO^t)

Table 6.25 Chlorite analyses in amphibolites

Sample no.	1 56-135	2 idem	3 idem	4 49-526	5 idem	6 idem	7 20-505	8 idem	9 idem
SiO_2(wt%)	25.89	25.82	26.45	29.96	28.57	29.15	27.92	28.98	29.81
TiO_2	0.14	0.29	0.06	0.17	0.07	0.08	0.04	0.07	0.04
Al_2O_3	18.37	18.57	17.44	15.92	17.43	16.43	17.20	16.65	15.62
FeO	34.39	33.86	35.00	29.89	29.36	30.68	29.84	29.69	29.32
Cr_2O_3	0.01	0.01	0.01	0.01	0.01	0.01	0.01	0.01	0.01
MnO	0.23	0.35	0.11	0.16	0.24	0.24	0.14	0.09	0.12
MgO	10.66	10.57	10.02	13.70	14.48	13.64	13.81	13.90	14.26
CaO	0.04	0.12	0.05	0.05	0.13	0.06	0.05	0.09	0.08
Na_2O	0.01	0.01	0.01	0.01	0.01	0.01	0.03	0.01	0.01
K_2O	0.02	0.02	0.03	0.65	0.33	0.20	0.06	0.09	0.08
Total	89.76	89.62	89.18	90.52	90.63	90.50	89.10	89.58	89.35
	number of ions on the basis of 14 oxygens								
Si	2.803	2.797	2.889	3.124	2.968	3.049	2.959	3.044	3.130
Ti	0.011	0.023	0.004	0.013	0.005	0.006	0.003	0.005	0.003
Al	2.344	2.371	2.245	1.957	2.134	2.026	2.149	2.061	1.933
Fe	3.114	3.067	3.197	2.607	2.551	2.684	2.645	2.608	2.575
Cr	0.000	0.000	0.000	0.000	0.000	0.000	0.000	0.000	0.000
Mn	0.021	0.032	0.010	0.014	0.021	0.021	0.012	0.008	0.010
Mg	1.720	1.707	1.631	2.129	2.243	2.127	2.182	2.177	2.232
Ca	0.004	0.013	0.005	0.005	0.014	0.006	0.005	0.010	0.008
Na	0.002	0.002	0.002	0.002	0.002	0.002	0.006	0.002	0.002
K	0.002	0.002	0.004	0.085	0.043	0.026	0.008	0.012	0.010
Fe^t/Mg	1.809	1.797	1.959	1.224	1.137	1.261	1.212	1.198	1.153
Fe^t/Fe^t+Mg	0.644	0.642	0.662	0.550	0.532	0.557	0.548	0.545	0.534

FeO calculated as total iron (FeO^t) 1 to 5 alteration of biotite
7- alteration of hastingsite 8 and 9 alteration of biotite

Table 6.26 Chlorite analyses in iron formation

Sample no.	1 56-2805	2 idem	3 idem	4 idem	5 idem	6 idem	7 50-6821	8 idem
SiO_2(wt%)	26.07	26.45	27.89	27.26	27.10	24.03	26.22	26.60
TiO_2	0.06	0.08	0.09	0.13	0.04	0.04	0.05	0.05
Al_2O_3	17.32	17.38	15.98	17.98	18.14	17.65	18.69	17.73
FeO*	41.64	42.59	41.05	40.50	40.21	40.17	38.24	38.27
Cr_2O_3	0.01	0.01	0.01	0.01	0.01	0.01	0.01	0.01
MnO	0.76	0.74	0.92	0.65	0.55	0.70	0.19	0.16
MgO	5.90	5.85	5.00	5.11	5.41	5.20	7.58	7.61
CaO	0.02	0.04	0.02	0.02	0.03	0.02	0.05	0.08
Na_2O	0.01	0.01	0.01	0.02	0.02	0.01	0.01	0.01
K_2O	0.07	0.07	0.41	0.99	0.06	0.22	0.10	0.20
Total	91.86	92.72	91.38	92.67	91.57	90.05	91.14	90.82
	number of ions on the basis of 14 oxygens							
Si	2.870	2.891	3.075	2.995	2.951	2.905	2.843	2.908
Ti	0.005	0.006	0.007	0.010	0.003	0.003	0.004	0.004
Al	2.247	2.239	2.076	2.297	2.328	2.322	2.388	2.276
Fe	3.834	3.893	3.785	3.672	3.662	3.750	3.468	3.486
Cr	0.000	0.000	0.000	0.000	0.000	0.000	0.000	0.000
Mn	0.070	0.059	0.085	0.059	0.050	0.066	0.017	0.014
Mg	0.968	0.889	0.821	0.825	0.878	0.865	1.225	1.235
Ca	0.002	0.004	0.002	0.002	0.003	0.002	0.005	0.008
Na	0.002	0.002	0.002	0.004	0.004	0.002	0.002	0.002
K	0.008	0.008	0.057	0.136	0.008	0.031	0.013	0.027
Fe^t/Mg	3.959	4.389	4.606	4.446	4.169	4.334	2.830	2.821
Fe^t/Fe^t+Mg	0.798	0.814	0.821	0.816	0.806	0.812	0.738	0.738

FeO calculated as total iron (FeO*) 2- 6- chlorite replacing biotite
3-7-8- chlorite replacing garnet

Table 6.27 Chlorite analyses in metagraywackes

Sample no.	1 17-3506	2 idem	3 idem	4 idem	5 idem	6 idem	7 20-520	8 idem	9 idem
SiO_2(wt%)	23.21	24.83	24.95	24.36	24.38	27.21	28.64	28.78	28.33
TiO_2	0.13	0.11	0.10	0.11	0.39	0.40	0.03	0.06	0.04
Al_2O_3	21.70	20.97	22.59	21.23	21.27	20.06	20.78	19.62	20.84
FeO^t	38.42	39.36	40.61	40.28	40.53	38.88	18.36	19.00	18.63
Cr_2O_3	0.15	0.13	0.19	0.22	0.24	0.24	0.01	0.01	0.01
MnO	0.01	0.01	0.01	0.01	0.01	0.01	0.15	0.10	0.11
MgO	3.88	4.19	3.92	4.02	4.26	3.93	20.34	18.74	20.00
CaO	0.05	0.02	0.08	0.02	0.04	0.07	0.01	0.05	0.02
Na_2O	0.01	0.01	0.22	0.01	0.01	0.01	0.01	0.01	0.01
K_2O	0.07	0.02	0.08	0.09	0.15	1.85	0.10	0.03	0.05
Total	87.63	89.65	92.75	90.35	91.28	92.66	88.43	86.40	88.04
	number of ions on the basis of 14 oxygens								
Si	2.639	2.754	2.680	2.698	2.680	2.927	2.865	2.956	2.851
Ti	0.011	0.001	0.008	0.009	0.032	0.032	0.002	0.004	0.003
Al	2.909	2.742	2.860	2.772	2.756	2.544	2.450	2.375	2.472
Fe	3.654	3.652	3.649	3.731	3.726	3.498	1.536	1.632	1.568
Cr	0.013	0.011	0.016	0.019	0.020	0.020	0.000	0.000	0.000
Mn	0.001	0.000	0.000	0.000	0.000	0.000	0.012	0.008	0.008
Mg	0.657	0.693	0.627	0.663	0.698	0.630	3.033	2.869	3.000
Ca	0.006	0.002	0.009	0.002	0.004	0.008	0.001	0.005	0.002
Na	0.002	0.002	0.045	0.002	0.002	0.002	0.001	0.002	0.002
K	0.010	0.002	0.011	0.012	0.021	0.253	0.012	0.003	0.006
Fe^t/Mg	5.555	5.270	5.812	5.621	5.337	5.550	0.506	0.568	0.522
Fe^t/Fe^t+Mg	0.847	0.840	0.853	0.849	0.842	0.847	0.336	0.362	0.343

FeO calculated as total iron (FeO^t) 1-2-9- chlorite replacing biotite
4- chlorite replacing of tourmaline

Table 6.28 Chlorite analyses in quartzites

Sample no.	1 20-221	2 idem	3 idem	4 idem
SiO_2(wt%)	26.87	24.13	26.64	24.68
TiO_2	0.35	0.08	0.41	0.23
Al_2O_3	17.48	20.05	18.08	19.36
FeO^t	43.47	44.33	39.93	42.66
Cr_2O_3	0.01	0.01	0.01	0.01
MnO	0.32	0.23	0.03	0.25
MgO	2.42	1.95	1.82	2.11
CaO	0.05	0.05	0.05	0.04
Na_2O	0.06	0.01	0.02	0.01
K_2O	1.83	0.16	1.48	0.59
Total	92.86	91.00	88.47	89.94
number of ions on the basis of 14 oxygens				
Si	2.975	2.721	3.039	2.803
Ti	0.029	0.006	0.035	0.019
Al	2.281	2.665	2.431	2.592
Fe	4.025	4.181	3.809	4.053
Cr	0.000	0.000	0.000	0.000
Mn	0.030	0.022	0.002	0.024
Mg	0.399	0.327	0.309	0.357
Ca	0.005	0.006	0.006	0.004
Na	0.012	0.002	0.004	0.002
K	0.258	0.023	0.215	0.085
Fe^t/Mg	10.077	12.754	12.308	11.342
Fe^t/Fe^t+Mg	0.909	0.927	0.924	0.919

FeO calculated as total iron (FeO^t)

Table 6.29 Chlorite analyses in veins

Sample no.	1 50-6821	2 idem	3 idem	4 idem	5 56-135	6 idem	7 idem	8 49-526	9 idem
SiO_2(wt%)	26.99	25.70	27.16	25.91	25.63	26.85	26.52	26.24	28.20
TiO_2	0.06	0.07	0.16	0.05	0.01	0.07	0.04	0.07	0.06
Al_2O_3	18.41	18.37	17.71	18.54	17.18	16.90	19.29	20.89	16.95
FeO^t	37.38	37.51	37.13	37.81	34.81	35.28	33.45	26.23	29.48
Cr_2O_3	0.01	0.01	0.01	0.01	0.01	0.01	0.01	0.20	0.04
MnO	0.35	0.17	0.14	0.16	0.18	0.25	0.23	0.01	0.01
MgO	7.34	7.12	7.48	7.25	10.56	10.50	10.50	15.39	13.27
CaO	0.04	0.03	0.06	0.08	0.05	0.03	0.14	0.05	0.10
Na_2O	0.01	0.01	0.01	0.01	0.01	0.01	0.03	0.01	0.01
K_2O	0.16	0.11	0.78	0.09	0.03	0.02	0.03	0.02	0.01
Total	90.75	89.10	90.64	89.91	88.47	89.92	90.24	89.11	88.13
	number of ions on the basis of 14 oxygens								
Si	2.923	2.851	2.955	2.848	2.831	2.912	2.829	2.727	3.013
Ti	0.004	0.005	0.013	0.004	0.000	0.005	0.003	0.005	0.004
Al	2.350	2.402	2.271	2.402	2.236	2.160	2.426	2.559	2.134
Fe	3.386	3.480	3.379	3.475	3.215	3.200	2.985	2.280	2.634
Cr	0.000	0.000	0.000	0.000	0.000	0.000	0.000	0.016	0.003
Mn	0.032	0.016	0.012	0.014	0.016	0.023	0.020	0.000	0.000
Mg	1.185	1.177	1.213	1.188	1.738	1.697	1.670	2.385	2.113
Ca	0.004	0.003	0.007	0.009	0.005	0.003	0.016	0.005	0.011
Na	0.002	0.002	0.002	0.002	0.002	0.002	0.006	0.002	0.002
K	0.022	0.015	0.108	0.012	0.004	0.002	0.004	0.002	0.001
Fe^t/Mg	2.857	2.955	2.784	2.925	1.894	1.885	1.787	1.704	1.246
$Fe^t/(Fe^t+Mg)$	0.740	0.747	0.735	0.745	0.649	0.653	0.641	0.630	0.554

FeO^t calculated as total iron (FeO^t) 1 to 4 veins in iron formation
5 to 9 veins in amphibolite

Table 6.29 Chlorite analyses in veins (continued)

Sample no.	1 20-505	2 idem	3 idem
SiO_2(wt%)	29.38	29.01	29.52
TiO_2	0.04	0.05	0.04
Al_2O_3	17.11	15.98	15.79
FeO^t	29.86	28.44	29.20
Cr_2O_3	0.01	0.01	0.01
MnO	0.17	0.09	0.14
MgO	15.05	14.39	14.55
CaO	0.05	0.21	0.12
Na_2O	0.01	0.01	0.01
K_2O	0.44	0.04	0.12
Total	92.12	88.23	89.50
number of ions on the basis of 14 oxygens			
Si	3.003	3.079	3.097
Ti	0.003	0.004	0.003
Al	2.061	1.999	1.952
Fe	2.552	2.534	2.562
Cr	0.000	0.000	0.000
Mn	0.014	0.008	0.012
Mg	2.293	2.276	2.275
Ca	0.005	0.023	0.013
Na	0.002	0.002	0.002
K	0.057	0.005	0.016
Fe^t/Mg	1.113	1.108	1.125
Fe^t/Fe^t+Mg	0.526	0.525	0.529

FeO calculated as total iron (FeO^t)
1 to 3 vein in amphibolite

Table 6.30 Tourmaline analyses in gneisses and amphibolite

Sample no.	1 20-505	2 idem	3 idem	4 idem	5 31-311	6 idem	7 idem	8 29-658	9 idem
SiO_2(wt%)	36.54	36.16	36.56	36.35	36.94	37.31	36.91	37.77	37.64
TiO_2	1.80	1.54	1.73	1.62	0.05	0.30	0.27	0.00	0.00
Al_2O_3	26.73	26.71	26.95	27.07	35.64	34.39	33.63	34.75	34.84
FeO^t	12.95	12.19	12.51	12.85	5.48	5.84	5.45	6.72	6.64
MnO	0.00	0.00	0.00	0.02	0.00	0.00	0.00	0.00	0.00
MgO	7.19	7.02	7.14	7.47	6.98	7.53	7.06	6.55	6.64
CaO	1.08	1.01	1.30	1.78	0.39	0.53	0.56	0.19	0.21
Na_2O	2.43	2.63	2.29	2.08	2.08	2.34	2.20	2.53	2.29
K_2O	0.03	0.00	0.04	0.04	0.03	0.06	0.05	0.01	0.01
Total	88.75	87.26	88.52	89.28	87.59	88.30	86.13	88.52	88.27
	number of ions on the basis of 29 oxygens and 3 boron atoms								
Si	6.099	6.110	6.101	6.032	5.862	5.911	5.975	5.969	5.957
Al	5.259	5.319	5.301	5.295	6.667	6.422	6.417	6.473	6.499
Fe	1.807	1.722	1.745	1.783	0.727	0.773	0.737	0.888	0.879
Mg	1.789	1.768	1.776	1.848	1.651	1.778	1.703	1.543	1.566
Ti	0.226	0.195	0.217	0.202	0.000	0.035	0.032	0.000	0.000
Mn	0.000	0.000	0.000	0.002	0.000	0.000	0.000	0.000	0.000
Na	0.786	0.861	0.741	0.669	0.640	0.718	0.690	0.775	0.702
Ca	0.193	0.182	0.232	0.316	0.066	0.090	0.097	0.032	0.035
K	0.006	0.000	0.008	0.008	0.006	0.012	0.010	0.002	0.002
Fe^t/Mg	1.01	.974	.983	.965	.440	.435	.433	.575	.561
Fe^t/Fe^t+Mg	.502	.493	.495	.491	.305	.303	.302	.365	.359

FeO calculated as total iron (FeO^t) 1 to 4 - amphibolite 1-core, 2-rim, 3-core, 4- rim, 5 to 9 - gneiss.

Table 6.31 Tourmaline analyses in iron formation and metagraywackes

Sample no.	1 50-6821	2 idem	3 idem	4 31-298	5 idem	6 idem	7 17-3504	8 idem
SiO_2(wt%)	35.98	35.37	35.86	37.85	36.99	37.71	36.52	35.34
TiO_2	0.65	0.74	0.66	0.50	0.55	0.53	0.52	0.55
Al_2O_3	30.00	30.21	29.96	31.13	30.31	31.60	35.28	35.35
FeO	13.21	12.82	13.24	6.90	7.33	6.65	10.75	10.78
MnO	0.03	0.00	0.01	0.00	0.00	0.02	0.00	0.00
MgO	4.86	5.01	4.91	8.90	9.03	8.78	3.45	3.38
CaO	0.96	0.73	1.03	1.95	2.63	1.84	0.50	0.75
Na_2O	2.30	2.48	2.52	1.91	1.48	1.82	1.38	1.68
K_2O	0.04	0.03	0.03	0.04	0.02	0.02	0.05	0.01
Total	88.03	87.39	88.22	89.18	88.34	88.47	88.45	87.84
	number of ions on the basis of 29 oxygens and 3 boron atoms							
Si	5.992	5.931	5.970	6.016	5.968	5.995	5.892	5.768
Al	5.889	5.971	5.879	5.833	5.764	5.921	6.709	6.801
Fe	1.840	1.797	1.843	0.917	0.988	0.884	1.450	1.471
Mg	1.206	1.252	1.218	2.109	2.172	2.080	0.829	0.822
Ti	0.081	0.093	0.082	0.059	0.066	0.063	0.063	0.067
Mn	0.004	0.000	0.009	0.000	0.000	0.002	0.000	0.000
Na	0.742	0.806	0.813	0.588	0.463	0.561	0.431	0.531
Ca	0.171	0.131	0.183	0.332	0.454	0.313	0.008	0.131
K	0.008	0.006	0.006	0.008	0.004	0.004	0.010	0.002
Fe^*/Mg	1.524	1.435	1.512	0.435	0.455	0.424	1.748	1.789
Fe^*/Fe^*+Mg	.604	.589	.602	.303	.312	.298	.636	.641

FeO calculated as total iron (FeO^*) 4 to 8 - metagraywackes
1 to 3 - Type II iron formation

Table 6.32 Oxide mineral analyses in iron formation and amphibolite

Sample no.	1 61-230 /3	2 56-217 /2-3	3 61-120 /2	4 49-351 /5A	5 50-127 /1	6 20-505	7 20-505
TiO_2(wt%)	0.04	0.09	0.18	0.46	0.00	0.20	51.36
Al_2O_3	0.31	0.31	2.14	0.86	0.29	1.51	0.19
Cr_2O_3	0.11	0.00	0.04	0.73	0.05	0.15	0.04
FeO*							47.80
Fe_2O_3=	71.73	70.78	68.57	70.32	71.40	70.05	0.00
FeO=	29.12	28.67	27.77	28.48	28.91	28.37	
MnO	0.14	0.07	0.00	0.00	0.02	0.00	1.11
MgO	0.00	0.00	0.00	0.02	0.03	0.00	0.02
Total	100.95	99.92	98.70	100.87	100.70	100.10	100.52

FeO*- FeO calculated as total iron; FeO= and Fe_2O_3= calculated from analyses 1 to 5 - magnetite in iron formation 1,2,3 and 5 - Type I iron formation 4 - Type II iron formation 6 -magnetite in amphibolite 7 - ilmenite in amphibolite

Table 6.33 Epidote analyses in veins

Sample no.	1 56-289	2 idem	3 56-288	4 idem	5 56-108	6 idem	7 20-544	8 idem
SiO_2(wt%)	38.08	37.54	37.75	37.92	38.38	37.96	38.11	38.54
TiO_2	0.04	0.05	0.03	0.00	0.02	0.07	0.10	0.03
Al_2O_3	21.10	21.82	20.70	20.75	22.07	21.58	21.56	22.03
Fe_2O_3	14.62	14.61	13.93	14.28	13.82	14.79	14.66	14.31
MnO	0.13	0.10	0.02	0.11	0.03	0.10	0.18	0.13
MgO	0.01	0.01	0.01	0.01	0.01	0.01	0.01	0.02
CaO	24.42	23.74	22.19	23.47	23.95	24.04	23.03	24.41
Na_2O	0.00	0.06	0.21	0.00	0.00	0.05	0.04	0.04
K_2O	0.03	0.02	0.10	0.03	0.02	0.01	0.00	0.02
Total	98.43	97.95	96.94	96.57	98.30	98.61	97.68	99.53
	number of ions on the basis of 13 oxygens							
Si	3.130	3.195	3.152	3.165	3.141	3.111	3.141	3.124
Al	2.044	2.121	1.999	2.041	2.128	2.085	2.095	2.104
Fe	1.005	1.007	0.985	0.997	0.945	1.013	1.010	0.970
Mn	0.008	0.007	0.001	0.007	0.002	0.006	0.012	0.008
Mg	0.001	0.001	0.001	0.001	0.001	0.001	0.001	0.002
Ti	0.002	0.003	0.001	0.000	0.001	0.004	0.006	0.001
Ca	2.150	2.097	2.011	2.099	2.100	2.111	2.034	2.120
Na	0.000	0.008	0.034	0.000	0.000	0.007	0.006	0.006
K	0.003	0.002	0.010	0.003	0.002	0.001	0.000	0.002
Ps	32.9	32.2	32.3	32.8	30.7	32.7	32.5	31.5

Total iron as Fe_2O_3. 1 to 6 epidote vein in gneiss, 1- centre, 2- margin 3-centre, 4- margin. 7 - 8 epidote vein in amphibolite, 7- brown core; 8- greenish rim.

Table 6.34 Allanite analyses

Sample no.	1 20-544	2 idem	3 idem	4 49-505	5 idem	6 idem	7 idem
SiO_2(wt%)	35.17	35.10	33.75	33.44	33.61	32.37	35.75
TiO_2	0.29	0.24	0.27	0.14	0.15	0.18	0.13
Al_2O_3	17.22	16.47	17.69	16.17	17.18	16.27	16.61
FeO*	14.42	14.64	12.39	11.23	10.39	11.11	9.66
MnO	0.69	0.58	0.59	0.73	0.79	0.81	0.73
MgO	0.36	0.22	0.43	0.42	0.35	0.49	0.42
CaO	14.18	14.63	13.71	9.80	10.18	10.00	10.09
Na_2O	0.18	0.25	0.24	0.13	0.22	0.29	0.17
Y_2O_3	0.44	0.37	0.69	0.64	0.54	0.58	0.69
U_2O_3	0.23	0.19	0.15	0.31	0.13	0.39	0.20
La_2O_3	5.01	4.34	5.38	6.91	7.15	7.01	6.47
Ce_2O_3	8.61	7.11	8.21	11.34	11.57	11.36	10.66
Total	96.79	94.14	93.51	91.27	92.25	90.87	91.57
number of ions on the basis of 13 oxygens							
Si	3.372	3.390	3.359	3.576	3.550	3.507	3.709
Al	1.946	1.874	2.075	2.038	2.139	2.077	2.031
Fe	1.156	1.182	1.031	1.004	0.918	1.006	0.838
Mn	0.056	0.047	0.049	0.066	0.070	0.074	0.065
Mg	0.051	0.031	0.063	0.067	0.055	0.079	0.065
Ti	0.020	0.017	0.020	0.011	0.011	0.014	0.010
Ca	1.456	1.514	1.462	1.123	1.152	1.160	1.121
Na	0.033	0.046	0.046	0.027	0.045	0.060	0.034

Total iron as FeO. 1 to 3 - amphibolite, 1- dark brown core, 2- light brown rim, 4 to 7 - gneiss, 5- brown core, 6- brownish rim

Table 6.35 Carbonate analyses in veins

Sample no.	1 56-135	2 idem	3 56-289	4 idem	5 idem	6 20-544	7 idem	8 idem
FeO*(wt%)	0.08	0.12	0.00	0.04	0.00	0.00	0.01	0.00
MnO	0.04	0.33	0.00	0.00	0.00	0.00	0.02	0.00
MgO	0.05	0.07	0.03	0.03	0.01	0.05	0.03	0.07
CaO	56.05	54.95	56.47	56.05	56.32	56.15	55.45	55.35
Total	56.22	55.47	56.50	56.12	56.33	56.20	55.51	55.43
$FeCO_3$	0.13	0.19	0.00	0.06	0.00	0.00	0.02	0.00
$MnCO_3$	0.06	0.53	0.00	0.00	0.00	0.00	0.03	0.00
$MgCO_3$	0.10	0.15	0.06	0.06	0.02	0.10	0.06	0.15
$CaCO_3$	100.04	98.07	100.79	100.04	100.52	100.21	98.97	98.80
Total	100.33	98.95	100.85	100.16	100.54	100.32	99.08	98.95

FeO calculated as total iron (FeO*) 1 and 2- same vein in amphibolite 1.margin, 2. centre 3, 4 and 5- same vein in gneiss 3. centre, 4 margin, 5 opposite margin 6, 7 and 8- same vein in amphibolite 6. centre, 7 margin, 8 opposite margin

Table 6.36 Greenalite analyses in iron formation

Sample no.	1 49-351 -4	2 idem	3 idem	4 61-230 -3	5 idem	6 idem	7 idem
SiO_2(wt%)	36.87	35.58	36.65	36.97	35.05	36.07	36.03
TiO_2	0.09	0.10	0.09	0.07	0.06	0.09	0.07
Al_2O_3	0.99	0.17	0.23	0.02	0.00	0.20	0.07
FeO*	49.50	51.76	49.83	54.68	55.76	54.86	55.10
MnO	0.54	0.54	0.59	0.58	0.72	0.60	0.63
MgO	3.89	3.72	3.96	0.71	0.13	0.13	0.13
CaO	0.03	0.12	0.09	0.07	0.09	0.07	0.07
Na_2O	0.00	0.02	0.00	0.00	0.00	0.00	0.00
K_2O	0.08	0.08	0.06	0.02	0.05	0.04	0.03
Total	91.99	92.09	91.50	93.12	91.86	92.06	92.06
	number of ions on the basis of 14 oxygens						
Si	4.186	4.115	4.206	4.294	4.168	4.234	4.233
Al	0.132	0.023	0.031	0.002	0.000	0.027	0.008
Ti	0.007	0.008	0.007	0.006	0.005	0.007	0.006
Fe	4.700	5.007	4.782	5.311	5.546	5.386	5.415
Mn	0.051	0.052	0.057	0.057	0.072	0.059	0.062
Mg	0.658	0.641	0.677	0.022	0.023	0.022	0.022
Ca	0.003	0.014	0.011	0.008	0.011	0.008	0.008
Na	0.000	0.004	0.000	0.000	0.000	0.000	0.000
K	0.011	0.011	0.008	0.003	0.007	0.006	0.004
Fe*/Mg	7.139	7.806	7.059	235.97	240.63	236.75	237.79
Fe*/Fe*+Mg	.868	.878	.875	.995	.995	.995	.995

FeO calculated as total iron (FeO*) 1 to 3 alteration of hastingsite
4 - 5 - 7 - veins 6 - alteration of fayalite

Table 6.37 Stilpnomelane analyses in vein

Sample no.	1 61-124-3	2 idem	3 idem
SiO_2 (wt%)	37.48	36,44	38.33
TiO_2	0.05	0.09	0.09
Al_2O_3	8.83	8.38	7.93
FeO^t	43.64	44.54	42.34
MnO	0.87	0.97	0.88
MgO	0.70	0.69	0.74
CaO	0.16	0.19	0.14
Na_2O	0.00	0.07	0.05
K_2O	1.61	1.98	1.79
Total	93.34	93.35	92.29
ions on the basis of 22 oxygens			
Si	6.337	6.240	6.516
Al	1.760	1.692	1.589
Ti	0.006	0.120	0.120
Fe	6.171	6.379	6.020
Mn	0.125	0.141	0.127
Mg	0.176	0.176	0.188
Ca	0.029	0.035	0.026
Na	0.000	0.023	0.016
K	0.347	0.433	0.388
Fe^t/Mg	35.67	36.24	32.02
Fe^t/Fe^t+Mg	0.972	0.973	0.970

FeO calculated as total iron (FeO^t)
1- margin 2- centre 3- opposite margin

APPENDIX B

SUMMARY OF ANALYTICAL TECHNIQUES

1. Mineral analyses

Mineral chemical analyses were carried out in a Material Analysis Company, model 400 (MAC 400) microprobe, equipped with three difratometers and fitted with a KRISEL automation system. The minerals were analyzed using 15 kV excitation voltage and 0.25 to 0.5 μA beam current. The standards used were natural minerals and synthetic glasses carefully selected to minimize corrections. The MAGIC corrections program was used for all mineral analyses.

Fe_2O_3 in amphibole analyses (presented in the tables) is the "mid-point" Fe_2O_3 calculated through Papike et al., (1974) computer program.

2.Rock analyses

Sample preparation

Rock slices 0.5 to 1 cm thick were diamond saw-cut, sandpapered to eliminate brass and pen mark contamination, washed and dried thoroughly. They were next put into plastic bags, between papers, on a steel board, where they were hammered. The samples were then pulverized, to less than 200 mesh with a tungsten-carbide coated Bleuler mill.

Analytical techniques

Major elements were determined by X-ray fluorescence spectrometry (XRF) at Geolab laboratory, Minas Gerais, Brazil (granitoid rocks) and at X-ray Assay Laboratories, Don Mills, Ontario (remaining rock types).

The trace elements Co, Ni, Cu, Zn, Mo, Pb, Cr, Rb, Sr, Y, Zr, Nb, Ba, Ga, La, V, U, Th were determined by X-ray fluorescence spectrometry (XRF) in a Phillips PW-1450 spectrometer (fitted with W tube) on pressed pellets, with reference to selected international standards. Data were reduced using interference and matrix calculations through program TRACE developed by G. Barker, H. Hunter and T. LaTour (Unpublished, U.W.O.).

International standards and duplicate samples were run for checks on accuracy. Compared to international standards the accuracy of trace elements is in general within 10%, except for Nb and Cu (25%).

In granitoid rocks, Zn and Pb were determined by instrumental atomic absorption; Th, Ba, Rb and Sr by X-ray fluorescence spectrometry in pressed pellets; and Cu, Ni, Ga, B, Cr, Y, Zr and V by emission spectrometry (EOS) at Geolab laboratory, Minas Gerais, Brazil.

Gold was analyzed by instrumental atomic absorption after preconcentration by fire assay, and silver was

determined by instrumental atomic absorption at Docegeo laboratory, Bahia, Brazil.

REE in granitoid rocks were analyzed by plasma emission spectrometry (ICP) at Geolab laboratory, Brazil. In the remaining rock types La, Ce, Nd, Sm, Eu, Tb, Dy, Yb and Lu were determined by instrumental neutron activation analysis and Pr, Gd, Ho, Er and Tm by plasma emission spectroscopy at X-ray Assay laboratories, Don Mills, Ontario.

3.Semi-quantitative mass balance calculations

The coefficients of the molar reactions presented in chapter 7, correspond to the number of moles of each mineral involved in the reaction.

This number of moles was obtained by dividing the modal percentage of each mineral by its respective molar volume (Table 7.1).

The modal percentage determination was carried out by means of a point counter, on rounded thin-polished sections with 2.5 cm in diameter. The counting interval ranged from 0.3 to 1.0 mm, depending on rock grain-size. The number of counted points in each section varied from 100 to 650. The modal percentage thus obtained is equal to area percentage, which was also admitted as equal to volume percent.

The volume percent of each one of the two reacting mineral assemblages (A and B), was then recalculated to 100%.

When reactions from the first to the second metamorphic event were studied in chlorite/greenalite bearing rocks, the percentage of these minerals was added to the mineral which originated them, in a later event.

When possible, the modal percentage of quartz was estimated in mineral assemblages A and B. Though, this number was not taken into account in the reactions. Quartz-bearing rocks were considered silica saturated, and the amount of SiO_2 presented in the reactions reflects only the total necessary for reaction balancing.

REFERENCES

ALMEIDA, F. F., HASUI, I., BRITO NEVES, B. B., and FUCK, R. A. 1981. Brasilian Structural Provinces. Earth Science Reviews 17: 1-29.

----------, and HASUI, I. 1984 O Embasamento da Plataforma Sul-Americana. In O Pre-Cambriano do Brasil. Edited by F. F. Almeida and Y. Hasui. Edgard Blucher Ltda. São Paulo, pp. 1-5.

AMARAL, G. 1984. Provincias Tapajós e Rio Branco. In O Pre-Cambriano do Brasil. Edited by F. F. Almeida and I. Hasui. Edgard Blucher Ltda. São Paulo, pp. 6-35.

ANDERSON, J. L. 1983. Proterozoic anorogenic granite plutonism of North America. In Proterozoic Geology. Edited by L. G. Medaris, C. W. Byers, D. M. Mickelson, W. C. Shanks. Geological Society of America, Memoir. Vol. 161, pp. 133-154.

----------, and CULLERS, R. L. 1978. Geochemistry and evolution of the Wolf River batholith, a Late Precambrian rapakivi massif in north Winsconsin, U.S.A. Precambrian Research, 7: 287-324.

----------, and ----------. 1986. Crust-enriched, mantle-derived tonalites in the early Proterozoic Penokean orogen of Winsconsin. Journal of Geology, 95: 139-154.

ANNERSTEN, H. 1968. A mineral chemical study of a metamorphosed iron formation in northern Sweden. Lithos, 1: 374-397.

ARMSTRONG, N. V., WILSON, A. H., and HUNTER, D. R. 1986. The Nsuze Group, Pongola sequence, South Africa: Geochemical evidence for Archean volcanism in a continental setting. Precambrian Research, 34: 175-203.

ARTH, J. G. 1979. Some trace elements in trondhjemites - their implications to magma genesis and paleotectonic setting. In Trondhjemites Dacites and related rocks. Edited by F. Barker. Developments in Petrology 6. Elsevier Science Publishing Co. Inc., New York, pp. 123-132.

AYRES, D. E. 1972. Genesis of Iron-Bearing Minerals in Banded Iron Formation Mesobands in The Dales Gorge Member, Hamersley Group, Western Australia. Economic Geology 67: 1214-1233.

BARNES, H. L. 1979. Geochemistry of hydrothermal ore deposits. John Wiley & Sons, New York.

BARKER, F. 1979. Trondhjemite: Definition, environment and hypotheses of origin. In Trondhjemites, Dacites and Related Rocks. Edited by F. Barker. Developments in Petrology 6. Elsevier Science Publishing Co. Inc., New York, pp. 1-12.

---------, and MILLARD Jr., H. T. 1979. Geochemistry of the Type Trondhjemite and Three Associated Rocks. In Trondhjemites, Dacites and Related Rocks. Edited by F. Barker. Developments in Petrology 6. Elsevier Science Publishing Co. Inc., New York, pp. 517-530.

----------, ----------, and, Lipman P. W. 1979. Four low K siliceous rocks of the western U.S.A. In Trondhjemites Dacites and related Rocks. Edited by F. Barker. Developments in Petrology 6. Elsevier Science Publishing Co. Inc., New York, pp. 415-433.

BAVINGTON, O. A., and Taylor, S. R. 1980. Rare Earth element geochemistry of Archean metasedimentary rocks from Kambalda, Western Australia. Geochimica et Cosmochimica Acta, 44: 639-648.

BAYLISS, P. 1975. Nomenclature of the trioctahedral chlorites. Canadian Mineralogist, 13: 178-180.

BEISIEGEL, V. R., BERNARDELLI, A. L., DRUMMONT, N. F., RUFF, A. W., and TREMAINE, J. W. 1973. Geologia e Recursos Minerais da Serra dos Carajás. Revista Brasileira de Geociencias, 3: 215-242.

BEISIEGEL, V. R., and FARIAS, N. F. 1978. Ocorrencia de cobre na Serra dos Carajás. In Proceedings of the XXXth, Congresso Brasileiro de Geologia, Recife, 1978. Sociedade Brasileira de Geologia, Vol. 4, pp. 1419-1430.

BERGMAN, I. A. 1986. Origin of banded quartz in Precambrian iron formations. Doklady Akademii Nauk SSSR, 289: 173-176.

BERNARDELLI, A. L., and BEISIEGEL, V.R. 1978. Geologia Econômica da jazida de manganês do Azul. In Proceedings of the XXXth Congresso Brasileiro de Geologia, Recife, 1978. Sociedade Brasileira de Geologia, Vol.4, pp. 1431-1444.

BONNICHSEN, B. 1975. Geology of the Biwabik Iron Formation, Dunka River Area, Minnesota. Economic Geology 70: 319-340.

BOSTROM, K. 1970. Submarine volcanism as source for iron. Earth and Planetary Science Letters, 9: 348-354.

BREITKOPF, J. H. 1988. Iron formations related to mafic volcanism and ensialic rifting in the southern margin zone of the Damara Orogen, Namibia. Precambrian Research, 38: 111-130.

BROWN, G. C., and FYFE, W. S. 1970. The production of granitic melts during ultrametamorphism. Contributions to Mineralogy and Petrology 28: 310-318.

BUTLER, Jr. B. 1969. Mineral Compositions and Equilibria in the Metamorphosed Iron Formation of the Gagnon Region, Quebec, Canada. Journal of Petrology ,Part I, 10: 56-101.

BUTTON, A. 1976. Transvaal and Hamersley basins - Review of basin development and mineral deposits. Minerals Science and Engineering, 8: 262-293.

CHAPPELL, B. W., and WHITE, A. J. R. 1974. Two contrasting granite types. Pacific Geology, 8: 173-174.

CHAPPELL, B.W., and WHITE, A.J.R. 1982. I and S type granites in the Lachlan fold belt, Southeastern Australia. Proceedings of the International Symposium on Geology of granites and their metallogenetic significance. Nanjing, China, pp. 87-101.

COISH, R. A. 1977. Ocean floor metamorphism in the Betts cove ophiolite, Newfoundland. Contributions to Mineralogy and Petrology, 60: 255-270.

COLLERSON, K. D., and BRIDGWATER, D. 1979. Metamorphic Development of early Archean tonalitic and trondhjemitic gneisses: Saglek Area, Labrador. In Trondhjemites Dacites and Related Rocks. Edited by F. Barker, Developments in Petrology 6. Elsevier Science Publishing Co. Inc., New York, pp. 205-274.

COLLINS, W. J., BEAMS, S. D., WHITE, A. J. R., CHAPPELL, B. W. 1982. Nature and Origin of A-Type Granites with Particular Reference to Southeastern Australia. Contributions to Mineralogy and Petrology, 80: 189-200.

CONDIE, K. C. 1981. Archean Greenstone Belts, Developments in Precambrian Geology 3. Elsevier Science Publishing Co. Inc., New York.

----------. 1984. Secular variation in the Composition of Basalts: an Index to mantle evolution. Journal of Petrology, Part 3, 26: 545-563.

----------. 1989. Geochemical changes in basalts and

andesites across the Archean-Proterozoic boundary: identification and significance. Lithos, 23: 1-18.

----------. and Hunter, D. R. 1976. Trace element geochemistry of Archean granitic rocks from the Barberton region. South Africa. Earth and Planetary Science Letters, 29: 383-400.

----------. 1978. Geochemistry of Proterozoic granitic plutons from New Mexico, U.S.A. Chemical Geology, 21: 131-149.

CORDANI, U. 1981. Comentarios sobre as determinações geocronológicas da Região da Serra dos Carajás. Universidade de São Paulo-Docegeo, unpublished report.

----------, TASSINARI, C., and KAWASHITA, K. 1984. A Serra dos Carajás como regiao limítrofe entre provincias tectônicas. Ciencias da Terra, 9: 6-11.

CORDEIRO, A. A. C., and SAUERESSIG, R. 1980. Serra das Andorinhas: geologia e principais ocorrencias de ouro. Docegeo, unpublished report.

COX, K. G. 1980. A model for flood basalt vulcanism. Journal of Petrology, 21: Part 4, 629-650.

CULLERS, R. L., and GRAF, J. L. 1984. Rare Earth Elements in Igneous Rocks of the Continental Crust: Intermediate and Silicic Rocks-Ore Petrogenesis. In Rare Earth Elements Geochemisty. Edited by P. Henderson. Developments in Geochemistry 2. Elsevier Science Publishing Co., Inc. New York, pp. 275-316.

CURTIS, C. D., and SPEARS, D. A. 1968. The Formation of sedimentary Iron Minerals. Economic Geology 63: 257-270.

CVRD/GICOR/DOCEGEO. 1988. Projeto Cobre Carajás, Jazida de Salobo. Geologia e avaliação de reservas. Companhia Vale do Rio Doce, unpublished report.

DALL'AGNOLL, R. 1980. Etudes sur des granites du type "Rondonian" en Amazonie Orientale et leurs transformations Tardi-magmatiques. Université Paul Sabatier, Toulouse. Unpublished PhD Thesis.

DARDENNE, M. A., FERREIRA FILHO, C. F., and MEIRELLES, M. A. 1987. The role of shoshonitic and calc-alkaline suites in tectonic evolution of the Carajás District, Brazil. In Precambrian evolution of the Amazonian Region. [extended abstract] IUGS, Project 204. pp. 40-50.

DAVY, R. 1983. A contribution on the chemical composition

of Precambrian iron-formations. In Iron Formations: Facts and Problems. Edited by A.F Trendall and R.C. Morris. Developments in Precambrian Geology 8. Elsevier Science Publishing Co., Inc., New York, pp. 325-343.

DAY, H. W. 1973. The high temperature stability of muscovite plus quartz. American Mineralogist, 58: 255-262.

DOCEGEO, 1988. Revisão litoestratigráfica da Provincia Mineral de Carajás. In Proceedings of the XXXV Congresso Brasileiro de Geologia, Belem, 1988, Sociedade Brasileira de Geologia. pp. 11-56.

DRAKE, M. J. and WEILL, D. F. 1975. Partition of Sr, Ba, Ca, Y, Eu^{2+}, Eu^{3+} and other REE between plagioclase feldspar and magmatic liquid: An experimental study. Geochimica et Cosmochimica Acta, 39: 689-712.

DREVER, J. I. 1974. Geochemical Model for the Origin of Precambrian Banded Iron Formation. Geological Society of America Bulletin, 85: 1099-1106.

DYMEK, R. F., and KLEIN, C. 1988. Chemistry, Petrology and origin of banded iron formation lithologies from the 3800 Ma Isua supracrustal belt, west Greenland. Precambrian Research, 39: 247-302.

EASTWOOD, G. E. P. 1965. Replacement Magnetite on Vancouver Island, British Columbia. Economic Geology, 60: 124-148.

ENGEL, A. E. J., and ENGEL, C. S. 1960. Progressive metamorphism and granitization of the major paragneiss, Northwest Adirondacks Mountains, New York. Part II: Mineralogy. Geological Society of America Bulletin, 71: 1-58.

ERMANOVICS, I. F., McRITCHIE, W. D., HOUSTON, W. N. 1979. Petrochemistry and tectonic setting of plutonic rocks of the Superior Province in Manitoba. In Trondhjemites Dacites and Related Rocks. Edited by F. Barker. Developments in Petrology 6. Elsevier Science Publishing Co., Inc., New York, pp. 323-362.

EVANS, B. W. 1965. Application of the reaction-rate method to the breakdown equilibria of muscovite plus quartz. American Journal of Science, 263: 647-667.

EWERS, W. E., and MORRIS, R. C. 1981. Studies of the Dales Gorge Member of the Brockman Iron Formation, Western Australia. Economic Geology, 76: 1929-1953.

FARIAS, N. F. 1981. Projeto Cobre Carajás- Jazidas Salobo 3A e 4A - Relatório de pesquisa. Rio Doce Geologia e Mineração S/A. Docegeo, unpublished report.

----------, and SAUERESSIG, R. 1982. Pesquisa geológica da jazida de cobre Salobo 3A. In Proceedings of the Ist Simposio de Geologia da Amazônia, Belem, 1982. Sociedade Brasileira de Geologia. Vol. 2, pp. 39-45.

----------, ----------. 1982 (a). Jazida de cobre Salobo 3A. In Proceedings of the Ith Simposio de Geologia da Amazonia. Belem, 1982. Sociedade Brasileira de Geologia, (Special volume). pp. 61-77.

FARIAS, N. F., and SAUERESSIG, R. 1982 (b). Salobo 3A copper deposit. In International Symposium of Archean and Early Proterozoic, Geological Evolution and Metallogenesis. Salvador, Brazil. Abstracts and Excursions, pp. 67-71.

FERREIRA FILHO, C. F. 1985. Geologia e mineralizações sulfetadas do prospecto Bahia, Provincia Mineral de Carajás. Universidade de Brasilia, unpublished MSc. Thesis.

----------, and DANNI, J. C. M. 1985. Petrologia e mineralizações sulfetadas do Prospecto Bahia-Carajás. In Proceedings of the IInd Simposio de Geologia da Amazônia. Belem, 1985. Sociedade Brasileira de Geologia, Vol. 3, pp. 34-47.

FERRY, J. M. and BURT, D.M. 1982. Characterization of metamorphic fluid composition through mineral equilibria. Reviews in Mineralogy, 10: 207-262.

FERRY, J. M., and SPEAR, F. S. 1978. Experimental calibration of the partitioning of Fe and Mg between biotite and garnet. Contributions to Mineralogy and Petrology, 66: 113-117.

FIGUEIRAS, A. J. M., and VILLAS, R. N. N. 1984. Estudo petrológico e sedimentológico da sequencia clástica (Pos-Grupo Grão Pará) da Serra dos Carajás, Estado do Pará. In Proceedings of the XXXIIIth Congresso Brasileiro de Geologia. Rio de Janeiro, 1982. Sociedade Brasileira de Geologia, Vol. 2, pp. 832-846.

FIGUEIREDO, B. 1982. Caracterização do Minério da Jazida do Cobre do Salobo -3A- Carajas. Universidade de Campinas-Docegeo, unpublished report.

FLEET, A., J. 1984. Aqueous and sedimentary geochemistry of the rare earth elements. In Rare Earth Element Geochemistry. Edited by P. Henderson. Developments in Geochemistry 2, Elsevier Science Publishing Co. Inc., New York, pp. 343-373.

FLOOD, R.H., and SHAW, S.E. 1975. A cordierite bearing

granite suite from the New England Batholith, N. S. W. Australia. Contributions to Mineralogy and Petrology, 52: 157-164.

FLOYD, P. A., and WINCHESTER, J. A. 1975. Magma type and tectonic setting discrimination using immobile elements. Earth and Planetary Science Letters, 27: 211-218.

----------, and ----------. 1978. Identification and discrimination of altered and metamorphosed volcanic rocks using immobile elements. Chemical Geology, 21: 291-306.

FLORAN, R. J., and PAPIKE, J. J. 1975. Petrology of the Low-Grade Rocks of the Gunflint Iron-Formation, Ontario-Minnesota. Geological Society of America Bulletin, 86: 1669-1190.

----------, and ----------. 1978. Mineralogy and Petrology of the Gunflint Iron-Formation, Minnesota-Ontario: Correlation of Compositional and Assemblage Variations at Low to Moderate Grade. Journal of Petrology, Part 2, 19: 215-288.

FONAREV, V.I., GRAFCHIKOV, D. I., BOGACH, D. I., and VAN, K. V. 1986. Physicochemical conditions of metamorphism for iron formations in the Belaya Tserkov-Odessa Zone.International Geology Review, 28: 905-919.

FORBES, W. C. 1977. Stability relations of grunerite, $Fe_7Si_8O_{22}(OH)_2$. American Journal of Science, 277: 735-749.

FOSTER, M. D. 1960. Interpretation of the composition of trioctahedral micas. U.S. Geological Survey Professional Paper, 354-B, 11-46.

FROST, B. R. 1982. Contact metamophic effects of the Stillwater Complex, Montana: the concordant iron-formation: a discussion of the role of buffering in metamorphism of iron-formation. American Mineralogist, 67: 142-148.

FRYER, J. B. 1977. Rare earth evidence in iron-formations for changing Precambrian oxidation states. Geochimica et Cosmochimica Acta, 41: 361-367.

FYFE, W. S. 1983. Advances in understanding subduction and Continental structure above subduction zone. In Conference on Geology and Mineral Resources of Thailand. Departament of mineral Resources. Bangkok, pp. 1 - 7.

---------- 1987. Granites and thermal structures in the lithosphere. Geologische Rundschau, 76: 15 - 22.

---------- and LONSDALE, P. 1981. Ocean floor hydrothermal activity. In The Oceanic Lithosphere, The Sea, Vol.7. Edited by C. Emiliani. John Wiley & Sons, Inc. New York, pp. 589 - 638.

---------- ; PRICE, N. J. and THOMPSON, A. B. 1978. Fluids in the Earth's Crust. Developments in Geochemistry 1. Elsevier Science Publishing Co.Inc., Amsterdam.

GAAL, G. 1983. Structural Geology of the Salobo Copper Deposit in Carajas; Para State. Docegeo, unpublished report.

GHENT, E. D. 1976. Plagioclase-garnet-Al_2SiO_5-quartz: a potential geobarometer-geothermometer. American Mineralogist, 61: 710-714.

GIBBS, A. K., WIRTH, K. R., HIRATA, W. K., and OLSZEWSKI Jr., W. J. 1986. Age and composition of Grao Para Group volcanics, Serra dos Carajas. Revista Brasileira de Geociencias 16: 201-211.

GOLE, M. J. 1980. Mineralogy and petrology of very low metamorphic grade Archaean banded iron formations, Weld Range, Western Australia. American Mineralogist, 65: 8-25.

----------. 1981. Archean Banded Iron-Formations, Yilgarn Block, Western Australia. Economic Geology, 76: 1954-1974.

----------, and Klein, C. 1981. High-grade metamorphic Archean banded iron-formations, Western Australia: assemblages with coexisting pyroxenes±fayalite. American Mineralogist, 66: 87-99.

----------, and --------. 1981. Banded iron formations through much of precambrian time. Journal of Geology 89: 169-183.

GONÇALEZ, M. G. B., DALL'AGNOL, R., VIEIRA, E. A. P., MACAMBIRA, M. J. B., DELLA SENTA, N. 1988. Geologia do maciço anorogênico Cigano. Vale do Rio Farauapebas, Pará. In Proceedings of the XXXVth Congresso Brasileiro de Geologia, Belem, 1988. Sociedade Brasileira de Geologia. Vol. 3, pp. 1132-1146.

GOODWIN, A. M., MONSTER, J., and THODE, H. G. 1976. Carbon and Sulfur Isotope Abundances in Archean Iron-Formations and Early Precambrian Life. Economic Geology 71: 870-891.

GOVETT, G. J. S. 1966. Origin of banded iron formations. Geological Society of America Bulletin, 77: 1191-1212.

GRAF, J. L. 1977. Rare earth elements as a hydrothermal tracers during the formation of massive sulfide deposits in volcanic rocks. Economic Geology, 72: 527-548.

----------. 1978. Rare earth elements, iron formations and sea water. Geochimica et Cosmochimica Acta, 42: 1845-1850.

GRAHAM, C. M., and POWELL, R. 1984. A garnet-hornblende geothermometer: calibration, testing, and application to the Pelona Schist, Southern California. Journal of Metamorphic Geology, 2: 13-31.

GROSS, G. A., and McLEOD, C. R. 1980. A preliminary assessment of the chemical composition of iron formations in Canada. Canadian Mineralogist, 18: 223-229.

GRUBB, P. L. C. 1971. Silicates and Their Paragenesis in Brockman Iron Formation of Wittenoom Gorge, Western Australia. Economic Geology, 66: 281-292.

GUIDOTTI, C. V., 1984. Micas in Metamorphic Rocks. In Micas. Edited by S. W. Bailey. Reviews in Mineralogy 13, Mineralogical Society of America, pp. 357-467.

----------,CHENEY, J. T., and HENRY, D. J. 1988. Compositional variation of biotite as a function of metamorphic reactions and mineral assemblage in the pelitic schists of western Maine. American Journal of Science, 288 A: 270-292.

GUIMARÃES, I. G. 1987. Petrologia da Formação Ferrífera na area Salobo 3A-Provincia Mineral de Carajás, Pará. Universidade de São Paulo, unpublished MSc. Thesis.

HAASE, C. S. 1982. Phase equilibria in metamorphosed iron-formations: Qualitative T-X(CO2) petrogenetic grids. American Journal of Science, 282: 1623-1654.

----------.1982. Metamorphic petrology of the Negaunee iron formation, Marquette district, Northern Michigan: Mineralogy, Metamorphic reactions and phase equilibria. Economic Geology, 77: 60-81.

HALL, R. P. 1985. Mg-Fe-Mn distribution in amphiboles, pyroxenes, and garnets and implications for conditions of metamorphism of high-grade early Archaean iron-formation, southern West Greenland. Mineralogical Magazine, 49: 117-128.

HANSON, G. N. 1978. The application of trace elements to the petrogenesis of igneous rocks of granitic composition.

Earth and Planetary Science Letters, 38: 26-43.

HASSLER, S. W., and SIMONSON, B. M. 1989. Deposition and alteration of volcaniclastic strata in two large, early Proterozoic iron-formations in Canada. Canadian Journal of Earth Sciences, 26: 1574-1585.

HASUI, Y. 1981. Observações Geológico-estruturais na jazida do Salobo-3A, Provincia do Carajás, Docegeo, unpublished report.

HEIER, K. S., and BILLINGS, G. K. 1972. Rubidium. In Handbook of Geochemistry. Edited by K., H. Wedepohl. Vol. II-4. Springer Verlag, Berlin, pp. 37-B-1 - 37-N-1.

HENRY, D. J., and GUIDOTTI, C. V. 1985. Tourmaline as a petrogenetic indicator mineral: an example from the staurolite-grade metapelites of NW Maine. American Mineralogist, 70: 1-15.

HERZBERG, C. T., FYFE, W. S., and CARR, M.J. 1983. Density Constraints on the Formation of the Continental Moho and Crust. Contributions to Mineralogy and Petrology, 84: 1-5.

HEWITT, D. A., and WONES, D.R. 1975. Physical properties of some synthetic Fe-Mg-Al trioctahedral biotites. American Mineralogist, 60: 854-862.

HIRATA, W. K. 1982. Geologia Regional da Provincia Mineral de Carajás. In Proceedings of the Ist Simposio de Geologia da Amazônia, Belem, 1982. Sociedade Brasileira de Geologia, pp. 13-16.

HIRATA, W. K., Rigon, J. C., Kadekaru, K., Cordeiro, A. A. C., and Meirelles, E. M. 1982. Geologia Regional da Província Mineral de Carajás. In Proceedings of the Ist Simposio de Geologia da Amazônia, Belem, 1982. Sociedade Brasileira de Geologia, pp. 100-110.

HIRATA, W. K., BEISIEGEL, V. R., BERNARDELLI, A. L., FARIAS, N. F., SAUERESSIG, R., MEIRELES, E. M., and TEIXEIRA, J. F. 1982 (a). Serra dos Carajás - Pará State: iron, manganese, copper, and gold deposits. Ist International Symposium of Archean and Early Proterozoic Geologic Evolution and Metallogeny. Salvador, Bahia, Brazil. Abstracts and Excursions pp. 40-76.

HOLDAWAY, M. J. 1972. Thermal stability of Al-Fe epidote as a function of f_{O_2} and Fe content. Contributions to Mineralogy and Petrology, 37: 307-340.

HOISCH, T. D. 1989. A muscovite-biotite geothermometer. American Mineralogist, 74: 565-572.

HOLM, P. E. 1985. The geochemical fingerprints of different tectonomagmatic environments using hygromagmatophile element abundances of tholeiitic basalts and basaltic andesites. Chemical Geology, 51: 303-323.

HUGHES, C. J. 1982. Igneous Petrology. Developments in Petrology 7. Elsevier Science Publishing Co. Inc., Amsterdam.

HUMPHRIS, S. E., and THOMPSON, G. 1978. Trace element mobility during hydrothermal alteration of oceanic basalts. Geochimica et Cosmochimica Acta, 42: 127-136.

HUTCHINSON, R. W. 1979. Report on Docegeo Copper Projects MM1, Salobo and regional Geological Relationships, Pará, Brazil, Docegeo unpublished report.

IMMEGA, I. P., and KLEIN, C. 1976. Mineralogy and petrology of some metamorphic Precambrian Iron-formations in southwestern Montana. American Mineralogist, 61: 1117-1144.

IANHEZ, A. C., SOUZA, A. M. S., and MONTALVÃO, R. M. G. 1980. Geologia da sequência vulcano-sedimentar da Serra do Inajá - Santana do Araguaia. In Proceedings of the XXXIth Congresso Brasileiro de Geologia, Camboriu, 1980. Sociedade Brasileira de Geologia, Vol. 5, pp. 2918-2928.

IRVINE, T. N., and BARRAGAR, W. R. A. 1971. A Guide to the Chemical Classification of the Common Volcanic Rocks. Canadian Journal of Earth Sciences, 8: 523-548.

ISHIHARA, S. 1981. The granitoid series and Mineralization. Economic Geology, 75th Anniversary Volume, pp. 458-484.

JAHN, B. M., SHIH, C. Y., RAMA MURTHY, V. 1974. Trace element geochemistry of Archean volcanic rocks. Geochimica et Cosmochimica Acta, 38: 611-627.

JAMES, H. L. 1954. Sedimentary facies of iron-formations. Economic Geology, 49: 235-293.

----------. 1955. Zones of Regional Metamorphism in the Precambrian of Northern Michigan. Geological Society of America Bulletin, 66: 1455-1488.

----------. 1966. Chemistry of the iron-rich sedimentary rocks. U.S. Geological Survey Professional Paper 440-W61.

JENNER, G. A., FRYER, B. J., and McLENNAN, S. M. 1981. Geochemistry of the Archean Yellowknife Supergroup. Geochimica et Cosmochimica Acta, 45: 1111-1129.

JENSEN, L. S. 1976. A new cation plot for classifying subalkalic volcanic rocks. Ontario Division of Mines, Miscellaneous Paper, 66.

KALLIOKOSKI, J. 1965. The metamorphosed iron ore of el Pao, Venezuela. Economic Geology 60: 100-116.

KERRICK, D. M. 1972. Experimental determination of muscovite + quartz stability with $P_{H_2O} < P_{total}$. American Journal of Science 272: 946-958.

KIMBERLEY, M. M. 1979. Geochemical distinctions among environmental types of iron formations. Chemical Geology, 25: 185-212.

KLEIN, C. 1966. Mineralogy and Petrology of the Metamorphosed Wabush Iron Formation, Southwestern Labrador. Journal of Petrology, Part 2, 7: 246-305.

--------. 1968. Coexisting Amphiboles. Journal of Petrology, Part 2, 9: 281-330.

--------. 1976. Petrology of the Sokoman Iron Formation in the Howells River Area, at the Western Edge of the Labrador Trough. Economic Geology 71: 453-487.

--------. 1983. Diagenesis and metamorphism of Precambrian Banded Iron Formation. In Iron Formation: Facts and Problems. Edited by A. F. Trendall and R. C. Morris. Developments in Precambrian Geology 6. Elsevier Science Publishing Co. Inc., Amsterdam, pp. 417-470.

KRANCK, S. H. 1961. A Study of Phase Equilibria in a Metamorphic Iron Formation. Journal of Petrology, Part 2, 2: 137-184.

KUNO, H. 1968. Differentiation of basalt magmas. In Basalts: The Poldervaart Treatise on rocks of basaltic composition. Edited by H. H. Hess and A. Poldervaart. John Wiley & Sons, New York. pp. 623-688.

LaBERGE, G. L. 1966 (a), Altered pyroclastic rocks in South African iron-formation. Economic Geology, 61: 572-581.

----------. 1966 (b), Altered pyroclastic rocks in Iron-formation in the Hamersley Range, Western Australia. Economic Geology, 61: 147-161.

LAIRD, J. 1988. Chlorites: Metamorphic Petrology. In Hydrous Phyllosilicates (exclusive of micas). Edited by P. H. Ribbe. Reviews in Mineralogy Vol.19, Mineralogical Society of America, pp. 405-454.

---------, and Albee, A. L., 1981, Pressure, temperature,

and time indicators in mafic schist: Their application to reconstructing the polymetamorphic history of Vermont. American Journal of Science, 281: 127-175.

LASKOWSKY, N., and KRONER, A. 1985. Geochemical characteristics of Archaean and Late Proterozoic to Palaeozoic fine-grained sediments from Southern Africa and significance for the evolution of the continental crust. Geologische Rundschau, 74: 1-9.

LEAKE, B. E. 1965. The relationship between tetrahedral aluminum and the maximum possible octahedral aluminum in natural calciferous and sub-calciferous amphiboles. American Mineralogist, 50: 843-851.

----------1968. Nomenclature of Amphiboles. Canadian Mineralogist, 16: 501-520.

LIOU, J. G., KUNIYOSHI, S., and ITO, K. 1974. Experimental studies of the phase relations between greenschist and amphibolite in a basaltic system. American Journal of Science, 274: 613-632.

LINDENMAYER, Z. G. 1981. Geologia do depósito do Salobo 3 Alfa. Docegeo, unpublished report.

----------, FYFE, W. S., and MACHADO, N. 1988. Deposito do Salobo: Efeitos do metamorfismo e metassomatismo sobre a mineralização. In the Proceedings of the XXXVth Congresso Brasileiro de Geologia. Belem, 1988. Sociedade Brasileira de Geologia, Vol. 3, pp. 1243-1250.

LIREN, W. 1985. Mesozoic granitoids in east China. In The Crust - The significance of granites gneisses in the lithosphere. Theophrastus Publications S.A., Athens, pp. 201-216.

LOISELLE, M. C., and WONES, D. R. 1979. Characteristics and origin of anorogenic granites. Geological Society of America. Program with abstracts 11: 468.

MACHADO, N., LINDENMAYER, D. H., and LINDENMAYER, Z. G. 1988. Geocronologia U-Pb da província metalogenetica de Carajás, Pará: Resultados Preliminares. In the Proceedings of the VIIth Congresso Latino-Americano de Geologia. Belem, 1988. Sociedade Brasileira de Geologia. pp. 339-347.

MACHADO, N., LINDENMAYER, Z. G., KROGH, T. E., and LINDENMAYER, D. H. 1990. U-Pb Geochronology of Archean magmatism and basement reactivation in the Carajas area, Amazon Shield, Brazil. Precambrian Research (in press).

MARSH, J. S., BOWEN, M. P., ROGERS, N. W., and BOWEN, T. B. 1989. Volcanic rocks of the Witwatersrand Triad, South Africa. II: Petrogenesis of Mafic and Felsic Rocks of the Dominium Group. Precambrian Research, 44: 39-65.

MARTINS, L. P. B., SAUERESSIG, R., and VIEIRA, M. A. M. 1982. Aspectos petrograficos das principais litologias da Sequência Salobo. In Proceedings of the Ist Simposio de Geologia da Amazônia. Belem, 1982. Sociedade Brasileira de Geologia, Vol. 2, pp. 253-262.

McLENNAN, S. M., FRYER, B. J., and YOUNG, G. Y. 1979. Rare earth elements in Huronian (Lower Proterozoic) sedimentary rocks: composition and evolution of the post-Kenoran upper crust. Geochimica et Cosmochimica Acta, 43: 375-388.

McLENNAN, S. M., and TAYLOR, S. R. 1984. Archean Sedimentary Rocks and Their Relation to the Composition of the Archean Continental Crust. In Archean Geochemistry. Edited by A. Kroner, G. N. Hansen and A. M. Goodwin. Springer-Verlag, Berlim, pp. 47-72.

MEDEIROS FILHO, C.A., and MEIRELES, E. M. 1985. Dados preliminares sobre a ocorrência de cromita na area Luanga. In Proceedings of the IInd Simposio de Geologia da Amazônia, Belem, 1985. Sociedade Brasileira de Geologia, Vol. 3, pp. 90-96.

MEDEIROS NETO, F. A. de, and VILLAS, R. N. N., 1985, Geologia da jazida de Cu-Zn do corpo 4E-Pojuca, Serra dos Carajás. In Proceedings of the IInd Simposio de Geologia da Amazônia, Belem, 1985. Sociedade Brasileira de Geologia, Vol. 3, pp. 97-112.

MEIRELES, E. M., and TEIXEIRA, J. T. 1982. Geologia do depósito de ouro de Serra Pelada. In Proceedings of the Ist Simposio de Geologia da Amazonia, Belem, 1982. Sociedade Brasileira de Geologia, pp. 75-85.

MESHEDE, M. 1986. A method of discriminating between different types of mid-ocean ridge basalts and continental tholeiites with the Nb-Zr-Y diagram. Chemical Geology, 56: 207-218.

MEYER, D. J. K., and FARIAS, N. F. 1980. O deposito de cobre Salobo 3Alfa-Serra dos Carajás. In XXXIth Congresso Brasileiro de Geologia. Camboriu, 1980. Sociedade Brasileira de Geologia. Bulletin 2, pp. 382.

MICHARD, A., ALBAREDE, F., MICHARD, G., MINSTER, J. F., and CHARLOU, J. L. 1983. Rare-earth elements and uranium in high-temperature solutions from East Pacific Rise

hydrothermal vent field (13 N). Nature, 303: 795-797.

MIYANO, T. 1982. Stilpnomelane, iron-rich mica, K-feldspar and hornblende in banded iron-formation assemblages of the Dales Gorge member, Hamersley Group, Western Australia. Canadian Mineralogist, 20: 189-202.

---------, and BEUKES, N. J. 1984. Phase relations of stilpnomelane, ferri-annite, and riebeckite in very low-grade metamorphosed iron-formations. Transactions of the Geological Society of South Africa, 87: 111-124.

---------, and KLEIN, C. 1983. Phase relations of orthopyroxene, olivine, and grunerite in high grade metamorphic iron-formation. American Mineralogist, 68: 699-716.

MIYASHIRO, A., SHIDO, F., and EWING, M. 1971. Metamorphism in the Mid-Atlantic Ridge near 24° and 30°N. Philosophical Transactions of the Royal Society of London. A 268: 589-603.

----------. 1972. Pressure and temperature conditions and tectonic significance of regional and Ocean-Floor metamorphism. Tectonophysics, 13: 141-159.

----------. 1973. Metamorphism and metamorphic bel . George Allen & Unwin Ltd., London.

----------. 1974. Volcanic rock series in island arcs and active continental margins. American Journal of Science, 274: 321-355.

----------. and SHIDO, F. 1984. Tschermak substitution in Low and middle-grade pelitic schists. Journal of Petrology, Part 2, 26: 449-487.

MOODY, J. B., MEYER, D., and JENKINS, J. E. 1983. Experimental characterization of the greenschist/ amphibolite boundary in mafic systems. American Journal of Science, 283: 48-92.

MOTTL, M. J., and HOLLAND, H. D. 1978. Chemical exchange during hydrothermal alteration of basalt by seawater-I. Experimental results for major and minor components of seawater. Geochimica et Cosmochimica Acta, 42: 1103-1115.

MUELLER, R. F. 1960. Compositional Characteristics and Equilibrium Relations in Mineral Assemblages of a Metamorphosed Iron Formation. American Journal of Science, 258: 449-497.

NANCE, W. B., and TAYLOR, S. R. 1977. Rare earth element

patterns and crustal evolution-II. Archean sedimentary rocks from Kalgoorlie, Australia. Geochimica et Cosmochimica Acta, 41: 225-231.

NICOLLET, C., LEYELOUP, A., DUPUY, C. 1979. Petrogenesis of high pressure trondhjemitic layers in eclogites and amphibolites from southern Massif Central, France. In Trondhjemites Dacites and Related Rocks. Edited by F. Barker. Elsevier Science Publishing Co. Inc., New York. pp. 435-464.

O'CONNOR, J. T. 1965. A classification for quartz-rich igneous rocks based on feldspar ratios. U.S. Geological Survey Professional Paper 525-B, pp. B79-B84.

OLIVEIRA, A. I., and LEONARDOS, O. 1943. Geologia do Brasil. Servico de Informacao Agricola. Rio de Janeiro.

OLSZEWSKI, W. J., WIRTH, K. R., GIBBS, A. K., and GAUDETTE, H. E. 1989. The age, origin and tectonics of the Grao Para Group and associated rocks, Serra dos Carajas, Brazil: Archean Continental Volcanism and rifting. Precambrian Research, 42: 229-254.

PEARCE, J. A. 1975. Basalt geochemistry used to investigate past tectonic environments on Cyprus. Tectonophysics, 25: 41-67.

----------. 1980. Geochemical evidence for the genesis and eruptive setting of lavas from Tethyan ophiolites. In Proceedings of the International Ophiolite Symposium, Cyprus, 1980. Edited by A. Panayiotou. Cyprus Geological Survey Department. pp. 251-272.

----------, and Cann, J. R. 1971. Ophiolitic origin investigated by discriminant analysis using Ti, Zr and Y. Earth and Planetary Science Letters, 12: 339-349.

----------, and ----------. 1973, Tectonic Setting of basic volcanic rocks determined using trace element analyses. Earth and Planetary Science Letters, 19: 290-300.

----------, and GALE, G. H. 1977. Identification of ore deposition environments from trace element geochemistry of associated igneous host rocks. In Volcanic Processes in Ore Genesis. Geological Society of London, 7: 14-24.

----------, HARRIS, N. B. W., and TINDLE, A. G. 1984. Trace Element Discrimination Diagrams for the Tectonic Interpretation of Granitic Rocks. Journal of Petrology, Part 4, 25: 956-983.

----------, and NORRY, M. J. 1979. Petrogenetic implications of Ti, Zr, Y and Nb variations in volcanic rocks. Contributions to Mineralogy and Petrology, 69: 33-47.

PETERS, T., VALARELLI, J. V., COUTINHO, J. M. V., SOMMERAUER, J., and RAUMER, J. von. 1977. The manganese deposits of Buritirama, Para, Brazil. Schweizerische Mineralogische und Petrographische Mittellungen, 57: 313-327.

PETTIJOHN, F. J. 1975. Sedimentary rocks. Harper & Row, Publishers, New York.

PIDGEON, R. T. 1984. Geochronological constraints on early volcanic evolution of the Pilbara Block, Western Australia. American Journal of Earth Science, 31: 237-242.

PIPER, D., Z. 1974. Rare earth elements in the sedimentary cycle: a summary. Chemical Geology, 14: 285-304.

----------, and GRAEF, P., A. 1974. Gold and rare earth elements in sediments from the East Pacific Rise. Marine geology, 17: 287-297.

POPP, R. K., and FRANZ, J.D. 1979. Mineral solution equilibria - II. An experimental study of mineral solubilities and the thermodynamic properties of aqueous $CaCl_2$ in the system CaO-SiO_2-H_2O-HCl. Geochimica et Cosmochimica Acta, 43: 1777-1790.

POPP, R. K., GILBERT, M. C., and CRAIG, J. R. 1977. Stability of Fe-Mg amphiboles with respect to oxygen fugacity. American Mineralogist, 62: 1-12.

RAASE, P. 1974. Al and Ti Contents of Hornblende, Indicators of Pressure and Temperature of Regional Metamorphism. Contributions to Mineralogy and Petrology, 45: 231-236.

RAMOS, J. F. F., MOURA, C. A. V., MELO, C. F., PEREIRA, J. L., SERIQUE, J. S. C. B., and RODRIGUES, R.M. 1984. Uma discussão sobre sequências sedimentares tidas como Rio Fresco, Sudeste do Pará. In Proceedings of the XXXIIIth Congresso Brasileiro de Geologia. Rio de Janeiro, 1984. Sociedade Brasileira de Geologia. Vol. 2, pp. 862-872.

RICHARDS, J. R. 1984. The base of the Fortescue Group, Western Australia: further galena lead isotope evidence on its age. Australian Journal of Earth Science, 31: 257-268.

RICHARDS, S. M. 1966. The banded iron formations at Broken

Hill, Australia, and their relationship to the lead-zinc ore bodies. Economic Geology, 61: 72-96.

ROLLINSON, H. R., and WINDLEY, B. F. 1980. An Archean Granulite Grade Tonalite-Trondhjemite-Granite Suite from Scourie, NW Scotland: Geochemistry and Origin. Contributions to Mineralogy and Petrology, 72: 265-281.

SHARP, Z. D., O'NEIL, J. R., and ESSENE, E. J. 1988. Oxygen isotope variations in granulite-grade iron formations: constraints on oxygen diffusion and retrograde isotopic exchange. Contributions to Mineralogy and Petrology, 98: 490-501.

SHERATON, J. W., and BLACK, L. P. 1983. Geochemistry of Precambrian gneisses: relevance for the evolution of the East Antarctic Shield. Lithos, 16: 273-296.

----------, ELLIS, D. J., and KUEHNER, S. M. 1985. Rare-Earth element geochemistry of Archean orthogneisses and evolution of the East Antarctic shield. Journal of Australian Geology & Geophysics, 9: 207-218.

SILVA, G. G., LIMA, M. I. C., ANDRADE, A. R. F., ISSLER, R. S., and GUIMARÃES, G. 1974. Geologia das Folhas SB-22 Araguaia e parte da SC-22 Tocantins. Projeto Radam. Ministério das Minas e Energia, Departamento Nacional da Produção Mineral, Brasilia, Vol. 4, pp. 1-143.

SPEAR, F. S. 1981. An experimental study of hornblende stability and compositional variability in amphibolite. American Journal of Science, 281: 697-734.

STEWARD, D. B., and FLOHR, M. K. 1984. Systematic compositional variation in layer silicates from chlorite to cordierite grade, coastal volcanic belt, Maine. Geological Society of America. Program with abstracts, 16: 618.

STRECKEISEN, A. 1976. To each plutonic rock its proper name. Earth Sciences Review, 12: 1-33.

SUITA, M., T., F. and NILSON, A., A. 1988. Geologia do Complexo máfico-ultramáfico Luanga (Província Carajás - Pará) e das unidades encaixantes. In Proceedings of the XXXVth Congresso Brasileiro de Geologia. Belem, 1988. Sociedade Brasileira de Geologia. Vol. 6, pp. 2813-2823.

TASSINARI, C., HIRATA, W. K., and KAWASHITA, K. 1982. Geologic evolution of the Serra dos Carajás, Pará, Brazil. Revista Brasileira de Geociencias 12: 263-267.

TAYLOR, S. R., and McLENNAN, S. M. 1985. The continental

crust: Its composition and evolution. Blackwell Scientific Publications, Oxford.

----------, RUDNICK, R. L., McLENNAN, S. M., and ERIKSSON, K.A., 1986, Rare Earth Element patterns in Archean high-grade metasediments and their tectonic significance. Geochimica et Cosmochimica Acta, 50: 2267-2279.

TEIXEIRA, J. B. G., and SILVA, L. J. D'EL REY. 1987. Jazida Salobo 3-Alfa. Caracterização Geológica do Minério (Cu-Au-Ag-Mo-Fe) e sua Aplicação no Aproveitamento Econômico do Minério. Docegeo, unpublished report.

THOMAS, W. M. 1982. Stability relations of the amphibole hastingsite. American Journal of Science, 282: 136-164.

TOLBERT, G. E., TREMAINE, J. W., MELCHER, G. C., and GOMES, C.B. 1971. The Recently Discovered Serra dos Carajas Iron Deposits, Northern Brazil. Economic Geology, 66: 985-994.

TRACY, R. J. 1978. High grade metamorphic reactions and partial melting in pelitic schist, West-Central Massachusetts. American Journal of Science, 278: 150-178.

---------- 1982. Compositional zoning and inclusions in metamorphic minerals. In Characterization of Metamorphism through Mineral Equilibria. Edited by P. H. Ribbe. Reviews in Mineralogy Vol. 10. Mineralogical Society of America. pp. 335-397.

TRENDALL, A. F. 1968. Three Great Basins of Precambrian Banded Iron Formation Deposition: A Systematic Comparison. Geological Society of America Bulletin, 79: 1527-1544.

----------. 1983. The Hamersley basin. In Iron Formation: Facts and Problems. Edited by A. F. Trendall and R. C. Morris. Developments in Precambrian Geology 6. Elsevier Science Publishing Co. Inc., New York. pp. 69-129.

----------, and BLOCKLEY, J. G. 1970. The iron formations of the Precambrian Hamersley Group, Western Australia. Western Australia Geological Survey, Bulletin 119.

VANIMAN, D. T., PAPIKE, J. J., and LABOTKA, T. 1980. Contact-metamorphic effects of the Stillwater Complex, Montana: the concordant iron-formation. American Mineralogist, 65: 1087-1102.

VOGT, J. H. L. 1932. The Physical Chemistry and magmatic differentiation of igneous rocks, Journal of Geology, 29: 319-350.

VIEIRA, E. A. P., SAUERESSIG, R., SIQUEIRA, J. B., SILVA, E. R. P., REGO, J. L., and CASTRO, F. D. C. 1988. Caracterização geológica da jazida polimetalica do Salobo 3A-reavaliação. In Proceedings of the XXXVth Congresso Brasileiro de Geologia. Belem, 1988. Sociedade Brasileira de Geologia. pp. 97-114.

VIEIRA, M. A. M., GUIMARÃES, I. G., and AMARAL, M. A. M. 1984. Perfil de alteração de xistos da jazida de cobre do Salobo (Para). Proceedings of the IInd Symposium Amazônico. Manaus, 1984. Sociedade Brasileira de Geologia. pp. 313-326.

WALKER, G. P. L. 1989. Gravitational (density) controls on volcanism, magma chambers and intrusions. Australian Journal of Earth Sciences, 36: 149-165.

WANG, G. F., BANNO, S., and TAKEUCHI, K. 1986. Reactions to define the biotite isograd in the Ryoke metamorphic belt, Kii Peninsula, Japan. Contributions to Mineralogy and Petrology, 93: 9-17.

WEAVER, B. L., and TARNEY, J. 1981. Lewisian gneiss geochemistry and Archean crustal development models. Earth Planetary Science Letters, 55: 171-180.

WHALEN, J. B., CURRIE, K. I., CHAPPELL, B. W. 1987. A-Type granites: geochemical characteristics, discrimination and petrogenesis. Contributions to Mineralogy and Petrology 95: 407-419.

WIRTH, K. R. 1986. The Geology and Geochemistry of the Grao Para Group, Serra dos Carajas, Para, Brazil. Cornell University, Ithaca, New York. Unpublished M.Sc. Thesis.

WINCHESTER, J. A., and FLOYD, P. A. 1976. Geochemical Magma Type Discrimination: Application to Altered and Metamorphosed Basic Igneous Rocks. Earth and Planetary Science Letters, 28: 459-469.

----------, and ----------. 1977. Geochemical discrimination of different magma series and their differentiation products using immobile elements. Chemical Geology, 20: 325-343.

WHITE, D. A. 1954. The Stratigraphy and Structure of the Mesabi Range, Minnesota. Minnesota Geological Survey. The University of Minnesota Press.

WILDEMAN, T. R., and CONDIE, K. C. 1973. Rare earths in Archean graywackes from Wyoming and from the Fig Tree Group, South Africa. Geochimica et Cosmochimica Acta, 37: 439-453.

WINKLER, H. G. F. 1976. Petrogênese das rochas metamorficas. Edgard Blucher Ltda. São Paulo, Brasil.

WOLF, K. H. 1976. Conceptual Models in Geology. In Handbook of Strata-Bound and Stratiform Ore Deposits. Edited by K. H. Wolf. Elsevier Science Publishing Co. Inc., New York, pp. 11-78.

WOOD, D. A., GIBSON, I. L., and THOMPSON, R. N. 1976. Elemental Mobility during Zeolite Facies Metamorphism of Tertiary Basalts of Eastern Iceland. Contributions to Mineralogy and Petrology, 55: 241-254.

----------, JORON, J. L, and TREUIL, M. 1979. A reappraisal of the use of trace elements to classify and discriminate between magma series erupted in different tectonic settings. Earth and Planetary Science Letters, 45: 326-336.

WRIGHT, J. B. 1969. A simple alkalinity ratio and its application to questions of non-orogenic granite genesis. Geological Magazine, 106: 370-384.

WYBORN, L. A. I. 1988. Petrology, Geochemistry and origin of a major Australian 1880-1840 Ma felsic volcano-plutonic suite: A model for intracontinental felsic magma generation. Precambrian Research, 41: 37-60.

XAVIER, R. P. 1983. Estudo Petrográfico do Minério da Jazida Salobo-3A/Carajás-Pará. Universidade de Campinas-Docegeo, unpublished report.

YODER, H. S. Jr., and TILLEY, C. E. 1962. Origin of Basalt magmas: An Experimental Study of Natural and Synthetic Rock Systems. Journal of Petrology, Part 3, 3: 342-532.